A Magnetotelluric Investigation of Geoelectrical Dimensionality and Study of the Central Betic Crustal Structure

Anna Martí i Castells
Barcelona, 2006
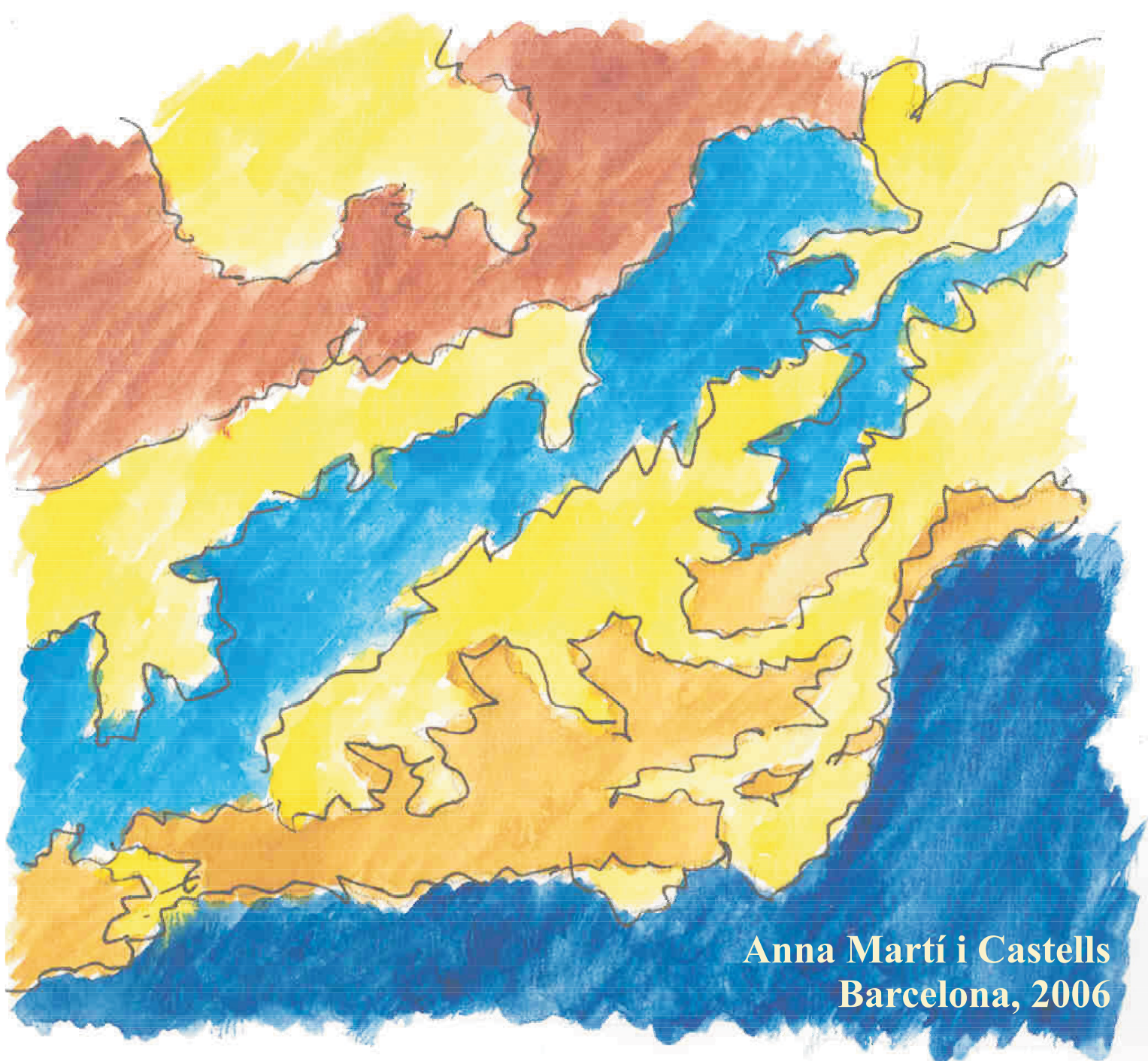
Universitat de Barcelona

Departament de Geodinàmica i Geofísica

A Magnetotelluric Investigation of Geoelectrical Dimensionality and Study of the Central Betic Crustal Structure

Memòria presentada per Anna Martí i Castells per optar al Títol de Doctora en Física

Aquesta tesi ha estat realitzada dins el Programa de Doctorat Ciències de la Terra, bienni 1999-2001, de la Universitat de Barcelona, sota la direcció de la Dra. Pilar Queralt i Capdevila i el Dr. Eduard Roca i Abella.

Anna Martí i Castells

Barcelona, maig de 2006

Dra. Pilar Queralt i Capdevila   Dr. Eduard Roca i Abella

Als meus pares

Table of Contents

List of Tables

List of Figures

Nomenclature, Abbreviations and Terminology

Nomenclature

$\vec{E}$ (V/m)   electric field

$\vec{H}$ (A/m)   magnetic field

$\vec{B}$ (T)   magnetic induction

$\vec{D}$ (C/m^2)   electric displacement

ρ_V (C/m^3)   electric charge density (free charges).

$\vec{j}$ (A/m^2)   current density

σ (S/m)   electric conductivity

ρ (=1/σ)($\Omega \cdot$m) electric resistivity

ε (F/m)   dielectric permittivity

μ (H/m)   magnetic permeability

t (s)   time

ω (rad/s)   angular frequency

f (Hz)   frequency

T (s)   period

δ (m)   skin depth

$\underline{Z}$ (ω) (Ω)   impedance tensor (2x2)

$\underline{M}$ (ω) (m/s)   magnetotelluric tensor (2x2) [1]

ρ_{ij} (ω) ($\Omega\cdot$m)   apparent resistivity [2]

φ_{ij} (ω) (^{o})   phase

$\vec{T}$ tipper vector (x,y components)

---

[1] $\underline{M}_R$ regional tensor; $\underline{M}_m$ measured tensor; $\underline{M}_{2D}$ two-dimensional tensor; $\underline{M}'$ measured in a rotated reference frame.

[2] $ij=xx,xy,yx,yy$; or ij=11,12,21,22; or ij=TE (transversal electric), TM (transversal magnetic), 1D (one-dimensional), 2D (two-dimensional).

$\alpha\ (^{o})$	arbitrary rotation angle
$\theta\ (^{o})$	strike angle
C	galvanic distortion matrix (2x2)
$\varphi_t,\ \varphi_e,\ \varphi_s\ (^{o})$	twist, shear and anisotropy angles (Groom & Bailey notation)
$g,\ t,\ e,\ s$	gain, twist, shear and anisotropy parameters (Groom & Bailey notation)
$g_1,\ g_2$	distortion parameters (Smith notation)
$\phi_1,\ \phi_2\ (^{o})$	distortion angles (Smith notation)
var(x)	variance of magnitude x
σ_x (or $\sigma(x)$)	standard deviation of x
δ_x (or $\delta(x)$)	error of x
xyz and x'y'z'	reference frames and reference frame rotated around z axis
$R_\alpha,\ R^T{}_\alpha$	clockwise rotation matrix and its transpose
$S_1,\ S_2,\ D_1,\ D_2$ (m/s)	modified impedances
$\kappa,\ \mu,\ \eta,\ \Sigma$	Bahr invariant parameters
$\zeta_i = \xi_i + \eta_i i$ (m/s)	linear combinations of M_{ij} components (i=1,2,3,4)
d_{ij}	complex parameters computed from ζ_i and ζ_j
I_1 (m/s), I_2 (m/s), $I_3,\ I_4,\ I_5,\ I_6,\ I_7,\ Q$	WAL rotational invariant parameters
$\alpha,\ \beta,\ \gamma,\ \delta\ (^{o})$	Mohr circle related angles
$\theta_1,\ \theta_2,\ \theta_3,\ \theta_D\ (^{o})$	strike angles obtained for different dimensionality cases from WAL criteria
$X,\ Y$ (m/s)	real and imaginary parts of tensor $\underline{M}$
Φ	phase tensor (2x2)
S	singular matrix of the phase tensor
$\Phi_{Max},\ \Phi_{min}$	maximum and minimum components of the singular matrix S
$\varphi_{Max},\ \varphi_{min}\ (^{o})$	arctangents of Φ_{Max} and Φ_{min}
α_P and $\beta_P\ (^{o})$	phase tensor related angles. β_P = phase tensor skew
rndG(x)	pseudo-random number following a Gaussian distribution with average zero and standard deviation x
n	number of realizations
N	number of resamples
τ_x	threshold value for a magnitude x

x

Acronyms and Abbreviations

MT	Magnetotelluric Method
TE	Transversal electric
TM	Transversal magnetic
1D	one-dimensional
2D	two-dimensional
3D	three-dimensional
3D/2D	galvanic distortion over a regional 2D
3D/2Dtwist	galvanic distortion (only twist component) over a regional 2D
3D/1D2D	galvanic distortion over a regional 1D or regional 2D (indistinguishable)
3D/2Ddiag	galvanic distortion over a regional 2D resulting in a diagonal tensor
WAL	Weaver *et al.* (2000)
B-Q	Bahr-Q method
RR	Remote reference
DG-UB	Departament de Geodinàmica i Geofísica. Universitat de Barcelona
DG-UG	Departamento de Geodinámica. Universidad de Granada
MS03	Metronix equipment, 1st generation
GMS-06	Metronix equipment, 2nd generation
ADU-06	Metronix data logger
MFS-06	Metronix coils

Terminology

true value (x)	value of a magnitude computed directly from the values of the magnitudes from which it is dependent
statistical value (x')	value of a magnitude obtained as the mean value of different estimations of the magnitudes from which it is dependent by using random values of these magnitudes inside their error bars.
bias	absolute value of the difference between the statistical and true values of the same magnitude

Resum

Introducció, Objectius i Estructura

Des de les dècades dels 80 i 90, la majoria d'estudis corticals i litosfèrics inclouen – de manera complementària a altres propietats geofísiques – la caracterització de la conductivitat elèctrica del subsòl que aporta una informació molt valuosa a l'hora d'interpretar l'estructura i evolució tectònica d'una determinada zona (p.ex. Jones, 1992; Hjelt and Korja, 1993; Brown, 1994; Nover, 2005; i referències incloses). Degut al seu ampli rang de variació, la conductivitat elèctrica aporta informació independent de les propietats físiques de l'escorça, inaccessible mitjançant altres mètodes geofísics, com ara la sísmica.

La conductivitat elèctrica és molt sensible a un ampli rang de paràmetres petrològics i geofísics: l'abundància i distribució de minerals conductors, el volum i forma dels porus en les roques i la conductivitat dels fluids circulant per aquests porus. En els primers centenars de metres, aquestes propietats estan controlades per les litologies més superficials, salinitat i contingut d'aigües subterrànies, distribució de les fractures i contingut d'argiles. En l'escorça terrestre, estan controlades per les unitats geològiques, les concentracions i connectivitat de materials metàl·lics i grafit, zones de fractura, fases aquoses i temperatura. Al mantell superior, altres processos, com ara fusió parcial i possiblement difusió d'hidrògen, juguen un paper important.

La conductivitat elèctrica del subsòl a escales corticals o inferiors s'obté normalment mitjançant sondeigs magnetotel·lúrics. El mètode magnetotel·lúric (MT) utilitza energia electromagnètica de font natural per a caracteritzar les propietats elèctriques de les estructures

del subsòl, permet un marge molt ampli de penetració, és sensible a variacions laterals i verticals de la conductivitat i permet caracteritzar estructures volumètriques.

En aquest context, la Serralada Bètica (o Bètiques) és un orogen Alpí situat a la part més occidental de la Mediterrània, en el que els estudis d'MT poden contribuir a augmentar el coneixement de la seva estructura cortical, mitjançant els models geoelèctrics resultants. En aquesta tesi s'han processat, modelitzat i interpretat dades de la part central de les Bètiques, procedents de campanyes anteriors i de la campanya realitzada dins d'aquesta tesi (2004).

Una part molt important en qualsevol estudi d'MT és l'anàlisi de la dimensionalitat de les dades, en particular del tensor magnetotel·lúric, que permet modelitzar les estructures com a 1D, 2D o 3D.

Les dades MT poden estar afectades de distorsions, que emmascaren la dimensionalitat de les estructures geoelèctriques. Aquestes distorsions s'han d'identificar i corregir, o, alternativament, incloure-les en la modelització.

Existeixen diferents mètodes per a realitzar l'anàlisi de la dimensionalitat i la identificació i correcció de les distorsions, que han contribuït significativament al desenvolupament del mètode magnetotel·lúric. No obstant, la majoria d'aquests mètodes es centren en un tipus determinat de dimensionalitat, utilitzant un conjunt particular de paràmetres que caracteritzen només una part del tensor magnetotel·lúric. Com a conseqüència, en diverses ocasions aquests mètodes s'han utilitzat incorrectament, enlloc de limitar la seva aplicació a ser simplement una eina per al contrast d'hipòtesis. Aquest fet comporta sovint una modelització automàtica 2D de les dades. En comptes d'això, caldria fer una anàlisi més acurat de la dimensionalitat de les dades, per tal de poder limitar per a quin subconjunt de dades és valida cada descripció de la dimensionalitat.

En aquest sentit, la primera part de la tesi s'ha concentrat en l'anàlisi de la dimensionalitat. S'han estudiat i comparat diferents mètodes, alguns ben coneguts i altres més recents, emfatitzant en solucionar els problemes associats a les dades reals, on cal considerar els errors i la no correspondència amb els casos ideals. Tota aquest treball ha estat guiat per la idea que és necessari treballar amb el màxim d'informació possible de les dades, en aquest cas, les components del tensor MT, i que cal assumir que les dades són 3D, amb casos particulars en que poden ser 1D o 2D. Aquesta recerca ha estat realitzada utilitzant les bases de dades COPROD2 i BC87 (ben conegudes per la comunitat MT, apèndixs B i C), dades de models sintètics, i dades adquirides a la part central de la Serralada Bètica.

La segona part de la tesi ha consistit en l'estudi magnetotel·lúric de la part central de la Serralada Bètica. Aquest estudi ha comprès l'adquisició i processat de les dades, l'anàlisi de la dimensionalitat, en el qual s'han aplicat algunes de les millores desenvolupades en la primera part; i la modelització. Gràcies als avenços en tècniques informàtiques, especialment en velocitat i capacitat de memòria, es va construir un model geoelèctric 3D de l'estructura cortical

de les Bètiques centrals. Prèviament, es va fer una revisió del model 2D ja existent, i es van crear nous models 2D com a imatges prèvies del model 3D.

Així, els objectius d'aquesta tesi es poden resumir en dos:

1) realitzar un estudi dels mètodes d'anàlisis de la dimensionalitat en dades d'MT, i crear unes eines útils per a realitzar aquest anàlisi en dades afectades de soroll.

2) obtenir un model geoelèctric de l'estructura cortical de la part central de la Serralada Bètica, a partir d'un estudi complert de les dades adquirides amb anterioritat i al llarg de la realització de la tesi.

La memòria de la tesi s'ha organitzat en tres parts principals:

Part I: "Introducció al Mètode Magnetotel·lúric". S'introdueixen els fonaments del mètode MT i els principals elements en qualsevol estudi (capítol 1). En el capítol 2 s'expliquen amb més detall els mètodes utilitzats en l'anàlisi de la dimensionalitat. Aquests mètodes són els invariants de WAL, els paràmetres de Bahr, i el tensor magnetotel·lúric de les fases, amb què s'han basat els aspectes metodològics desenvolupats en aquesta tesi.

Part II: "Contribucions Metodològiques a l'Estudi de la Dimensionalitat Geoelèctrica". En aquesta part es presenten els estudis realitzats en l'anàlisi de la dimensionalitat. El capítol 3 mostra com implementar el criteri dels invariants de WAL en dades afectades de soroll, incidint en la propagació d'errors i en la determinació del valor llindar. S'ha creat un programa informàtic (WALDIM) per implementar el mètode proposat. El capítol 4 proposa la unificació dels criteris de WAL i Bahr, fent-los compatibles. El capítol 5 presenta un estudi del tensor magnetotel·lúric de les fases, com a una nova eina per determinar la dimensionalitat. S'aplica a diferents dades sintètiques i reals, i es compara amb altres mètodes.

Part III: "Estudi Magnetotel·lúric de l'estructura cortical de les Bètiques Centrals". En aquesta part es mostra tota la recerca portada a terme a la part central de les Bètiques. El marc geològic i geofísic es presenta al capítol 6. El capítol 7 explica els processos d'adquisició i processat de dades, que inclouen l'ús de diferents instruments i eines de processat, així com una descripció de les respostes MT obtingudes, i la seva qualitat. El capítol 8 mostra els resultats de l'anàlisi de la dimensionalitat, utilitzant el programa WALDIM, i contrastant-los amb altres mètodes. En el capítol 9 es presenta una revisió del model 2D MT previ i els resultats dels nous models 2D obtinguts mitjançant diferents algorismes d'inversió a la Zona Interna de les Bètiques. El capítol 10 descriu la construcció del model 3D, el model resultant, els ajustos de les respostes i la interpretació i discussió del model.

Finalment es presenten les conclusions de la tesi i les perspectives de futur, tant en el context de la dimensionalitat com en el coneixement de l'estructura geoelèctrica de les Bètiques.

Aquesta memòria es complementa amb sis apèndixs: expressions dels errors dels invariants de WAL, informació dels conjunts de dades utilitzats, detalls de l'adquisició de les dades MT de les Bètiques i les seves respostes, comparacions entre les respostes de les dades i del model 3D, i una demostració matemàtica.

Part del treball desenvolupat en aquesta tesi ha estat publicada en tres articles en la revista Geophysical Journal International:

Ledo, J.J., Queralt, P., Martí, A. and Jones, A.G., 2002. Two-dimensional interpretation of three-dimensional magnetotelluric data: an example of limitations and resolution. *Geophys. J. Int.,* **150**, 127-139.

Martí, A., Queralt, P. and Roca, E., 2004. Geoelectric dimensionality in complex geologic areas: application to the Spanish Betic Chain. *Geophys. J. Int*., **157**, 961-974.

Martí, A., Queralt, P., Jones, A.G. and Ledo, J.J., 2005. Improving Bahr's invariant parameters using the WAL approach. *Geophys. J. Int*., **163**, 38-41.

Actualment, es troba en preparació un quart article sobre la modelització 3D i interpretació de les dades MT de la part central de les Bètiques.

A continuació es presenta un resum dels capítols desenvolupats dins de les dues parts principals de la tesi: **Contribucions Metodològiques a l'Estudi de la Dimensionalitat Geoelèctrica** i **Estudi Magnetotel·lúric de l'Estructura Cortical de la Part Central de la Serralada Bètica**. Aquest resum finalitza amb la presentació de les contribucions i conclusions finals de la tesi i les perspectives de futur.

Contribucions Metodològiques a l'Estudi de la Dimensionalitat Geoelèctrica

Tal com ja s'ha dit, el principal objectiu d'aquesta part ha estat fer un estudi crític dels principals mètodes per a l'anàlisi de la dimensionalitat geoelèctrica a partir del tensor d'impedàncies o el tensor magnetotel·lúric. Els mètodes investigats han estat els criteris dels invariants de WAL (Weaver *et al.*, 2000), els paràmetres invariants de Bahr (Bahr, 1991) i el tensor magnetotel·lúric de les fases (Caldwell *et al.*, 2004), tots ells explicats al capítol 2.

Capítol 3: Anàlisi d'errors i valors llindar en els invariants rotacionals de WAL

En aquest capítol es desenvolupen diferents aspectes analitzats en l'estimació d'errors dels invariants de WAL i la determinació del valor llindar a utilitzar en l'anàlisi de la dimensionalitat. Així, es proposa un nou mètode que permet la caracterització de la

dimensionalitat geoelèctrica en situacions reals. Addicionalment, s'ha creat un programa informàtic per a poder implementar aquest mètode.

El mètode de WAL utilitza set paràmetres del tensor magnetotel·lúric ($\underline{M}$) que són independents i invariants sota rotacions (invariants), i el paràmetre depenent, també invariant, Q (I_1, I_2, I_3, I_4, I_5, I_6, I_7 i Q). Els criteris de dimensionalitat es basen en l'anul·lació o no anul·lació d'alguns d'aquests paràmetres (I_1 i I_2 no s'utilitzen ja que aporten informació sobre la magnitud de la resistivitat però no de la dimensionalitat). Els casos de dimensionalitat que es poden determinar són: 1D, 2D o 3D, i els casos afectats de distorsió galvànica: 3D/1D2D, 3D/2Dtwist, 3D/2Ddiag i 3D/2D (Taula 2.2).

No obstant, fora de les condicions ideals, és a dir, degut a l'error de les dades i a que les estructures reals mai s'ajusten a casos perfectament 1D, 2D o 3D, és necessari introduir un valor llindar per a poder discernir entre diferents tipus de dimensionalitat. Altrament, els invariants mai podrien ser considerats nuls i es tindrien sempre estructures 3D. Donat que els invariants utilitzats en els criteris de la dimensionalitat són adimensionals i estan normalitzats a la unitat, es pot utilitzar el mateix valor llindar per a tots ells.

Així, s'ha realitzat un estudi del mètode de WAL per tal de fer-lo extensiu a l'anàlisi de la dimensionalitat en dades reals afectades de soroll i tenint en compte fins a quin punt les estructures geoelèctriques es poden aproximar als casos ideals 1D, 2D i 3D. Per a dur a terme aquesta tasca, s'han investigat la propagació d'errors de les dades als invariants i els valor llindars a utilitzar per a establir els criteris de dimensionalitat.

Pel que fa a l'estimació dels errors, s'han abordat tres mètodes utilitzant dades reals amb soroll (estacions 85_314 de la base de dades COPROD2 i b23 de les dades MT de les Bètiques): propagació clàssica d'errors (apèndix A), generació de soroll gaussià, i mètodes de remostreig, concretament el Bootstrap. D'entre aquests mètodes, la propagació clàssica d'errors ha demostrat ser la més estable per a l'estimació dels errors dels invariants, mentre que la generació de soroll gaussià és més adequada per a l'estimació de la direcció de l'*strike* i els angles de distorsió.

Per a la determinació del valor llindar, s'ha treballat amb les mateixes dades reals, tenint en compte els seus errors. D'aquesta manera, per tal d'establir si un invariant és nul o no, cal tenir en compte la seva barra d'error i la seva posició respecte l'error llindar (Figura 3.4). S'han analitzat els resultats de l'anàlisi de la dimensionalitat, amb les corresponents direccions d'*strike*, angles de distorsió i errors, havent utilitzat diferents valors llindar. L'objectiu ha estat trobar un rang de valors llindar que donin uns tipus de dimensionalitat coherents amb els paràmetres associats, per exemple: que en els casos 2D, la direcció de l'*strike* quedi determinada amb un error baix. Per a les dades utilitzades, amb una qualitat de les dades mitja - alta, aquest rang de valors és de 0.1 a 0.15.

Com a producte d'aquest treball, s'ha creat un programa informàtic per a dur a terme l'anàlisi de la dimensionalitat de dades MT utilitzant els criteris de WAL i considerant que les dades poden estar afectades de soroll (Figura 3.10). El programa permet a l'usuari determinar el tipus d'estimació dels errors, triar el valor llindar dels invariants, i classificar i promitjar els resultats per rangs de períodes. Aquest programa, anomenat WALDIM, ha estat provat amb èxit en diferents conjunts de dades.

Capítol 4: Millora dels paràmetres de Bahr mitjançant el mètode de WAL

Amb anterioritat als criteris de WAL, els paràmetres de Bahr (κ, μ, η i Σ) (Bahr, 1991; amb modificacions de Szarka, 1999) han estat, i són encara, molt utilitzats per a fer l'anàlisi de la dimensionalitat. Aquests paràmetres són quatre, també invariants sota rotacions, i permeten establir uns criteris (Taula 2.1) basats en uns valors llindar definits per l'autor, per a classificar els tipus de dimensionalitat i la distorsió de que poden estar afectats.

No obstant, aquests criteris sovint han estat utilitzats inadequadament. Particularment, per al paràmetre η (Skew regional), utilitzat per a identificar si la dimensionalitat és 3D, sovint s'imposa en ambdós sentits una condició que només és vàlida en un, fet que porta a interpretacions incorrectes.

Al costat dels criteris de WAL, que utilitzen 8 paràmetres, l'ús de només quatre paràmetres en Bahr porta també a ambigüitats i a no poder distingir els mateixos casos de dimensionalitat que utilitzant el mètode de WAL. A més a més, els valors dels llindars usats en cadascun dels mètodes porten a diferents descripcions de la dimensionalitat (Taula 4.1).

És per això que s'ha treballat en fer una comparació entre els mètodes de WAL i Bahr, i en modificar el mètode de Bahr, ja que és el que no aporta tanta informació com el mètode de WAL i el que dóna lloc a més ambigüitats, per tal de fer ambdós mètodes equivalents.

Inicialment s'han calculat les relacions analítiques entre els paràmetres de Bahr i els de WAL, posant els primers en funció dels segons, concretament dels invariants I_3, I_4, I_5, I_6, I_7 i Q, i r, definit com el quocient entre I_2 i I_1 (veure equacions 4.2).

A partir d'aquestes relacions, s'han determinat els valors que han de prendre els paràmetres de Bahr, en els casos ideals de dimensionalitat definits pels criteris de WAL, és a dir, fixant els invariants de WAL a valors iguals o diferents a zero. Així, s'han obtingut les següents condicions, que modifiquen els criteris de Bahr:

a) Si la dimensionalitat és 1D o 2D, el paràmetre μ ha de ser nul.

b) Les condicions $\kappa \neq 0$ i $\mu \neq 0$ no són necessàries per a la tridimensionalitat.

c) Si l'estructura no és 3D, $\eta = 0$ (el contrari no té perquè complir-se).

El següent pas ha estat redefinir uns nous valors llindars per als paràmetres de Bahr a partir de les relacions analítiques i del llindar utilitzat en WAL, τ_W. Aquests nous llindars també depenen de r, ja que el valor d'aquest paràmetre no ve condicionat pel tipus de dimensionalitat.

Analíticament és impossible trobar exactament aquestes relacions, ja que la condició per a cada tipus de dimensionalitat és que els valors dels paràmetres estiguin dins d'uns determinats rangs (per sobre o per sota d'un valor llindar), sense que aquests valors siguin iguals entre ells ni que prenguin valors concrets.

És per aquesta raó que s'ha abordat el problema mitjançant dos desenvolupaments diferents:

1) Desenvolupament analític aproximat, en el que es suposa que tots els invariants de WAL prenen un mateix valor llindar, τ_W. A partir d'aquí es van determinar les expressions, aproximades, dels llindars dels paràmetres de Bahr, τ_κ, τ_μ, τ_η i τ_Σ (equacions 4.8 i Figura 4.1).

2) Desenvolupament estadístic: per cada tipus de dimensionalitat es van generar valors aleatoris per cadascun dels invariants, per sobre o per sota del valor llindar, segons correspongués. A partir de cada generació de valors, es van calcular els quatre paràmetres de Bahr, tenint en compte les relacions analítiques (equacions 4.2), agafant el valor $r = 1$ (aproximació vàlida per a dades experimentals). Finalment, es van calcular els promigs i desviació d'aquestes realitzacions i es van obtenir els nou valors dels llindars de Bahr. Aquest desenvolupament es va realitzar per a diferents valors de τ_W.

Dels resultats del segon desenvolupament, s'han pogut constatar les equivalències entre els llindars de Bahr i de WAL, algunes ja trobades en el primer. Els nous llindars obtinguts són, en conjunt, significativament diferents dels anteriorment definits per Bahr. També s'han establert les noves condicions de dimensionalitat, ara igualades a les de WAL. No obstant, ja que Bahr utilitza un paràmetre menys, aquest mètode no pot distingir entre els casos 3D/1D2D i 3D/2Dtwist.

Aquesta ambigüitat s'ha resolt mitjançant l'addició de l'invariant Q als paràmetres de Bahr. Així, es va definir el mètode Bahr-Q (taula 4.4), que utilitza els quatre paràmetres de Bahr, κ, μ, η i Σ, l'invariant Q, i els corresponents llindars redefinits τ_κ, τ_μ, τ_η, τ_Σ i τ_Q, per a obtenir un anàlisi de la dimensionalitat equivalent al de WAL. El nou mètode ha estat verificat amb dades sintètiques i reals, amb diferents nivells de soroll.

Capítol 5: Aplicació del tensor magnetotel·lúric de les fases i comparació amb altres mètodes

L'objectiu d'aquest capítol ha estat el d'analitzar el tensor magnetotel·lúric de les fases (o tensor de les fases) i aplicar-lo a dades sintètiques i reals per a determinar la resolució dels seus paràmetres, comparar-lo amb els mètodes de WAL, i Groom and Bailey (1989), aquest darrer utilitzat per a la descomposició del tensor d'impedàncies. Finalment, s'ha fet un ajust de la informació aportada pel tensor de les fases a una descripció 2D de les dades.

El tensor de les fases, Φ, és un tensor real de 2x2 components, que es defineix com la fase del tensor magnetotel·lúric $\underline{M}$ (equació 2.28). El tensor de les fases no es veu afectat de distorsió galvànica, però en canvi no és invariant rotacional. Per als diferents tipus de dimensionalitat, 1D, 2D o 3D, el tensor pren expressions i representacions gràfiques particulars, i, juntament amb l'anàlisi dels valors de quatre angles, α_P, β_P, φ_{Max} i φ_{min} (menys el primer, tots invariants rotacionals), permeten utilitzar-lo per a discernir el tipus de dimensionalitat. No obstant, al ser invariant sota distorsió, no permet distingir si les dades n'estan afectades o no.

Després d'exemplificar les expressions del tensor de les fases per als diferents tipus de dimensionalitat, el tensor de les fases, així com els seus errors, s'han calculat per a dades corresponents a un model sintètic (Ledo *et al.*, 2002b), a les que se'ls hi ha afegit errors i distorsió i per a les dades de les estacions 85_314 de COPROD2 i 14 del BC87. En tots els casos, els errors s'han determinat mitjançant la generació de soroll gaussià. Els resultats mostren que la dimensionalitat determinada mitjançant el tensor de les fases s'adiu, en el primer cas, a l'estructura del model sintètic, i en els altres, a la dimensionalitat determinada amb els mètodes de WAL i Bahr-Q. Pel que fa als efectes dels errors i a la distorsió, se n'han tret les següents conclusions:

1) Els errors dels angles del tensor de les fases, així com els biaixos entre els seus valors reals i estadístics, són importants, fins i tot amb nivells de soroll de les dades molt baix (1% i 2.5%).

2) En casos de distorsió extrema (angles de *twist* i *shear* propers a 45°), el tensor de les fases no és invariant, i els valors de φ_{Max} i φ_{min} prenen valors extremadament elevats.

En la comparació entre el tensor de les fases i els invariants de WAL, s'ha trobat una coincidència entre la diferència d'angles $\varphi_{Max} - \varphi_{min}$ i l'invariant rotacional Q, quan les dades no estan afectades de distorsió galvànica. Pel contrari, en presència de distorsió, $\varphi_{Max} - \varphi_{min}$ segueix tenint el mateix valor, mentre que el valor de Q varia (Q no és invariant sota distorsió, excepte en el cas 3D/1D2D), i, per tant, aquesta equivalència desapareix. Aquesta relació entre la equivalència o no depenent de l'existència o no de la distorsió galvànica obre la porta a un

mètode per a poder identificar la distorsió galvànica, fins i tot en casos 3D, on els altres mètodes no permeten fer-ho.

El mètode de Groom and Bailey (1989) (G&B) consisteix en la descomposició del tensor d'impedàncies com el producte d'una matriu de distorsió afectant un tensor 2D, més una rotació. Donat que la distorsió galvànica és independent del període de mesura, si en una mateixa estació s'obtenen els mateixos paràmetres de distorsió, i entre diferents estacions una mateixa direcció d'*strike*, és possible recuperar el tensor regional 2D per a una posterior modelització. Aquest mètode es va comparar amb el tensor de les fases, ja que ambdós permeten recuperar la direcció de l'*strike*. Utilitzant el site 14 del BC87, de la qual se'n coneixen diferents descomposicions obtingudes a partir de G&B (Jones *et al.*, 1993), s'han pogut constatar les diferències entre els dos mètodes, degudes a la hipòtesis de bidimensionalitat que s'aplica en G&B, i al fet de treballar només amb la informació de les fases (la meitat de la del tensor magnetotel·lúric) en el tensor de les fases.

Finalment, s'ha desenvolupat un codi per a ajustar les dades del tensor de les fases a un model 2D, similarment al mètode de G&B. Els resultats han estat bastant inconsistents, degut al limitat nombre de dades amb que es treballa, pel fet ja citat, de treballar amb la meitat de la informació del tensor d'impedàncies.

Estudi Magnetotel·lúric de l'Estructura Cortical de la Part Central de la Serralada Bètica

Capítol 6: Context geològic i geofísic

Aquest capítol recull una descripció geològica general i el coneixement geofísic de la Serralada Bètica i el Mar d'Alborà, amb l'objectiu de restringir la posterior interpretació de les dades magnetotel·lúriques adquirides a la part central de les Bètiques.

La Serralada Bètica (o Bètiques) (Figura 6.1) és una serralada alpina situada a l'extrem occidental del Mediterrani. S'estén des del Golf de Càdis fins al Cap de la Nao, i continua cap al nord-est fins a les Illes Balears. Juntament amb la cadena del Rif a Àfrica, formen un arc orogènic que envolta l'actual Conca d'Alborà. Aquest arc es va formar com a conseqüència de la convergència entre les plaques Africana i Ibèrica des del Cretaci Superior (60 Ma).

Segons la seva evolució geològica, la Serralada Bètica es divideix en dues zones ben diferenciades estratigràficament i estructural: la *Zona Externa* i la *Zona Interna* (Figura 6.2).

La **Zona Externa** està constituïda per la cobertora Mesozoica del paleomarge Sud Ibèric de l'antic oceà Tethys i aflora a la part nord-est de la serralada. Comprèn les zones *Prebètica*, formada per sediments marins poc profunds, i *Subbètica*, formada per fàcies pelàgiques i materials volcànics.

Entre les zones Externa i Interna, hi ha les unitats del *Flysch*, sediments marins profunds, que estructuralment se situen, en general, per sota de la Zona Interna.

La **Zona Interna**, al sud-est, està formada per roques metamòrfiques del Paleozoic i Mesozoic pertanyents al Domini d'Alborà (Balanyá i García-Dueñas, 1987). La seva estructura és molt complexa, formada per diverses làmines encavalcants emplaçades durant el Miocè, i posteriorment afectades per falles normals de baix angle, durant l'obertura de la Conca d'Alborà (finals de l'Oligocè-Miocè). Aquestes falles extensionals s'associen al desenvolupament de les conques intramontanyoses en el Neogen i Quaternari. Una d'aquestes conques, a la zona del Cap de Gata, inclou roques calc-alcalines del vulcanisme del Neogen.

D'acord amb els registres estràtigràfics i les condicions de metamorfisme, les diferents làmines encavalcants de la Zona Interna es divideixen en tres complexos metamòrfics separats per falles normals de gran angle. D'inferior a superior, aquests són: el complex Nevado-Filábride, l'Alpujárride i el Maláguide-Dorsal (Figura 6.3).

La Serralada Bètica encavalca sobre el Massís Ibèric, pertanyent a la orogènica Varisca. Prop de la Serralada Bètica, el Massís Ibèric és cobert pels sediments neogens de la Conca de Guadalquivir, que, elongada ENE-WSW, constitueix la conca d'avantpaís de la Serralada Bètica.

En l'actualitat, s'accepta que l'evolució geodinàmica de la regió Bètica-Alborà-Rif (BAR) inclou un estadi de subducció i acreció orogènica, seguida d'un estadi de compressió al llarg de l'arc de Gibraltar, coetània a una extensió que va obrir la Conca d'Alborà. No obstant queden qüestions a resoldre sobre aquests processos, dels que se n'han proposat diferents models geodinàmics: Sobre la subducció inicial (Doglioni *et al.*, 1999, veure Figura 6.4; Jolivet and Faccenna, 2000); i sobre la natura de la compressió i extensió i simultànies. D'aquest darrer, se n'han proposat principalment tres models (Figura 6.5): a) Destitució convectiva de litosfera engruixida (Platt and Vissers, 1989); b) Col·lapse gravitatori d'una litosfera engruixida (Seber *et al.*, 1996); i c) regressió cap al oest d'un fragment de la placa Africana subduint (Royden, 1993; Lonergan and White, 1997; Gutsher *et al.*, 2002).

Dins d'aquest context geodinàmic, un nombre significatiu d'estudis geofísics realitzats mostren que l'estructura de l'escorça i litosfera de les Bètiques és molt complex i difícil de caracteritzar, fet que ha portat al desenvolupament d'interpretacions molt diferents sobre l'estructura profunda de la Serralada Bètica.

En aquesta tesi, se subratllen els principals resultats dels diferents estudis geofísics realitzats a les Bètiques, posant èmfasi a l'estructura cortical i litosfèrica de la seva zona central. Aquests inclouen **gravimetria** (secció 6.2.1; Figura 6.6), **magnetisme** (6.2.2; Figura 6.7), **sísmica de refracció** (6.2.3), **sísmica de reflexió** (6.2.4; Figura 6.9 i Figura 6.10), **anàlisi de la sismicitat i tomografia sísmica** (6.2.5; Figura 6.11 i Figura 6.12), **flux de calor** (6.2.6; Figura

6.13) i **magnetotel·lúrica** (6.2.7; Figura 6.14); a més de diversos estudis multidisciplinars. Les principals característiques que es reconeixen són:

- Gruixos corticals entre 30 km i 40 km sota les zones Interna i Externes, superiors en promig als del Massís Ibèric (30 km – 35 km). El gruix cortical màxim, d'acord amb estudis gravimètrics, es localitza sota la Conca de Guadix-Baza, fet que indica l'absència d'una arrel significativa sota les màximes elevacions de les Bètiques, a Sierra Nevada. El gruix cortical decreix cap a la costa, on assoleix valors de 20 km – 25 km, i continua decreixent fins assolir valors mínims sota el Mar d'Alborà (13 km – 16 km).
- Continuïtat del Massís Ibèric per sota de les Bètiques.
- Presència d'un cos anòmal a nivells d'escorça inferior sota la Zona Interna, amb baixa resistivitat elèctrica i baixes velocitats sísmiques.
- Fragment d'elevada velocitat sísmica en el mantell litosfèric sota la Zona Interna i el Mar d'Alborà.

Capítol 7: Adquisició i processat de dades: avaluació de les respostes MT

Les dades utilitzades en l'estudi magnetotel·lúric de les Bètiques es van adquirir en les campanyes realitzades durant els anys 1994 i 1995, en que les dades s'han processat o reprocessat, i en la nova campanya, realitzada dins aquesta tesi, el 2004, realitzant tota l'adquisició i reprocessat (apèndix D).

En les primeres campanyes (94-95) es van registrar fins a 41 estacions, localitzades aproximadament al llarg d'un perfil NW-SE, coincidint amb línies sísmiques ja existents, creuant des del Sud del Massís Ibèric fins al Mar d'Alborà (Figura 7.1). El reprocessat de les dades s'ha fet mitjançant una inspecció visual de les sèries temporals. Les respostes obtingudes tenen un rang de períodes de 4 ms a 4000 s, valors de coherència mitjà-alt, i barres d'errors grans, especialment als períodes més llargs. En total es va recuperar un conjunt de 33 estacions. Respecte al processat ja existent, la qualitat de les respostes s'ha mantingut on aquesta ja era alta, i s'ha millorat en les estacions amb coherències més baixes i barres d'errors grans.

La campanya de 2004 es va realitzar en col·laboració entre el DG-UB i el DG-UG, utilitzant equips Metronix de nova generació, que presenten importants avantatges (millor qualitat de les dades, bobines sensibles a un rang més ample de períodes i possibilitat de fer adquisició en referència remota) respecte als equips antics. En total es van adquirir dades de 10 estacions, localitzades des de l'est de Granada fins a Almeria, creuant els complexos Nevado-Filábride i Alpujárride, amb l'objectiu d'obtenir una major cobertura d'aquesta zona (Figura 7.1). Les sèries temporals s'han processat mitjançant el software Mapros. Les respostes, amb un rang de períodes de 1 ms a 1000 s i 4000 s, es caracteritzen per un alt elevat nivell de soroll, coherències baixes, però qualitat mitjana-alta.

Malgrat realitzar també adquisició en la banda HF, aquestes dades no s'han inclòs, degut a la seva baixa qualitat. El processat en referència remota va funcionar per a la banda LF3, mentre que a la banda LF4, hauria estat necessària una major distància entre estacions i, per tant, no es va poder utilitzar.

Les resistivitats aparents avaluades a la Zona Interna presenten una part central en que tant ρ_{xy} and ρ_{yx} són decreixents, el que suggereix la presència d'un cos conductor en profunditat.

Capítol 8: Anàlisi de la dimensionalitat geoelèctrica en les dades MT de la Serralada Bètica

L'anàlisi de la dimensionalitat de les dades MT de Bètiques s'ha realitzat mitjançant el programa WALDIM, considerant els errors de les dades i utilitzant uns valor llindars τ_W=0.15 i τ_Q=0.1. En els casos 2D (amb o sense distorsió), l'ambigüitat de la direcció de l'strike s'ha resolt mitjançant la informació dels vectors d'inducció.

Degut als errors, la dimensionalitat no s'ha pogut determinar en un 30% de casos, corresponent majoritàriament a períodes llargs.

Els resultats en cada estació s'han agrupat en bandes de períodes (dècades logarítmiques), per tal de representar la dimensionalitat prevalent i les direccions de l'strike en les diferents àrees i per diferents penetracions (Figura 8.5).

La dimensionalitat és principalment 3D, amb alguns casos 1D localitzats a les conques i pels períodes més curts. Sobre les zones al·lòctones (és a dir, Bètiques Internes i conques) hi ha estructures bidimensionals amb orientacions de N-S a NNE-SSW i de E-W a WNW-ESE, mentre que a les zones autòctones (Massís Ibèric) aquestes estructures bidimensionals s'orienten d'E-W a ENE-WSW. La dimensionalitat més complexa de les Bètiques s'interpreta com a deguda a la superposició de processos que van actuar en la seva evolució, mentre que el Massís Ibèric, només afectat per l'orogènia Varisca, mostra una dimensionalitat més simple. L'abundància de casos 3D augmenta cap al sud i per als períodes més llargs.

La dimensionalitat obtinguda s'ha comparat amb l'obtinguda per altres mètodes. La descomposició de Groom and Bailey utilitzant el programa Strike només s'ajusta a la descripció de WAL si s'utilitzen subconjunts de dades, amb una única estació i pocs períodes (p. ex. Taula 8.1). No obstant, es corrobora que les dades de Bètiques no es poden descriure com a 2D amb una única direcció d'strike prevalent. Els mapes del tensor de les fases (Figura 8.8) confirmen el caràcter complex de la dimensionalitat de les dades.

Els resultats de la dimensionalitat apunten a la modelització 3D com a la millor estratègia per a reproduir les estructures geoelèctriques de l'escorça de les Bètiques centrals. No obstant, es poden construir models 2D utilitzant subconjunts de dades, que poden aportar una imatge prèvia de la distribució de conductivitats.

Capítol 9: Modelització 2D

Malgrat que en el capítol anterior s'ha vist que cal fer un model 3D de la zona d'estudi, els codis d'inversió 3D són molt recents, i els models es segueixen construint mitjançant assaig i error. Mentrestant, la inversió 2D és encara l'eina de modelització més utilitzada. És per això que es presenta aquest capítol sobre modelització 2D, amb els objectius de fer una revisió crítica de l'únic model 2D previ existent, i d'explorar les possibilitats de fer una inversió 2D de dades que són 3D.

El primer model MT de Bètiques (MT1, Pous *et al.*, 1999) es va construir a partir de dades de 15 estacions, projectades al llarg d'un perfil NW-SE (Figura 9.1), d'acord amb la direcció obtinguda en la descomposició de G&B i la informació dels vectors d'inducció. Les correccions d'static shifts es van realitzar només a la part central de la Zona Interna, on les corbes de resistivitat van ser pujades a 1000 Ω·m. El model resultant presentava diferents conductors i resistors superficials, dels que destacava la presència d'un cos conductor sota la Zona Interna, entre 20 km i 40 km de profunditat, que es va interpretar com a fusió parcial.

L'anàlisi de la dimensionalitat ja ha mostrat una major complexitat de la zona. Particularment, a la zona del conductor, aquesta dimensionalitat és 3D (Figura 9.2).

Per tal de determinar la resolució del conductor i la validesa de l'aproximació 2D, s'ha realitzat un estudi de sensibilitat (Schwalenberg *et al.*, 2002) del model MT1. Els resultats (Figura 9.3) mostren que el model té bona resolució fins a 20 km aproximadament, mentre que a profunditats més baixes aquesta disminueix. Les respostes del model són sensibles a la presència del conductor profund. No obstant, pels resultats de la dimensionalitat, la seva continuïtat no està assegurada.

S'han creat tres models 2D a la Zona Interna: EW, NS1 i NS2, al llarg i travessant el complex Nevado-Filábride (Figura 9.4), on les estacions s'han projectat seguint unes direccions d'strike hipotètiques. Els models s'han obtingut mitjançant els codis RLM2DI, invertint el modes TM (Figura 9.7).

El punt feble d'aquestes inversions està en que les dades no són exactament 2D, i que les estacions s'han projectat segons unes direccions d'strike molt qüestionables. Així, estructures locals poden aparèixer extrapolades a tot el model.

El model EW mostra una alternança d'estructures conductores i resistives, fet que es podria atribuir a anisotropia, però que és conseqüència d'haver fet la inversió al llarg d'un hipotètic strike. El conductor més gran assoleix una profunditat màxima de 18 km. Els models NS1 i NS2 presenten també un cos conductor, localitzat sota els aflorament del Nevado-Filábride, amb profunditats màximes de 10 km i 15 km, molt més somers que el cos conductor obtingut del model MT1 previ.

El model NS1 s'ha comparat amb els resultats obtinguts d'altres codis d'inversió, REBOCC i DetREBOCC (REBOCC modificat per a la inversió del determinant), que permeten

invertir el tipper. Amb petites variacions, tots els models presenten un cos conductor amb la seva base localitzada a uns 20 km de profunditat.

D'entre els diferents codis, donada la natura de les dades utilitzades, la inversió del determinant sembla ser la més raonable, ja que inverteix una resposta que conté tota la informació del tensor d'impedàncies i està menys influenciada per la direcció de l'strike.

Capítol 10: Modelització 3D de l'estructura geoelèctrica de les Bètiques centrals

Finalment, s'ha fer la modelització 3D a escala cortical de les Bètiques centrals. El model 3D s'ha construït a partir d'un model inicial, modificat mitjançant assaig i error, a partir de la comparació entre les dades i les respostes del model (calculades mitjançant el codi de Mackie *et al.*, 1993).

Les dades han estat corregides d'static shift, de manera que les corbes xy i yx d'una mateixa estació comencin al mateix nivell, i s'han eliminat els períodes amb més error o amb canvis abruptes en les respostes.

El model inicial s'ha construït a partir de la interpolació de les inversions 1D obtingudes en cada estació. Posteriorment, el model s'ha estès per incloure part del Mar d'Alborà, a la capa d'aigua de la qual se li ha assignat una resistivitat de 0.5 Ω·m. A les primeres capes del model, algunes de les zones conductores o resistents s'han estès per reproduir la geologia superficial. Aquest model inicial té una grandària de 270(NS)x220(EW)x100(z) km, amb una malla de 50x50x25 elements (Figures 10.1 i 10.2).

Després de 140 passos, s'ha obtingut un model satisfactori (bet3D-140), tant pel que fa a l'ajust entre les dades i les respostes (veure Apèndix E), quantificat mitjançant l'rms, com a la suavitat de les seves estructures (Figura 10.3). Aquest model té una bona resolució fins a 40 km de profunditat. Seguint les estructures geològiques en superfície, les principals característiques del model són:

Massís Ibèric: Valors moderats-alts de resistivitat (entre 100 Ω·m i 500 Ω·m). A la part més NW del model apareix el resistent **RIM**, on s'hi encaixa el conductor **CIM**, entre 2.15 i 17.5 km de profunditat.

Conca de Guadalquivir: Valors baixos de conductivitat, que reprodueixen la forma de la conca, amb algunes irregularitats, fins a 900 m (**CGB**). Per sota, els valors de la resistivitat són similars als del Massís Ibèric.

Zona Prebètica: Fins a 2.15 km, valors moderats de resistivitat (20 Ω·m – 50 Ω·m), limitats per sota per valors més alts, d'entre 100 Ω·m i 500 Ω·m. Localment, continuació del conductor **CGB**, fins a 650 m de profunditat.

Zona Subbètica i Conca de Guadix-Baza: Distribució de resistivitats en profunditat similar a la de la Zona Prebètica, amb l'excepció de dues zones conductores, C-20 i C27-38,

localitzades a la part més interna de la zona, assolint profunditats màximes de 7 km i 2.8 km respectivament. Continuació del conductor **CGB** fins a 1.2 km, mentre que el rebliment de la conca de Guadix-Baza no queda ben reproduït.

Zona Interna: És la zona més complexa, amb una zona resistent (**RI**), en la que s'hi encaixen diferents conductors poc profunds localitzats sota la Sierra de las Estancias (**CE**), Sierra de Filabres (**CF1** i **CF2**) i Sierra de Alhamilla (**C-31**) (Figura 10.4). Entre 3.8 km i 17.5 km apareix el conductor **CF3**, sota els **CF1** i **CF2**, amb valors de resistivitat d'entre 1 $\Omega \cdot m$ i 5 $\Omega \cdot m$ (Figura 10.5).

Per tal de conèixer la resolució del model, concretament del darrer conductor **CF3**, s'han fet uns tests de sensibilitat. Aquests tests han consistit en modificar el model, i recalcular els rms, comparant-los amb els del model original. Així, s'ha pogut constatar l'estabilitat de la malla emprada (Taula 10.1). Pel que fa al conductor **CF3**, aquest pot estendre's més cap a l'oest però no reduir la seva extensió horitzontal (Figures 10.9, 10.10 i 10.11); ha de tenir una profunditat màxima situada entre 17.5 i 30 km (Figura 10.12 i Taula 10.2), i ha d'estar en continuïtat amb els conductors CF1 i CF2, o, en tot cas, separat d'ells per una capa resistent prima (< 400 m) (Figura 10.13 i Taula 10.3).

Comparat amb els perfils de sísmica de reflexió fets a la zona, el conductor CGB es pot correlacionar amb el reflector TVB i la base del conductor **CF3** coincideix localment amb el reflector UCR (Figura 10.14). No obstant, el model de conductivitats no permet identificar ni el límit entre l'escorça superior i inferior, ni la Moho; així tampoc es possible detectar la presència d'una arrel cortical sota la Zona Interna. El conductor **CF3** es troba localitzat en una zona de baixa activitat sísmica (Figura 10.16), velocitats v_p relativament altes (Figura 10.17) i coincideix parcialment amb una zona d'anomalia magnètica situada a la part NNW de la Sierra de los Filabres (Figura 10.15). També coincideix amb una topografia elevada, a la que segons els estudis gravimètrics no s'hi associa una arrel cortical significativa.

Interpretació:

Les principals zones resistents del model s'han interpretat com a roques metamòrfiques i granítiques del Massís Ibèric (**RIM**, NW del model), les quals continuen per sota la Zona Externa de les Bètiques, i com a roques metamòrfiques de la Zona Interna de les Bètiques (**RI**). El conductor **CGB** que s'associa al rebliment de la conca de Guadalquivir permet reconèixer la continuació d'aquests sediments per sota la Zona Externa. La conductivitat relativament alta a la Zona Externa s'explica per la circulació de fluids en les roques carbonatades de que està formada. A la Zona Subbètica Interna, la conductivitat és encara més elevada (**C20** i **C27-38**), fet que s'associa a un major contingut en lutites i a la presència de roques basàltiques. En el cas del conductor **C20**, l'augment de la conductivitat es relaciona amb l'existència d'una unitat dels flysch. El model permet veure que aquestes unitats sedimentàries queden parcialment

encavalcades per les roques de la Zona Interna. Els conductors poc profunds situats a la Zona Interna s'interpreten com a circulació de fluids al llarg dels contactes entre les complexes Nevado-Filábride i Alpujárride, o entre diferents unitats del Nevado-Filábride.

Per la seva posició i geometria, el conductor **CF3** s'emplaça en roques Domini d'Alborà. A partir d'informació geològica i geofísica complementària, es descarten la fusió parcial i la circulació de fluids i s'estableix com a causa de la seva elevada conductivitat la presència de fases minerals conductores. Així, el conductor s'associa amb ofiolites o roques d'escorça inferior amb algun tipus de mineralització (grafit o pirita) que fa augmentar la seva conductivitat. Aquesta unitat litològica estaria situada sota el complex Nevado-Filábride, al llarg del nucli del principal antiforme, i estaria limitat en la seva base pel desenganxament basal de els Bètiques (Figura 10.21).

Conclusions

Les contribucions i conclusions d'aquesta tesi es presenten separadament en les seves dues parts principals:

Contribucions metodològiques a l'estudi de la dimensionalitat geoelèctrica

De la revisió dels criteris dels invariants de WAL, aplicats a dades reals, i considerant situacions en que les dades no s'ajusten exactament als casos ideals 1D, 2D i 3D:

- S'ha fet l'estimació dels invariants rotacionals de WAL, els angles relacionats i els seus errors utilitzant tres mètodes, aplicats a dades reals: propagació clàssica d'errors, generació de soroll gaussià i el mètode de remostreig Bootstrap. Els tres mètodes condueixen a resultats semblants, tot i que la propagació clàssica dels errors és el mètode més estable per a l'estimació dels errors dels invariants. Les direccions d'strike i dels angles de distorsió s'han d'estimar utilitzant la generació de soroll gaussià, en que es recomana utilitzar un valor de n=100.

- Pel que fa al valor llindar, s'han analitzat els resultats de la dimensionalitat, amb les corresponents direccions d'strike, angles de distorsió i errors utilitzant diferents valors llindar. S'ha definit com a vàlid el rang de valors que donen una descripció de la dimensionalitat més estable, d'acord amb els errors observats. Aquest rang és de 0.1 a 0.15, vàlid per a dades de qualitat mitja – alta.

- Producte d'aquest estudi, s'ha creat un programa per a dur a terme l'anàlisi de la dimensionalitat segons els criteris de WAL considerant els errors de les dades. Aquest programa, WALDIM, s'ha aplicat amb èxit a diferents conjunts de dades.

De la comparació entre els mètodes de WAL i Bahr, i la revisió del segon per fer-los equivalents:

- S'han obtingut les relacions analítiques entre els paràmetres de WAL i Bahr.
- S'ha proposat un nou mètode, Bahr-Q, que utilitza els paràmetres de Bahr i l'invariant Q. Utilitzant els nous valors llindars definits, ambdós mètodes són equivalents. Els paràmetres de Bahr estan menys afectats d'error i, per tant, el mètode Bahr-Q es pot considerar més robust que el de WAL.

De l'estudi del tensor magnetotel·lúric de les fases:

- S'ha aplicat el tensor de les fases a diferents casos de dimensionalitat, incloent errors i distorsió. S'ha vist com en situacions extremes de distorsió (angle de shear proper a 45°) el tensor de les fases no és invariant sota distorsió.
- Quan les dades no estan afectades de distorsió, la diferència φ_{Max} - φ_{min} calculada a partir del tensor de les fases i el paràmetre Q, tenen valors similars, la qual cosa permetria identificar l'existència de distorsió fins i tot quan afecta estructures regionals 3D.
- La inversió de les dades del tensor de les fases per ajustar-les a una descripció 2D no porta en general a bons resultats, degut a la utilització de només la meitat d'informació del tensor magnetotel·lúric.

Conclusions generals de la primera part:

- En l'anàlisi de la dimensionalitat és important considerar els errors, ja que afecten la determinació de la dimensionalitat sigui quin sigui el mètode utilitzat.
- L'anàlisi de la dimensionalitat més òptim s'obté quan s'utilitza tota la informació del tensor d'impedàncies (o tensor magnetotel·lúric). Les hipòtesis a priori sobre una descripció determinada de la dimensionalitat s'haurien d'utilitzar només per a testejar hipòtesis (en ocasions s'utilitzen com a anàlisi de la dimensionalitat, conduint a interpretacions incorrectes).
- Cal anar en compte a l'utilitzar mètodes com el tensor de les fases, ja que aporten una descripció compacta de la dimensionalitat però, de cara a la modelització, no aporten informació de la distorsió i ,per tant, les dades no es poden corregir.

Estudi Magnetotel·lúric de l'Estructura Cortical de la Part Central de la Serralada Bètica

S'ha presentat una síntesi de les dades geològiques i geofísiques de les Bètiques Centrals, el reprocessat de les dades MT ja existents, i l'adquisició i processat de noves dades,

amb el que s'ha obtingut un conjunt més complert amb el que treballar. De l'anàlisi de la dimensionalitat de les dades, la modelització 2D i 3D i les interpretacions del model, es destaquen els següents resultats i conclusions:

- L'anàlisi de la dimensionalitat mostra la complexitat de les dades MT, pel que s'apunta al 3D com a millor estratègia de modelització. A més, la distribució dels casos 2D sobre la zona d'estudi es poden relacionar amb els processos que han tingut lloc a les Bètiques i al Massís Ibèric: la dimensionalitat més complexa de les Bètiques es relaciona amb els diferents processos que hi han tingut lloc (orogènia Alpina superposada amb materials deformats per l'orogènia Varisca), mentre que el Massís Ibèric, només afectat per l'orogènia Varisca, presenta una dimensionalitat més simple amb una direcció d'strike més constant.

- L'anàlisi de la dimensionalitat i el test de sensitivitat del model previ 2D mostra que no està assegurada l'extensió lateral del conductor profund.

- Els nous models 2D obtinguts de la Zona Interna mostren la presència d'un cos conductor sota la Sierra de los Filabres, més somer que el cos obtingut del model 2D previ.

- De la comparació dels codis d'inversió 2D RLM2DI, REBOCC i DetREBOCC, el darrer, que inverteix les dades del determinant, ha resultat molt eficaç quan les dades no són exactament 2D. Així, la utilització del determinant pot ser també una bona eina per a la modelització 3D.

- Finalment, s'ha creat un model geoelèctric de l'escorça de la part central de les Bètiques. Partint d'un model inicial obtingut de la inversió 1D del determinant i fixant la geometria de les estructures geològiques conegudes, el model s'ha obtingut mitjançant assaig i error, mitjançant el codi de Mackie *et al.* (1993) i utilitzant l'rms per comparar diferents respostes de les dades i el model.

- S'han realitzat diferent tests sobre l'estabilitat del model enfront a la malla utilitzada i sobre l'extensió i profunditat dels cossos principals. A més, el model reprodueix de manera general la dimensionalitat de les dades.

- El model mostra aquestes principals característiques:

  - una zona resistent al Massís Ibèric que s'associa a roques metamòrfiques i granítiques, dins el qual s'hi troba una zona conductora que s'interpreta com a grafit interconnectat. La prolongació de la zona resistent per sota la Zona Externa confirma la continuació del basament Ibèric per sota les Bètiques.
  - un conductor somer relacionat amb circulació de fluids en els sediments de la Conca de Guadalquivir. La forma del conductor mostra que el rebliment de la conca continua per sota de les Bètiques Externes.

- conductivitats moderadament altes a la Zona Externa, associades a circulació de fluids en les roques carbonatades del Prebètic i del Subbètic. En el Subbètic Intern la conductivitat més elevada s'associa a un major contingut de lutites i roques basàltiques, i a la part més oriental d'aquesta zona, a roques de les unitats del flysch.

- a la Zona Interna, una àmplia zona resistent que arriba a uns 13 km de profunditat s'interpreta per la presència de roques metamòrfiques dels complexes Nevado-Filábride i Alpujárride. Diferents conductors poc profunds s'interpreten com a circulació de fluids al llarg dels contactes entre aquests dos complexes o entre diferents unitats del Nevado-Filábride.

- Sota la Sierra de los Filabres, enter 4 km i 17.5 km s'emplaça un cos conductor. D'acord amb els tests de sensibilitat realitzats, aquest cos pot tenir una orientació entre WNW-ESE i E-W i podria assolir profunditats màximes de 30 km.

- D'acord amb la informació geològica i geofísica complementària, el cos conductor profund s'interpreta com una unitat litològica diferenciada formada per ofiolites o roques de l'escorça inferior que contenen una fase mineral conductora, sota el complex Nevado-Filábride. Aquest cos estaria localitzat al nucli de l'anfiforme de Sierra Nevada i Sierra de los Filabres i s'estendria en profunditat fins al nivell de desenganxament de les Bètiques.

Perspectives de futur

Aquesta tesi, que ha resolt alguns aspectes relacionats amb la determinació de la dimensionalitat geoelèctrica en MT i ha obtingut una descripció de les estructures geoelèctriques de l'escorça de les Bètiques centrals, deixa encara una porta oberta a noves investigacions en aquestes mateixes direccions. A continuació es presenten quines són les perspectives de futur com a continuació d'aquesta tesi:

En relació a la determinació de la dimensionalitat geoelèctrica a partir de dades MT:

- Continuar investigant els mètodes basats en els paràmetres invariants rotacionals. Millorar el programa WALDIM mitjançant l'ús de lògica difusa, enlloc d'uns valors llindar fixos, i permetre fer promigs regionals (juntament amb promigs per bandes de períodes). Permetre fixar certes hipòtesis a priori, que es quantificarien mitjançant un valor del desajust (misfit). Finalment, incloure la informació del tipper per eliminar l'ambigüitat de 90° en la determinació de l'strike.

- Investigar l'ús dels invariants rotacionals del tensor MT en presència d'anisotropia. Estudiar si permeten caracteritzar aquesta propietat en les estructures geoelèctriques.
- Optimitzar l'ús dels invariants en la modelització per comparar les respostes de les dades amb les dels models.
- Continuar investigant les relacions entre els angles del tensor de les fases φ_{Max} - φ_{min} i el paràmetre Q de WAL. Establir valors llindar per a tots els paràmetres del tensor de les fases per establir el tipus de dimensionalitat.

En relació a l'estructura geoelèctrica de les Bètiques, el principal resultat ha estat l'obtenció d'un model 3D de l'estructura cortical de les Bètiques centrals, en el que s'ha identificat un cos conductor sota la Zona Interna, a profunditats d'escorça superior – mitja. Investigacions futures d'MT a les Bètiques permetran obtenir més informació sobre aquest cos i cobrir una zona d'estudi més ampla:

- Realitzar una inversió 3D de les dades MT de Bètiques utilitzant el codi de Siripurnvaraporn *et al.* (2005). Actualment s'estan realitzant diferents proves en la utilització del codi. Intentar millorar els ajustos entre les respostes de les dades i del model i comparar-ho amb el model actual.
- Adquirir noves dades, registrant períodes més llargs, per obtenir una millor resolució en profunditat i cobrir una zona d'estudi més ampla. Obtenir dades complementàries per corregir l'static shift i poder fixar els valors de la resistivitat a les capes més superficials.

Degut a l'interès creixent de la zona, dins de la Iniciativa de Recerca PICASSO (Program to Investigate the Cause of the Alboran-AtlaS System convective Overturn) i el projecte de recerca que es desenvoluparà dins d'aquesta iniciativa, les contribucions d'aquesta tesi (conjunt MT de dades, caracterització de la dimensionalitat i model 3D de la zona central de les Bètiques) han proporcionat un punt de partida per a nous estudis MT a realitzar en una zona tant àmplia i complexa. El principal objectiu de PICASSO és determinar l'estructura tridimensional de l'escorça i litosfera, especialment la geometria del mantell superior per reconèixer els processos litosfèrics que hi tenen lloc. S'adquiriran diferents dades geofísiques per a fer una interpretació integrada. Per exemple, una campanya d'MT recent (febrer de 2006), feta en col·laboració entre les universitats de Granada i Barcelona al nord del Marroc, apunta en aquesta direcció. A més, en un futur proper s'adquiriran noves dades d'MT de període llarg cobrint una àrea més ampla de les Bètiques, en col·laboració entre els DIAS, la UG i la UB.

Introduction

Since the 80s and 90s, most crustal and lithospheric studies include - complementary to other geophysical properties – an image of the electrical conductivity of the Earth that provides important constrains on the geological structure and tectonic evolution of a particular area (e.g. Jones, 1992; Hjelt and Korja, 1993; Brown, 1994; Nover, 2005; and references therein). Because of its wide range of variation, the electrical conductivity provides independent information on the physical properties of the crust, almost inaccessible by more traditional methods such as seismic.

The electrical conductivity of rocks is very sensitive to a wide range of petrological and physical parameters: the abundance and distribution of conductive minerals, the volume and shape of pores, and the conductivity of pore fluids. Within the firsts hundred meters these properties are controlled by the surface the lithology, groundwater content and salinity, fracture distribution and clay content. In the Earth's crust, these properties are affected by geological units, the concentrations and connectivity of metallic minerals and graphite, fracture zones, aqueous phases, and temperature. In the upper mantle, other processes, like the degree of chemical depletion, metasomatism, partial melting, and possibly hydrogen diffusion play an important role.

Information on electrical conductivity of the subsurface at a crustal or deeper scale is inferred mainly from magnetotelluric surveys. The magnetotelluric method (MT) utilises natural electromagnetic energy to electrically characterise Earth structures. Its main strengths are that its allowance for a broad range of penetration depths, its sensitivity to lateral and vertical electrical conductivity variations and its capability of imaging volumetric structures.

In this context, the Betic Chain (Spain) is an Alpine orogen located at the western end of the Mediterranean, in which MT studies can improve the knowledge of its complex crustal structure through the resulting geoelectric models. Data from the central part of the Betics, from a previous survey and from the survey performed during this thesis (2004), have been processed, modelled and interpreted.

An important part of any MT study is the dimensionality analysis of the data, in particular of the magnetotelluric tensor, which gives rise to modelling the geoelectric structures as 1D, 2D or 3D.

MT data can be affected by distortions, which mask the dimensionality of the geoelectric structures. These distortions must be identified and removed, or alternatively be included in the models.

Several methods have been presented on dimensionality analyses and the identification and removal of distortions, which have greatly contributed to the development of the MT method. However, most of these methods focus on a specific type of dimensionality, using a particular set of parameters that characterises only a part of the magnetotelluric tensor. As a consequence, sometimes these methods have been misused, as opposed to limiting their application to being a tool for hypothesis testing, resulting in an automatic 2D modelling of the data. Instead, a more careful analysis of the data dimensionality should be performed, limiting the subsets of data for which certain hypotheses are valid.

In this respect, the first part of the thesis concentrates on dimensionality analysis.

Some well known as well as some more recently published methods have been studied and compared, with an emphasis on solving the problems associated with real data, where the errors and the departure from ideal cases must be considered. All this work has been guided by the idea that it is necessary to work with as much information as possible from the data, in this case, the components of the MT tensor, and to assume that data are 3D, with particular cases that can be 1D or 2D. This research has been performed using the COPROD2 and the BC7 datasets (both well known by the MT community), data from synthetic models and data acquired in the central Betic Chain.

The second part of the thesis focuses on the magnetotelluric study of the central Betic Chain. It comprises data acquisition and processing, dimensionality analyses - in which parts of the methodological improvements done in the first part were applied - and modelling. Thanks to the advances in computing tools, especially in speed and memory storage, a 3D geoelectric model of the central Betic crust could be constructed. Prior to this a revision of the existing 2D model was made and new 2D models were created as a preview of the 3D model.

Thus, the goals of this thesis can be summarised as two-fold: to conduct a thorough study of the MT data dimensionality methods and to construct a useful tool to perform this

analysis on real data; and to obtain a geoelectrical model of the central Betic crust from a complete study of the old and newly acquired MT data.

This dissertation has been organised into three main parts:

Part I: "Introduction to the Magnetotelluric Method". This consists of an introduction in which the basis and main elements involved in a MT study are described (chapter 1). In chapter 2, the methods used in dimensionality analyses of MT data are provided and reviewed in more detail. Specifically, WAL invariants, Bahr parameters and the magnetotelluric phase tensor methods are described, as these are the basis for the methodological aspects developed in this thesis.

Part II: "Methodological Contributions to Geoelectric Dimensionality". In this part, the investigations carried out in this thesis on dimensionality analyses are presented. Thus, chapter 3 shows how to implement WAL invariants criteria to analyse geoelectric dimensionality in noisy data, with a special emphasis on error propagation and the choice of threshold values. The resulting method was developed as a computing program (WALDIM). Chapter 4 proposes a unification of WAL and Bahr criteria, with the addition of a new parameter to the last one, allowing compatibility. To complete this part, chapter 5 presents a study of the magnetotelluric phase tensor as a new tool to investigate data dimensionality. It explores the relationships of this new tool with other methods and its effects on the data with consideration of its strong and weak points.

Part III: "Magnetotelluric Study of the central Betic crustal structure". The entire MT research carried out in the Central Betic Chain is shown here. The geological setting and the previous geophysical studies are reviewed in chapter 6. Chapter 7 explains the data acquisition and processing, which involves the use of different instrumentation and processing tools, as well as a description of MT data responses and quality. Chapter 8 presents the results of dimensionality analysis obtained from WALDIM software, which were contrasted with other methods. Chapter 9 revises the previous 2D MT model done in the area and presents the results from new 2D models obtained from different 2D inversion algorithms in the Internal Zone of the Betics. Chapter 10 describes the construction of the 3D model, its results and the responses' misfits. This chapter finishes with the interpretation and discussion of the resulting 3D model.

Finally, the conclusions of the thesis and the perspectives of future MT research, both in the context of dimensionality and the structure of the Betic Chain, are presented.

This dissertation is complemented with six appendices, which provide additional information on: error expressions, information on the datasets used, details of the acquisition and responses of Betics MT data, comparisons between model and data responses and a mathematical proof.

Part of the work developed in this thesis has been published as three papers in Geophysical Journal International:

Ledo, J.J., Queralt, P., Martí, A. and Jones, A.G., 2002. Two-dimensional interpretation of three-dimensional magnetotelluric data: an example of limitations and resolution. *Geophys. J. Int.,* **150**, 127-139.

Martí, A., Queralt, P. and Roca, E., 2004. Geoelectric dimensionality in complex geologic areas: application to the Spanish Betic Chain. *Geophys. J. Int.*, **157**, 961-974.

Martí, A., Queralt, P., Jones, A.G. and Ledo, J.J., 2005. Improving Bahr's invariant parameters using the WAL approach. *Geophys. J. Int.*, **163**, 38-41.

A forth paper on the 3D modelling and interpretation of the central Betics MT data is presently in preparation.

Part I. Introduction to the Magnetotelluric Method

1. The Magnetotelluric Method
2. Geoelectric Dimensionality and Rotational Invariants of the Magnetotelluric Tensor

Chapter 1: The Magnetotelluric Method

This chapter presents the generalities on the magnetotelluric method. It is a description of the basis of the method and its ruling equations, how it is applied and the problems that must be overcome to succeed at doing so. Special care has been taken in describing its current research status and its latest developments.

1.1 Introduction

The magnetotelluric method or magnetotellurics (MT) is an electromagnetic geophysical exploration technique that images the electrical properties (distribution) of the Earth.

The source of energy in the magnetotelluric method is the natural electromagnetic field. When this external energy, known as the primary electromagnetic field, reaches the Earth's surface, part of it is reflected, whereas the remainder penetrates into the Earth, which acts as a conductor, inducing an electric field (known as telluric currents) that at the same time produces a secondary magnetic field.

Magnetotellurics is based on the simultaneous measurement of the total electromagnetic field time variations at the Earth's surface ($\vec{E}(t)$ and $\vec{B}(t)$).

The electrical properties (e.g. electrical conductivity) of the underlying materials can be determined from the relationship between the components of the measured electric and

magnetic field variations, or transfer functions. These are the horizontal electric (E_x and E_y) and the horizontal (B_x, B_y) and vertical (B_z) magnetic components.

According to the behaviour of electromagnetic waves in conductors, the penetration of an electromagnetic wave depends on the oscillation frequency. Hence, the frequency of the electromagnetic fields being measured determines the study depth.

The origins of MT are attributed to Tikhonov (1950) and Cagniard (1953), who established the theoretical basis of the method. In half a century, important developments in formulation, instrumentation and interpretation techniques have yielded MT to be a competitive geophysical method, suitable to image a broad range of geological targets. A review of its historical evolution can be found in Dupis (1997).

1.2 Governing Equations

The electromagnetic fields within a material in a non-accelerated reference frame can be completely described by Maxwell's equations. These can be expressed in differential form and with the International System of Units (SI) as:

$$\vec{\nabla} \times \vec{E} = -\frac{\partial \vec{B}}{\partial t}, \qquad \text{Faraday's law} \qquad\qquad (1.1a)$$

$$\vec{\nabla} \times \vec{H} = \vec{j} + \frac{\partial \vec{D}}{\partial t}, \qquad \text{Ampere's law} \qquad\qquad (1.1b)$$

$$\vec{\nabla} \cdot \vec{D} = \rho_V, \qquad \text{Gauss's law} \qquad\qquad (1.1c)$$

$$\vec{\nabla} \cdot \vec{B} = 0, \qquad \text{Gauss's law for magnetism} \qquad\qquad (1.1d)$$

where $\vec{E}$ (V/m) and $\vec{H}$ (A/m) are the electric and magnetic fields, $\vec{B}$ (T) is the magnetic induction, $\vec{D}$ (C/m^2) is the electric displacement and ρ_V (C/m^3) is the electric charge density owing to free charges. $\vec{j}$ and $\partial \vec{D} / \partial t$ (A/m^2) are the current density and the displacement current respectively.

The vectorial magnitudes in Maxwell's equations can be related through their constitutive relationships:

$$\vec{j} = \sigma \vec{E}, \qquad\qquad (1.2a)$$

$$\vec{D} = \varepsilon \vec{E}, \qquad\qquad (1.2b)$$

$$\vec{B} = \mu \vec{H}. \qquad\qquad (1.2c)$$

σ, ε and μ describe intrinsic properties of the materials through which the electromagnetic fields propagate. σ (S/m) is the electrical conductivity (its reciprocal being the electrical resistivity $\rho = 1/\sigma$ ($\Omega \cdot m$)), ε (F/m) is the dielectric permittivity and μ (H/m) is the magnetic permeability. These magnitudes are scalar quantities in isotropic media. In anisotropic materials they must be expressed in a tensorial form. In this work, it will be assumed that the properties of the materials are isotropic.

The electrical conductivity of Earth materials has a wide variation (up to ten orders of magnitude) (Figure 1.1) and is sensitive to small changes in minor constituents of the rock. Since conductivity of most rock matrices is very low (10^{-5} S/m), the conductivity of the rock unit depends in general on the interconnectivity of minor constituents (by way of fluids or partial melting) or on the presence of highly conducting minerals such as graphite (Jones, 1992).
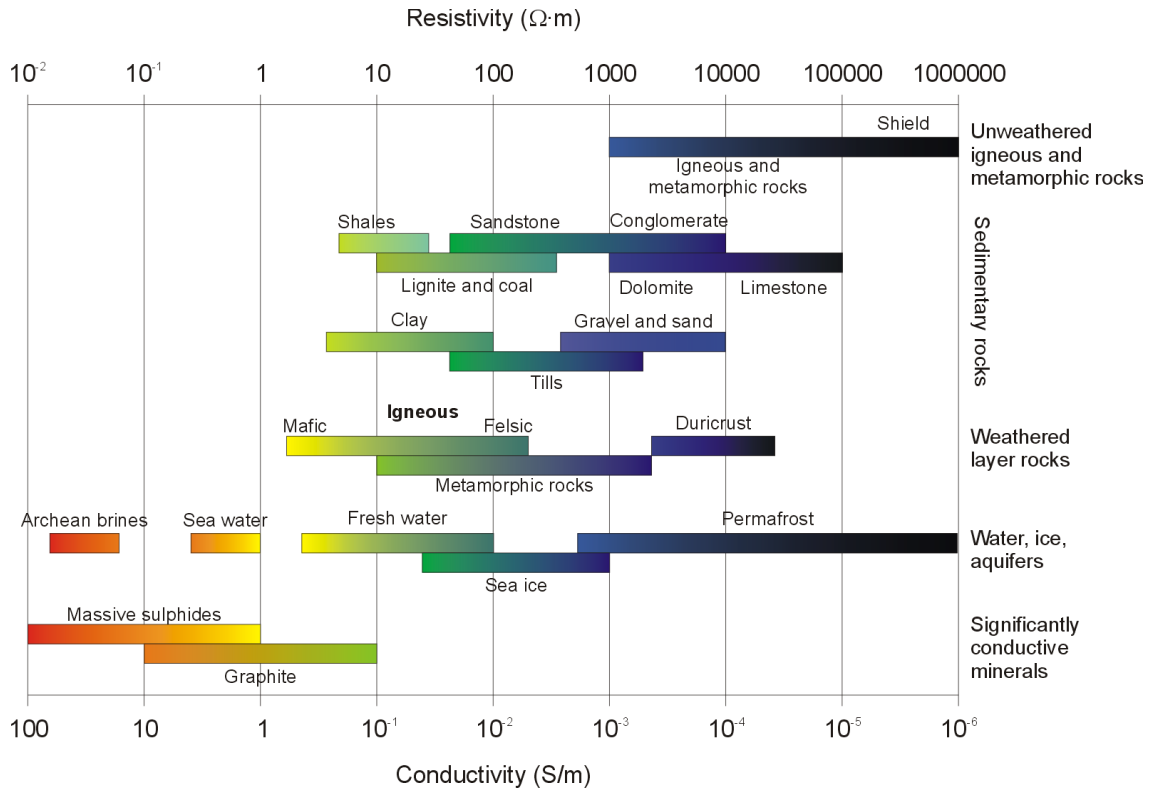
Figure 1.1: Electrical conductivity of Earth materials (modified from Palacky, 1987).

In a vacuum, the dielectric permittivity is $\varepsilon = \varepsilon_0 = 8.85 \cdot 10^{-12}$ F/m. Within the Earth, this value ranges from ε_0 (vacuum and air) to $80\varepsilon_0$ (water), and it can also vary depending on the frequency of the electromagnetic fields (Keller, 1987).

For most of the Earth materials and for the air, the magnetic permeability μ can be approximated to its value in a vacuum, $\mu_0 = 4\pi \cdot 10^{-7}$ H/m. However, in highly magnetised materials this value can be greater, for example, due to an increase in the magnetic susceptibility just below the Curie point temperature (Hopkinson effect, e.g. Radhakrishnamurty and Likhite, 1970).

Across a discontinuity between two materials, named 1 and 2, the boundary conditions to be applied to the electromagnetic fields and currents described by Maxwell's equations are:

$$\hat{n} \times (\vec{E}_2 - \vec{E}_1) = 0 \,, \tag{1.3a}$$

$$\hat{n} \times (\vec{H}_2 - \vec{H}_1) = \vec{j}_S \,, \tag{1.3b}$$

$$\hat{n} \cdot (\vec{D}_2 - \vec{D}_1) = \rho_S \,, \tag{1.3c}$$

$$\hat{n} \cdot (\vec{B}_2 - \vec{B}_1) = 0 \,, \tag{1.3d}$$

$$\hat{n} \cdot (\vec{j}_2 - \vec{j}_1) = 0 \,, \tag{1.3e}$$

where $\hat{n}$ is the unit vector normal to the discontinuity boundary, $\vec{j}_S$ (A/m^2) is the current density along the boundary surface and ρ_S (C/m^2) is the surface charge density. In the absence of surface currents, and considering constant values of ε and μ, only the tangential component of $\vec{E}$ and the normal component of $\vec{j}$ are continuous, whereas both the tangential and normal components of $\vec{B}$ are continuous across the discontinuity.

Due to the nature of the electromagnetic sources used in MT, the properties of the Earth materials and the depth of investigations considered, two hypotheses are applicable:

a) Quasi-stationary approximation: Displacement currents ($\partial \vec{D} / \partial t$) can be neglected relative to conductivity currents ($\vec{j}$) (eq. 1.1b) for the period range 10^{-5} s to 10^5 s [1] and for not extremely low conductivity values. Therefore, the propagation of the electromagnetic fields through the Earth can be explained as a diffusive process, which makes it possible to obtain responses that are volumetric averages of the measured Earth conductivities.

b) Plane wave hypothesis: The primary electromagnetic field is a plane wave that propagates vertically towards the Earth surface (z direction) (Vozoff, 1972).

---

[1] In MT, the terms angular frequency (ω), frequency (f) and period (T) are employed. ω is mainly used in Maxwell's equations and in both the time and the frequency domains. f (s^{-1}=Hz) and T(s) are used mostly in the frequency domain, and the choice of using one or another depends usually on the studied frequency (or period) range. In this thesis, ω will be used mainly for theoretical developments and T for data treatment. The relationships between these three magnitudes are: $\omega = 2\pi f$ and T=1/f.

The searched solutions of the electromagnetic fields from Maxwell's equations can be expressed through a linear combination of harmonic terms:

$$\vec{E} = \vec{E}_0 \cdot e^{i(\omega t + \vec{k}\vec{r})} \,, \tag{1.4a}$$

$$\vec{B} = \vec{B}_0 \cdot e^{i(\omega t + \vec{k}\vec{r})} \,, \tag{1.4b}$$

where ω (rad/s) is the angular frequency of the electromagnetic oscillations, t (s) is the time, $\vec{k}$ (m^{-1}) and $\vec{r}$ (m) are the wave and position vectors respectively. In both expressions, the first term in the exponent corresponds to wave oscillations and the second term represents wave propagation.

Using these harmonic expressions of the electromagnetic fields (eqs. 1.4a and 1.4b) and their constitutive relationships (eqs. 1.2a to 1.2c), if MT hypothesis a) (quasi-stationary approximation) is applied, Maxwell's equations in the frequency domain are obtained:

$$\vec{\nabla} \times \vec{E} = -i\omega\vec{B} \,, \tag{1.5a}$$

$$\vec{\nabla} \times \vec{B} = \mu_0 \sigma \vec{E} \,, \tag{1.5b}$$

$$\vec{\nabla} \cdot \vec{E} = \frac{\rho_V}{\varepsilon} \,, \tag{1.5c}$$

$$\vec{\nabla} \cdot \vec{B} = 0 \,, \tag{1.5d}$$

where the value of the magnetic permeability (μ) is considered equal to the value in a vacuum (μ_0).

In the absence of charges, the right term of eq. 1.5c vanishes, and the electric and magnetic field solutions depend solely upon angular frequency (ω) and conductivity (σ).

Finally, using hypothesis b) (plane wave) and applying the boundary conditions (eqs. 1.3a to 1.3e) across discontinuities, the solutions of Maxwell's equations can be obtained.

In the case of an homogeneous structure, the components of the electric and magnetic fields take the form:

$$A_k = A_{k0} \cdot e^{i\omega t} \cdot e^{-i\alpha z} \cdot e^{-\alpha z} \,, \tag{1.6}$$

with $\alpha = \sqrt{\mu_0 \sigma \omega / 2}$ (m^{-1}). The first factor of the equation is the wave amplitude, the second and third factors (imaginary exponentials) are sinusoidal time and depth variations respectively and

the fourth is an exponential decay. This decay can be quantified by the skin depth, δ, the value of z for which this term decays to 1/e (Vozoff, 1991):

$$\delta = \sqrt{\frac{2}{\mu_0 \sigma \omega}} \approx 500\sqrt{\rho T} \quad (m).$$ (1.7)

The skin depth permits the characterisation of the investigation depth, which, as can be seen, increases according to the square root of the product of medium resistivity and period. Although it has been defined for homogeneous media, its use can be extended to heterogeneous cases as well (e.g. geologic structures).

1.3 Magnetotelluric Transfer Functions

Magnetotelluric transfer functions (MTFs) or magnetotelluric responses are functions that relate the registered electromagnetic field components at given frequencies.

The MTFs depend only on the electrical properties of the materials and not on the electromagnetic sources. Hence, they characterise the conductivity distribution of the underlying materials according to the measured frequency.

The MTFs used in this thesis are the Impedance and Magnetotelluric Tensors and the Geomagnetic Transfer Function.

1.3.1 Impedance Tensor and Magnetotelluric Tensor

The *impedance tensor*, $\underline{Z}(\omega)$ (Ω), is a second-rank tensor (2x2 components). It relates the horizontal complex components of the electric ($\vec{E}$) and magnetic ($\vec{H} = \vec{B}/\mu_0$) fields at a given frequency (ω) (Cantwell, 1960):

$$\begin{pmatrix} E_x(\omega) \\ E_y(\omega) \end{pmatrix} = \begin{pmatrix} Z_{xx} & Z_{xy} \\ Z_{yx} & Z_{yy} \end{pmatrix} \cdot \begin{pmatrix} B_x(\omega)/\mu_0 \\ B_y(\omega)/\mu_0 \end{pmatrix}.$$ (1.8)

Weaver *et al.* (2000) introduced the term *magnetotelluric tensor*, $\underline{M}(\omega)$ (m/s), which uses $\vec{B}$ instead of $\vec{H}$ to define the relationships between the field components:

$$\begin{pmatrix} E_x(\omega) \\ E_y(\omega) \end{pmatrix} = \begin{pmatrix} M_{xx} & M_{xy} \\ M_{yx} & M_{yy} \end{pmatrix} \cdot \begin{pmatrix} B_x(\omega) \\ B_y(\omega) \end{pmatrix}. \tag{1.9}$$

In this thesis the use of the magnetotelluric tensor (MT tensor) is preferred, since it defines most of the parameters utilized [2].

The components of $\underline{M}$, M_{ij} (ij=xx,xy,yx,yy), are also complex magnitudes. Their expressions are M_{ij}=Re(M_{ij})+i·Im(M_{ij}) in Cartesian form and $M_{ij} = |M_{ij}|e^{i\varphi}$ in polar form.

From the modulus and phase of the polar expression of M_{ij}, two scalar magnitudes, which are real and frequency-dependent, are defined:

1) The apparent resistivity, which is an average resistivity for the volume of Earth sounded at a particular period:

$$\rho_{ij}(\omega) = \frac{\mu_0}{\omega}|M_{ij}(\omega)|^2 \ (\Omega\cdot m). \tag{1.10}$$

2) The impedance phase (or simply phase) is the phase of the M_{ij} component. It provides additional information on the conductivity of structures:

$$\varphi_{ij}(\omega) = \arctan\left(\frac{\mathrm{Im}(M_{ij}(\omega))}{\mathrm{Re}(M_{ij}(\omega))}\right). \tag{1.11}$$

1.3.2 Geomagnetic Transfer Function

The Geomagnetic Transfer Function (also known as the tipper vector or, tipper), $\vec{T}$, is a dimensionless complex vectorial magnitude, $\vec{T} = \mathrm{Re}(\vec{T}) + i\cdot\mathrm{Im}(\vec{T})$, and is defined as the relation between the vertical and the two horizontal components of the magnetic field:

$$B_z(\omega) = (T_x(\omega), T_y(\omega)) \cdot \begin{pmatrix} B_x(\omega) \\ B_y(\omega) \end{pmatrix}. \tag{1.12}$$

---

[2] $\underline{Z}$ and $\underline{M}$ are related to $\vec{H}$ and $\vec{B}$ through $\underline{Z} = \mu_0\underline{M}$. In the literature and in the usual codes sometimes $\underline{M}$ is used instead of $\underline{Z}$, although it is referred to as $\underline{Z}$.

The tipper vector can be decomposed into two real vectors in the xy plane, corresponding to its real and imaginary parts. These real vectors are called induction vectors or induction arrows, and represent a projection of the vertical magnetic field on the horizontal xy plane. They are used to infer the presence of lateral variations in conductivity.

$$\vec{T}_{re}(\omega) = \left(\mathrm{Re}\left(T_x\right), \mathrm{Re}\left(T_y\right) \right),$$ (1.13)

$$\vec{T}_{im}(\omega) = \left(\mathrm{Im}\left(T_x\right), \mathrm{Im}\left(T_y\right) \right).$$ (1.14)

The graphical representation of the real induction arrows can be reversed (Parkinson convention) or non-reversed (Schmucker or Weise convention). Using the Parkinson convention the real induction arrow points to concentrations of currents, i.e., to more conductive zones.

1.4 Earth MT Dimensionality Models

The MT transfer functions, and particularly the relationships between their components, are reduced to specific expressions depending on the spatial distribution of the electrical conductivity being imaged. These spatial distributions, known as geoelectric dimensionality, can be classified as 1D, 2D or 3D. Other particular expressions of the transfer functions can be obtained when data are affected by galvanic distortion, a phenomenon caused by minor scale (local) inhomogeneities near the Earth's surface.

This section presents a summary of the characteristics of the different types of geoelectric dimensionality, regarding its geometry, the behaviour of the electromagnetic fields through them and the expressions of the related transfer functions. Galvanic distortion is also explained along with the type of transfer functions associated with this phenomenon.

1.4.1   1D

In this case the conductivity distribution is depth dependent only ($\sigma=\sigma(z)=1/\rho(z)$) and Maxwell's equations can be analytically solved by properly applying the boundary conditions (eqs. 1.3a to 1.3e). The solutions are electromagnetic waves, with the electromagnetic field always orthogonal to the magnetic field, that travel perpendicular to the surface of the Earth in a constant oscillation direction. They attenuate with depth depending on their period and conductivity values (eq. 1.7).

As a result, the MT transfer functions are independent of the orientation of the measured axes and are a function only of the frequency.

The magnetotelluric tensor is a non-diagonal tensor (diagonal elements = 0) with its two components equal in modulus but with opposite signs:

$$\underline{M}_{1D}(\omega) = \begin{pmatrix} 0 & M(\omega) \\ -M(\omega) & 0 \end{pmatrix},$$

(1.15a)

with the corresponding resistivity and phases:

$$\rho_{xy}(\omega) = \rho_{yx}(\omega) = \frac{\mu_0}{\omega}\left|M(\omega)\right|^2 \left(\Omega \cdot m\right),$$

(1.15b)

$$\varphi(\omega) = \arctan\left(\frac{\mathrm{Im}\left(M(\omega)\right)}{\mathrm{Re}\left(M(\omega)\right)}\right),$$

(1.15c)

$$\varphi_{yx}(\omega) = \varphi_{xy} - \pi.$$

(1.15d)

The simplicity of the components of the magnetotelluric tensor allows working with only two scalar frequency-dependent quantities: These being the scalar apparent resistivity and phase:

$$\rho_{app}(\omega) = \rho_{xy}(\omega) = \rho_{yx}(\omega) \quad \left(\Omega \cdot m\right),$$

(1.15e)

$$\varphi_{app}(\omega) = \varphi_{xy}(\omega).$$

(1.15f)

For the particular case of a half-space homogeneous Earth with conductivity σ ($= 1/\rho$), the MT tensor is frequency-independent and takes the form of eq. 1.15a, with $\mathrm{Re}(M) = \mathrm{Im}(M) = \sqrt{\rho\omega/2\mu_0}$. The apparent resistivity is equal to the resistivity of the medium, ρ. The impedance phase is 45°.

With regard to the tipper, there is not a net component of the vertical magnetic field, B_z, due to the assumption that the incidence of the electromagnetic fields is perpendicular to the Earth's surface, and the fact that in a 1D model these fields do not change direction with depth. Therefore, the two components of the tipper, T_x and T_y are zero.

1.4.2   2D

In a two-dimensional Earth the conductivity is constant along one horizontal direction while changing both along the vertical and the other horizontal directions. The direction along which the conductivity is constant is known as the *geoelectrical strike* or *strike*. In the following

description, it is considered that the strike direction is parallel to the x axis (x ≡ x', i.e. $\theta = 0°$) of the reference frame used in an MT survey (Figure 1.2) and therefore the variations of σ occur along y and z axes: $\sigma(y,z)$.

In these cases, there is an induced vertical magnetic field, B_z, and Maxwell's equations can be decoupled into two modes, each one relating 3 different electric and magnetic perpendicular components:

Mode xy (E_x, B_y, B_z), also known as Transversal Electric (TE) mode, with currents (electric fields) parallel to the strike direction:

$$\frac{\partial E_x}{\partial z} = -i\omega B_y,$$
(1.16a)

$$\frac{\partial E_x}{\partial y} = i\omega B_z,$$
(1.16b)

$$\frac{\partial B_z}{\partial y} - \frac{\partial B_y}{\partial z} = \mu_0 \sigma E_x.$$
(1.16c)

Mode yx (B_x, E_y, E_z), or Transversal Magnetic (TM) mode, with currents perpendicular to the strike:

$$\frac{\partial E_y}{\partial z} - \frac{\partial E_z}{\partial y} = i\omega B_x,$$
(1.17a)

$$\frac{\partial B_x}{\partial z} = \mu_0 \sigma E_y,$$
(1.17b)

$$\frac{\partial B_x}{\partial y} = -\mu_0 \sigma E_z.$$
(1.17c)

The magnetotelluric tensor $\underline{M}$ in 2D models is non-diagonal and may be expressed as:

$$\underline{M}_{2D}(\omega) = \begin{pmatrix} 0 & M_{xy}(\omega) \\ M_{yx}(\omega) & 0 \end{pmatrix} = \begin{pmatrix} 0 & M_{TE}(\omega) \\ M_{TM}(\omega) & 0 \end{pmatrix},$$
(1.18a)

where M_{xy} (E_x/B_y) and M_{yx} (E_y/B_x) come from TE and TM sets of equations respectively, and usually have opposite signs.

The values of the apparent resistivities and phases for xy and yx have different values and can be computed from eqs. 1.10 and 1.11. Since M_{xy} and M_{yx} have opposite signs, xy and yx phases belong to the 1st and 3rd quadrants.

The tipper is different from zero, and is related to the horizontal component y of the magnetic field, i.e., to the TE mode (eq. 1.16c):

$$\bar{T}_{2D}(\omega) = \left(0, T_y\right) = (0, B_z / B_y).$$

(1.18b)

Both the real and imaginary induction arrows are oriented perpendicular to the strike direction (in this case x), and, according to Parkinson convention, point towards the zone of maximum conductivity.

In a 2D Earth, the measurements are, in general, not performed in the strike reference frame (x ≠ strike direction) because this is not known *a priori*. As a consequence, the magnetotelluric transfer functions cannot be expressed as in eqs. 1.18a and 1.18b.

However, it is possible to rotate the measuring axes an angle θ (strike angle) through the vertical axis, so the diagonal components of the magnetotelluric tensor become zero and the new x' axis is parallel to the geoelectrical strike. In the rotated reference frame (x', y', z) the rotated transfer functions are $\underline{M}'$ and T':

$$\underline{M}'(\omega) = R_\theta \cdot \underline{M}(\omega) \cdot R_\theta^T,$$

(1.19)

$$\bar{T}'(\omega) = R_\theta \cdot \bar{T}(\omega),$$

(1.20)

where R_θ is a clockwise rotation matrix:

$$R_\theta = \begin{pmatrix} \cos\theta & \sin\theta \\ -\sin\theta & \cos\theta \end{pmatrix},$$

(1.21)

and R_θ^T its transpose.

In the rotated reference frame (x', y', z), TE and TM modes can be equally defined according to the strike direction.

The retrieval of the strike angle from the MT tensor can be done using several methods that will be reviewed in the next chapter. It is important to note that this retrieval has 90° of ambiguity, which can be solved through the information given by the tipper vector, the variation of MT responses along different locations and geology.
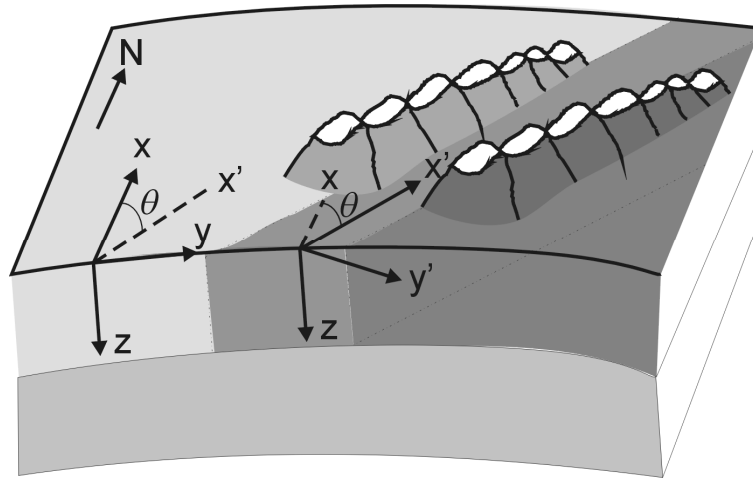
Figure 1.2: Sketch of an Earth model with reference frame axes used in an MT survey and in the analyses of their responses. (x, y, z): measurement system coordinates. x and y are the horizontal axes, where x usually points towards North and y points towards East. The z axis points vertically inward. Commonly, a reference frame rotated around the z axis (x', y', z) is also used. θ indicates the angle between the x' and x axes.

1.4.3   3D

This is the most general type of geoelectrical structure. Here, the conductivity changes along all directions ($\sigma = \sigma$(x,y,z)). In this case, Maxwell's equations can not be separated into two modes.

MT transfer functions take the general forms with all components non-zero (eqs. 1.9 to 1.14), because M_{xx} and M_{yy} are not null. There is not any rotation direction through which the diagonal components of the magnetotelluric tensor or any component of the tipper vector can vanish.

1.4.4 The Galvanic Distortion Phenomenon

Distortion in magnetotellurics is a phenomenon produced by the presence of shallow and local bodies or heterogeneities, which are much smaller than the targets of interest and skin depths. These bodies cause charge distributions and induced currents that alter the magnetotelluric responses at the studied or regional scale (Kaufman, 1988; Chave and Smith, 1994). In the case that these bodies are of the same proportions as the interest depth, they can be modeled in a 3D environment.

Distortion can be inductive or galvanic. Inductive distortion is generated by current distributions, has a small magnitude and decays with the period. Under the condition $\sigma >> \omega\varepsilon$ (quasi-stationary approximation) it can be ignored (Berdichevsky and Dmitriev, 1976).

Galvanic distortion is caused by charge distributions accumulated on the surface of shallow bodies, which produce an anomalous electromagnetic field. This anomalous magnetic field is small, whereas the anomalous electric field is of the same order of magnitude as its regional counterpart and is frequency-independent (Bahr, 1988; Jiracek, 1990). Hence the galvanic distortion is treated as the existence of an anomalous electric field, $\vec{E}_a$.

Mathematically, the effect of this electric field on the transfer functions can be represented by a 2x2 real, frequency-independent and non-dimensional matrix, C (Berdichevsky and Dmitriev, 1976):

$$C = \begin{pmatrix} C_1 & C_2 \\ C_3 & C_4 \end{pmatrix}. \tag{1.22}$$

The elements of C depend on the geometry and position of the distorting body as well as on the resistivity contrast between the body and the surrounding medium (Jiracek, 1990).

The magnetotelluric tensor that accounts for the measurement of the regional and distorted fields is then:

$$\underline{M}_m(\omega) = C \cdot \underline{M}_R(\omega), \tag{1.23}$$

where $\underline{M}_m$ is the measured tensor and $\underline{M}_R$ is the regional tensor, which corresponds to the regional structure. Also, $\underline{M}_m$ can have been measured in a reference frame rotated an angle α with respect to the regional reference frame:

$$\underline{M}_m(\omega) = R_\alpha \cdot C \cdot \underline{M}_R(\omega) \cdot R_\alpha^T. \tag{1.24}$$

The effects of galvanic distortion depend on the type of dimensionality of the regional media.

In the case of a 1D regional Earth, galvanic distortion produces a constant displacement of the apparent resistivity along all frequencies. This is known as *static shift*, and does not affect the phases. A static shift also occurs in a 2D Earth with one of the measurements axes aligned with the strike direction. Although it seems to be a minor problem, static shift represents one of the main handicaps in the analysis of MT responses. There is no a general analytical or numerical way to model the cause of static shift and thus to correct it by using MT itself. This makes it necessary to use information from other methods that are less affected (TEM) or to compare the responses with geological information. Some proposals to correct static shift can be

found in Jones (1988) and Ogawa (2002), and new methods are being developed (Ledo *et al.*, 2002a; Tournerie *et al.*, 2004; Meju, 2005).

In contrast, if distortion affects a 2D tensor rotated a certain angle θ from the strike direction, or a 3D structure, both phases and resistivities are affected with a dependence on the frequency.

Since the main target of interest in a MT survey is the regional structure and not the distorting bodies, different decomposition techniques exist to remove the effects of distortion and recover the regional responses.

There are different methods to correct galvanic distortion over one-dimensional and two-dimensional structures (Zhang *et al.*, 1987; Bahr, 1988; Groom and Bailey, 1989 and Smith, 1995). These methods consider a galvanic distortion affecting a 2D regional structure, with the magnetotelluric tensor measured in a reference frame that is rotated an angle θ from the regional strike:

$$\underline{M}_m = R_\theta \cdot C \cdot \underline{M}_{2D}(\omega) \cdot R_\theta^T . \tag{1.25}$$

In the method proposed by Groom and Bailey (1989) the distortion is described by the contribution of four effects, represented by the gain (*g*) parameter, which accounts for the static shift, and the twist (φ_t), shear (φ_e) and anisotropy (φ_s) angles or their tangents (*t*, *e* and *s* respectively):

$$C = g \cdot \begin{pmatrix} (1+s)(1-te) & (1-s)(e-t) \\ (1+s)(e+t) & (1-s)(1+te) \end{pmatrix} . \tag{1.26}$$

Alternatively, Smith (1995) uses two gain parameters, g_1 and g_2, and two distortion angles, ϕ_1 and ϕ_2:

$$C = \begin{pmatrix} g_1 \cos\phi_1 & -g_2 \sin\phi_2 \\ g_1 \sin\phi_1 & g_2 \cos\phi_2 \end{pmatrix} . \tag{1.27}$$

The relationships between both sets of parameters are:

$$g_{1 \atop 2} = g(1 \pm s) , \tag{1.28}$$

$$\phi_{1 \atop 2} = \varphi_t \pm \varphi_e . \tag{1.29}$$

An alternative decomposition of the galvanic distortion matrix is shown in Appendix F.

The aim of these decomposition methods is to solve a linear system of equations (8 equations) that allow determining the values of the distortion parameters, the strike angle and the regional magnetotelluric tensor components (9 parameters in total). The gain (static shift) remains unknown and additional information is necessary to retrieve its value. McNeice and Jones (2001) developed the Multisite Multifrequency tensor decomposition code (Strike), which, based on a statistical approach, retrieves twist and shear distortion parameters in accordance with a 2D regional model with a unique strike direction.

In three-dimensional geoelectric structures it is not easy to perform the decomposition unless the characteristics of the distortion are well known. In these cases, several approaches have been proposed to correct galvanic distortion over regional 3D structures (Ledo *et al.*, 1998; Garcia and Jones, 1999; Utada and Munekane, 2000).

In the most general cases, it is not possible to discern whether data are affected or not by galvanic distortion and the type of regional structure. Further analyses must be carried out to obtain such information, commonly based on the use of the invariant parameters of the magnetotelluric tensor.

1.5 Electromagnetic Sources in MT

"The dependence of MT on natural fields is both its major attraction and its greatest weakness" (Vozoff, 1991).

The electromagnetic oscillations of interest in magnetotellurics have a period range from about 10^{-5} s to 10^{5} s, which belong to the lowest part of the known electromagnetic spectrum, from the long radio waves ($\lambda \approx 1$ km) to $\lambda \approx 10^{10}$ km (Figure 1.3). These frequencies permit range of investigation depths from ten meters to hundreds of kilometres. The natural phenomena that generate the electromagnetic fields with these frequencies are thunderstorm activity world-wide and the interaction between the solar wind and the Earth's magnetosphere.

For periods shorter than 1s, lightning discharges are the main source of electromagnetic waves. The energy released from lightning at a frequency of about 8 Hz (Schuman resonance) and its multiple harmonics up to 2000 Hz are trapped in an insulating waveguide between the conductive Earth and the conductive ionosphere, such that this energy can travel for long distances. It is estimated that occurrences of lightning somewhere in the world (from 100 to 1000 per second) is sufficient to have a continuous energy source at any location over the Earth's surface (Malan, 1963; Kaufman and Keller, 1981; Vozoff, 1991). In MT, measurements in the range from 10^{5} Hz to 1 Hz are referred to as Audiomagnetotellurics (AMT).
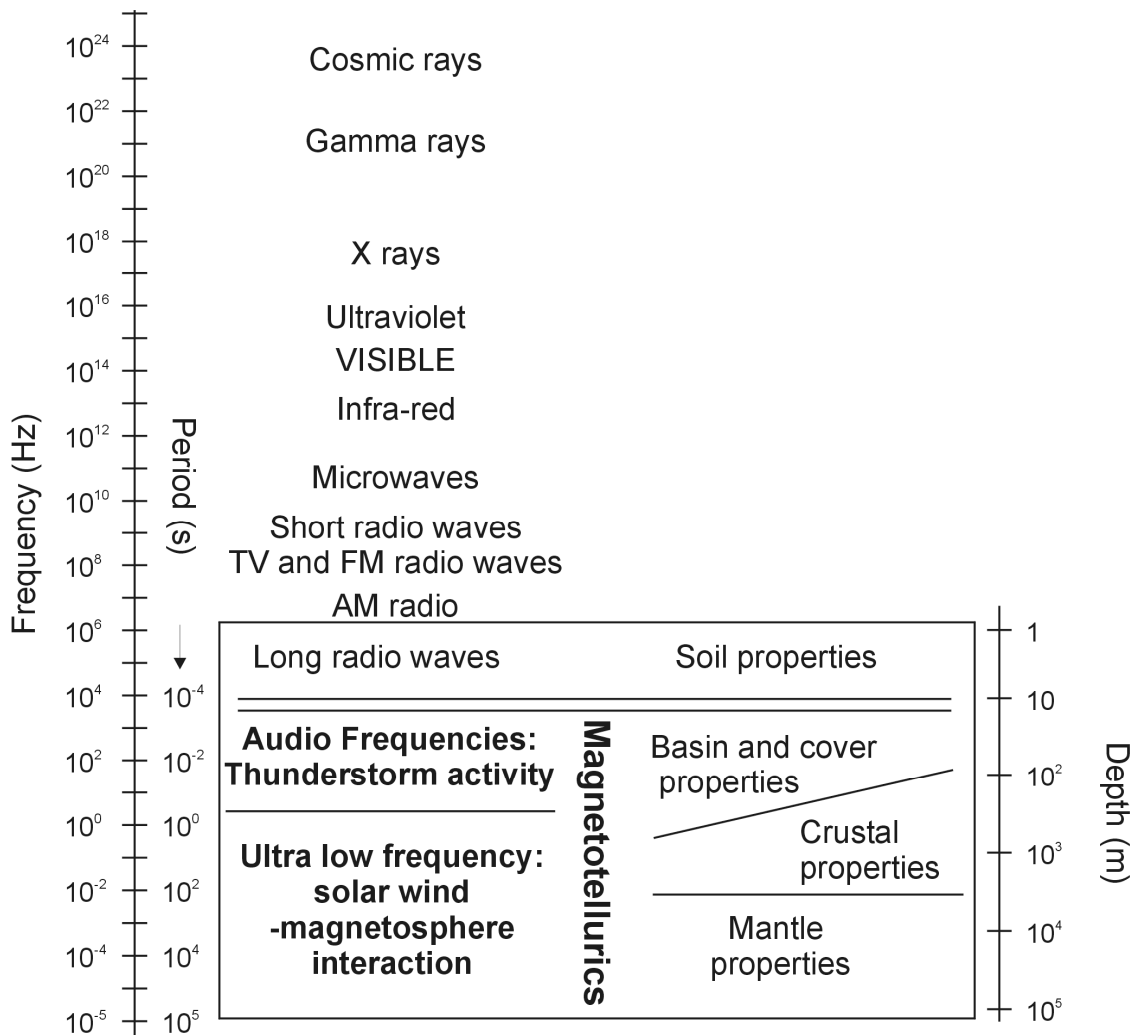
Figure 1.3: Schematic representation of the known electromagnetic spectrum. The box corresponds to the part of the spectrum used in magnetotellurics, where the MT sources, targets and investigation depths are indicated.

For periods from 1 s to 10^5 s, the electromagnetic activity is dominated by hydromagnetic waves in the Earth's magnetosphere, mainly generated by the solar wind (Campbell, 2003; McPherron, 2005). The solar wind consists of highly energetic ions ejected from the Sun and its magnetic field, which interact with the Earth's magnetic field, changing its intensity and geometry. Within the Earth's magnetosphere, the ionosphere is an atmospheric layer between 100 km and 1000 km of altitude. It is highly conductive because its particles are ionised by ultraviolet and other solar radiation. The interaction between the solar wind and gases in the ionosphere result in several processes (McPherron, 2002) that produce an electromagnetic field. The field travels through the lower layers of the atmosphere and reaches the Earth surface. This interaction is also responsible for the Northern and Southern lights, visible at high latitudes. At these latitudes, auroral effects must be corrected to satisfy the MT method hypotheses (Pirjola,

1992; Garcia *et al.*, 1997). When MT measurements are made at low latitudes, the effects of the equatorial electrojet, an Eastward current caused by the Earth's magnetic field being horizontal at these latitudes (Padilha, 1999; Campbell, 2003), can be important and must be corrected also.

Around 1 s, in the limit between thunderstorm activity and solar wind – ionosphere interaction, there is a narrow period range (0.2 s - 2 s), known as the dead band, in which the power spectrum of the natural electromagnetic field has a minimum (Figure 1.4) that produces low-amplitude MT signals.
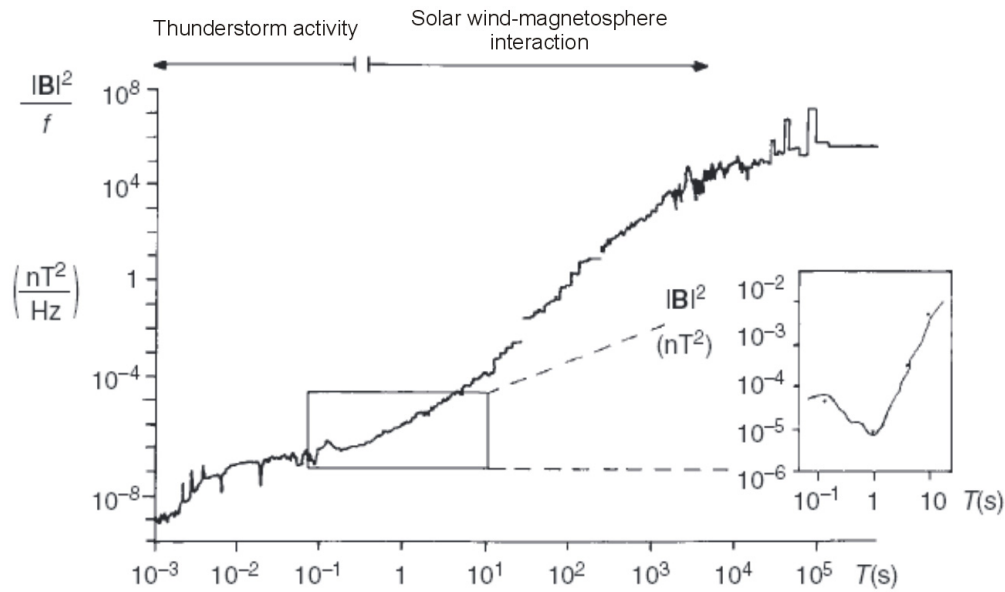
Figure 1.4: Power spectrum of natural magnetic field variations. The inset depicts the minimized signal power in the dead band. (Modified from Junge, 1996).

To these two natural sources, other electromagnetic signals can be added, known as noise. In terms of data processing, noise can be defined as that part of the data which cannot be explained by the framework of a theory (Junge, 1996). In general, any factor, which makes the MT method assumptions invalid, is considered noise. The sources of electromagnetic noise can be instrumental, environmental (seismic, electromagnetic signals of no interest in Earth studies, biological) as well as cultural or man-made noise (electric devices, power stations and lines, railways, electric fences, radio and TV transmitters...). The effects of noise could be minimised by the use of filters in the acquisition instruments, accurate signal processing methods (see section 1.7) and the use of one or more remote references (Gamble *et al.*, 1979).

Below 10^{-4} s, the natural electromagnetic signal is very weak and other types of electromagnetic sources are needed in order to effectively explore the shallow subsurface. This

is achieved by Controlled Source Audio Magnetotellurics (CSAMT), consisting of the use of antennas radiating at short periods, such that MT theory assumptions are fulfilled (Zonge and Hughes, 1991).

1.6 Instrumentation

The equipment necessary for MT data acquisition consists of sensors that measure the electric and magnetic field components (channels) and one data logger that controls and performs the acquisition process and the data storage.

The electric field components E_x and E_y are indirectly measured through the potential difference ΔV between two electrodes separated a distance d along the desired direction: $\Delta V = E_i / d$. Both electrodes stay in contact with the soil and are connected to the data logger that closes the circuit and stores the measured signal. The separation between the electrodes must guarantee enough voltage to be registered by the data logger, and also account for the fact that the voltage decreases as a function of period. The sensitivity of the acquisition systems used at present allows a separation of 10 m – 20 m for AMT frequencies and 50 m – 100 m for the rest. In any case, the choice of the distance is many times limited by the topography of the terrain. Within the AMT frequency range steel electrodes are used. Outside this range the electrodes must be non-polarisable to avoid additional electrochemical currents. Normally, these electrodes consist of a KCl or $PbCl_2$ solution in a ceramic container that is designed to ensure a good contact between the outside wires and the soil.

For the magnetic field, the most commonly used sensors are induction coils. According to the Faraday-Lenz law, under a magnetic flux time variation, an electromotive force (*emf* (V)) is induced in a coil. Coils must be oriented along the direction of the component to be measured (usually B_x, B_y and B_z). The number of loops in the magnetometers must be in agreement with the induced *emf*, which decreases along with the period. Nowadays, the same size coil is valid for a broad range of periods, and the data must be posteriorly calibrated according to their sensitivity to the different voltage values. At very long periods, another type of magnetic sensor, the flux magnetometer, is used.

The data logger (e.g. Figure 1.5) is the control unit of the MT measuring system. It controls the acquisition process, filters and amplifies the sensors signals and converts these data into digital format through an A/D converter.

The sensors' signals are stored in the data logger using a certain sampling frequency, which, according to Nyquist theorem, must be at least twice the value of the highest frequency to be evaluated. In order to avoid an oversampling of the longest period data to save disk space

and aliasing, the data acquisition process is separated into several frequency bands, each one with a different sampling frequency. This acquisition in data bands also permits adaptation of the A/D converter to the signal amplitudes and to the sensors' sensitivities at the given band.
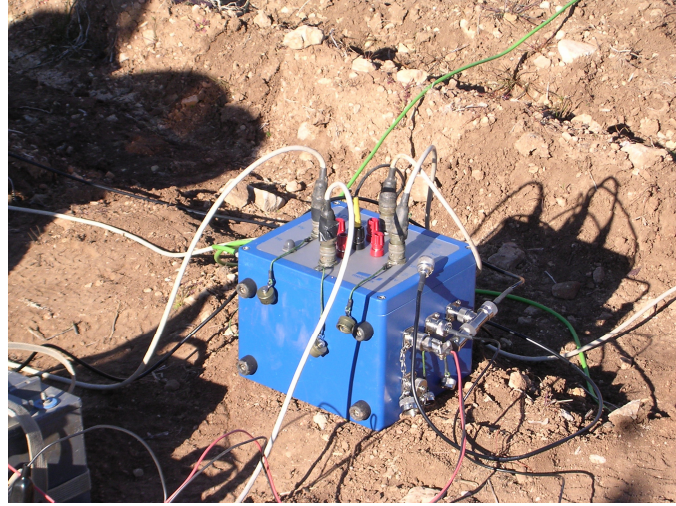
Figure 1.5: Metronix ADU-06 data logger.

Table 1.1: presents the recording bands of the Metronix ADU-06 system, one of the systems used in this study. In this system, the data at a given band can be obtained by the use of low-pass filters during recording (bands HF, LF1, LF2 and Free) or by a posterior sampling of the final time series (bands LF3, LF4 and LF5).

Band	Sampling frequency/period	Frequency/period range
HF	40960 Hz	20000 Hz – 500 Hz
LF1	4096 Hz	1000 Hz - DC
Free	128, 256, 512, 1024 or 2048 Hz	60, 120, 240, 480 or 960 Hz to DC
LF2	64 Hz	30 Hz – DC
LF3	2 Hz	0.9 Hz – DC
LF4	2 s or 16 s	5s or 35s to DC
LF5	8 s, 64 s or 512 s	20s, 150s or 1200s to DC

Table 1.1: Recording bands for the Metronix ADU-06 system, indicating their corresponding sampling frequency/period and recorded ranges.

1.7 Time Series Processing

1.7.1. General overview

The MT transfer functions are obtained from time series processing of the acquired data. Commonly, processing is carried out separately for each measured band, involving three main steps: 1) data set up and preconditioning, 2) time to frequency domain conversion and 3) estimation of the magnetotelluric transfer functions.

1) Data set up and preconditioning

The recorded time series are divided into M segments containing N samples each. The value of N is chosen depending on the recorded band such that each segment contains an elevated number of periods. In addition, each band must be divided into a sufficient number of segments for further statistical estimation of the transfer functions.

Once the segments have been defined, they are inspected in order to identify and remove trends and noise effects (spikes). This is performed manually and/or automatically using specific software.

2) Time to frequency domain conversion

From each segment, the measured channels E_i (i=x,y) and B_j (j=x,y,z) are converted from time to frequency domain using the Discrete Fourier Transform (Brigham, 1974) or Cascade Decimation (Wight and Bostick, 1980), both based on the Fast Fourier Transform (FFT), or using the Wavelet transform (Zhang and Paulson, 1997; Trad and Travassos, 2000; Arango, 2005). Hence, a raw spectrum with N/2 frequencies is obtained. From these, evaluation frequencies, equally distributed in a logarithmic scale, optimally 6-10 per period decade, are chosen. The final spectra are smoothed by averaging over neighbouring frequencies using a Parzen window function. Each field component must be calibrated according to the instrument sensitivity at a given frequency. The auto and cross spectra of a segment k, which are the products of the field components and their complex conjugates, are then obtained for each frequency: $E_{ki}(\omega) \cdot E^*_{ki}(\omega)$, $B_{kj}(\omega) \cdot B^*_{kj}(\omega)$, $E_{ki}(\omega) \cdot B^*_{kj}(\omega)$ and $B_{kj}(\omega) \cdot E^*_{ki}(\omega)$. These are stored in the so-called spectral matrix, which contains the contributions from all the segments at a specific frequency.

3) Estimation of the magnetotelluric transfer functions

The evaluation of the MT transfer functions from eqs. 1.9 and 1.12 needs at least two independent observations of the corresponding field components in the frequency domain, which can be obtained from two segments:

$$E_x(\omega) = M_{xx}(\omega) \cdot B_x(\omega) + M_{xy}(\omega) \cdot B_y(\omega), \tag{1.30}$$

$$E_y(\omega) = M_{yx}(\omega) \cdot B_x(\omega) + M_{yy}(\omega) \cdot B_y(\omega), \tag{1.31}$$

$$B_z(\omega) = T_x(\omega) \cdot B_x(\omega) + T_y(\omega) \cdot B_y(\omega). \tag{1.32}$$

However, to solve these equations accurately, a larger number of segments is required, due to the presence of noise in the measured data as well as the fact that two segments may not contain all the evaluation frequencies. Hence, the transfer functions are evaluated after multiplying eqs. 1.30 to 1.32 by the conjugates of the horizontal magnetic field ($B_x{}^*(\omega)$ and $B_y{}^*(\omega)$). This allows obtaining six independent equations whose parameters are elements of the spectral matrix. The conjugates $B_x{}^*(\omega)$ and $B_y{}^*(\omega)$ are used, instead of other possible combinations of field components, as they have the highest degree of independence (Vozoff, 1972) and provide the most stable results:

$$M_{xx} = \frac{\langle E_x B_x^* \rangle \langle B_y B_y^* \rangle - \langle E_x B_y^* \rangle \langle B_y B_x^* \rangle}{DET_1}, \tag{1.33}$$

$$M_{xy} = \frac{\langle E_x B_x^* \rangle \langle B_x B_y^* \rangle - \langle E_x B_y^* \rangle \langle B_x B_x^* \rangle}{DET_2}, \tag{1.34}$$

$$M_{yx} = \frac{\langle E_y B_x^* \rangle \langle B_y B_y^* \rangle - \langle E_y B_y^* \rangle \langle B_y B_x^* \rangle}{DET_1}, \tag{1.35}$$

$$M_{yy} = \frac{\langle E_y B_x^* \rangle \langle B_x B_y^* \rangle - \langle E_y B_y^* \rangle \langle B_x B_x^* \rangle}{DET_2}, \tag{1.36}$$

$$T_x = \frac{\langle B_z B_x^* \rangle \langle B_y B_y^* \rangle - \langle B_z B_y^* \rangle \langle B_y B_x^* \rangle}{DET_1}, \tag{1.37}$$

$$T_y = \frac{\langle B_x B_x^* \rangle \langle B_z B_y^* \rangle - \langle B_x B_y^* \rangle \langle B_z B_x^* \rangle}{DET_1}, \tag{1.38}$$

where $DET_1 = \langle B_x B_x^* \rangle \langle B_y B_y^* \rangle - \langle B_x B_y^* \rangle \langle B_y B_x^* \rangle$ and $DET_2 = \langle B_y B_x^* \rangle \langle B_x B_y^* \rangle - \langle B_y B_y^* \rangle \langle B_x B_x^* \rangle$.

Cross and power spectra $<AB^*>$ are constructed from the individual segments k, through a variety of methods, all of which perform a segment selection to obtain an optimal estimation of the transfer functions.

The following is a summary of the most common methods for estimating TFs:

The first methods utilised least squares (LS) (Sims *et al.*, 1971), which minimises the quadratic sum of the difference between the measured fields and those computed from the MT transfer functions, assuming equally distributed Gaussian errors. These methods failed since the errors highly depend on the strength of the signal and are extremely sensitive to the presence of noise.

The magnetic remote reference acquisition method was introduced by Gamble *et al.* (1979) as a way to eliminate uncorrelated noise in the recorded fields. It is based on the fact that the magnetic field is stable over large distances and that the local noise recorded in the magnetic and electric fields can be detected and removed. It consists of the simultaneous recording of local and remote magnetic fields. The transfer functions are estimated as in eqs. 1.33 to 1.38, using the remote magnetic fields as the conjugate components.

Robust processing (Huber, 1981) consists of identifying and removing outliers to make estimates more "robust", which means that the estimates are not greatly affected by these outliers and respond slowly to the addition of more data. In the processing of magnetotelluric data, different robust methods have been developed:

- Egbert and Booker (1986) developed a robust method, similar to LS, with a weighting based on the errors, and the introduction of a "loss function" (Huber, 1981), which reduced the effect of outliers.
- Jones and Jödicke (1984) presented a coherence rejection technique, based on the maximisation of the field coherences (relationships between the estimated and predicted field components), using the jacknife approach (see chapter 3). A similar method is the variance minimisation technique (Jones *et al.*, 1989).
- Chave and Thomson (2004) developed a code to estimate the MT transfer functions (BIRRP: Bounded Influence Remote Reference Processing) which introduced the use of a bounded influence estimator to compare the measured and computed fields, and a hat matrix function to reduce the effects of outliers.

These three types of methods have been recently adapted to the use of single and multiple remote references.

The errors of the transfer functions are commonly estimated assuming that noise contributions are random and that the cross and power spectra from the individual segments follow a Gaussian distribution.

The variances of the MT tensor components are evaluated as (Bendat and Piersol,1971):

$$\text{var}\left(M_{ij}\right) = \frac{4}{v-4} F_{0.68}\left(1-\gamma^2\right) \frac{\left\langle E_i E_i^*\right\rangle \left\langle B_j B_j^*\right\rangle}{DET_j}, \tag{1.39}$$

where v is the number of degrees of freedom, $F_{0.68}(1-\gamma^2)$ is the upper limit of the Fisher-Schnedecor distribution for a given probability (68%), and γ^2 denotes the squared bivariate coherency between the predicted (P) and registered (R) field components:

$$\gamma^2(R,P) = \frac{\left\langle RP^*\right\rangle \left\langle PR^*\right\rangle}{\left\langle RR^*\right\rangle \left\langle PP^*\right\rangle}. \tag{1.40}$$

The error bars of the real and imaginary parts of the MT tensor components are equally determined to be the square root of the variance, which can be represented as a circle in the complex plane (Bendat and Piersol, 1971):

$$\delta(\text{Re}\, M_{ij}) = \delta(\text{Im}\, M_{ij}) = \delta(M_{ij}) = (\text{var}(M_{ij}))^{1/2}. \tag{1.41}$$

Through an error propagation process, the errors of the apparent resistivities and phases can also be estimated:

$$\delta(\rho_{ij}) = 2\frac{\delta(M_{ij})}{\left|M_{ij}\right|}\rho_{ij} = 0.4T\left|M_{ij}\right|\delta(M_{ij}), \tag{1.42}$$

$$\delta\left(\varphi_{ij}\right) = \arcsin\frac{\delta\left(M_{ij}\right)}{\left|M_{ij}\right|}. \tag{1.43}$$

A similar development leads to the error estimation of the tipper components.

Commonly, the error bars of the apparent resistivities are obtained as log (ρ_{ij}) rather than ρ_{ij}, which produce symmetrical error bars in a logarithmic plot. The errors of the phases are also are approximated, to remove the arcsine dependence:

$$\delta\left(\log\rho_{ij}\right) = 2\frac{d\log\left|M_{ij}\right|}{d\left|M_{ij}\right|}\delta\left(M_{ij}\right) = \frac{0.87}{\left|M_{ij}\right|}\delta\left(M_{ij}\right), \tag{1.44}$$

$$\delta(\varphi_{ij}) = \frac{0.71}{|M_{ij}|}\delta(M_{ij}) \quad .^{[3]}$$
(1.45)

1.7.2. Common processing techniques

At present, different processing software schemes are available, which implement some of the techniques explained above. In these, step 1) (data set up and preconditioning) is generally done automatically, using some of the windowing functions. The use of Cascade Decimation to transform the data from time to frequency domain (step 2) is almost generalised nowadays, as it presents important advantages over conventional FFT: less memory requirements, ability to compensate for rejected data in the time series, optimal results for broad band series and the conversion to frequencies in logarithmic scale.

With regard to the estimation of the MT transfer functions, robust methods with single (Jones *et al.*, 1989) and multiple (SAMTEX, 2004) remote references have been proven to give the best estimates.

However, when the data are highly affected by noise, these techniques may lead to similar, yet non-very satisfactory results, especially in the tipper function. It must be taken into account that each set of data has its particular characteristics and it is necessary to carefully inspect the time series, remove noisy segments in different ways and change some parameters in the windowing functions and the transfer functions estimation. Tools for quality control can be the coherency and the smoothness of the estimated functions.

---

[3] Proof:

Departing from the error of $\tan \varphi_{ij}$ ($\tan \varphi_{ij} = Im(M_{ij})/Re(M_{ij}) = y/x$):

$$\delta\left(\tan\varphi_{ij}\right) = \sqrt{\left(\frac{\partial \tan\varphi_{ij}}{\partial x}\right)^2 \delta^2(x) + \left(\frac{\partial \tan\varphi_{ij}}{\partial y}\right)^2 \delta^2(y)} = \sqrt{\left(\frac{-y}{x^2}\right)^2 \delta^2(x) + \left(\frac{1}{x}\right)^2 \delta^2(y)},$$

where, using eq. 1.41 ($\delta(x) = \delta(y) = \delta(M_{ij})$): $\delta\left(\tan\varphi_{ij}\right) = \frac{y}{x}\sqrt{\left(\frac{1}{x^2}+\frac{1}{y^2}\right)\delta^2\left(M_{ij}\right)} \approx \tan\varphi_{ij}\cdot\sqrt{2}\frac{\delta\left(M_{ij}\right)}{|M_{ij}|}$.

On the other hand: $\delta\left(\tan\varphi_{ij}\right) = \left|\frac{d\tan\varphi_{ij}}{d\varphi_{ij}}\right|\delta\left(\varphi_{ij}\right) = \left|\frac{1}{\cos^2\varphi_{ij}}\right|\delta\left(\varphi_{ij}\right)$.

Equaling both errors: $\frac{1}{\cos^2\varphi_{ij}}\delta\left(\varphi_{ij}\right) = \tan\varphi_{ij}\cdot\sqrt{2}\frac{\delta\left(M_{ij}\right)}{|M_{ij}|}$,

and $\delta\left(\varphi_{ij}\right) = \tan\varphi_{ij}\cdot\cos^2\varphi_{ij}\cdot\sqrt{2}\frac{\delta\left(M_{ij}\right)}{|M_{ij}|} = \sin\varphi_{ij}\cdot\cos\varphi_{ij}\cdot\sqrt{2}\frac{\delta\left(M_{ij}\right)}{|M_{ij}|} = \frac{\sin 2\varphi_{ij}}{2}\sqrt{2}\frac{\delta\left(M_{ij}\right)}{|M_{ij}|}$.

Assuming an average angle $\varphi_{ij} = 45^\circ$, $\delta\left(\varphi_{ij}\right) = \frac{\sqrt{2}}{2}\frac{\delta\left(M_{ij}\right)}{|M_{ij}|}$. QED.

1.8 Modelling and Inversion of MT Data

The conductivity distribution of the Earth in the region of interest is usually obtained through a modelisation process. In MT, a model consists of a region with a particular conductivity distribution, which can be 1D, 2D or 3D depending on the conductivity variations along different directions. The model parameters are the conductivity values at different model positions. The model responses are normally the resistivities and phases measured at the Earth's surface as a consequence of the electromagnetic fields travelling through these conductivity distributions, according to Maxwell's equations, although other functions can be used.

Depending on the dimensionality and complexity associated with the magnetotelluric transfer functions, 1D, 2D and 3D models are constructed using different modelling techniques.

Nowadays, the forward modelling can be solved efficiently for any dimensionality model, analytically in simple cases and numerically in general. One of the most used codes in 2D is PW2D (Wannamaker *et al.*, 1987), which uses the finite elements algorithm to compute the model responses, and is characterised by high numerical stability. In 3D, the Mackie *et al.* (1993) code solves the integral form of Maxwell's equations using the finite differences method. The Pek and Verner (1997) code uses finite differences to solve the forward modelling problem for anisotropic structures.

Inversion schemes search the relationships between the measured data and the model responses, modifying the model until an agreement is approached. In many cases these are a combination of forward modelling plus minimisation (or maximisation) algorithms. OCCAM 1D and 2D inversion codes (Constable *et al.*, 1987) are based on the minimisation or maximisation of a certain function using a Lagrange multiplier. In 2D, the RRI (Rapid Relaxation Inversion) (Smith and Booker, 1991), RLM2DI (Mackie *et al.*, 1997) and REBOCC (Siripunvaraporn and Egbert, 2000) codes are in common usage. Pedersen and Engels (2005) developed the application of the REBOCC code (DetREBOCC) to invert the determinant of the impedance tensor.

In relation to 3D conductivity models, MT inversion is still in the development stage, although several algorithms tested with synthetic data and simple models have already led to satisfactory results. 3D inversion codes will be available in the near future (Mackie and Madden, 1993; Newman and Alumbaugh, 2000; Zhdanov *et al.*, 2000; Sasaki, 2001). One of these codes is Siripunvaraporn *et al.* (2005), based on the data-space method, as an extension of the Occam approach, which has recently been officially released to public. Meanwhile, 3D MT interpretation is done by trial-and-error forward model fitting.

Chapter 2: Geoelectric Dimensionality and Rotational Invariants of the Magnetotelluric Tensor

In the previous chapter the concept of geoelectric dimensionality was introduced. This chapter investigates further into its characterisation. It introduces the rotational invariants of the magnetotelluric tensor and presents the most common methods used to obtain a description of the dimensionality and the recovery of the regional tensor. Moreover, at the end of the chapter, the main problems and limitations existing in the dimensionality characterisation are discussed. Finally, the different aspects of the work performed in this thesis, which allow totally or partially solving some of these problems and limitations, are indicated.

2.1. Introduction

As explained in chapter 1, analysis of dimensionality is a powerful tool that may provide information such as variation of strike direction with depth, which can be correlated with different processes and structure in the Earth's crust and mantle (e.g. Marquis *et al.,* 1995). Depending on the result of dimensionality analysis, MT data may be interpreted as being either one, two or three-dimensional. A proper dimensionality interpretation is important since a two-dimensional interpretation of three-dimensional data can be acceptable in some cases while not in others (Wannamaker, 1999; Park and Mackie, 2000; Ledo *et al*., 2002b; Ledo, 2005).

Most of the methods used to decipher the dimensionality of the geoelectric structures are based on the rotational invariants, i.e., sets of parameters computed from the observed MT

tensor that do not depend on the direction of the measuring axes. Different sets of rotational invariants have been proposed to assert particular categories of dimensionality (Swift, 1967; Berdichevsky and Dmitriev, 1976; Bahr, 1988; Bahr, 1991; Lilley, 1993, 1998a, 1998b). Fischer and Masero (1994) argued the existence of eight invariants, seven independent and one dependent and, later, Szarka and Menvielle (1997) determined a full set of MT tensor invariants and suggested their use for a compact dimensionality interpretation. Weaver *et al.* (2000) provided a method whereby dimensionality was characterised in terms of the annulment of some of the invariants. Other authors (Romo *et al.*, 1999) use invariant parameters defined from the geomagnetic transfer function to characterise 2D and 3D responses.

Alternatively, Caldwell *et al.* (2004) introduced the magnetotelluric phase tensor, defined as the relationship between the real and imaginary parts of the MT tensor. It is a practical tool to obtain information about the dimensionality of the regional structure, since it is not affected by galvanic distortion. However, because of this, its applications are limited, since it is not possible to recover the regional responses.

2.2. Fundamental Rotational Invariants of the Magnetotelluric Tensor

Under a rotation of an arbitrary angle α around the z-axis, a reference frame xyz is transformed into x'y'z. Accordingly, the magnetotelluric tensor can be defined in the new reference frame: $\underline{M}\,'(\omega) = R_\alpha \cdot \underline{M}(\omega) \cdot R_\alpha^T$ (eq. 1.19).
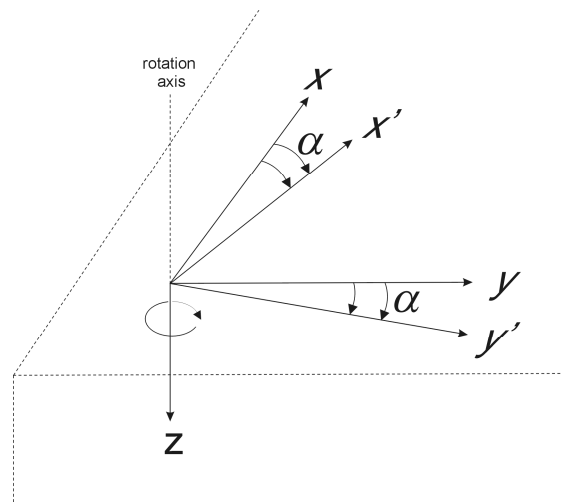
Figure 2.1: Reference frames used to define the magnetotelluric tensor components: xyz are the axes of the original frame. x'y'z are the new axes after a α clockwise rotation, around the z-axis.

For instance, if the rotation is clockwise, the components of $\underline{M}\,'$ are expressed as:

$$M'_{xx} = M_{xx} \cos^2 \alpha + M_{yy} \sin^2 \alpha + \left(M_{xy} + M_{yx}\right)\sin \alpha \cos \alpha \,, \qquad (2.1a)$$

$$M'_{xy} = \left(-M_{xx} + M_{yy}\right)\sin \alpha \cos \alpha + M_{xy} \cos^2 \alpha + M_{yx} \sin^2 \alpha \,, \qquad (2.1b)$$

$$M'_{yx} = \left(-M_{xx} + M_{yy}\right)\sin \alpha \cos \alpha - M_{xy} \sin^2 \alpha + M_{yx} \cos^2 \alpha \,, \qquad (2.1c)$$

$$M'_{yy} = M_{xx} \sin^2 \alpha + M_{yy} \cos^2 \alpha - \left(M_{xy} + M_{yx}\right)\sin \alpha \cos \alpha \,. \qquad (2.1d)$$

An important rotation-related property of the tensor is its 180° periodicity:

$$M'_{ij}(\omega)(\alpha + \pi) = M_{ij}(\omega)(\alpha) \,; \text{(ij=xx,xy,yx,yy)}. \qquad (2.2)$$

The rotational properties of the magnetotelluric tensor are those of a 2x2 complex tensor containing eight real and independent variables. Szarka and Menvielle (1997) suggested a set of seven independent real-valued rotational invariants based on three complex magnitudes traditionally used in magnetotellurics:

1) The trace:
$$S_1 = M_{xx} + M_{yy} \,. \qquad (2.3a)$$

2) The difference between off-diagonal elements:
$$D_2 = M_{xy} - M_{yx} \,. \qquad (2.3b)$$

3) The determinant:
$$\det M = M_{xx}M_{yy} - M_{xy}M_{yx} \,. \qquad (2.3c)$$

S_1 and D_2 are two of the four modified impedances (Vozoff, 1991), each one containing two rotational real-valued invariants: $\text{Re}(S_1)$, $\text{Im}(S_1)$ and $\text{Re}(D_2)$, $\text{Im}(D_2)$ respectively. From det(M) three independent real-valued invariants can be defined: $\det(\text{Re}(M))$, $\det(\text{Im}(M))$ and $\text{Im}(\det(M))$. This makes a total of seven real and independent rotational invariants.

Other sets of invariants can be defined as a function of these basic invariants. The seven rotational invariants, or just some of them, have been and are still widely used to study particular properties of the MT tensor and other magnitudes related to the measured electromagnetic fields.

2.3 Two-Dimensionality and Strike Direction: Swift's Angle and Skew

As stated in chapter 1, when the measured tensor corresponds to a structure with 2D geoelectric dimensionality, the measuring axes (x, y, z) can be rotated an angle θ (strike angle) such that one of the new axis (x' or y') matches the strike direction of the geoelectric structure. Accordingly, the tensor M' takes a non-diagonal form.

The strike angle can be determined for a perfectly 2D MT tensor by setting equations 2.1a and 2.1d equal to zero. In nature, most 2D MT tensors are not strictly non-diagonal and other strategies are necessary in order to obtain a reliable approximation of the strike direction.

The most common approximation is based on the maximisation of the non-diagonal components of the MT tensor and the minimisation of the diagonal ones, using the sum of the squared modulus of these components (Vozoff, 1972):

$$\left|M'_{xy}(\theta)\right|^2 + \left|M'_{yx}(\theta)\right|^2 = \text{maximum} , \tag{2.4a}$$

$$\left|M'_{xx}(\theta)\right|^2 + \left|M'_{yy}(\theta)\right|^2 = \text{minimum} . \tag{2.4b}$$

The resulting strike angle is known as Swift's angle (Swift, 1967):

$$\tan(4\theta) = \frac{2 \cdot \text{Re}(D_1 \cdot S_2)}{\left|D_1\right|^2 - \left|S_2\right|^2} , \tag{2.5}$$

where $D_1 = M_{xx} - M_{yy}$ and $S_2 = M_{xy} + M_{yx}$ are the remaining modified impedances (Vozoff, 1991), which are not rotational invariants.

From the modified impedances S_1 and D_2, a rotational invariant, the Swift's skew, can be defined. It relates the diagonal and non-diagonal components of the MT tensor and quantifies how accurately the MT tensor can represent a 2D structure:

$$\kappa = \frac{\left|S_1\right|}{\left|D_2\right|} . \tag{2.6}$$

If its value is small, the 2D hypothesis is valid and, hence, Swift's angle indicates the strike direction. Otherwise, the tensor corresponds to another type of structure.

2.4 Bahr Parameters

Bahr (1991), with modifications of Szarka (1999), proposed the use of four rotational real-valued invariant parameters to classify the types of the geoelectric dimensionality and distortion types that can affect it. These parameters were derived from the impedance tensor ($\underline{Z} = \mu_0 \cdot \underline{M}$), and its modified impedances ($S_1 = Z_{xx} + Z_{yy}$, $S_2 = Z_{xy} + Z_{yx}$, $D_1 = Z_{xx} - Z_{yy}$, $D_2 = Z_{xy} - Z_{yx}$):

$$\kappa = \frac{|S_1|}{|D_2|}, \text{ (Swift's Skew)}, \tag{2.7a}$$

$$\mu = \frac{\left([D_1, S_2] + [S_1, D_2]\right)^{\frac{1}{2}}}{|D_2|}, \tag{2.7b}$$

$$\eta = \frac{\left([D_1, S_2] - [S_1, D_2]\right)^{\frac{1}{2}}}{|D_2|}, \text{ (Regional skew or Phase sensitive skew)} \tag{2.7c}$$

$$\Sigma = \frac{\left(D_1^2 + S_2^2\right)}{D_2^2}, \tag{2.7d}$$

where $[A,B] = \text{Re}(A) \cdot \text{Im}(B) - \text{Re}(B) \cdot \text{Im}(A)$.

Bahr parameters are dimensionless. μ and η are normalised to unity whereas κ and Σ can have values greater than one in the presence of galvanic distortion.

κ is the Swift's Skew (see section 2.3) and μ is a measure of the phase difference between the components of the magnetotelluric tensor. η indicates if the magnetotelluric tensor can be described by a superimposition model (the product of a small 3D heterogeneity matrix with the regional 1D or 2D MT tensor, 3D/1D or 3D/2D), which is also a measure of three-dimensionality. Σ is related to two-dimensionality.

The quantification of these parameters, according to Bahr (1991), allows deciphering the geoelectric dimensionality cases (1D, 2D and 3D) and the types of distortion models defined by Larsen (1977) and Bahr (1988). The Larsen (1977) model consists of a galvanic distortion over a 1D structure (3D/1D). The model defined by Bahr (1988), known as superimposition model, consists of a galvanic distortion over a two-dimensional structure: 3D/2D.

The recommended threshold values of these parameters proposed such as to infer the types of geoelectric dimensionality and distortion are summarised in Table 2.1.

In two-dimensional cases (2 and 4) the strike angle, θ, is obtained by the expression:

$$\tan(2\theta) = \frac{[S_1, S_2] - [D_1, D_2]}{[S_1, D_1] + [S_2, D_2]}, \tag{2.8}$$

which is determined from the condition that a 2D MT tensor expressed in the strike reference frame, affected or not by galvanic distortion, has the same phase values in each of the MT tensor columns. This angle is the so-called phase-sensitive strike.

Case	Bahr Parameter Values	DIMENSIONALITY/ DISTORTION TYPE
1	$\kappa < 0.1;\ \Sigma < 0.1$	1D
2	$\kappa < 0.1;\ \Sigma > 0.1$	2D
3	$\kappa > 0.1;\ \mu = 0$	3D/1D (Larsen model)
4	$\kappa > 0.1;\ \mu \neq 0;\ \eta < 0.05$	3D/2D (Bahr model)
5	$\kappa > 0.1;\ \mu \neq 0;\ \eta > 0.3$	3D

Table 2.1: Bahr method criteria to characterise the geoelectric dimensionality and distortion types.

Among these 2D cases, Bahr (1991) also suggested the possibility that the condition cited above is not fulfilled. Instead there is a non-zero phase difference value for each column, which must be minimised when the axes are rotated to the strike direction. This model is known as an extension of the superimposition model, which is called the delta (δ) technique, and is valid under the condition $0.1 < \eta < 0.3$.

In the literature, Bahr parameters have been used sometimes incorrectly, when justifying that the data are 2D if $\eta < 0.3$; whereas it has been demonstrated (e.g. Ledo *et al.*, 2002b) that $\eta > 0.3$ is a sufficient condition for 3D, but that the contrary is not true ($\eta < 0.3$ does not imply that the structure is 2D). Simpson and Bahr (2005) also cite this common misuse of the regional skew η.

2.5 WAL Rotational Invariant Parameters

Weaver *et al*. (2000) presented a new formulation of the rotational invariant parameters of the MT tensor. The set of invariants (WAL hereafter) was redefined in the way that the invariants, with the exception of two, are non-dimensional, each one having a clear graphical representation and their vanishing has a physical interpretation, specifically the geoelectric dimensionality.

The WAL invariants were defined from a decomposition of the MT tensor into its real and imaginary parts, and by defining the complex parameters $\zeta_i = \xi_i + \eta_i i$ (i=1,4), which are

linear combinations of MT tensor components, $\zeta_1 = \left(M_{xx} + M_{yy} \right)/2$, $\zeta_2 = \left(M_{xy} + M_{yx} \right)/2$, $\zeta_3 = \left(M_{xx} - M_{yy} \right)/2$ and $\zeta_4 = \left(M_{xy} - M_{yx} \right)/2$:

$$\underline{M} = \begin{pmatrix} \zeta_1 + \zeta_3 & \zeta_2 + \zeta_4 \\ \zeta_2 - \zeta_4 & \zeta_1 - \zeta_3 \end{pmatrix} = \begin{pmatrix} \xi_1 + \xi_3 & \xi_2 + \xi_4 \\ \xi_2 - \xi_4 & \xi_1 - \xi_3 \end{pmatrix} + i \begin{pmatrix} \eta_1 + \eta_3 & \eta_2 + \eta_4 \\ \eta_2 - \eta_4 & \eta_1 - \eta_3 \end{pmatrix}. \tag{2.9}$$

Through this decomposition, the expressions of the WAL invariants are as follows:

$$I_1 = \left(\xi_1^2 + \xi_4^2 \right)^{\frac{1}{2}} \text{ (m/s)}, \tag{2.10}$$

$$I_2 = \left(\eta_1^2 + \eta_4^2 \right)^{\frac{1}{2}} \text{ (m/s)}, \tag{2.11}$$

$$I_3 = \frac{\left(\xi_2^2 + \xi_3^2 \right)^{\frac{1}{2}}}{I_1}, \tag{2.12}$$

$$I_4 = \frac{\left(\eta_2^2 + \eta_3^2 \right)^{\frac{1}{2}}}{I_2}, \tag{2.13}$$

$$I_5 = \frac{\xi_4 \eta_1 + \xi_1 \eta_4}{I_1 I_2}, \tag{2.14}$$

$$I_6 = \frac{\xi_4 \eta_1 - \xi_1 \eta_4}{I_1 I_2} = d_{41}, \tag{2.15}$$

$$I_7 = \left(d_{41} - d_{23} \right)/Q. \tag{2.16}$$

d_{ij} (i,j=1-4) and Q are also invariants that depend on parameters ξ_i η_i and on other invariants:

$$d_{ij} = \frac{\xi_i \eta_j - \xi_j \eta_i}{I_1 I_2}, \tag{2.17}$$

$$Q = \left[\left(d_{12} - d_{34} \right)^2 + \left(d_{13} + d_{24} \right)^2 \right]^{\frac{1}{2}}. \tag{2.18}$$

I_7 and Q are related in that if Q is too small, then I_7 approaches infinity and its value remains undetermined. It can be seen that I_3 to I_6 are normalized and that I_3 to I_7 and Q are dimensionless.

WAL rotational invariants can be represented, following the works of Lilley in a Mohr's circle diagram (Lilley, 1976, 1993, 1998a, 1998b), whose axes display the M_{11} (vertical) and M_{12} (horizontal) components of the MT tensor (Figure 2.2).

In this graphical representation P_1 $(\mathrm{Re}(M_{11}), \mathrm{Re}(M_{12}))$ and $P_2(\mathrm{Im}(M_{11}), \mathrm{Im}(M_{12}))$ are the positions of the real and imaginary parts of M_{11} and M_{12} while C and D points are located at coordinates (ξ_1, ξ_4) and (η_1, η_4) respectively. Through a 180° rotation of the measuring axes, P_1 and P_2 describe the complete real and imaginary Mohr circles, with centres located in C and D and radii equal to $(\xi_2^2 + \xi_3^2)^{\frac{1}{2}}$ and $(\eta_2^2 + \eta_3^2)^{\frac{1}{2}}$ respectively. Hence, a rotation of an angle α is translated into a 2α rotation of points P_1 and P_2.

I_1 and I_2 are the modulae of C and D position vectors, $I_1 = |OC|$ and $I_2 = |OD|$. I_3 and I_4 are the sines of γ and δ angles, i.e., the ratios between the circles' radii and I_1 or I_2: $I_3 = \sin\gamma$ and $I_4 = \sin\delta$. $I_5 = \sin(\beta+\alpha)$ and $I_6 = \sin(\beta-\alpha)$ relate the relative positions between the real and imaginary circles. $2\theta_1$ and $2\theta_2$ are the angles through which P_1 and P_2 must be rotated along the circle to reach the same vertical position as C and D, respectively:

$$\tan(2\theta_1) = -\frac{\xi_3}{\xi_2} \qquad \text{and} \qquad \tan(2\theta_2) = -\frac{\eta_3}{\eta_2}. \tag{2.19}$$

Consequently, θ_1 and θ_2 are, in the order given, the angles through which the measurement axes must be rotated so that the real and imaginary parts belonging to the non-diagonal components of the MT tensor have the same value. I_7 is defined as the sine of the difference between these two angles: $I_7 = \sin(\theta_1 - \theta_2)$.

Invariant Q is defined from a complex relation between the angle obtained from the intersection of the prolongation of $\overline{CP_1}$ and $\overline{DP_2}$, ψ, and angles α, β, δ and γ:

$$Q = \left(\sin^2\gamma + \sin^2\delta - 2\sin\gamma\sin\delta\cos(\beta-\alpha-\psi)\right)^{1/2}.$$

Invariants I_1 and I_2 provide information about the 1D magnitude and phase of the geoelectric resistivity:

$$\rho_{1D} = \mu_0 \frac{\left(I_1^2 + I_2^2\right)}{\omega}, \tag{2.20}$$

$$\varphi_{1D} = \arctan\left(\frac{I_2}{I_1}\right). \tag{2.21}$$
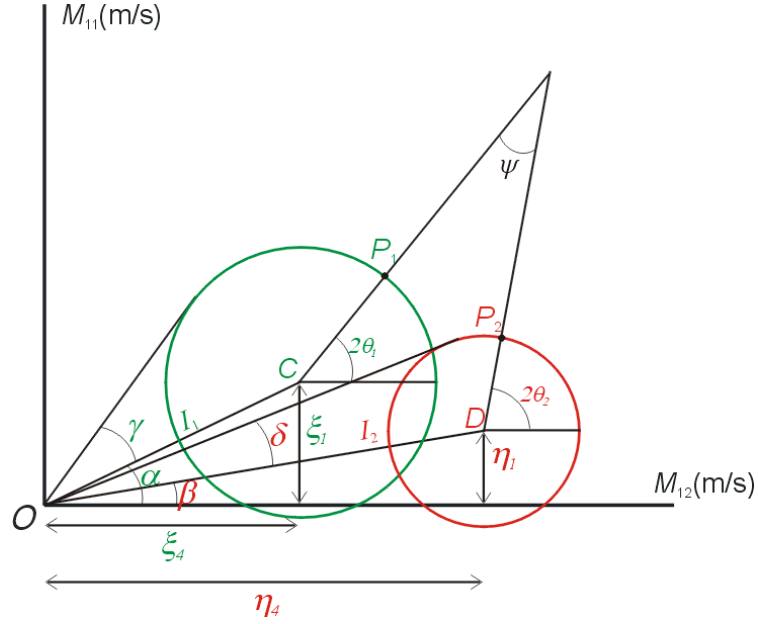
Figure 2.2: Graphical representation of real and imaginary Mohr circles, generated after a complete rotation of M_{12} and M_{11} components of the MT tensor. Green: real circle and related parameters and angles. Red: idem for imaginary.

Invariants I_3 to I_7 and Q make it possible to establish criteria (Weaver *et al.*, 2000; Weaver, pers. comm.) that are suitable to assess dimensionality and galvanic distortion (Table 2.2).

In a 1D geoelectric medium (case 1 in Table 2.2), characterised by a MT tensor with null diagonal components and equal non-diagonal components with opposite signs, the Mohr circles reduce to the two points corresponding to the real and imaginary values of M_{12}. With the exception of I_1 and I_2, all invariants are zero. Apparent resistivity and phase can be directly determined from eqs. 2.20 and 2.21.

For a MT tensor corresponding to a 2D medium (case 2 in Table 2.2), the centres of the Mohr circles are also located over the M_{12} axis, but have non-zero radii values. Along the strike direction, P_1 and P_2 are also located over the M_{12} axis, so both θ_1 and θ_2 are zero. For any other direction, the non-zero values of θ_1 and θ_2 must be the same (equation 2.19), in order to ensure that both real and imaginary diagonal components of the MT tensor become null along the same direction, that of the strike. Since $\overline{CP_1}$ and $\overline{DP_2}$ are parallel the angle ψ is zero. Therefore, in a 2D medium, I_3 and I_4 are non-zero. I_5 and I_6 are null, because α and β angles are null also. I_7 is null, although it may be undetermined if Q is very small (if $I_3 \approx I_4$).

Case	I_3 to I_7 and Q values	GEOELECTRIC DIMENSIONALITY
1	$I_3 = I_4 = I_5 = I_6 = 0$	**1D**
2	$I_3 \neq 0$ or $I_4 \neq 0$; $I_5 = I_6 = 0$; $I_7 = 0$ or $Q = 0$ ($\xi_4 \neq 0$ and $\eta_4 \neq 0$)	**2D**
3a	$I_3 \neq 0$ or $I_4 \neq 0$; $I_5 \neq 0$; $I_6 = 0$; $I_7 = 0$	**3D/2Dtwist** 2D affected by galvanic distortion (only twist)
3b	$I_3 \neq 0$ or $I_4 \neq 0$; $I_5 \neq 0$; $I_6 = 0$; $Q = 0$	**3D/1D2D** Galvanic distortion over a 1D or 2D structure (non-recoverable strike direction)
3c	$I_3 \neq 0$ or $I_4 \neq 0$; $I_5 = I_6 = 0$; $I_7 = 0$ or $Q = 0$ ($\xi_4 = 0$ and $\eta_4 = 0$)	**3D/1D2Ddiag** Galvanic distortion over a 1D or 2D structure resulting in a diagonal MT tensor
4	$I_3 \neq 0$ or $I_4 \neq 0$; $I_5 \neq 0$; $I_6 \neq 0$; $I_7 = 0$	**3D/2D** General case of galvanic distortion over a 2D structure
5	$I_7 \neq 0$	**3D** (affected or not by galvanic distortion)

Table 2.2: Dimensionality criteria according to the WAL invariants values of the magnetotelluric tensor (Modified from Weaver *et al.*, 2000).

Both 1D and 2D media can be affected by galvanic distortion, which, according to WAL invariants, can be grouped into four different cases:

- Galvanic distortion affecting a 2D medium, produced by a twist of the electric field (case 3a in Table 2.2): In this case the galvanic distortion is described by a matrix with parameters $g_1 = g_2$ and $\phi_1 = \phi_2$ ($e = 0$ and $t \neq 0$). In general, the values of M_{11} are not null and the centres of the Mohr circles are not located over the M_{12} axis. $\overline{OC}$ and $\overline{OD}$ have the same orientation, i.e., α and β are non-zero but have the same value. On the contrary, γ and δ are different. θ_1 and θ_2 have the same value ($\overline{CP_1}$ and $\overline{DP_2}$ are parallel), although it does not correspond to the strike direction. Consequently, $\psi=0$. Hence, I_3, I_4 (where $I_3 \neq I_4$), I_5 and Q are non-zero, whereas I_6 and I_7 are null.

- Galvanic distortion over 1D or 2D media with equal phases in E and B polarisations (case 3b in Table 2.2): These two situations are indistinguishable, and in the second (distortion over 2D media) it is not possible to determine the strike direction. The Mohr circles follow the same pattern as in case 3a, with the additional particularity that $\gamma = \delta$. Consequently, I_3, I_4 ($I_3 = I_4$) and I_5 are non-zero, and I_6 is null. Given that $I_3 = I_4$ and $\psi = 0$, Q is null and I_7 remains undetermined.

- Galvanic distortion over a 1D or 2D medium, resulting in a diagonal MT tensor (case 3c in Table 2.2): This is a very particular case of distortion, described by a non-diagonal matrix. Mohr circles are analogous to those of the 2D media, with the centres located over the M_{11} axis instead of M_{12}, and $\zeta_4 = 0$. WAL invariants can have the same values as in a 2D medium, so case 3c is distinguished from case 3a only by the condition $\zeta_4 = 0$. The strike direction, θ_D, after which the distorted diagonal tensor can be recovered, is computed using:

$$\tan(2\theta_D) = \frac{\xi_2}{\xi_3} = \frac{\eta_2}{\eta_3} . \tag{2.22}$$

- General case of galvanic distortion over a 2D medium (case 4 in Table 2.2): Mohr circles do not follow any particular pattern (the centres are outside of the M_{12} axis, γ and δ, and α and β are non-zero angles and have different values among them), with the exception that θ_1 and θ_2 have the same value. As a consequence, all invariants but I_7 are non-zero.

For cases 3a and 4, the strike angle, named θ_3, and the distortion parameters, ϕ_1 and ϕ_2 (see equations 1.27 and 1.29) can be retrieved:

$$\tan(2\theta_3) = \frac{d_{12} - d_{34}}{d_{13} + d_{24}} , \tag{2.23}$$

$$\tan(\phi_1) = \frac{\operatorname{Re} M'_{yy}}{\operatorname{Re} M'_{xy}} = \frac{\operatorname{Im} M'_{yy}}{\operatorname{Im} M'_{xy}} , \tag{2.24}$$

$$\tan(\phi_2) = \frac{\operatorname{Re} M'_{xx}}{\operatorname{Re} M'_{yx}} = \frac{\operatorname{Im} M'_{xx}}{\operatorname{Im} M'_{yx}} . \tag{2.25}$$

Finally, for a MT tensor corresponding to a 3D medium (case 5 in Table 2.2), the pattern of Mohr circles cannot be included in any of the previous descriptions. In this case, all invariants, including I_7 and Q are non-zero and have a finite value. However, it is not possible to distinguish whether the MT tensor is affected by galvanic distortion or not.

The main problem when WAL invariants criteria are used with real data is that the geoelectric dimensionality may be found to be 3D although other evidence (low MT diagonal components' responses, preferred strike direction among different sites and periods…) suggests that a 1D or 2D interpretation would be valid for modelling. This is because invariant values for real data are in general never exactly zero due to the presence of noise. Weaver *et al.* (2000) address this problem by introducing a threshold value, beneath which the invariants are taken to be zero.

The threshold value they suggest is 0.1. Since WAL invariants I_3 to I_7 and Q represent the sines of angles related to Mohr circles, this threshold corresponds to the sine of 5.7$^\mathrm{o}$, which, in relation to 90$^\mathrm{o}$, represents a 6% error. Although the choice of this threshold is subjective, it was tested using a synthetic model with 2% noise, which showed a valid dimensionality pattern consistent with the model structures.

2.6 The Magnetotelluric Phase Tensor

The magnetotelluric phase tensor (or phase tensor) (Caldwell *et al.*, 2004) was introduced as a tool to obtain information about the dimensionality of the regional structure, given that it is not affected by galvanic distortion.

The phase of a tensor with complex components is a real valued tensor, Φ, which is defined from the generalization of the phase of a complex number, i.e., as the inverse of the tangent of the ratio between its imaginary and real parts (Caldwell *et al.*, 2004):

Thus, for a complex tensor $\underline{M}=X+i\cdot Y$:

$$\Phi = X^{-1}Y \ . \tag{2.26}$$

In the case of the magnetotelluric or impedance tensor, which is a 2$^\mathrm{nd}$ rank tensor,

$$\underline{M} = \begin{bmatrix} X_{11} + iY_{11} & X_{12} + iY_{12} \\ X_{21} + iY_{21} & X_{22} + iY_{22} \end{bmatrix}, \tag{2.27}$$

the phase tensor (Φ) is expressed as:

$$\Phi = \begin{bmatrix} \Phi_{11} & \Phi_{12} \\ \Phi_{21} & \Phi_{22} \end{bmatrix} = \begin{bmatrix} X_{22}Y_{11} - X_{12}Y_{21} & X_{22}Y_{12} - X_{12}Y_{22} \\ X_{11}Y_{21} - X_{21}Y_{11} & X_{11}Y_{22} - X_{21}Y_{12} \end{bmatrix} / \det(X), \qquad (2.28)$$

where $\det(X) = X_{11}X_{22} - X_{12}X_{21}$.

Φ is not affected by galvanic distortion, although it is not invariant under rotation.

In the particular 1D case, the phase tensor takes a diagonal form, with their two component values equal to the tangent of the phase (equations 1.15c and 1.15d). As for a 2D MT tensor, the phase tensor is also diagonal, but their components have different values, which are the tangents of the TE and TM phases. In a general 3D case, the phase tensor displays the relationship between the phases of the horizontal components of the electric and magnetic fields.

The phase tensor can be represented through a Singular Value Decomposition (SVD) as the product of three matrixes:

$$\Phi = R^T(\alpha_P - \beta_P) \cdot S \cdot R(\alpha_P + \beta_P) = R^T(\alpha_P - \beta_P)\begin{bmatrix} \Phi_{Max} & 0 \\ 0 & \Phi_{min} \end{bmatrix} R(\alpha_P + \beta_P), \quad (2.29)$$

where $R(\delta)$ ($\delta = \alpha_P - \beta_P$ or $\delta = \alpha_P + \beta_P$) represents a clockwise rotation,

$$R(\delta) = \begin{bmatrix} \cos\delta & \sin\delta \\ -\sin\delta & \cos\delta \end{bmatrix}. \qquad (2.30)$$

$R^T(\alpha_P - \beta_P)$ and $R(\alpha_P + \beta_P)$ are the eigenvectors of the tensor products $\Phi^T\Phi$ and $\Phi\Phi^T$ respectively. The expressions of α_P and β_P are derived as [1]:

$$\alpha_P = \arctan\left(\frac{\Phi_{12} + \Phi_{21}}{\Phi_{11} - \Phi_{22}}\right)/2, \qquad (2.31)$$

$$\beta_P = \arctan\left(\frac{\Phi_{12} - \Phi_{21}}{\Phi_{11} + \Phi_{22}}\right)/2. \qquad (2.32)$$

S in eq. 2.29 is referred to as the Singular Matrix, where Φ_{Max} and Φ_{min} are the square roots of $\Phi^T\Phi$ or $\Phi\Phi^T$ eigenvalues, real numbers which are arranged in descending order in S:

---

[1] The original notation of Caldwell *et al.* (2004) used the notation α and β instead of α_P and β_P. In this thesis the subscript "*P*" was added to emphasize that it refers to the magnetotelluric **p**hase tensor notation.

$$\Phi^2_{\substack{Max \\ min}} = \frac{Tr(\Phi\Phi^T) \pm \sqrt{Tr(\Phi\Phi^T)^2 - 4\det(\Phi\Phi^T)}}{2} . \tag{2.33}$$

Since Φ is a 4 real component tensor, it has 4 associated parameters: One, the angle α_p, which is not a rotational invariant, and three rotational invariants: β_P, Φ_{Max} and Φ_{min} (eq. 2.29).

β_P is the skew of the phase tensor. In a two-dimensional medium its value is zero.

Simpler expressions of Φ_{Max} and Φ_{min} in terms of the phase tensor components can only be obtained for 1D and 2D geoelectric media. These expressions are the tangents of regional TE and TM mode phases, and, depending on which has the maximum and minimum values could be:

$$\Phi_{\substack{Max \\ min}} = \tan\varphi_{\substack{TE \\ TM}} \qquad \text{or} \qquad \Phi_{\substack{Max \\ min}} = \tan\varphi_{\substack{TM \\ TE}} . \tag{2.34}$$

Hence, each of these parameters is related to one of the two directions along which a linear polarization of the magnetic field leads to a linear polarization of the electric field. If Φ_{Max} and Φ_{min} have the same value, there is not a preferential direction and the structure is 1D, whereas if Φ_{Max} and Φ_{min} are different, these two directions exist and indicate that the structure is 2D, as long as $\beta_P=0$. For general 3D cases, Φ_{Max} and Φ_{min} are also different and $\beta_P \neq 0$, resulting in more complex expressions. In real datasets, the threshold of β_P to identify 3D cases is approximately 3°.

The phase tensor can be represented as an ellipse in which Φ_{Max} and Φ_{min} are the major and minor axis and α_P - β_P is the azimuth of the major axis (Figure 2.3). In the case that $\beta_P=0$, this azimuth coincides with α_P and represents the strike direction or its perpendicular, depending on which TE or TM modes has the largest phase value.

The way in which α_P, Φ_{Max} and Φ_{min} are related is that α_P has a physical meaning only if $\left|\Phi_{Max} - \Phi_{min}\right|$ is non-zero, i.e., in 2D and 3D cases. If data errors are considered, this assertion can be extended to the condition $\arctan\left|\Phi_{Max} - \Phi_{min}\right| > \sigma_{\alpha_P}$, where σ_{α_P} is the error in the determination of angle α_P.
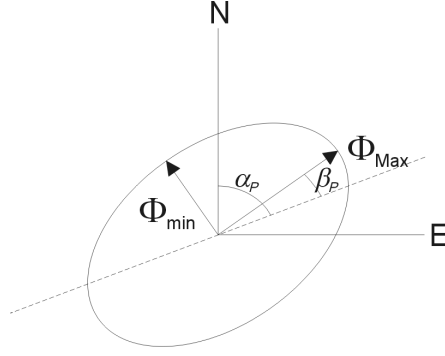
Figure 2.3: Graphical representation of the phase tensor. The lengths of the principal axes are Φ_{Max} and Φ_{min} and α_P - β_P is the azimuth of the ellipse major axis. N and E correspond to x and y coordinates axes respectively (Modified from Caldwell *et al.*, 2004).

Figure 2.4 shows the phase tensor characteristics and representation for 1D and 2D types of dimensionality: 1D media are represented by a circle, given that $\left| \Phi_{Max} - \Phi_{min} \right|$ is equal to zero and α_P has a meaningless value. 2D media are represented by an ellipse with the major axis aligned along the strike direction, α_P. For 3D geoelectrical media, the phase tensor is displayed as in Figure 2.3: an ellipse with β_P different from zero and consequently with an angle α_P that cannot be identified as the strike direction.
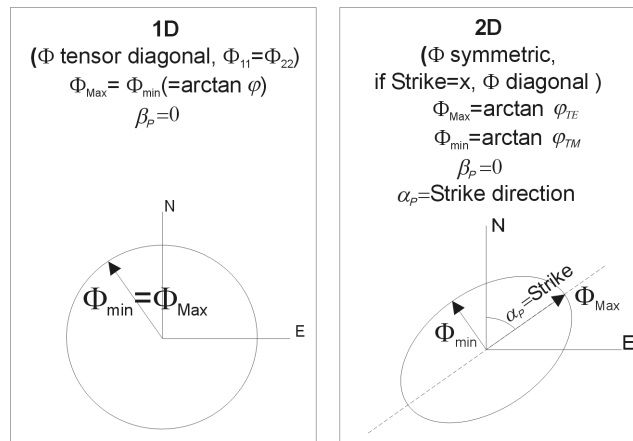
Figure 2.4: Phase tensor properties and representations of particular 1D and 2D dimensionality cases.

Summarizing, the phase tensor parameters involved in the characterization of dimensionality are: Φ_{Max} and Φ_{min}, which provide the arctangent of TE and TM mode phases;

their difference, $\left|\Phi_{Max} - \Phi_{min}\right|$, which indicates if the structure can be described as 2D; β_P, which quantifies the validity of a 2D description, and α_P, which provides the strike direction. In 2D media, the error of angle α_P is also important since, compared to $\left|\Phi_{Max} - \Phi_{min}\right|$, it allows discerning whether a 2D or 3D/2D description is valid or not.

Since the phase tensor is not affected by galvanic distortion, it preserves information of the regional structures. In this way, maps of the elliptical diagrams of the phase tensor at a given frequency reflect lateral variations of the regional structures, in which the major axes of the ellipses, Φ_{Max}, indicate the direction of the induced current flow (e.g. Caldwell *et al.*, 2004).

2.7 Problems and Present Limitations on the Determination of Dimensionality

As already seen, the determination of geoelectric dimensionality is not a simple nor easy task. It is a problem that must be solved through the use of methods such as Bahr and WAL parameters and the more recent phase tensor. All these methods, although allowing dimensionality characterisation, have some limitations, which make it difficult to solve the problem in many cases.

Firstly, the determination of geoelectric dimensionality corresponding to MT data utilise parameters that are affected by the errors in the data responses. It is important to take into account the errors of these parameters in the determination of dimensionality and to know to which degree the feasibility of the characterised structures is.

Another important aspect to consider is the fact that in real situations, the dimensionality of the data does not fit exactly to the theoretical models described. A compromise between both descriptions can be achieved by using threshold values in the dimensionality criteria.

However, the parameters used in the presented methods and the choice of the threshold values imply that the dimensionality is not characterised in the same way. Sometimes they provide inconsistent results or different types of information, which can lead to incorrect hypotheses in modelling and interpretation of the data.

In this context, the next part of the thesis presents the studies, comparisons and new developments carried out on the characterisation of geoelectric dimensionality. These propose solutions to partially or totally solve some of these problems and limitations. More specifically, these aspects are: Error analysis and threshold values in WAL rotational invariants (Chapter 3), Improving Bahr's invariant parameters using the WAL approach (Chapter 4) and Applications of the magnetotelluric phase tensor and comparison with other methods (Chapter 5).

Part II. Methodological Contributions to Geoelectric Dimensionality

3. Error Analysis and Threshold Values in WAL Rotational Invariants
4. Improving Bahr's Invariant Parameters Using the WAL Approach
5. Applications of the Magnetotelluric Phase Tensor and Comparison with other Methods

Chapter 3: Error Analysis and Threshold Values in WAL Rotational Invariants

This chapter develops new procedures which were carried out on the error estimation of the invariants and the choice of their threshold values. To this end, it proposes a new method that allows the characterisation of geoelectric dimensionality in real situations.

Two examples, with different levels of errors, are used to illustrate the problems that one must overcome in order to obtain an accurate dimensionality analysis, and thus, further modelling and interpretation.

With the aim of introducing a tool to automatically perform dimensionality analysis from a dataset, a program was developed based on WAL criteria, considering noise in the data and its implications for dimensionality determination.

Part of this work can also be found in Martí *et al.* (2004).

3.1. Dimensionality Criteria Using Real Data

The main problem when WAL invariants criteria are implemented on real, therefore noisy data is that the geoelectric dimensionality may be found to be 3D. Although, other evidence suggests a 1D or 2D interpretation would be valid for modelling. This is because invariant values for real data are, in general, never precisely zero. Weaver *et al.* (2000) address this problem by introducing a threshold value, beneath which the invariants are taken to be zero. The threshold value they suggest is 0.1, which, although subjective, has been tested using a synthetic model with 2% noise. Since experimental data usually have a higher percentage of

error (up 30% in some cases) which propagates to the invariants, it is necessary to redefine this threshold value, taking into consideration the invariant values and their errors. To date, no work has been done on the estimation of WAL invariant errors.

Using WAL criteria with the threshold defined, if the dimensionality obtained is 2D or 3D/2D (cases 2, 3a and 4 in table 2.2), the strike directions and distortion parameters must also be estimated with their errors.

To address these matters, different tests were performed to estimate the invariants, related parameters, and their errors, and to choose an optimum threshold value.

3.2. Estimation of the Invariants and their Errors

The values and errors of the invariants and related parameters are dependant upon the values of the MT tensor components and their errors, which result from the estimation of the transfer functions in the spectral domain, after time series processing. In standard processing methods, these errors are obtained as variances, $\mathrm{var}(M_{ij})$, after assuming that noise is independent of the signals and stationary, and, consequently, that the components of $\underline{M}$ are statistically independent (Chapter 1, section 1.7, eq. 1.41). The errors of the real and imaginary parts of the MT tensor components have the same value and are determined as the square root of its variance:

$$\delta(\mathrm{Re}\, M_{ij}) = \delta(\mathrm{Im}\, M_{ij}) = \delta(M_{ij}) = (\mathrm{var}(M_{ij}))^{1/2}. \tag{3.1}$$

Invariant errors reflect dimensionality uncertainties due to data errors. Hence, it is important to properly estimate both the invariants and their errors to have a consistent picture of how well determined the dimensionality of a MT tensors is. Similarly, the errors of the related parameters (strike angles and distortion parameters) indicate incorrect determinations of certain types of dimensionality.

Because of the non-linear dependence of the invariants and related parameters on the MT tensor components, the relationships between their errors are highly complex. Given the role that the errors play in the determination of the dimensionality, three approaches were tested in order to obtain a high level of confidence in the estimation of the invariants and related parameters and errors: **a**. Classical error propagation, **b**. Random Gaussian noise generation and **c**. Resampling methods. The results and stability using these approaches were compared to determine which is the most suitable for the particular parameters.

3.2.1. Error Estimation Approaches

a. Classical Error Propagation

The values of the invariants are computed directly from expressions 2.10 to 2.16, and are hereafter referred to as true values (I).

For small errors, the uncertainty of any function y=f(x_1, x_2,..., x_n) can be obtained from a Taylor expansion in terms of the errors (δx_1, δx_2,...δx_n) of the estimated variables x_1, x_2,..., x_n. Using a first order expansion, the error (δI_k) of each invariant (I_k) and the errors of the strike and distortion parameters can be expressed as functions of partial derivatives (of the corresponding invariant expressions) and the errors of the real and imaginary parts of the components of $\underline{M}$:

$$\delta I_k = \left(\sum_{i=1}^{2} \sum_{j=1}^{2} \left(\left(\left(\frac{\partial I_k}{\partial (\operatorname{Re} M_{ij})} \right)^2 + \left(\frac{\partial I_k}{\partial (\operatorname{Im} M_{ij})} \right)^2 \right) \cdot (\delta (M_{ij}))^2 \right) \right)^{1/2} . \qquad (3.2)$$

These expressions were obtained as functions of ξ_i and η_i, and are summarised in Appendix A.

b. Random Gaussian Noise Generation

This statistical approach is an alternative to the first, which can fail when the errors in $\underline{M}$ are large. The problem lies in the lack of knowledge about the statistical distribution of $\underline{M}$, since the only available data are the means and variances of their components.

Some authors assume a Gaussian distribution of $\underline{M}$ in order to compute new parameters and study their stability (Jones and Groom, 1993; Weaver *et al.*, 2000), or to obtain their probability functions and confidence limits (Lezaeta, 2002), both from synthetic and real data.

Thus, one way to estimate the invariants and their errors is to generate a set of n possible values of $\underline{M}$ components, M_{ij}^{l} $(l = 1, 2, ..., n)$, assuming Gaussian noise around their true values, with the variances of the MT tensor components:

$$\operatorname{Re} M_{ij}^{l} = \operatorname{Re} M_{ij} + \operatorname{rndG}(\delta M_{ij}); \quad l = 1, 2, ..., n , \qquad (3.3)$$

$$\operatorname{Im} M_{ij}^{l} = \operatorname{Im} M_{ij} + \operatorname{rndG}(\delta M_{ij}); \quad l = 1, 2, ..., n , \qquad (3.4)$$

where $\operatorname{rndG}(\delta M_{ij})$ are pseudo-random numbers that follow a Gaussian distribution with an average of zero and a standard deviation of δM_{ij}.

From this set of values, the corresponding n possible values of the invariants can be obtained:

$$I_k^l = f(\text{Re}\, M_{ij}^l, \text{Im}\, M_{ij}^l; i = 1, 2; j = 1, 2); \quad l = 1, 2, ..., n \qquad . \tag{3.5}$$

After obtaining this set of n realizations for each invariant at a determined site and period, its mean value ($I_k´$) and standard deviation ($\sigma_{I_k'}$), which is taken as the error, are estimated as:

$$I_k' = \frac{1}{n}\sum_{l=1}^{n} I_k^l \,, \tag{3.6}$$

$$\sigma_{I_k'} = \sqrt{\frac{1}{n}\sum_{l=1}^{n}\left(I_k' - I_k^l\right)^2} \,. \tag{3.7}$$

The value of n must be chosen to avoid biases between the true value (I_k) and the mean value ($I_k´$) of the invariant. One criterion to fix the optimum value of n is to ensure that the bias between I_k and $I_k´$ is not greater than the standard deviation (i.e. not a significant bias):

$$\left|I_k - I_k'\right| \le \sigma_{I_k'}. \qquad \text{(bias condition)}. \tag{3.8}$$

The same procedure can be used to obtain the mean value and standard deviation of the strike direction and distortion parameters.

c. Resampling Methods

Resampling methods are statistical procedures used to obtain confidence intervals for parameters whose probability distributions are unknown (Efron and Tibshirani, 1998). They are based on the construction of hypothetical populations derived from the measured data. No statistical distribution is assumed, although this distribution is preserved. It follows that the new populations can be analyzed individually to see how the statistics depend on random variations of the data.

Two well-known resampling methods are the jackknife (Lupton, 1993), and the bootstrap (Efron, 1979). These two methods differ in how the hypothetical populations are constructed for an original dataset of n datapoints. The Jackknife method constructs n populations of n-1 data points, omitting one different point in each. Some robust data processing in MT are based on this technique (Jones and Jödicke, 1984; Thomson and Chave, 1991). In the

bootstrap method, also known as 'resampling with replacement', a large number of populations (or resamples) with n elements each can be constructed, allowing duplicates and triplicates of some points while allowing the absence of others.

The bootstrap method searches for a good approximation of the unknown population distribution, such that the estimated parameters also resemble those of the original population. The bootstrap method has been demonstrated to provide optimal estimates of the distribution of many statistics under a wide range of circumstances (Efron and Tibshirani, 1998). For this reason, the bootstrap approach was chosen to test the estimation of the invariants and their errors.

The most common application of the bootstrap method is the nonparametric-bootstrap, in which all data points are given the same weight. In this case, the number of resamples (N) necessary to approximate the theoretical sampling distribution is on the order of $n \cdot (\log n)^2$ (Babu and Singh, 1983). For every bootstrap sample, a statistical estimator and its confidence intervals are computed, recreating an empirical sampling distribution of the estimator.

The estimation of the invariants and related parameters and their errors using the bootstrap method can be done departing from a set of n elements as the initial population. These elements are generated as random Gaussian noise (as in approach **b**) (one set for each invariant or parameter). N resamples with n elements each are then constructed. The mean and standard deviation of the parameter is obtained from the mean and standard deviation of each of the bootstrap populations.

This application of the bootstrap method has the limitation that the original datasets are constructed assuming a probability distribution (Gaussian, from approach **b**), and are not raw data. A more rigorous use of bootstrap could be done if the original cross-spectra of the MT tensor were available, such that n estimates of the invariants could be obtained, and thus be used as the initial population. In many cases, it is not possible to do so, since the only available data after time series processing are the final estimates of the MT transfer functions, their coherences and related parameters. However, it is worth testing as an additional alternative to estimate the invariant values and their errors.

The following subsections present the comparisons and results of the estimations of the invariants and their errors using the three approaches described. Two data examples are used, for which invariants I_3 to I_7 and Q (the ones used in the dimensionality determination) were considered.

3.2.2 Example 1

The first example is site 85_314 from the COPROD2 dataset (Jones, 1993) acquired in Saskatchewan and Manitoba (Canada). It has been widely employed by the MT community to test 2D inversion codes, since the data clearly display 2D features, with a well determined NS strike direction (Jones *et al.*, 2005). The location and MT responses at this site are presented in Appendix B. The measured MT tensor components, with periods ranging from 0.002 s to 1000 s, are of good quality. Diagonal components are one or two orders of magnitude smaller than the non-diagonal ones, this ratio decreasing as the period increases. The average level of noise is 5%, with a minimum of 1% between 5 s and 500 s. This minimum is a result of the high quality of the acquisition system, Phoenix MT-16, within this period band.

Determination of n and N values in Random Gaussian Noise and Bootstrap approaches

Prior to the estimation of the parameters and their errors from approaches **b** (Random Gaussian Noise Generation) and **c** (Bootstrap), some tests were carried out on the number of realizations (n) (approach **b**) and on the size of the samples and the number of resamplings (approach **c**), using this data example.

- Random Gaussian Noise

Several values of n (n=10, n=100 and n=1000) were tested to evaluate the dispersion of the invariants, their means and standard deviations, and were compared to their true values and classical errors in order to check whether the bias condition is satisfied or not. Invariants I_5 and Q were chosen as representatives of simple and complex dependencies on $\underline{M}$ components, respectively.

Figure 3.1 illustrates the realizations of I_5 and Q, their means and their standard deviations for three periods, T=0.67 s, T=0.0208 s and T=21.32 s, with high, medium and low noise levels respectively in the MT tensor components, using n=10 and n=100. These are compared to the true values and their errors obtained using approach **a** (n=1000 is not shown for simplicity and because it presents similar results to those of n=100). The numerical values of these estimations, including n=1000 and the results from the bootstrap, are shown in table 3.1. For these three periods, the following can be inferred:

At T=0.67 s (high noise level: 10% error in $\underline{M}$ non-diagonal components and up to 200% in the diagonal ones), I_5 and Q present a large dispersion and consequently large error bars. Errors of I_5 are similar to the classical errors and those of Q are smaller, independent of the value of n. The realisations and statistical estimations of Q are up-biased and, for small values of n (n=10), this bias is, in fact, significant (equation 3.9 is not satisfied). The estimations of I_5 are biased also, although, due to the small values, it is only appreciable numerically (Table 3.1).
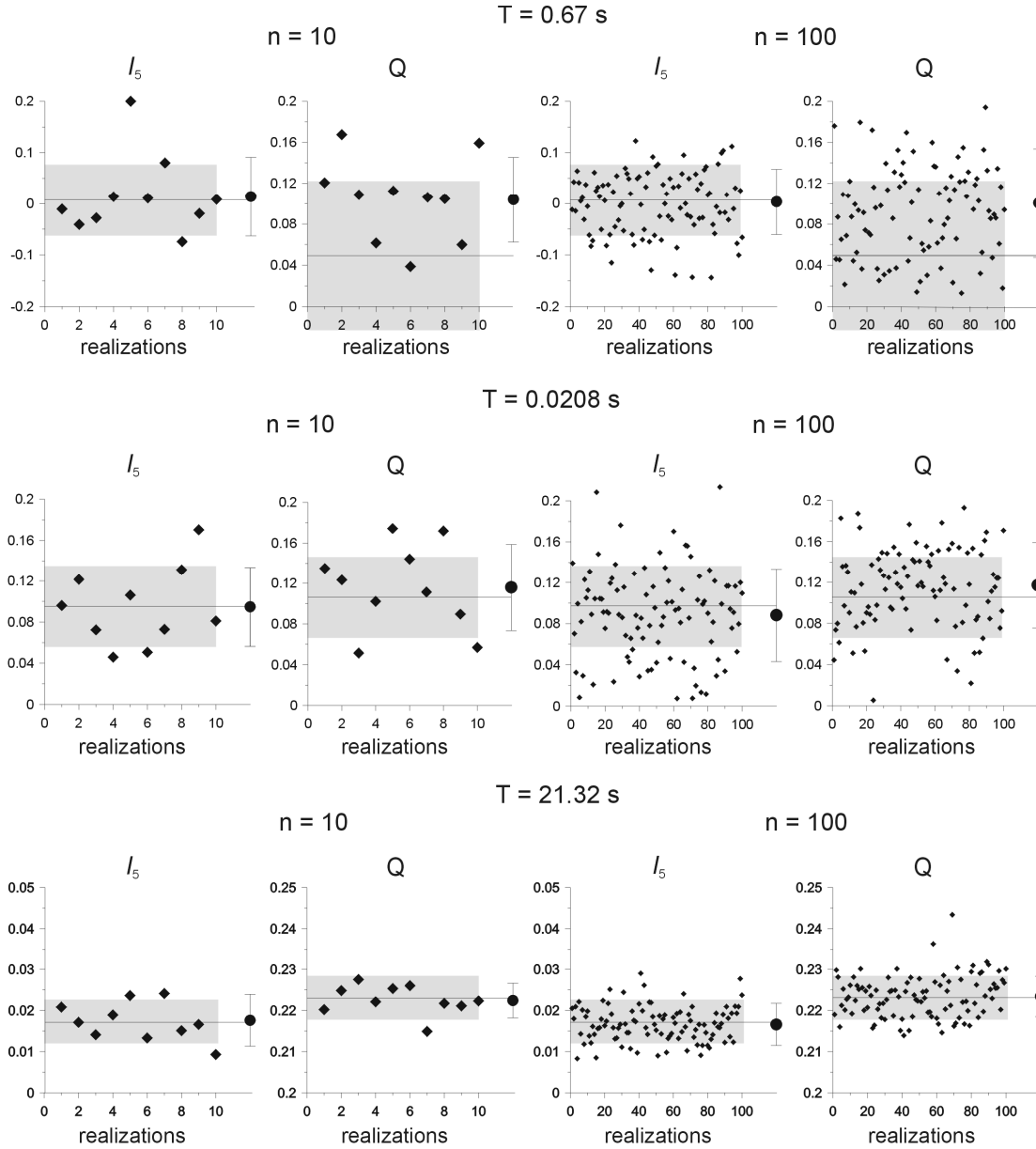
Figure 3.1: Plots of n=10 and n=100 realizations (diamonds) of invariants I_5 and Q at periods T=0.67 s (high noise level, upper panel), T=0.0208 s (medium noise level, middle panel) and T=21.32 s (low noise level, lower panel) from site 85_314 (COPROD2 dataset). The mean and standard deviations of these realizations are displayed at the right end of each plot (dot with error bar). Horizontal lines at each plot indicate the true value of the invariant. The shaded areas correspond to the confidence intervals, as obtained from classical error propagation (approach **a**).

At T=0.0208 s (medium noise level: 5% error in $\underline{M}$ non-diagonal components and up to 100% in the diagonal ones), the noise level of the invariants is about 40%. Both I_5 and Q show a uniform distribution of the random values around the true values, with similar errors, and there is not an appreciable bias between the true and statistical values.

At T=21.32 s (low noise: 0.5% error in the non-diagonal components, and 8% in the diagonal ones) the dispersion of both I_5 and Q is much smaller (note the different vertical scales on the plots). Error bars are similarly small and in all cases the bias condition (equation 3.9) is satisfied.

		T=0.67 s		T=0.0208 s		T=21.32 s	
		I_5	Q	I_5	Q	I_5	Q
True		0.0067 ± 0.0696	0.0492 ± 0.0717	0.0972 ± 0.0422	0.1057 ± 0.0428	0.0171 ± 0.0052	0.2231 ± 0.0052
Random	n=10	0.0140 ± 0.0769	0.1039 ± 0.0414 *	0.0935 ± 0.0446	0.1148 ± 0.0432	0.0179 ± 0.0054	0.2211 ± 0.0051
	n=100	0.0034 ± 0.0639	0.1005 ± 0.0529	0.0913 ± 0.0407	0.1229 ± 0.0396	0.0170 ± 0.0048	0.2230 ± 0.0045
	n=1000	0.0034 ± 0.0639	0.1005 ± 0.0529	0.0966 ± 0.0414	0.1145 ± 0.0399	0.0172 ± 0.0049	0.2231 ± 0.0050
Bootstrap	n=10 N=10	0.0070 ± 0.0668	0.1098 ± 0.0392 *	0.0979 ± 0.0599	0.0824 ± 0.0337	0.0178 ± 0.0050	0.2203 ± 0.0050
	n=100 N=400	0.0036 ± 0.0637	0.1009 ± 0.0527	0.0996 ± 0.0397	0.1094 ± 0.0394	0.0171 ± 0.0047	0.2230 ± 0.0044
	n=1000 N=9000	0.0036 ± 0.0637	0.1009 ± 0.0527	0.0967 ± 0.0443	0.1150 ± 0.0405	0.0170 ± 0.0052	0.2231 ± 0.0048

Table 3.1: Estimations of I_5 and Q and their errors at two periods from the COPROD2 dataset. True: True values and classical error propagation. Random: means and standard deviations from Random Gaussian generation (approach **b**), for n=10, n=100 and n=1000. Bootstrap: N resamplings of the initial samples from the Random approach. *: Cases with a significant bias between statistical and true values.

At all periods, the values of $\sigma_{I_k'}$ are similar for n=100 and n=1000. Although errors are not much larger, n=10 is not representative enough of all possible values of an invariant. Tests with other invariants and periods, using a broader range of values of n show a stable pattern of $\sigma_{I_k'}$ using n=100 to n=1000. Consequently, values of n=100 or greater are recommended to perform approach **b**.

- Bootstrap

A similar test was carried out for the same three periods with different values of n (size of the initial samples), and N (number of resamples $\approx$ n·(log n)^2). The samples of I_5 and Q generated in the previous test, with n=10, n=100 and n=1000, were resampled N$\approx$n·(log n)^2 times (N=10, N=400 and N=9000 respectively) and their means and standard deviations estimated.

The results (both statistical values and standard deviations), shown in Table 3.1, do not differ significantly to the ones with the corresponding value of n from approach **b**, especially when the noise level is moderate or low (T= 0.0208 s and T=21.32 s).

At T=0.67 s, with n=10, there is also a significant bias between the bootstrap and the true values of Q. This bias disappears for n=100 and n=1000.

In this approach, n=100 and n=1000 (and, consequently $N \approx 400$ and $N \approx 9000$) are valid to estimate the invariants and their errors using the bootstrap approach, although $N \approx 400$ is sufficient and is the value that will be used in the following comparison.

Comparison of the three approaches

Figure 3.2 shows the invariant values and error bars after using the three approaches **a**, **b** and **c**, at all the recorded periods of site 85_314. Approach **b** uses n=1000 and approach **c** utilises N=400, from an initial sample containing n=100 elements each.

Using the three approaches, invariants I_3, I_4, I_5 and I_6 present similar values and errors. Error bars are proportional to the noise level of the recorded data (note small error bars between T=5 s and T=500 s), and no appreciable biases are observed between the true values, **a**, and the statistical values of approaches **b** and **c**.

I_7 is characterised by large error bars, which only decrease between 5 s and 500 s, when Q becomes large, that is, when I_7 (which is inversely proportional to Q) is well determined. The differences between the estimations of I_7 using the three approaches are evident, especially seen in the sizes of the error bars. From approach **a** the error bars present an irregular distribution, with extremely large values at certain periods. Approaches **b** and **c** provide a smoother distribution of the errors, but introduce important biases with respect to the true values (note the differences in I_7 between (g), (h) and (i) in Figure 3.2). Invariant Q, on the contrary, presents similar estimations using any of the three methods, with small values and error bars, proportional to the data noise level.
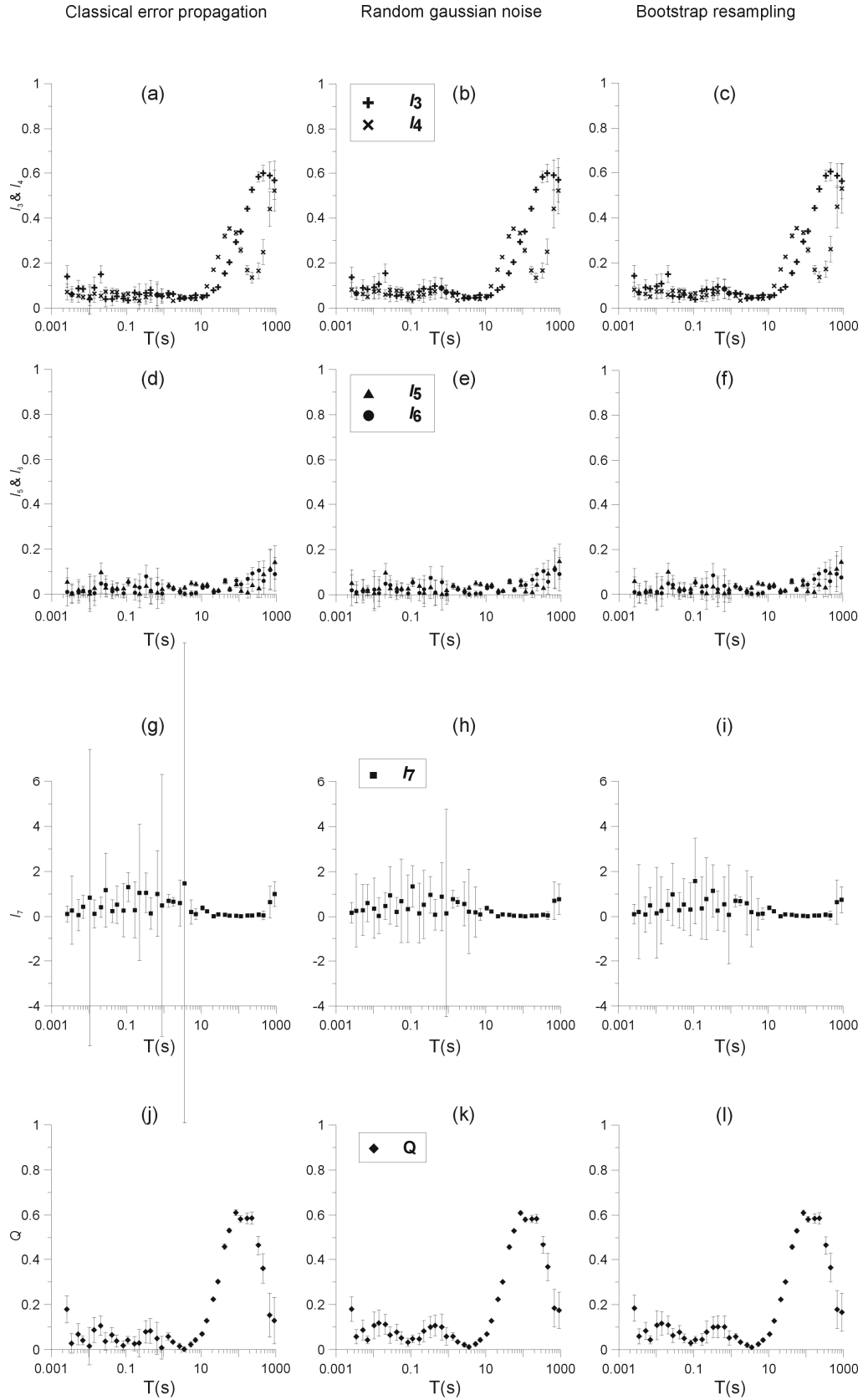
Figure 3.2: Invariant values at site 85_314 from the COPROD2 dataset and their errors computed in three ways: classical error propagation, Random Gaussian Noise (1000 realizations) and bootstrap resampling (400 realizations from an original sample with 100 elements for each invariant). I_3 and I_4 (a), (b) and (c); I_5 and I_6 (d), (e) and (f), I_7 (g), (h) and (i) and Q (j), (k) and (l).

3.2.3 Example 2

The second example illustrates a case with more complex dimensionality and higher noise levels. It corresponds to site b23, from the Betic Chain magnetotelluric dataset. The variances in the magnetotelluric tensor components, with the non-diagonals slightly larger than the diagonals, correspond approximately to 1% noise for the shortest periods, and increase up to 30% for the longest ones.

Comparison of the three approaches

The invariants and their errors were estimated using approaches **a**, **b** and **c**. In approaches **b** and **c** the values of n and N were the same as in COPROD2: n=1000 in approach **b** and N=400 (from an initial sample with n=100) in approach **c**.

Employing the three approaches, the values of I_3, I_4, I_5 and I_6 (Figure 3.3) are comparable and the errors resemble those of the components of the magnetotelluric tensor, which increase with the period. However, at long periods, biases between the values computed from the different approaches are appreciable and the statistical errors (approaches **b** and **c**) present extremely large values which were not observed in the COPROD2 example, due to the low noise level in the MT tensor components in this long period band.

I_7 and Q have the same behaviour as in the first example, with the small values and error bars of Q and the extremely large error bars and biases of I_7. Between 3s and 30s, as Q becomes large, I_7 becomes more precise, as in site 85_314. Hence, the estimation of I_7 depends not only on the noise level, but also on the value of Q.

3.2.4 Concluding remarks on error estimation

After these comparisons, having obtained similar estimations of the invariants and their errors, it can indeed be concluded that the three approaches can be used to estimate the invariants values and their errors, except for cases with large error levels or small values of Q. However, in order to avoid the possible biases that appear with approaches **b** and **c**, the use of classical error propagation (approach **a**) is preferred.

A similar test was performed for the estimation of the strike directions and distortion parameters. In these cases, errors are better estimated using random noise generation (approach **b**). Using classical error propagation, since these errors depend on the derivatives of trigonometric functions, the error bars would be considerably large, especially for high noise levels in the MT tensor components.
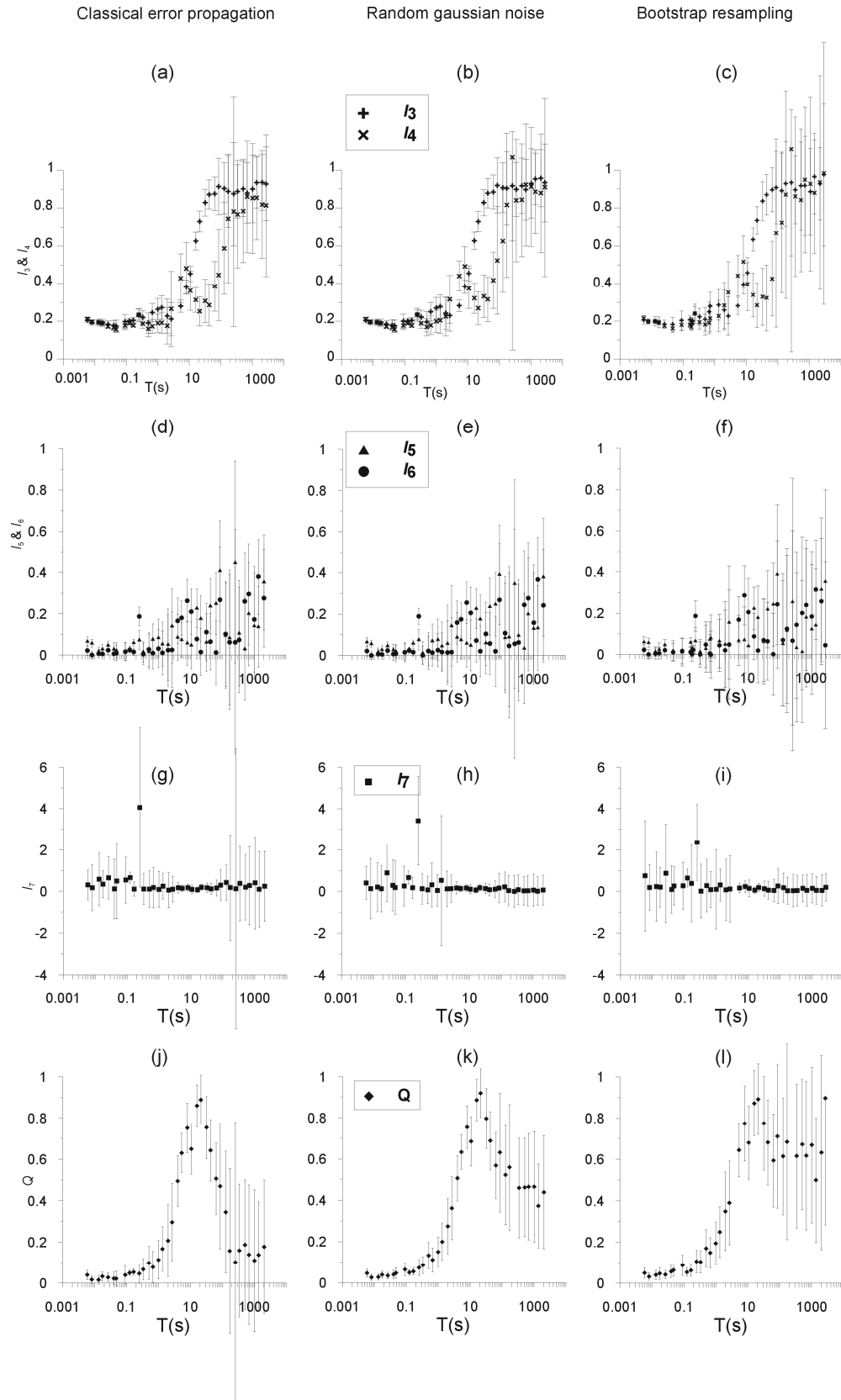
Figure 3.3: Invariant values corresponding to site b23 from the Betic dataset and their errors computed using the three approaches. For random Gaussian Noise, n=1000. In the bootstrap 400 realizations from an original sample with 100 elements for each invariant were used. I_3 and I_4 (a), (b) and (c); I_5 and I_6 (d), (e) and (f), I_7 (g), (h) and (i) and Q (j), (k) and (l).

3.3. The Threshold Value

For the determination of the dimensionality using WAL invariants, it is necessary to decide if an invariant can be considered null or not. This is a compromise between the threshold value (τ hereafter) and the error bar of each invariant. After considering the possible relationships between the thresholds and the confidence intervals of the invariants, the following criteria were adopted:

1) Ascertaining whether I_7 is undefined or not, by observing the values of Q, which is controlled by a threshold τ_Q (below which Q is regarded as too small a quotient of I_7), and the value of I_7:

1.a) $Q < \tau_Q$ and/or $I_7 > 1 \Rightarrow I_7$ is undefined,

1.b) $Q > \tau_Q$ and $I_7 < \tau \Rightarrow I_7 \approx 0$,

1.c) $Q > \tau_Q$ and $I_7 > \tau \Rightarrow I_7 \neq 0$.

Given that I_7 is highly sensitive to the data errors, its validity has been limited to its dependence on the value of Q. Otherwise, the errors of I_7 would dominate the dimensionality estimation, which would be always undetermined.

2) The rest of the invariants, I_3 to I_6, are considered null or not depending on the possible values of I_k and σ_k (Figure 3.4):

2.a) $I_k - \sigma_k$ and $I_k + \sigma_k < \tau \Rightarrow I_k \approx 0$ (Figure 3.4a),

2.b) $I_k > \tau$ and $I_k - \sigma_k > \tau \Rightarrow I_k \neq 0$ (Figure 3.4b),

2.c) $I_k < \tau$ and $I_k + \sigma_k > \tau \Rightarrow I_k \neq 0$ (Figure 3.4c), (Note that I_k would be regarded null had the error not been taken into account),

2.d) $I_k > \tau$ and $I_k - \sigma_k < \tau \Rightarrow I_k \neq 0$ (Figure 3.4d),

2.e) $I_k + \sigma_k > 1 \Rightarrow I_k$ is undefined (Figure 3.4f),

which can be reduced to the conditions:

$$I_k + \sigma_k < \tau \Rightarrow I_k \approx 0, \tag{3.9}$$

$$\tau < I_k + \sigma_k \leq 1 \Rightarrow I_k \neq 0, \tag{3.10}$$

and I_k is undefined for the rest of the cases.

If any of the invariants I_3 to I_6 are undefined (Figure 3.4e) the dimensionality of the corresponding tensor cannot be determined.
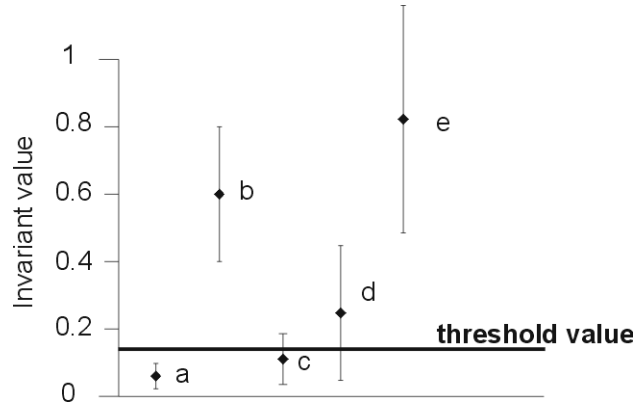
Figure 3.4: Different possibilities for the invariant values and their errors (τ= threshold value). (a) $I_k - \sigma_k < \tau$ and $I_k + \sigma_k < \tau$; (b) $I_k - \sigma_k > \tau$ and $I_k + \sigma_k > \tau$; (c) $I_k < \tau$ and $I_k + \sigma_k > \tau$; (d) $I_k > \tau$ and $I_k - \sigma_k < \tau$ and (e) $I_k + \sigma_k > 1$. Only in case (a) is invariant I_k considered to be zero.

The choice of the threshold value τ is a subjective decision, but it is important to have an appropriate range of values that works for a correct dimensionality analysis. A high value of τ produces invariants that are considered null, resulting in too simple a structure (1D for all sites and periods). On the contrary, a small value of τ implies that the invariants cannot be considered null and it gives rise to a more complex structure (3D in general).

An exhaustive study was carried out with the aim of determining the optimum range of threshold values that provides a stable and consistent dimensionality pattern, taking into account the errors of the invariants. This task was performed using the examples from the previous section, site 85_314 from COPROD2 and site b23 from the Betics, plus two additional Betics sites.

In both examples, the WAL dimensionality analysis was performed for different threshold values and the results were compared to determine those most appropriate. The threshold values tested were 0.08, 0.10, 0.12, 0.15, 0.20 and 0.30. In the second example, using three sites from the Betics dataset, a more detailed study was done, including an analysis on the determination of the strike directions and distortion parameters, and a comparison with decomposition techniques.

With regard to the threshold for invariant Q, τ_Q, which conditions the determination of invariant I_7, its value was fixed to 0.10. Posterior tests changing the value of τ_Q resulted in small

changes in the dimensionality. Nevertheless, I recommend not using a τ_Q value lower than 0.1, as the value of I_7 would be considered undefined even if it was much smaller than unity.

The dimensionality pattern corresponding to all the registered periods from site 85_314, for the different threshold values, is illustrated in Figure 3.5. Those cases undetermined as a consequence of the errors are also included, the number of which decreases as the threshold value increases. In general, and apart from the extreme values, 0.08 and 0.3, the dimensionality is stable among different threshold values, especially for the longest periods. Some particular changes are observed between the intermediate values, which are a consequence of the error bars crossing the threshold values. The same dimensionality analysis but, without considering errors, would result in the same dimensionality pattern, although without any undetermined cases.
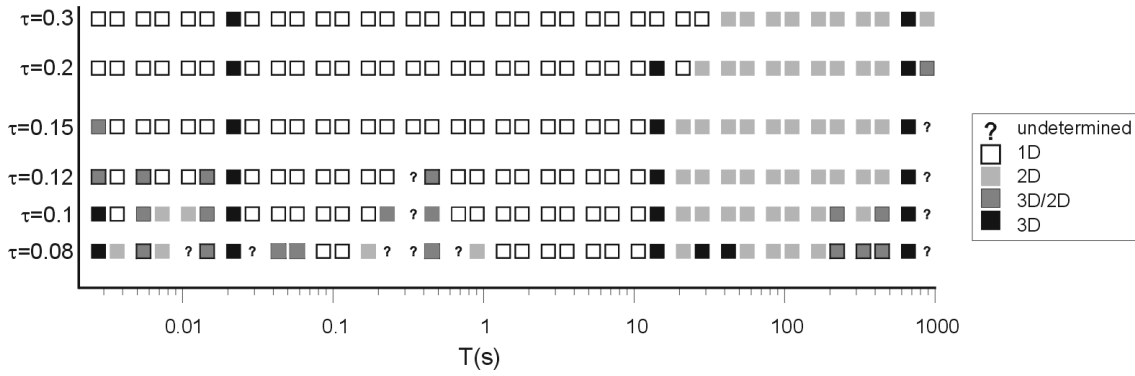
Figure 3.5: Dimensionality cases for site 85_314 from the COPROD2 dataset using different threshold values: 0.08, 0.10, 0.12, 0.15, 0.20 and 0.30, considering data errors.

Figure 3.6 shows the dimensionality cases obtained for each threshold value for the three sites from the Betics dataset, b01, b23 and b40. Independent of the threshold value, dimensionality remains undetermined for those periods with relative errors in the MT tensor components greater than approximately 30%.

The extreme values τ=0.08, τ=0.20 and τ=0.30 provide dimensionality patterns which are inconsistent. On the contrary, intermediate values, $\tau = 0.1$, 0.12 and 0.15, give a quite stable pattern and a characteristic behaviour can be observed at each site. Site b01 reflects a 3D/2D dimensionality for some periods up to 0.12s using $\tau = 0.1$, 0.12 and 0.15. Site b23 appears as 2D up to 0.2 s, for any threshold value, and as 3D/2D for longer periods up to 50 s, using $\tau = 0.12$, $\tau = 0.15$ and even $\tau = 0.2$. Site b40 shows a 1D dimensionality at short periods (up to 1 s) for the three intermediate τ values.
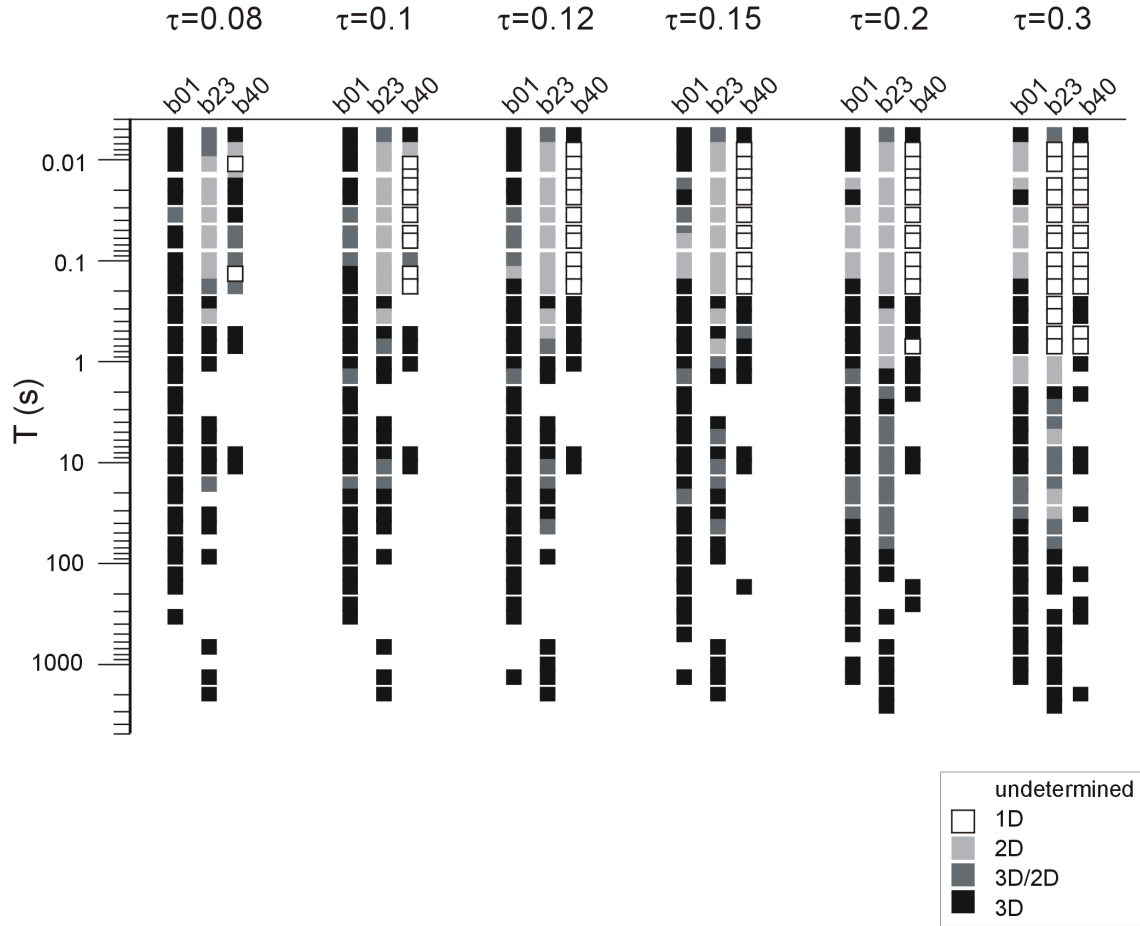
Figure 3.6: Dimensionality cases for sites b01, b23 and b40 from the Betics MT dataset using different threshold values: 0.08, 0.10, 0.12, 0.15, 0.20 and 0.30.

In order to confirm whether this description is valid or not, another test was performed, considering the determination of the strike angles and the distortion parameters. For all the periods of these three sites, two types of analysis were performed:

- Analysis A: the strike directions and errors corresponding to a 2D structure were determined (θ_1 and θ_2 in equation 2.19, equivalent to Swift's angle, equation 2.5).
- Analysis B: a 3D/2D structure was assumed, computing the strike and distortion angles and their errors (θ_3 in equation 2.23 and φ_t and φ_e in equations 2.24 and 2.25, equivalent to Groom and Bailey decomposition).

The strikes and errors obtained using both analyses made it possible to constrain frequencies for which a strike direction and/or distortion parameters could be determined. If θ_1 and θ_2 are similar with constant values and small error bars, the structure can be considered 2D.

If θ_3 is the angle with small error bars and constant values of distortion angles, it can be considered 3D/2D. For the analysed sites the main results are:

Site b01 (Figure 3.7): Analysis A (Figure 3.7a) gives a good determination of the strike directions up to 200 s, where the errors in θ_1 and θ_2 become large. However, since values θ_1 and θ_2 are dissimilar, it cannot correspond to a 2D structure. Analysis B (Figure 3.7b) shows large error bars, except for the period range between 0.02 s and 0.2 s, which can be described as 3D/2D because θ_3 and the distortion angles have a constant value.
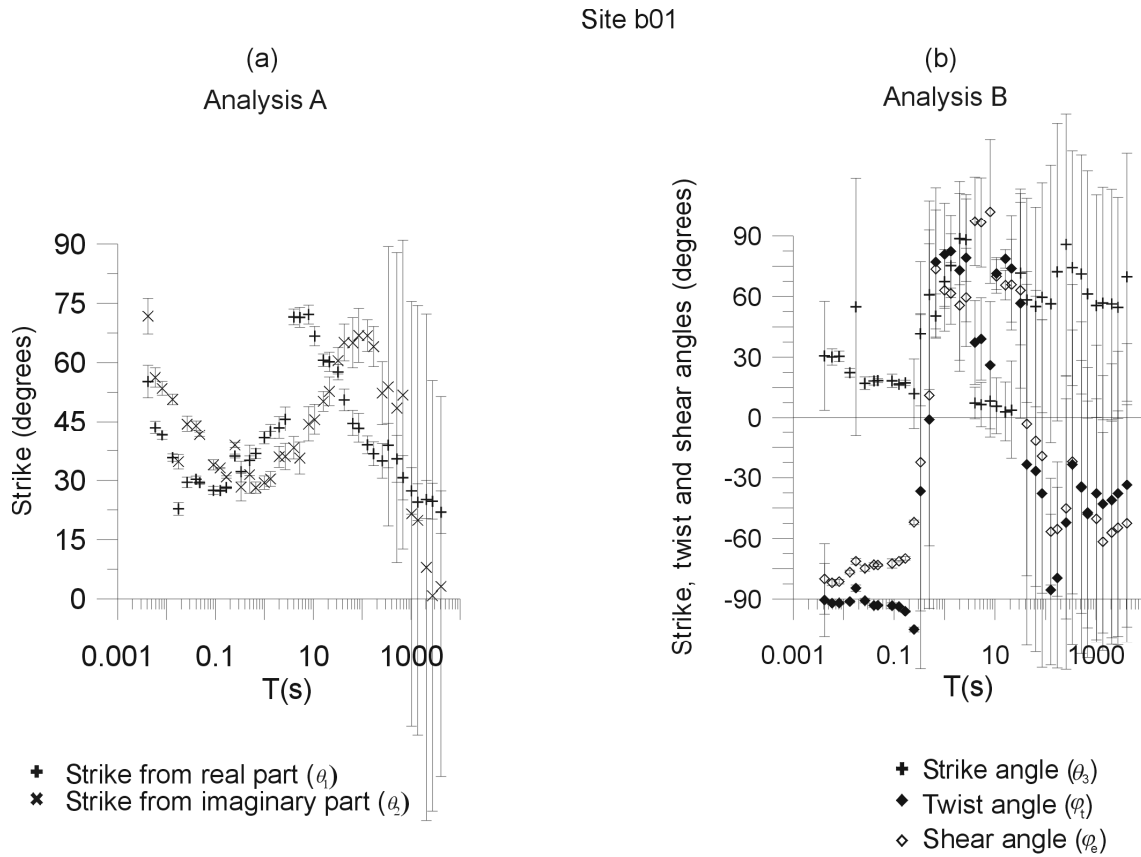
Figure 3.7: Strike directions and distortion parameters for site b01: (a) analysis A, (b) analysis B.

Site b23: Analysis A gives a good determination of the strike for the lowest periods up to 0.2s, which have the same value $\theta_1 = \theta_2$ (Figure 3.8a). Analysis B shows that constant strike direction and twist and shear angles can be inferred between 5 s and 50 s (Figure 3.8b).
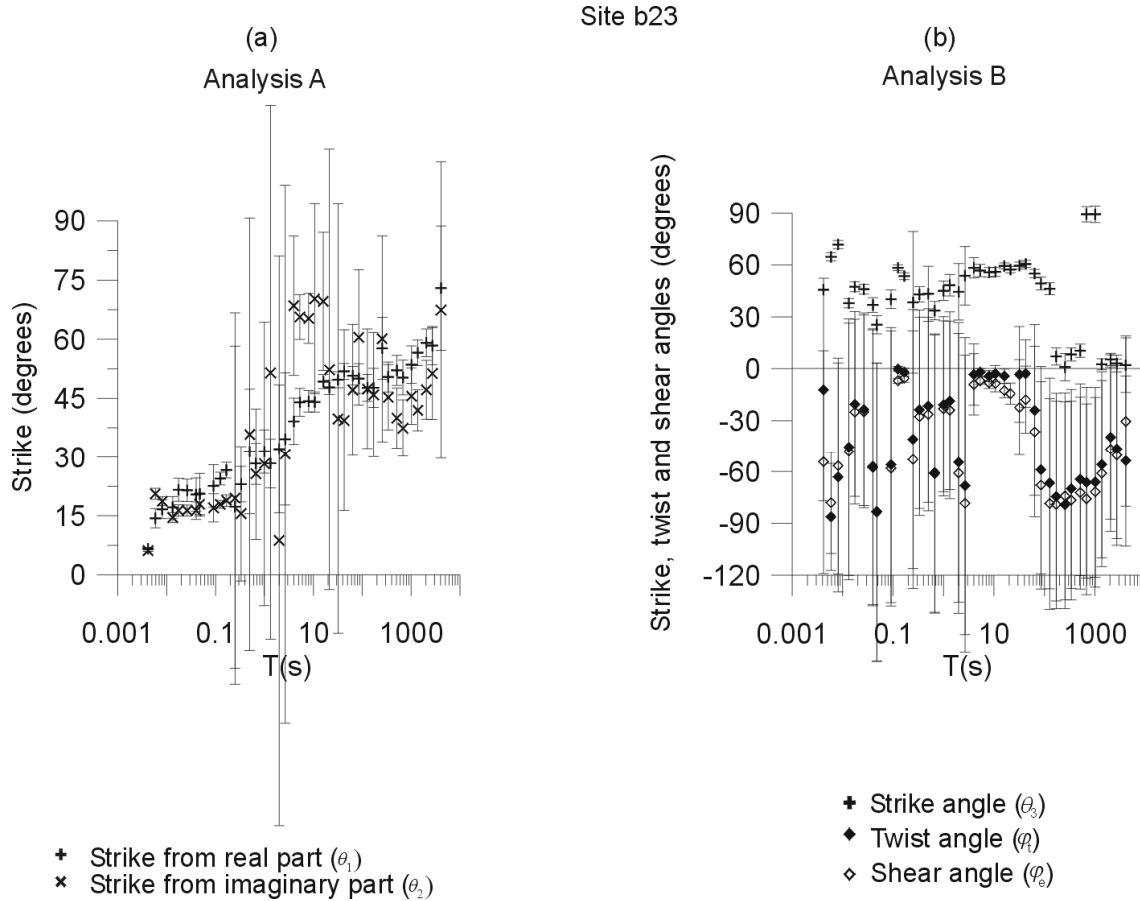
Figure 3.8: Strike directions and distortion parameters for site b23: (a) analysis A, (b) analysis B.

Site b40: neither analyses A and B nor the computation of θ_1, θ_2 and θ_3 (Figures 3.9a and 3.9b) give good determination of a possible 2D or 3D/2D structure. However, up to periods of about 1s, the MT tensor corresponds to a 1D case ($M_{xy} = -M_{yx}$ and $M_{xx} = M_{yy} = 0$), and the computed apparent resistivities (Figure 3.9c) and phases (Figure 3.9d) have the same value for xy and yx modes. These values are the same as those obtained from invariants I_1 and I_2 (equations 2.23 and 2.24). This is consistent with a 1D interpretation of the data for the short and middle periods of this site.

The results from these analyses correspond to the dimensionality obtained using threshold values between 0.1 and 0.15. Hence, this threshold range is appropriate for a dimensionality analysis of data with up to 30% noise in the impedance tensor components.

Site b40

(a)

Analysis A

(b)

Analysis B

+ Strike from real part (θ_1)
✖ Strike from imaginary part (θ_2)

+ Strike angle (θ_3)
◆ Twist angle (φ_t)
◇ Shear angle (φ_e)

(c)

(d)

——— 1D App. resistivity (from I_1 and I_2)
● xy App. resistivity
◆ yx App. resistivity

——— 1D Phase (from I_1 and I_2)
● xy Phase
◆ yx Phase
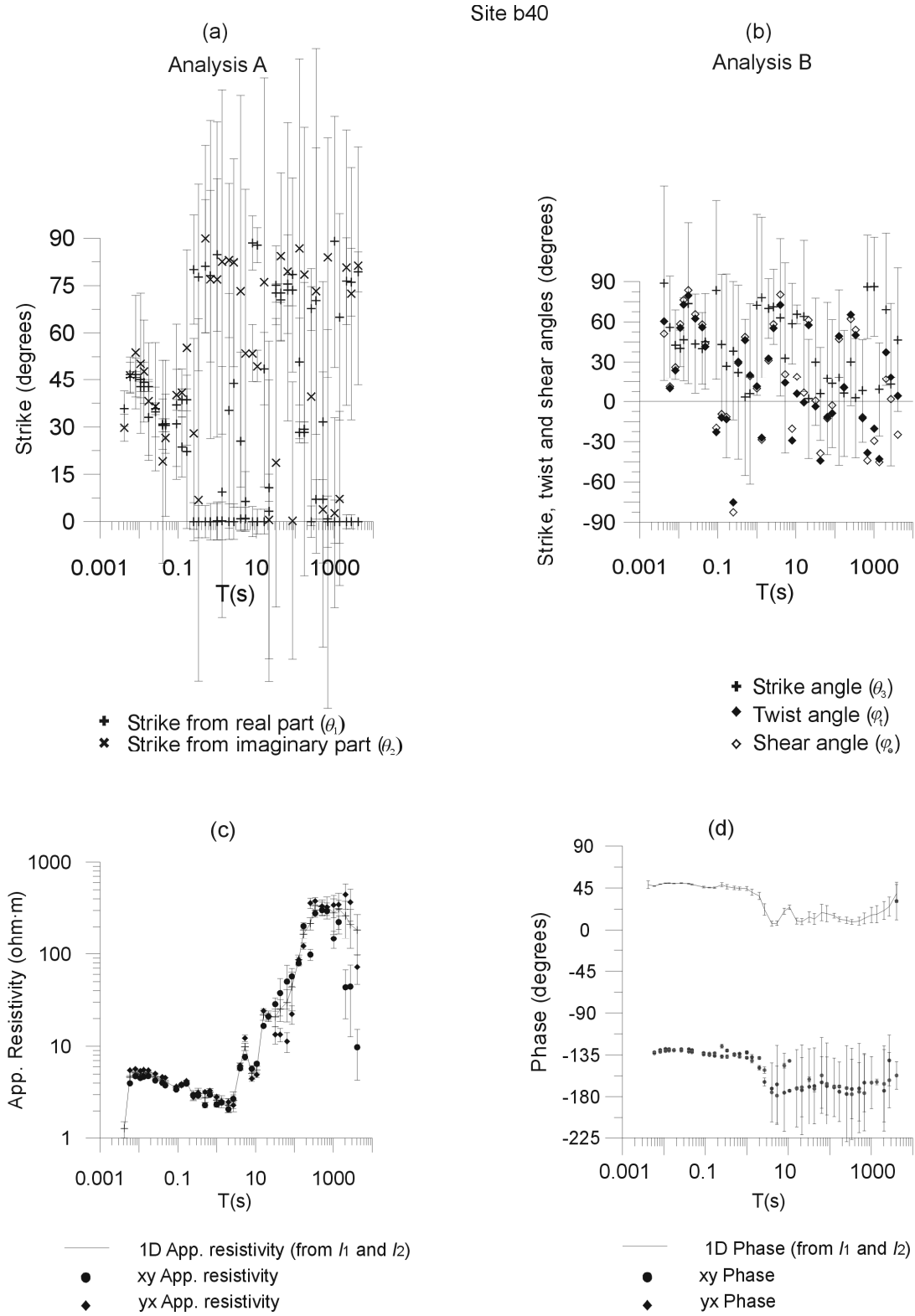
Figure 3.9: Strike directions and distortion parameters for site b40: (a) analysis A, (b) analysis B, (c) and (d): xy and yx apparent resistivities and phases computed directly from the MT tensor and I_1 and I_2 invariants.

3.4. Practical Criteria

After performing these tests on the error treatment and the threshold value, these final recommendations are given:

(1) Determine the errors of the invariants using any of the described approaches, **a**, **b** or **c**. However, classical error propagation (approach **a**) is recommended to avoid biases.

(2) Determine the dimensionality using WAL criteria with a threshold value between 0.1 and 0.15, letting I_7 be undetermined if Q is below τ_Q, and giving consideration to the error bars. Note that dimensionality will be well determined when relative errors in M are not greater than approximately 30%.

(3) Compute the strike directions and/or distortion angles corresponding to 2D and 3D/2D cases and their errors, using Random Gaussian Noise generation.

3.5. WALDIM Program

A Compaq Visual Fortran 2000® application, termed WALDIM, was created. It is a tool to automatically obtain the dimensionality analysis from a set of raw or synthetic MT data, based on WAL criteria while considering noise in the data.

The main functions of this program are to compute WAL invariants, related parameters and errors corresponding to each MT tensor and to determine the dimensionality, following WAL criteria, and according to the errors and the threshold value. In those cases related to two-dimensional structures and/or the presence of distortion, apart from the dimensionality, the strike and distortion parameters with their errors are provided as relevant information.

The strike angles are all determined in the first quadrant. As stated in chapter 1, the 90° ambiguity should be solved using the tipper information.

The program also solves some inconsistencies that can appear regarding two-dimensionality and strike directions: On some occasions, WAL criteria indicate 2D dimensionality, whereas θ_1 and θ_2 strike angles have significantly different values. This is a consequence of having defined a lower than required threshold value. The program solves this by changing the dimensionality of these cases into 3D/2D and assigning θ_3, ϕ_1 and ϕ_2 as the strike direction and distortion parameters respectively. The difference between θ_1 and θ_2 is set to

a maximum of 10°, or a minimum of 80°, given that one of the angles can have a 90° ambiguity, although these values may be modified.

A broad range of parameters and options remain open for the user, which may be chosen depending on the quality or type of data, or to continue investigating the threshold values and error analysis. The values of thresholds τ and τ_Q can be chosen by the user. Data errors can be those in the MT tensor components, or can be computed as a noise level specified by the user. The error estimation in the computed parameters can be done as in approach **a** (classical error propagation) or as in **b** [1] (Random Gaussian Noise generation), which in the program is referred to as "statistical approach". Bootstrap resampling can be performed by calling an external program.

Another option of WALDIM is to classify the dimensionality into groups of periods for each site such as to have a more general image of the dimensionality therein. In this classification, a specific period range is divided into groups made up of multiples or fractions of the decades contained within this range. For each site, the dimensionality of a group is the mode of the data in the group. In the case that the mode has more than one dimensionality type, priority is given to that which is less complex. If the dimensionality of the group needs computation of strike and distortion parameters, these and their errors are the average and standard deviation of the group data with that type of dimensionality. If inconsistencies in the determination of 2D strike angles appear, these are solved by changing the cases to 3D/2D as previously explained.

Figure 3.10 schematizes the general flowchart of the program. It has been tested for different datasets, some of which appear in the dimensionality studies carried out in this thesis.

3.6. Conclusions

A method has been developed to determine the geoelectric dimensionality using the WAL invariants, taking into account the data errors. The errors of the invariants and related parameters were estimated using three approaches: classical error propagation, generation of Random Gaussian Noise and bootstrap resampling. Different threshold values were tested to ensure a stable dimensionality pattern.

The errors of the invariants can be properly estimated by classical error propagation, but the generation of random values is more robust, thus ensuring stability in the errors of strike direction and distortion parameters. The use of a threshold value between 0.1 and 0.15 is recommended for real data of medium to high quality.

---

[1] Subroutine Gasdev (Press *et al.*, 1992)

A program named WALDIM to perform MT dimensionality analysis using WAL criteria and considering data noise, has been developed. It offers several options with regard to error estimation and threshold values, and has been successfully tested.
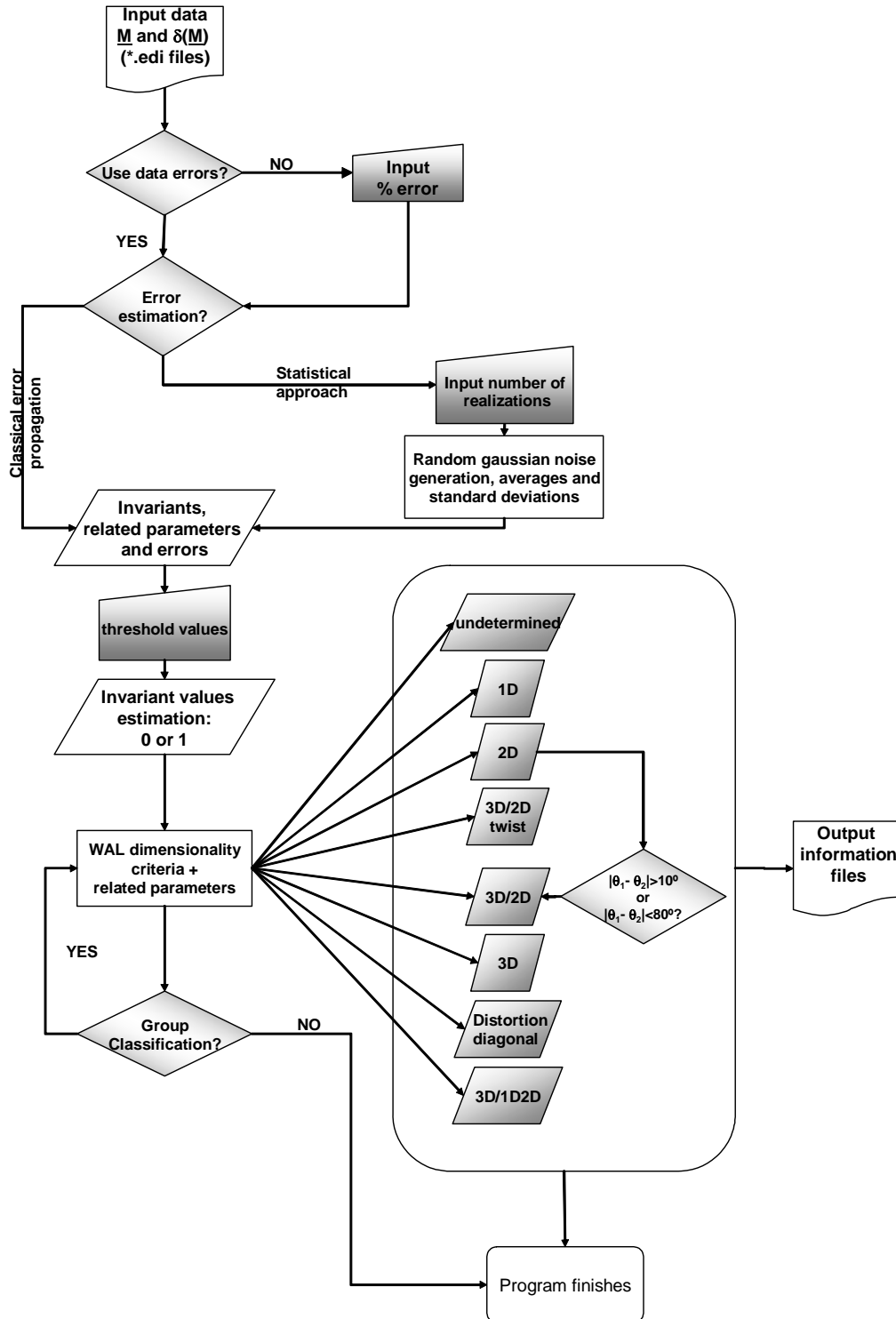
Figure 3.10: General overview flowchart of WALDIM program.

Chapter 4: Improving Bahr's Invariant Parameters Using the WAL Approach

This chapter presents a comparison between Bahr and WAL parameters and their dimensionality criteria. It led to a proposal of a unification of the existing threshold values used in these dimensionality analyses. And, to the improving of Bahr's criteria with the addition of the Q parameter, from the WAL invariants set. The new method was hence termed the Bahr-Q method.

The motivation for this work came from the previous work of Ledo *et al.* (2002b), on the limitations of a 2D interpretation of 3D data. Among different aspects concerning their effects in modelisation, it demonstrated the misuse of some of the Bahr parameters at ascertaining whether data are 3D or not.

Part of this work has been already published in Martí *et al.* (2005).

4.1 Introduction

As already described in chapter 2, both the Bahr and WAL methods use a set of rotational invariant parameters of the magnetotelluric tensor and establish a classification of these values to determine the kind of dimensionality associated with the measured data.

Among the four parameters defined by Bahr (1991) (Chapter 2, section 2.4), only the skew, κ, and regional skew, η, are commonly used to test the validity of dimensionality, as opposed to the four of them being fully taken into account to characterise it. The use of the

WAL method (Chapter 2, section 2.5), although limited, is increasing (Jones *et al.*, 2002; Martí *et al.*, 2004).

When the data are of good quality (low noise and low distortion) and the subsurface materials being imaged can be approximated by 2D structures, both methods work reasonably well and give similar results. When dealing with more complex structures and with real data, propagation of data errors and oversimplification of the physical models used will lead, in most cases, to more confusing situations.

The aim of this work was to study the Bahr and WAL methods and to propose a new one that makes both dimensionality methods consistent.

To accomplish this, the analytical relationships between both sets of parameters were derived and the threshold values of each method were revised and compared. To illustrate the results of this study one set of synthetic data and two sets of real data were used, including error effects.

4.2 Bahr and WAL Methods

The dimensionality information given by both sets of parameters, and the recommended threshold values are summarised in Table 4.1.
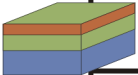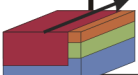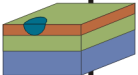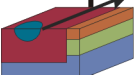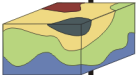
Case	Bahr invariants	WAL invariants	Dimensionality case
1	$\kappa < 0.1$, $\Sigma < 0.1$	$I_K = 0$ (k=3-7)	1D
2	$\kappa < 0.1$, $\Sigma > 0.1$	$I_3 \neq 0$ or $I_4 \neq 0$	2D
3	$\kappa > 0.1$, $\mu < 0.05$		3D/1D
3		$I_3 \neq 0$ or $I_4 \neq 0$ and $I_5 \neq 0$	a) 3D/2D (twist) (if I_7=0) b) 3D/2D or 3D/1D (if I_7 undefined)
4	$\kappa > 0.1$, $\mu > 0.05$, $\eta < 0.1$	$I_6 \neq 0$	3D/2D
5	$\kappa > 0.1$, $\mu > 0.05$, $\eta > 0.3$	$I_7 \neq 0$	3D

Table 4.1: Dimensionality cases according to Bahr and WAL rotational invariants. In case 3, red and green colours refer to Bahr and WAL criteria respectively. The WAL method can distinguish cases 3a) from 3b) whereas the Bahr method cannot.

One of the main limitations of the Bahr method is that the threshold values do not have a justified physical or mathematical meaning, nor are they set in a statistical framework. As is shown below, the use of only these four parameters is insufficient to completely characterise the dimensionality.

The number of WAL invariants used for determining dimensionality is five (I_3 to I_7) plus invariant Q, which determines whether I_7 is meaningless or not. This total of six can be reduced to five since I_3 and I_4 are used together in the dimensionality classification.

In order to compare the reliability of both methods, an example was used which consisted of a magnetotelluric tensor $\underline{M}$, clearly representing a two-dimensional structure with different phases in the xy and yx polarisations. Table 4.2 shows the components of this tensor and the dimensionality interpretation using Bahr and WAL criteria. It is clear that in some circumstances, Bahr's criteria may lead to incorrect interpretations.

The use of only four parameters in the Bahr method is an important limitation in determining dimensionality. Furthermore, the classification of the dimensionality types, as well as the threshold values, should be revised such that they are concise and consistent.

As a first step, the next section presents the analytic relationships between the Bahr and WAL parameters.

MT Tensor	Bahr invariants	WAL invariants	
$M=\begin{bmatrix} 0 & 25+9i \\ -15-12i & 0 \end{bmatrix}$	$\kappa = 0$ $\mu = 0$ $\eta = 0$ $\Sigma = 0.05$	$I_1=20$ $I_2=10.5$ $I_3=0.25$ $I_4=0.14$ $I_5=0$ $I_6=0$ $I_7=0$ Q=0.39	
	κ and $\Sigma<0.1$, η and $\mu \approx 0 \rightarrow$ 1D or 3D/1D	I_3 and $I_4 \neq 0$, I_5, I_6 and $I_7 = 0 \rightarrow$ 2D	

Table 4.2: Example showing how both methods, using the threshold values established by the authors, lead to different interpretations.

4.3 Analytical Relationships and Equivalencies for Ideal Cases

Using the same decomposition as in Weaver *et al.* (2000), where the magnetotelluric tensor components are expressed as a function of the complex parameters $\zeta_j = \xi_j + i \cdot \eta_j$ (eq. 2.9), Bahr rotational invariants were rewritten as:

$$\kappa = \frac{\left(\xi_1^2 + \eta_1^2\right)^{\frac{1}{2}}}{\left(\xi_4^2 + \eta_4^2\right)^{\frac{1}{2}}}, \quad \text{(Swift Skew)} \tag{4.1a}$$

$$\mu = \frac{\left(\left|\xi_3\eta_2 - \xi_2\eta_3\right| + \left|\xi_1\eta_4 - \xi_4\eta_1\right|\right)^{\frac{1}{2}}}{\left(\xi_4^2 + \eta_4^2\right)^{\frac{1}{2}}}, \tag{4.1b}$$

$$\eta = \frac{\left(\left|\xi_3\eta_2 - \xi_2\eta_3 - \xi_1\eta_4 + \xi_4\eta_1\right|\right)^{\frac{1}{2}}}{\left(\xi_4^2 + \eta_4^2\right)^{\frac{1}{2}}}, \quad \text{(Regional skew or Phase sensitive skew)} \tag{4.1c}$$

$$\Sigma = \frac{\xi_2^2 + \xi_3^2 + \eta_2^2 + \eta_3^2}{\xi_4^2 + \eta_4^2}. \tag{4.1d}$$

Departing from these expressions, the analytical relationships were obtained by expressing Bahr parameters as functions of WAL invariants and are given as:

$$\kappa = f(r, I_5, I_6) = \sqrt{\frac{1+r^2}{1 - \frac{(I_5 - I_6)^2}{2\left(1 - I_5 I_6 + \sqrt{1 + I_5^2 I_6^2 - I_5^2 - I_6^2}\right)} + \frac{r^2}{2}\left(1 - I_5 I_6 + \sqrt{1 + I_5^2 I_6^2 - I_5^2 - I_6^2}\right)} - 1} = \sqrt{\frac{1+r^2}{1 - \frac{a}{2b} + \frac{r^2 b}{2}} - 1} \tag{4.2a}$$

$$\mu = f(r, I_5, I_6, I_7, Q) = \sqrt{\frac{|I_7 Q + I_6| + |I_6|}{\frac{1}{r}\left(1 - \frac{(I_5 - I_6)^2}{2\left(1 - I_5 I_6 + \sqrt{1 + I_5^2 I_6^2 - I_5^2 - I_6^2}\right)}\right) + \frac{r}{2}\left(1 - I_5 I_6 + \sqrt{1 + I_5^2 I_6^2 - I_5^2 - I_6^2}\right)}} = \sqrt{\frac{|I_7 Q + I_6| + |I_6|}{\frac{1}{r}\left(1 - \frac{a}{2b}\right) + \frac{rb}{2}}}$$

$$\tag{4.2b}$$

$$\eta = f(r, I_5, I_6, I_7, Q) = \sqrt{\frac{|I_7 Q|}{\frac{1}{r}\left(1 - \frac{(I_5 - I_6)^2}{2\left(1 - I_5 I_6 + \sqrt{1 + I_5^2 I_6^2 - I_5^2 - I_6^2}\right)}\right) + \frac{r}{2}\left(1 - I_5 I_6 + \sqrt{1 + I_5^2 I_6^2 - I_5^2 - I_6^2}\right)}}$$

$$\tag{4.2c}$$

$$\Sigma = f(r, I_3, I_4, I_5, I_6) = \frac{I_3^2 + I_4^2 r^2}{1 - \frac{(I_5 - I_6)^2}{2\left(1 - I_5 I_6 + \sqrt{1 + I_5^2 I_6^2 - I_5^2 - I_6^2}\right)} + \frac{r^2}{2}\left(1 - I_5 I_6 + \sqrt{1 + I_5^2 I_6^2 - I_5^2 - I_6^2}\right)} = \frac{I_3^2 + I_4^2 r^2}{1 - \frac{a}{2b} + \frac{r^2 b}{2}}$$

$$\tag{4.2d}$$

where a and b depend on I_5 and I_6: $a = \left(I_5 - I_6 \right)^2$ and $b = 1 - I_5 I_6 + \sqrt{1 + I_5^2 I_6^2 - I_5^2 - I_6^2}$. r is the quotient between I_2 and I_1, which appears in all the relationships due to the different normalisation used in each set of parameters.

Relating these identities to WAL dimensionality criteria, parameter κ is the one that distinguishes between undistorted and distorted cases (depending on whether I_5 and I_6 are null or not). μ and η also depend on the product $I_7 \cdot Q$, but not on their individual values. Σ is the only parameter that depends on I_3 and I_4, and, consequently, that deals with two-dimensionality.

The analytical relationships presented allow the particular expressions of Bahr parameters to be easily obtained for the ideal cases following the WAL conditions (in parenthesis):

1) 1D ($I_3 - I_6$=0 and I_7=0 or Q=0)

$$\kappa = \mu = \eta = \Sigma = 0 . \tag{4.3}$$

2) 2D (I_3 or $I_4 \neq 0$, I_5, I_6=0 and I_7=0 or Q=0)

$$\kappa = \mu = \eta = 0 , \tag{4.4a}$$

$$\Sigma = f_4 \left(r, I_3, I_4 \right) = \frac{I_3^2 + I_4^2 r^2}{1 + r^2} . \tag{4.4b}$$

3) a) 3D/2Dtwist and b) 3D/1D2D (I_3 or $I_4 \neq 0$, $I_5 \neq 0$, I_6=0 and I_7=0 or Q=0)

$$\mu = \eta = 0 , \tag{4.5a}$$

$$\kappa = f_1 \left(r, I_5 \right) , \tag{4.5b}$$

$$\Sigma = f_4 \left(r, I_3, I_4, I_5 \right) . \tag{4.5c}$$

Cases 3a and 3b are non-distinguishable using the Bahr method because it is not possible to know which of I_7 or Q is null.

4) 3D/2D ($I_6 \neq 0$ and I_7=0): κ, μ and Σ have the values corresponding to the general expressions (eqs. 4.2a-4.2d):

$$\eta = 0 , \tag{4.6a}$$

$$\kappa = f_1\left(r, I_5, I_6\right), \tag{4.6b}$$

$$\mu = f_2\left(r, I_5, I_6\right), \tag{4.6c}$$

$$\Sigma = f_4\left(r, I_3, I_4, I_5, I_6\right). \tag{4.6d}$$

5) 3D ($I_7 \neq 0$ and $Q \neq 0$): κ, μ, η and Σ have the values corresponding to the general expressions 4.2a-4.2d. However, there is no condition on the values of $I_3 - I_6$, therefore these invariants could have any value from 0 to 1.

$$\kappa = f_1\left(r, I_5, I_6\right), \tag{4.7a}$$

$$\mu = f_2\left(r, I_5, I_6, I_7, Q\right), \tag{4.7b}$$

$$\eta = f_3\left(r, I_5, I_6, I_7, Q\right), \tag{4.7c}$$

$$\Sigma = f_4\left(r, I_3, I_4, I_5, I_6\right). \tag{4.7d}$$

From these relationships some important points arise that modify the Bahr criteria (Table 4.1):

a) If the dimensionality is 1D or 2D, parameter μ must be null.

b) $\kappa \neq 0$ and $\mu \neq 0$ conditions are not necessary for three-dimensionality.

c) If the structure is not 3D, η vanishes.

4.4 Threshold Values

Given that in real situations data are affected by noise and that geoelectric structures do not exactly fit the assumed ideal cases, invariant values are never precisely zero. Weaver *et al.* (2000) address this problem by introducing a threshold value (τ_W), the same for all invariants I_3 to I_7, beneath which they are considered to be zero.

In order to make the Bahr and WAL criteria equivalent, first it was necessary to obtain the relationships between WAL and Bahr threshold values and then to redefine the thresholds used in the Bahr method. It was accomplished with two approaches: an analytical development and a statistical one.

a) Analytical Development

As a first approach, Bahr thresholds were computed from the analytical relationships, using the WAL threshold τ_W in place of invariants I_3 - I_7. The chosen value of Q was unity, thus the product $I_7 \cdot Q$ was replaced by τ_W. Parameters a and b in equations 4.2a to 4.2d were approximated by $a=(2 \cdot \tau_W)^2$ and $b=2$, after replacing I_5 and I_6 by the threshold value τ_W, excluding second order terms.

It was assumed that all WAL invariants are equal to the threshold value. This is not the situation for every dimensionality case but makes it possible to obtain preliminary expressions of Bahr thresholds. τ_κ, τ_μ, τ_η and τ_Σ depend on τ_W and r (the relationship between I_2 and I_1):

$$\tau_\kappa = \sqrt{\frac{1+r^2}{1+r^2-\tau_W^2}-1}\,, \tag{4.8a}$$

$$\tau_\mu = \sqrt{\frac{3\tau_W}{\sqrt{\frac{1}{r}\left(1-\tau_W^2\right)+1}}}\,, \tag{4.8b}$$

$$\tau_\eta = \sqrt{\frac{2\tau_W}{\sqrt{\frac{1}{r}\left(1-\tau_W^2\right)+1}}}\,, \tag{4.8c}$$

$$\tau_\Sigma = \frac{\tau_W^2\left(1+r^2\right)}{1+r^2-\tau_W^2}\,. \tag{4.8d}$$

Despite the approximation used, these expressions are useful to see which of the Bahr parameters are the most sensitive to τ_W and r. The dependencies of Bahr thresholds on the WAL threshold, for different values of r, are represented in Figure 4.1.
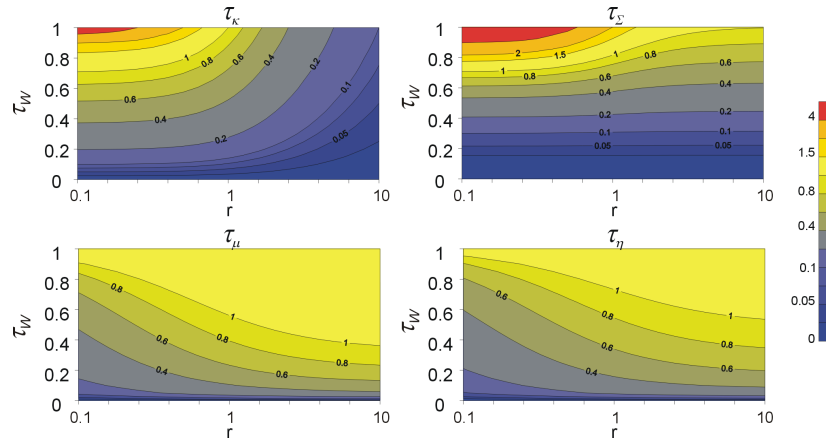
Figure 4.1: Bahr thresholds values obtained analytically for different values of the WAL threshold (τ_W) and r. Note that τ_W is represented on a linear scale and r on a logarithmic scale.

It can be observed that, for low values of r, τ_κ can be approximated to the constant value $\tau_\kappa \approx \dfrac{\tau_W}{\sqrt{2}}$, whereas for higher values of r its value decreases with r.

τ_μ and τ_η, which keep a $\sqrt{3/2}$ relation (eqs. 4.8b and 4.8c), smoothly increase in relation to both τ_W and r.

Threshold τ_Σ, except for high values of τ_W, has a low dependence with r, and take a constant value, $\tau_\Sigma \approx \tau_W^2$.

For a more accurate approach, instead of defining the new thresholds analytically, a statistical analysis was performed.

b) Statistical Development

For each dimensionality case, random values of the invariants, above or below their corresponding threshold range, τ_W, were generated, and Bahr parameters were computed using the analytical relationships in equations 4.2a to 4.2d. The value of r was chosen to be r=1, which is a valid approximation since, for experimental data, I_1 and I_2 are of the same order of magnitude (r represents the relation between the imaginary and real parts of the magnetotelluric tensor components). Thus, it was possible to establish the new thresholds for Bahr parameters, τ_κ, τ_μ, τ_η and τ_Σ, as well as the new dimensionality conditions. This development was made for different values of τ_W.

The following results were observed:

1) Thresholds τ_κ and τ_Σ can easily be related to τ_W using the approaches $\tau_\kappa \approx \dfrac{\tau_W}{\sqrt{2}}$ and $\tau_\Sigma \approx \tau_W^2$, as shown by the analytical development (eqs. 4.8a and 4.8d using r=1). The threshold τ_κ differentiates 1D and 2D from the rest of the cases, except 3D, which can take any value of κ. Values of Σ greater than τ_Σ indicate that the structure is not 1D, but 2D, with or without galvanic distortion (cases 2, 3 and 4). 3D cases can have any value of Σ.

2) The dependence of τ_μ on τ_W is more complex, since these parameters become more sensitive to the value of r, and, consequently the approximation r=1 is not the most appropriate.

In order to distinguish cases 1, 2 and 3 from case 4, there is a statistical value of τ_μ, although sometimes there is an overlap of possible values among these different cases.

3) In the case of parameter η, in order to differentiate between cases 4 and 5, it is also necessary to consider WAL parameter Q, which determines if I_7 is meaningless or not. This is accomplished assuming that the condition $\eta > \tau_\eta$ is only valid if Q is not meaningless, whereby

the threshold τ_Q is defined. The value of Q is also useful to differentiate case 3a from 3b, as in the WAL criteria.

Table 4.3 shows the values of τ_κ, τ_μ, τ_η and τ_Σ that correspond to r=1, τ_W= 0.1 and τ_Q=0.1. These thresholds, especially τ_Σ, differ significantly from the thresholds proposed by Bahr (1991).

Bahr parameters	τ_W=0.1
τ_κ	0.06
τ_μ	0.34
τ_η	0.12
τ_Σ	0.01

Table 4.3: Threshold values τ_κ, τ_μ, τ_η and τ_Σ, for r=1 , τ_W= 0.1 and τ_Q=0.1.

4.5 Bahr-Q Method

From the new threshold values obtained for Bahr parameters, the appropriate dimensionality conditions can be defined. However, there is a limitation by using only four parameters, compared to the five of the WAL method. In this section, the Bahr method is extended to be internally consistent with WAL invariants.

To classify dimensionality it is necessary to take into account parameters κ, μ, η, Σ and the thresholds as defined in the previous section. Also, in order to distinguish the two subcategories of case 3, it is necessary to use parameter Q. This new method has been named the Bahr-Q (B-Q) method. Table 4.4 shows the conditions necessary to classify the dimensionality using B-Q parameters (κ, μ, η, Σ and Q) with the thresholds values defined in the preceding section.

The application of the B-Q method in the example from Table 4.2 leads to the same interpretation as does WAL criteria: $\kappa = \mu = \eta = 0$, $\Sigma > \tau_\Sigma$ and Q>τ_Q, which indicates two-dimensionality.

B-Q method					
Dimensionality Case	κ	μ	Σ	η	Q
1) 1D	$<\tau_\kappa$	$<\tau_\mu$	$<\tau_\Sigma$	$<\tau_\eta$	---
2) 2D	$<\tau_\kappa$	$<\tau_\mu$	$>\tau_\Sigma$	$>\tau_\eta$ $<\tau_\eta$ $>\tau_\eta$	$Q<\tau_Q$ --- $Q<\tau_Q$
3) a) 3D/2D twist b) 3D/1D2D	$>\tau_\kappa$	$<\tau_\mu$	$>\tau_\Sigma$	$<\tau_\eta$ ---	a) **Q**$>\tau_Q$ b) $Q<\tau_Q$
4) 3D/2D	$>\tau_\kappa$	$>\tau_\mu$	$>\tau_\Sigma$	$<\tau_\eta$ $>\tau_\eta$	--- $Q<\tau_Q$
5) 3D	---	---	---	$>\tau_\eta$	**Q**$>\tau_Q$

Table 4.4: The Bahr-Q method criteria to characterise geoelectric dimensionality.

4.6 Application to Synthetic and Real Data

Three sets of data were used in order to compare the dimensionality obtained using WAL, Bahr and B-Q methods. The first is a synthetic set from the model used in Weaver *et al.* (2000). The second and third sets, increasing in complexity, consist of real data from the COPROD dataset, already used in the previous chapter, and from the BC87 dataset, also well known by the MT community. In the BC87 datasets, errors were taken into account.

Set 1: Synthetic Data

Set 1 consists of seven magnetotelluric tensors (A-G) selected from the synthetic model used in Weaver *et al.* (2000). It consists of a cubic conductive anomaly (0.5 Ω·m) embedded on the surface of an otherwise 2D structure, formed by a vertical fault that separates a layered medium of 10 Ω·m, 100 Ω·m and 1 Ω·m from a homogeneous medium of 1Ω·m (Figure 4.2).
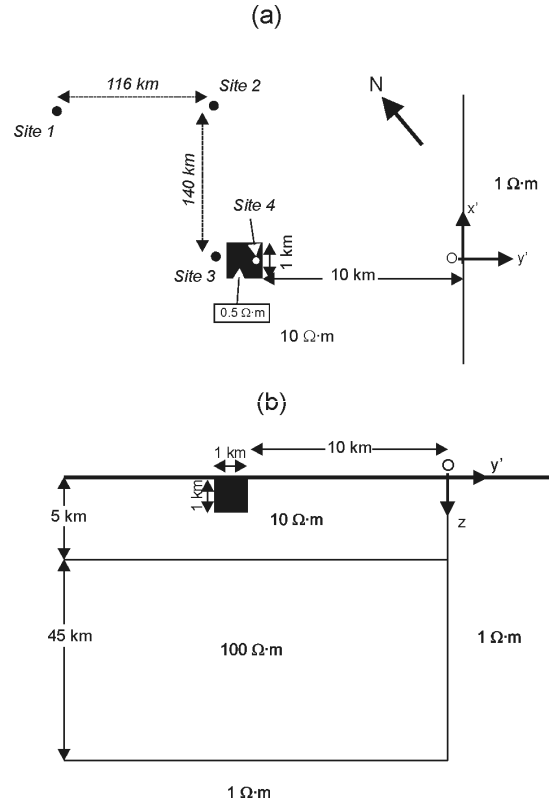
Figure 4.2: Synthetic model from Weaver *et al.* (2000). a) Plane view at z=0, b) Vertical cross section at x'=0.

The magnetotelluric tensors computed from the model for four sites at different periods exemplify the different types of dimensionality that can be identified using the WAL criteria with a threshold value of 0.1:

A: Site 1, 100s: 1D;

B: Site 2, 1000s: 2D with equal phases for xy and yx;

C: Site 2, 100s: 2D with different phases for xy and yx;

D: Site 3, 1000s; 3D/1D2D;

E: Site 2, 100s where E field was rotated 10°: 3D/2Dtwist;

F: Site 3, 100s: 3D/2D;

G: Site 4, 1s: 3D.

Table 4.5 presents the values of Bahr parameters and Q for each tensor, showing which are above (grey background) or below the threshold.

MT Tensor	κ (τ_κ=0.06)	μ (τ_μ=0.34)	Σ (τ_Σ=0.01)	η (τ_η=0.12)	Q (τ_Q=0.1)
A (1D)	0	0	0	0	0
B (2D)	0	0	0.09	0	0.01
C (2D)	0	0	0.05	0	0.36
D (3D/1D2D)	0.13	0.07	0.25	0.01	0.03
E (3D/2D twist)	0.18	0.02	0.05	0.01	0.36
F (3D/2D)	0.09	0.37	0.20	0.06	0.31
G (3D)	0.13	0.25	0.21	0.17	0.28

Table 4.5: Bahr parameters and Q, with their corresponding thresholds values, derived from τ_W=0.1, for tensors A-G from Set 1 (in parenthesis, the dimensionality according to the WAL method). In grey, parameters values greater than the threshold.

Table 4.6 shows the dimensionality that one would obtain using two types of analysis:

1) The Bahr method

2) The B-Q method: Bahr parameters and invariant Q, using τ_κ, τ_μ, τ_η and τ_Σ from τ_W=0.1 (see Table 4.3). Q is considered meaningless if its value is below 0.1.

The results present some equivalences but also some divergences showing how the B-Q method proposed improves the classical Bahr method. They also prove the consistency between B-Q and WAL methods.

MT Tensor (WAL dimensionality)	Bahr method	B-Q method
A (1D)	1D	1D
B (2D)	1D	2D
C (2D)	1D	2D
D (3D/1D2D)	3D/2D	3D/1D2D
E (3D/2D twist)	3D/1D	3D/2D twist
F (3D/2D)	2D	3D/2D
G (3D)	?	3D

Table 4.6: Dimensionality obtained for tensors A-G using the Bahr method and B-Q method.

In A (1D according to WAL) both criteria agree because the Bahr parameters are below the established thresholds, which indicate that the structure is 1D.

B and C data (2D according to WAL) are one-dimensional according to Bahr, whilst the magnetotelluric tensor has non-zero diagonal components and a well-defined strike direction (Weaver *et al.*, 2000). Using the B-Q method, these tensors are interpreted as 2D. This inconsistency between Bahr and B-Q methods is due to the new definition of τ_Σ, which is the square of τ_W. However, Bahr's method uses $\tau_\Sigma = 0.1$, which would correspond to a higher value for τ_W (0.31). As a result, tensors that are clearly 2D, may be interpreted as 1D.

In D (3D/1D2D according to WAL), the Bahr method would infer the following:

1) The structure is not 1D ($\kappa > 0.1$);

2) There is a phase difference between the tensor components ($\mu > 0.05$);

3) It can be interpreted as a distortion over a 1D or 2D structure ($\eta < 0.05$) and

4) The regional structure is 2D ($\Sigma > 0.1$).

According to B-Q, the distortion occurs over a 1D or 2D structure with equal phases in the non diagonal components of the MT tensor. Now, the inconsistency between Bahr and B-Q comes from the value of τ_μ: the value 0.05 established by Bahr (1991) is too low, and hence provides a very strict criterion to consider when phase values are different (less than 3° in this case).

In E (3D/2Dtwist), with the exception of κ, all the parameters are below the thresholds defined by Bahr and the structure could be considered 3D/1D. With the B-Q method, since Q is not meaningless, it corresponds to a 3D/2D structure, affected only by twist.

It must be noted that the use of parameter Q in the B-Q method allows one to distinguish two types of dimensionalities, 3D/1D2D and 3D/2Dtwist, in D and E.

In F (3D/2D according to WAL), the Bahr method states that the dimensionality is 2D, because both κ and Σ are greater than 0.1. B-Q agrees with a 3D/2D interpretation because only η is below the threshold.

In G (3D according to WAL), the Bahr method cannot ascertain if the structure is 3D because η is not greater than 0.3. By contrast, the B-Q method identifies the structure as 3D because $\eta > \tau_\eta$ and Q > 0.1.

From this analysis it can be concluded that the B-Q method, consisting of the use of Bahr parameters and WAL invariant Q, with the new conditions and a suitable threshold for each invariant, is consistent with WAL invariants criteria, used to determine the dimensionality of the magnetotelluric tensor.

Set 2: COPROD2 Dataset: Site 85_314

As it was shown in the previous chapter, the data responses of site 85_314 from the COPROD2 dataset (Appendix B) have in general a 1D behaviour at short periods (up to 10s). From 10s to 1000s the data display a 2D behaviour with a NS strike direction (Jones *et al.*, 2005), as determined from the multisite-multifrequency decomposition code of McNeice and Jones (2001), based on Groom and Bailey (1989) (G&B).

Table 4.7 shows Bahr and Q parameters related to the threshold values and the dimensionality derived from the B-Q method, compared to the ones obtained using G&B decomposition, WAL and Bahr methods.

The Bahr and G&B methods provide the simplest dimensionality descriptions, whereas WAL and B-Q also depict 3D cases at the longest periods. The WAL and B-Q results are coincident, describing the dimensionality as 1D up to 20s, 2D from 20s to 300s and 3D up to 1000s. G&B decomposition infers an optimum 2D description from 10 to 1000s and the Bahr method results in a 1D description up to 100s and 2D for the remainder.

G&B decomp.	Bahr Method	WAL Method	κ	μ	Σ	η	Q	B-Q Method
						$<\tau_\eta$		
		1D			$<\tau_\Sigma$	Alternating $<\tau_\eta$ and $>\tau_\eta$	$<\tau_Q$	1D
	1D		$<\tau_\kappa$	$<\tau_\mu$				
2D		2D				$<\tau_\eta$		2D
	2D				$>\tau_\Sigma$		$>\tau_Q$	
		3D	$>\tau_\kappa$			$>\tau_\eta$		3D

T (s): 0.01, 0.1, 1, 10, 100, 1000

Table 4.7: Dimensionalities obtained from the Groom and Bailey, Bahr, WAL and B-Q methods for site 85_314, COPROD2 set. The B-Q method uses τ_κ, τ_μ, τ_η and τ_Σ obtained from τ_{WAL}=0.1, and τ_Q=0.1 (Table 4.3). The grey area represents the range of periods for which G&B decomposition resulted in large errors.

Hence, all methods coincide with a 1D description up to 10s. G&B decomposition at this period range provided large error values, which is consistent with 1D dimensionality. The main difference is in the period at which the transition between 1D and 2D takes place, which is significant (about 1 decade with respect to the other methods) for the Bahr method. Furthermore, the 3D dimensionality cases at the longest periods are only shown in the WAL and B-Q methods.

The lowest misfit on the 3D/2D decompositions (Strike program) are obtained when the range 10s-300s is considered (B-Q method), as opposed to the 10s-1000s (Jones *et al.*, 2005) and 100s-1000s (Bahr Method). These results, together with large values of the invariant I_7 observed at the longest periods, confirm the validity of the dimensionality description obtained through the B-Q method.

Set 3: BC87 Dataset: Site 4

The BC87 dataset was acquired in British Columbia (Appendix C) and is commonly used to test and compare new methods in analysis and interpretation of MT data. The data display complex 3D effects, due both to local effects and the presence of the Nelson batholithic body (western part of profile). Site 4 is located above this body.

Table 4.8 summarises the kind of structures derived from the new B-Q method and compares them to those obtained using the WAL and Bahr methods, in both cases departing from τ_W=0.1, τ_Q=0.1 and without considering data errors. The WAL and B-Q methods give the same dimensionality interpretation, except for some periods.

The differences between the B-Q and WAL methods are due to parameters η and Q that have values close to the thresholds, which, as stated before, were not defined analytically but, rather, statistically.

B-Q and WAL interpretation is more complete than that of using the classical Bahr method, whose conditions, $\eta < 0.05$ and $\eta > 0.3$, do not allow the identification of data affected by distortion and 3D cases.

The dimensionality obtained using WAL and B-Q shows that up to 1s distortion can be removed from the data, which can be interpreted as 2D. For periods longer than 1s the dimensionality is 3D, with the exception of some particular periods, where 3D/2D cases are obtained.

This description agrees, in general, with Jones *et al.* (1993). Accordingly, a 3D/2D decomposition of the data is possible for periods shorter than 1s and longer than 10s. From 1s to 10s the data show a 3D behaviour, due to the presence of the Nelson Batholith. The difference with B-Q and WAL dimensionality results becomes evident at longer periods, where these

methods identify the data as 3D, whereas Jones *et al.* (1993) make a 3D/2D decomposition, with moderate misfit values in the retrieval of the regional responses.

κ and Σ (τ_κ=0.06) (τ_Σ=0.01)	μ (τ_μ=0.34)	η (τ_η=0.12)	Q (τ_Q=0.1)	Bahr Method	B-Q Method	WAL Method
	$>\tau_\mu$	$>\tau_\eta$			3D	3D
		$<\tau_\eta$			3D/2Dtwist	3D/2D twist
		$>\tau_\eta$			3D	3D
	$<\tau_\mu$	$<\tau_\eta$	$>\tau_Q$	3D/2D	3D/2Dtwist	3D/2Dtwist
$>\tau_\kappa$		$>\tau_\eta$			3D	3D
		$<\tau_\eta$	$<\tau_Q$		3D/1D2D	3D/2Dtwist
	$>\tau_\mu$				3D/2D	
	$<\tau_\mu$	$>\tau_\eta$			3D	3D
		$<\tau_\eta$			3D/2D	3D/2D
$>\tau_\Sigma$	$>\tau_\mu$	$>\tau_\eta$	$>\tau_Q$	3D / 3D	3D	3D
		$<\tau_\eta$			3D/2D	3D/2D
		$>\tau_\eta$		3D / 3D	3D	3D
		$<\tau_\eta$			3D/2D	3D/2D

T(s) axis: 0.01, 0.1, 1, 10, 100, 1000

Table 4.8: B-Q parameters and dimensionality obtained from the Bahr, B-Q and WAL methods for the data from site 4, BC87 dataset. Parameters shaded in grey are those with values greater than the threshold.

When data errors are considered, which in turn influence the computed parameters, one of the consequences is that the dimensionality can be undetermined if the error bars cross the threshold values, since in these cases there are ambiguities in the classification. Another consequence is the bias that can appear between the true values (computed directly from the tensor components) and the statistical values (computed as the average of the different Gaussian generations) (chapter 3).

Figure 4.3 and Figure 4.4 show the values of the WAL and Bahr parameters and their errors that correspond to site 4 for two noise levels: 1% and 10%, where only half of the periods have been plotted. For WAL invariants I_7 and Q the biases are also presented (for the remainder of the parameters the biases are insignificant, as can be seen by comparing the statistical values for the different noise levels).
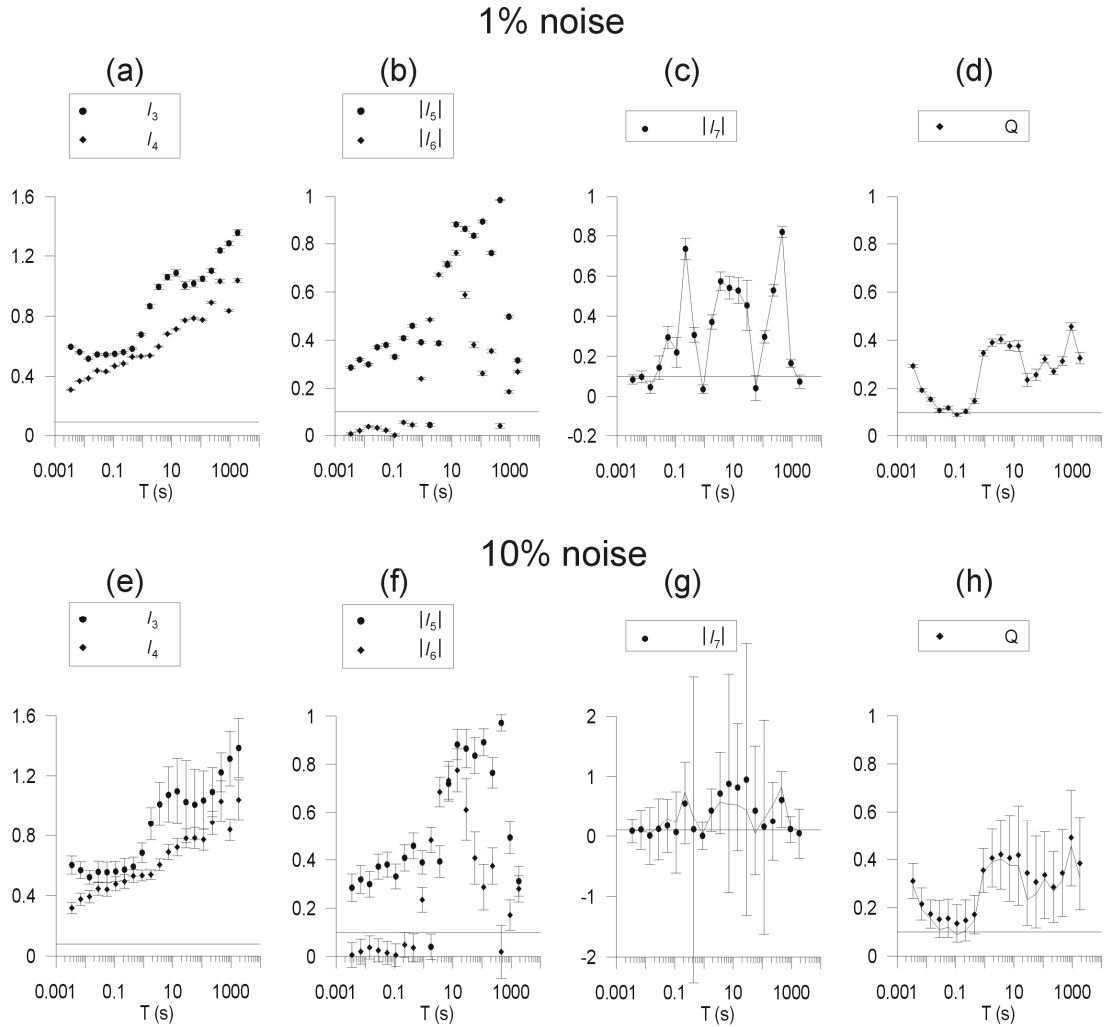
Figure 4.3: Invariants $I_3 - I_7$ and Q, with their error bars, for 20 recorded periods of site 4 from BC87 dataset. 1% noise level (a, b, c and d) and 10% noise level (e, f, g and h). For invariants I_7 and Q (d and h) the biases between the true and statistical values are also presented (continuous line). Horizontal continuous line: threshold value τ_W=0.1.

The error bars of WAL parameters are, in general terms, proportional to the noise level, with the exception of I_7, which displays large error bars at some periods. With 10% noise, at the third last period of I_6, most of the periods of I_7 and some periods of Q, the error bars cross the threshold value, with the consequence that it is not possible to discern whether these invariants can be considered null or not. A second problem is caused by the biases of I_7, which add more uncertainty in the parameter estimation. On the contrary, the biases of Q are not important.

The error bars of Bahr parameters are smaller and, apart from the lowest periods of η with 10% noise, it is always possible to discern if Bahr parameters are above or below the threshold.
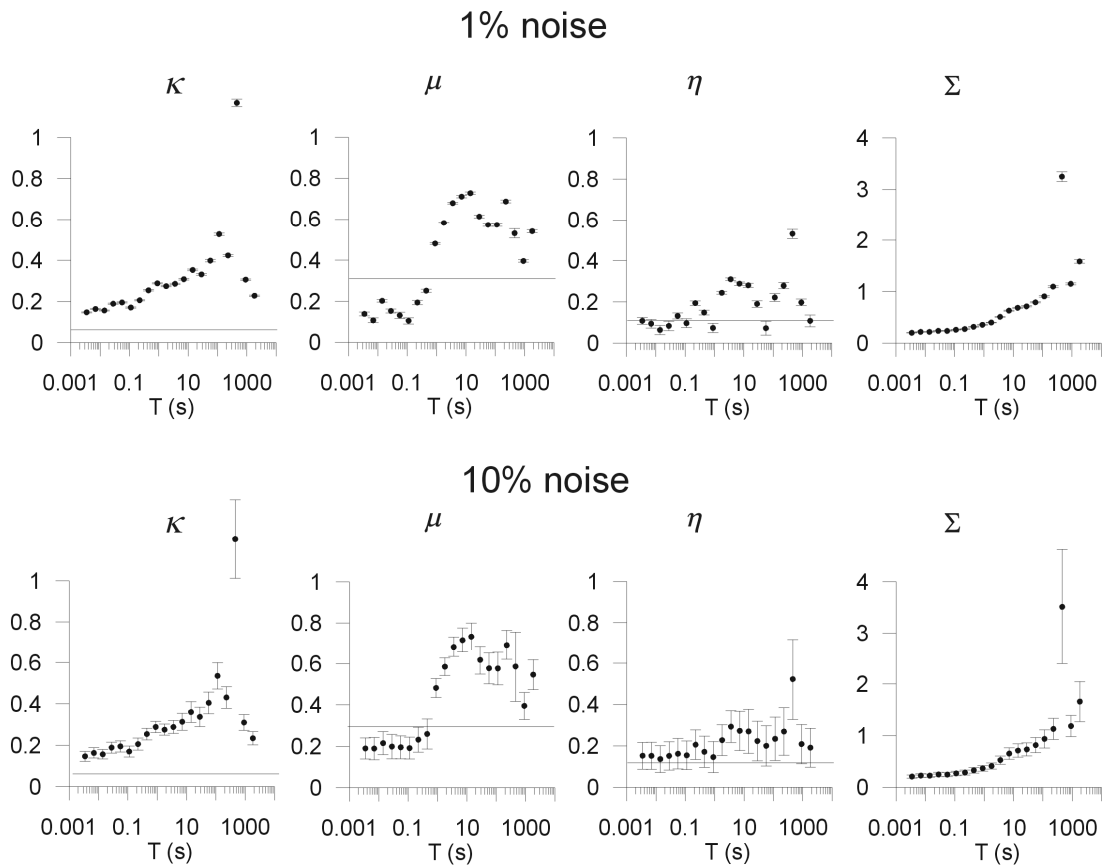
Figure 4.4: Bahr parameters with their error bars, for 20 recorded periods of site 4 from the BC87 dataset. Upper line: 1% noise. Lower line: 10% noise.

Consequently, having contrasted the large errors and biases of invariant I_7 versus the stability of Bahr and Q parameters, it can be stated that the Bahr-Q method is more robust under the presence of errors, in determining dimensionality.

A complete analysis of the dimensionality using the WAL and B-Q methods taking into account these errors would lead to a good determination of all periods for 1% noise. When the noise level is 10%, WAL invariant I_7 is undetermined at most periods. It limits the determination of the type of dimensionality using WAL criteria to only a few periods. With the same 10% noise level the Bahr-Q method provides a dimensionality description for a broader range of periods which, as already observed in the error bars, makes it more suitable for dimensionality analysis of noisy data.

4.7 Conclusions

In this chapter, two of the methods used to characterise the geoelectric dimensionality from MT data (the Bahr method and the WAL method) were studied. An important conclusion is that, compared to WAL, the Bahr method does not provide complete dimensionality interpretations. The reasons are that it uses only four parameters (whilst WAL uses five) and that the thresholds' values suggested lead to ambiguities or to situations where the dimensionality cannot be determined.

The redefinition of Bahr thresholds and the addition of the invariant Q allowed the establishment of a new dimensionality criterion (Bahr-Q) consistent with the WAL method.

The Bahr-Q method was tested with synthetic and real data corresponding to all types of dimensionality, obtaining the same interpretation as the WAL method. When the data are affected by a significant level of noise (10% or higher), the errors and biases of Q can be important and, consequently, the dimensionality obtained from either method can be undetermined. However, Bahr and Q parameters are more stable under noise effects and make Bahr-Q a more robust method.

Chapter 5: Applications of the Magnetotelluric Phase Tensor and Comparison with other Methods

The goal of this chapter is to analyse the phase tensor proposed by Caldwell *et al.* (2004) and apply it to synthetic and real data in order to determine the resolution of the parameters involved.

The phase tensor and its associated parameters and errors were analysed, and, together with the information obtained, compared to the WAL and Groom and Bailey methods. A last step consisted of fitting the phase tensor information to a 2D description of the data.

The phase tensor, and its related parameters and graphic representations were computed using a code created with Compaq Visual Fortran 2000[®] and a Matlab[®] application provided by Hugh Bibby.

5.1 The Phase Tensor for Different Dimensionality Cases

The phase tensor (see chapter 2, section 2.6) displays distinct expressions for particular cases of dimensionality and orientations of the measuring axes. The expressions of the phase tensors with their SVD (Singular Value Decomposition) and related parameters were computed for four particular cases (1D, 2D and 3D/2D with different orientations, and 3D), which are summarized, together with a numerical example in each case (Table 5.1). Note that the 2D example (B) is the same MT tensor used in chapter 4 (Table 4.2), which is rotated 30° in example C.

A	1D
Impedance tensor	$\begin{bmatrix} 0 & M \\ -M & 0 \end{bmatrix}$
Phase tensor	$\begin{bmatrix} -Y/-X & 0 \\ 0 & Y/X \end{bmatrix} = \begin{bmatrix} \tan(\varphi \pm \pi) & 0 \\ 0 & \tan\varphi \end{bmatrix}$
SVD Parameters	$\alpha_P = 0/0 \;\; (undefined)$, $\Phi_{\substack{Max \\ min}} = \tan\varphi$; $\beta_P = 0^\circ$
Numerical example	**1D with φ=26.56º**
Impedance tensor	$\begin{bmatrix} 0 & 10+5i \\ -10-5i & 0 \end{bmatrix}$
Phase tensor	$\begin{bmatrix} 0.5 & 0 \\ 0 & 0.5 \end{bmatrix} = \begin{bmatrix} \tan(26.56^o) & 0 \\ 0 & \tan(206.56^o) \end{bmatrix}$
SVD	$\begin{bmatrix} 1 & 0 \\ 0 & 1 \end{bmatrix}\begin{bmatrix} 0.5 & 0 \\ 0 & 0.5 \end{bmatrix}\begin{bmatrix} 1 & 0 \\ 0 & 1 \end{bmatrix}$
SVD Parameters	$\alpha_P = 0/0 \;\; (undefined)$; $\Phi_{\substack{Max \\ min}} = 0.5$; $\beta_P = 0^\circ$

Table 5.1: Synopsis and numerical examples of the phase tensor and SVD parameters for particular dimensionality cases: (a) 1D case.

B	2D or 3D/2D along strike direction	
Impedance tensor	$\begin{bmatrix} 0 & M_{12} \\ M_{21} & 0 \end{bmatrix}$	$\begin{bmatrix} 0 & M_{TE} \\ M_{TM} & 0 \end{bmatrix}$
Phase tensor	$\begin{bmatrix} Y_{21}/X_{21} & 0 \\ 0 & Y_{12}/X_{12} \end{bmatrix} = \begin{bmatrix} \tan\varphi_{21} & 0 \\ 0 & \tan\varphi_{12} \end{bmatrix}$	$\begin{bmatrix} Y_{TM}/X_{TM} & 0 \\ 0 & Y_{TE}/X_{TE} \end{bmatrix} = \begin{bmatrix} \tan\varphi_{TM} & 0 \\ 0 & \tan\varphi_{TE} \end{bmatrix}$
SVD Parameters	$\alpha_P = 0^\circ$, $\Phi_{\substack{Max \\ min}} = \tan\varphi_{\substack{12 \\ 21}}$, $\beta_P = 0^\circ$	
Numerical example	**2D along strike direction (example from chapter 4, table 4.2)**	
Impedance tensor	$\begin{bmatrix} 0 & 25+9i \\ -15-12i & 0 \end{bmatrix}$	
Phase tensor	$\begin{bmatrix} 0.8 & 0 \\ 0 & 0.36 \end{bmatrix} = \begin{bmatrix} \tan 38.66^\circ & 0 \\ 0 & \tan 19.79^\circ \end{bmatrix}$	
SVD	$\begin{bmatrix} 1 & 0 \\ 0 & 1 \end{bmatrix}\begin{bmatrix} 0.8 & 0 \\ 0 & 0.36 \end{bmatrix}\begin{bmatrix} 1 & 0 \\ 0 & 1 \end{bmatrix}$	
SVD Parameters	$\alpha_P = 0^\circ$; $\begin{array}{l}\Phi_{Max} = 0.8 = \tan(38.66^\circ) \\ \Phi_{min} = 0.36 = \tan(19.79^\circ)\end{array}$; $\beta_P = 0^\circ$	

Table 5.1 (cont.) (b) 2D or 3D/2D measured along the strike

C	2D or 3D/2D rotated an angle θ clockwise
Impedance tensor	$\begin{bmatrix} (M_{12}+M_{21})\sin\theta\cos\theta & M_{12}\cos^2\theta-M_{21}\sin^2\theta \\ -M_{12}\sin^2\theta+M_{21}\cos^2\theta & -(M_{12}+M_{21})\sin\theta\cos\theta \end{bmatrix}$
Phase tensor	$\begin{bmatrix} (Y_{21}/X_{21})\cos^2\theta+(Y_{12}/X_{12})\sin^2\theta & (-Y_{21}/X_{21}+Y_{12}/X_{12})\sin\theta\cos\theta \\ (-Y_{21}/X_{21}+Y_{12}/X_{12})\sin\theta\cos\theta & (Y_{21}/X_{21})\sin^2\theta+(Y_{12}/X_{12})\cos^2\theta \end{bmatrix}=$ $\begin{bmatrix} \Phi_{11}\cos^2\theta+\Phi_{22}\sin^2\theta & (-\Phi_{11}+\Phi_{22})\sin\theta\cos\theta \\ (-\Phi_{11}+\Phi_{22})\sin\theta\cos\theta & \Phi_{11}\sin^2\theta+\Phi_{22}\cos^2\theta \end{bmatrix}$
SVD Parameters	$\alpha_P=-\theta$, $\Phi_{\substack{Max \\ min}}=\tan\varphi_{\substack{12 \\ 21}}, \beta_P=0º$
Numerical example	**2D (example B) rotated 30º**
Impedance tensor	$\begin{bmatrix} 4.33-1.29i & 22.5+9.75i \\ -17.5-11.25i & -4.33+1.29i \end{bmatrix}$
Phase tensor	$\begin{bmatrix} 0.69 & -0.1905 \\ -0.1905 & 0.47 \end{bmatrix}$
SVD	$\begin{bmatrix} 0.866 & 0.5 \\ -0.5 & 0.866 \end{bmatrix}\begin{bmatrix} 0.8 & 0 \\ 0 & 0.36 \end{bmatrix}\begin{bmatrix} 0.866 & -0.5 \\ 0.5 & 0.866 \end{bmatrix}$
SVD Parameters	$\alpha_P=-30º$; $\begin{array}{l}\Phi_{Max}=0.8=\tan(38.66º) \\ \Phi_{min}=0.36=\tan(19.79º)\end{array}$; $\beta_P=0º$

Table 5.1 (cont.) (c) 2D or 3D/2D rotated

D	3D case
Impedance tensor	$\begin{bmatrix} M_{11} & M_{12} \\ M_{21} & M_{22} \end{bmatrix}$
Phase tensor	General expression (eq. 2.28)
SVD Parameters	General expressions (eqs. 2.31, 2.32 and 2.33)
Numerical example	**3D case**
Impedance Tensor	$\begin{bmatrix} 1.405+2.23i & 5.33+2.5i \\ -7.45-4.23i & 1.45+3.29i \end{bmatrix}$
Phase Tensor	$\begin{bmatrix} 0.617 & -0.333 \\ 0.256 & 0.557 \end{bmatrix}$
SVD	$\begin{bmatrix} 0.97 & 0.22 \\ -0.22 & 0.97 \end{bmatrix}\begin{bmatrix} 0.7061 & 0 \\ 0 & 0.6076 \end{bmatrix}\begin{bmatrix} 0.77 & -0.6335 \\ 0.6335 & 0.77 \end{bmatrix}$
SVD parameters	$\alpha_P=-26º$; $\begin{array}{l}\Phi_{Max}=0.706=\tan(35.22º) \\ \Phi_{min}=0.607=\tan(31.28º)\end{array}$; $\beta_P=-13º$

Table 5.1 (cont.) (d) 3D case.

The phase tensor ellipses corresponding to the numerical examples A, B, C and D are represented in Figure 5.1. As expected, the 1D case (A) representation is a circle, with an undefined value of α_P. 2D cases (B and C) are ellipses with clearly differentiated major and minor axes, aligned along the strike direction. The 3D case (D) is characterized by almost equal values of major and minor ellipse axes, although with well defined values of α_P and β_P, which in this case both have a non-zero value.
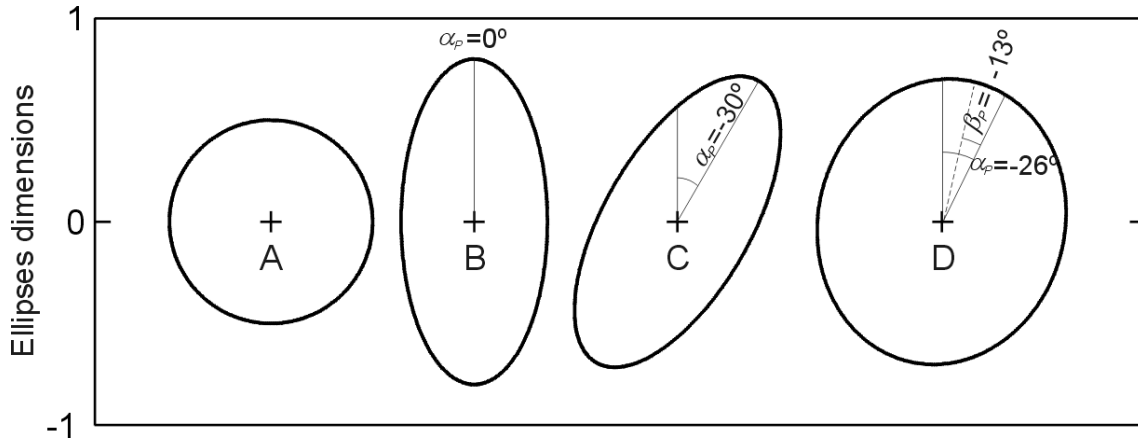
Figure 5.1: Representation of the phase tensor ellipses corresponding to the synthetic examples A, B, C and D displayed in Table 5.1.

5.2 Application to Synthetic and Real Datasets

5.2.1 Synthetic model dataset

The first dataset consists of the responses of a synthetic model, previously used in the work of Ledo *et al.* (2002), which studied the 3D effects in the 2D interpretation of magnetotelluric data. It consists of a 3D body embedded in a 2D structure (Figure 5.2).

The responses correspond to 30 sites along a profile, with 11 periods from 0.01 s to 1000 s. Random galvanic distortion C, with gain $g = 1$ and without anisotropy (equation 1.26), was added to each site in order to see the effects of distortion over 3D regional responses.

To make the responses representative of real data, Gaussian noise was added, which is not proportional to the signal amplitude. Thus, the same error, the relative error of the largest of the four components, was added to all tensor components. Additionally, the values of the components were randomly scattered around their errors, such that the final values of the tensor components were the means of these scattered values.

Once distortion was added to the responses, two datasets were created, each one with a different level of noise: dataset SIT-1, with 1% error, and SIT-2.5, with 2.5% error. The original dataset, without distortion or noise, was also employed and referred to as SIT.
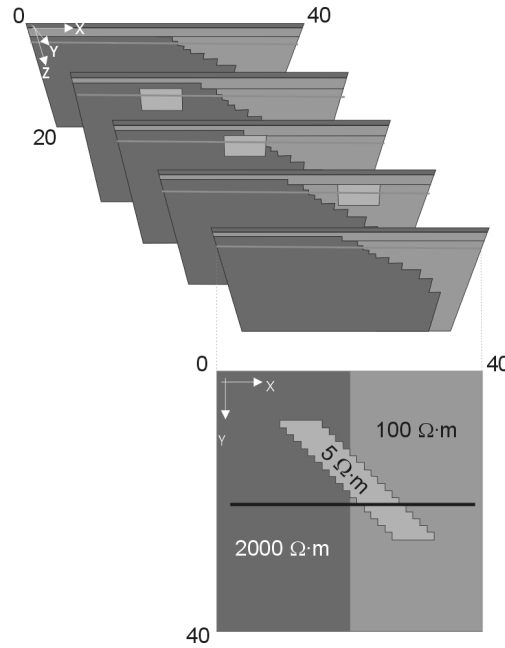
Figure 5.2: 3D electrical conductivity regional model used to generate synthetic responses. Black line on XY view indicates the position of the profile.

The estimations of the phase tensor parameters and their errors were computed using Random Gaussian Noise generation (statistical values and errors) (chapter 3, approach **b**), using n=100. The true values of the parameters were also considered.

The phase tensor ellipses of dataset SIT are displayed in Figure 5.3, together with the arrows indicating the direction given by angle α_P. Figure 5.4 represents the associated parameters Φ_{Max}, Φ_{min}, α_P, β_P, the difference Φ_{Max} - Φ_{min} and, except for the original dataset SIT, the error of angle α_P.

At the shortest and longest periods, the phase tensor representations (Figure 5.3) are circles, with different radii values, signifying changes in the phase values. These circles are characterised by low values of Φ_{Max} - Φ_{min} (Figure 5.4), and a wide variation of angle α_P along the different phase tensor representations. The angle β_P allows discerning whether the circles indicate a 1D or 3D structure. This angle has a range of values between -2° and 2°, which suggests that the circles can be interpreted as 1D.

At middle periods, the phase tensors are represented by general ellipses, with a gradual change in orientation, from the left side (90°, perpendicular to the model strike), to the right side (ellipses aligned along the model strike) of the profile. This change reflects the variations in the TE and TM phase values. In the same way as the other methods to determine the strike direction, the phase tensor representation also involves a 90° ambiguity in its determination.
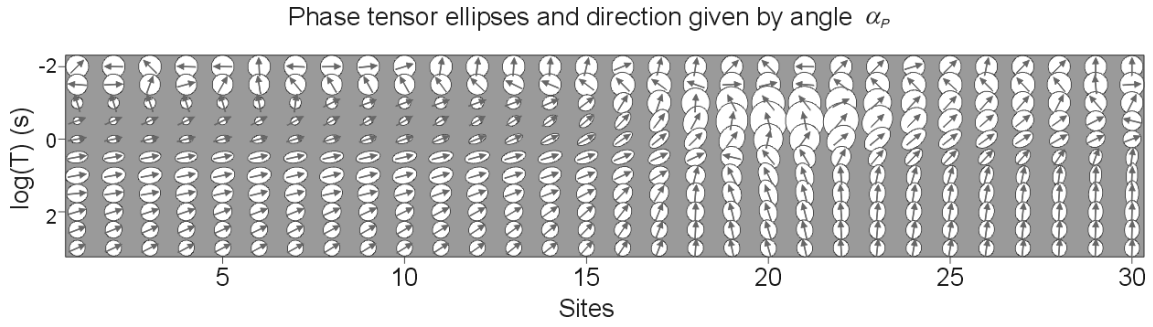
Figure 5.3: Ellipse representations of the phase tensor for SIT dataset responses, along with the direction given by α_P, plotted along the profile of the synthetic model for the 11 computed periods.

As for the datasets in which distortion and errors were added, at site 12 from SIT1 and sites 12, 20 and 25 from SIT2.5 there are important overflows of Φ_{Max} and, for all the parameters, the differences with the original dataset SIT are evident (Figure 5.4). These significant variations with respect to the original dataset rely on the high dependence of the phases on small changes in the values of the impedance tensor components, especially when their values are small. At the rest of sites, there is good agreement between the original and distorted data, as is expected from the property of invariance under distortion of the phase tensor. However, some remarkable points arise:

1) The statistical values of Φ_{Max} are in general higher than its true values, whereas those of Φ_{min} are smaller that the true ones. This implies that the difference between Φ_{Max} and Φ_{min} computed from the statistical values is greater than the true difference, which in some cases leads to a 2D misinterpretation of the data. This larger difference is a consequence of the errors, that results in a greater value of the radicand in eq. 2.33, consequential upon a larger value of the sum, Φ_{Max}, and a smaller value of the difference, Φ_{min}.
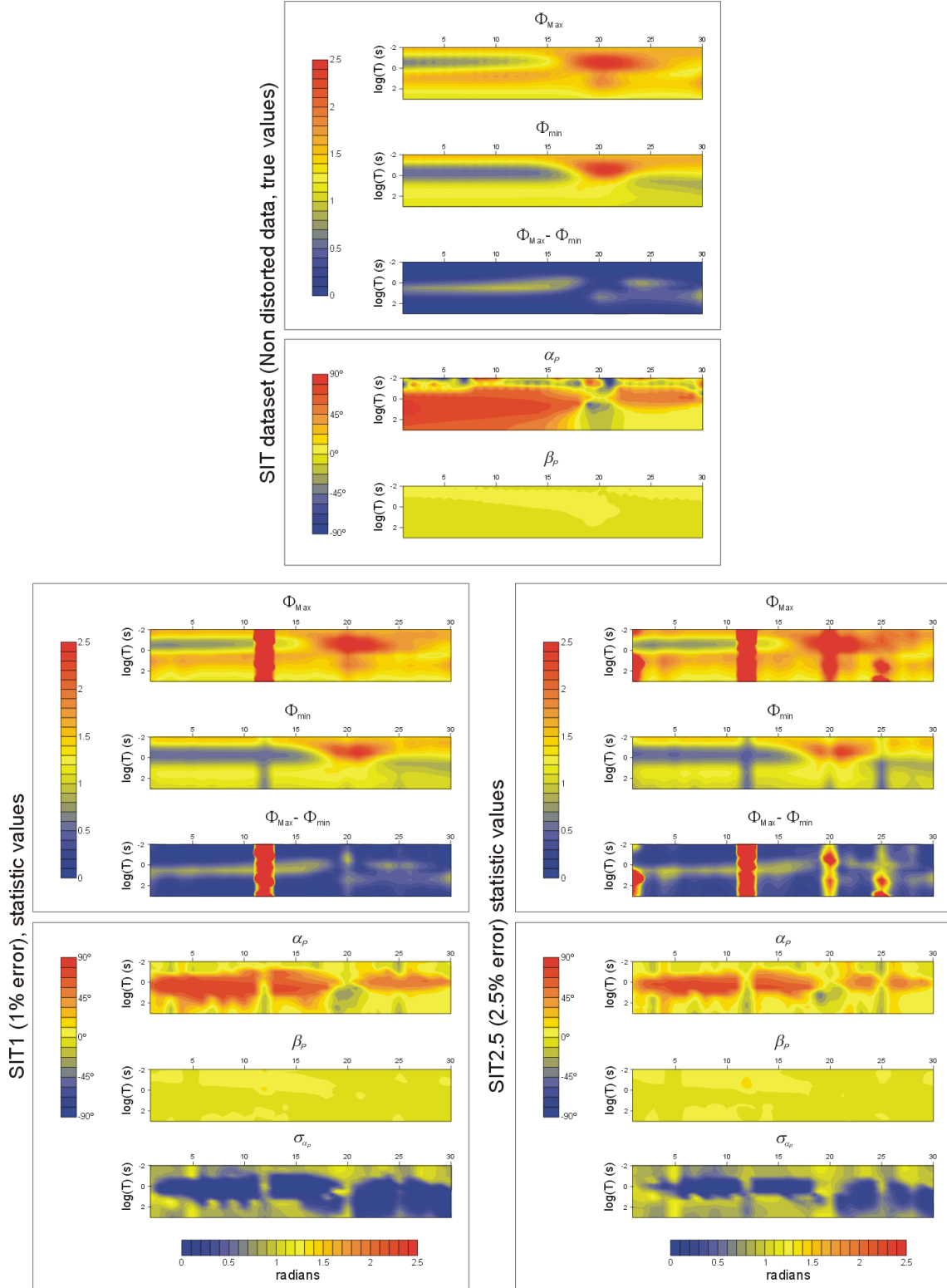
Figure 5.4: Cross sections of the phase tensor parameters corresponding to the three datasets computed from the synthetic model, plotted along the profile for the 11 computed periods. Upper panel: original dataset SIT, without errors or distortion. Lower panels: datasets in which distortion has been applied, and error added. Left: SIT1, with 1% error. Right: SIT2.5, with 2.5% error. The plotted parameters are Φ_{Max}, Φ_{min}, α_P, β_P, Φ_{Max}-Φ_{min} and σ_{α_P} (only for the datasets with errors).

2) The values of angle α_P for SIT1 and SIT2.5, at sites 1 to 15, present significant variations with respect to SIT, especially at long periods (Figure 5.4). Namely, whithout distortion, $\alpha_P \approx 90^o$, whereas for the distorted data $\alpha_P \approx 0^o$- 45°. This difference is explained by incorrect determination of this angle when the difference between Φ_{Max} and Φ_{min} is small. At these sites and periods, σ_{α_P} is greater than Φ_{Max}-Φ_{min}, so a 1D or 3D description of the data is more suitable. At middle periods, σ_{α_P} is small, so α_P is well determined and takes the same values for the original responses as for the two noise levels in the distorted data. At the shortest periods α_P is poorly resolved too, as is indicated by the small difference between Φ_{Max} and Φ_{min}.

As an illustration of how the bias between the statistical and true values affects the determination of angle α_P, Figure 5.5 represents the normalized biases of α_P ($bias_{norm} = \left|(\alpha_{Pstat} - \alpha_{Ptrue})/\alpha_{Ptrue}\right|$) for 1% and 2.5% noise. The areas with the greatest biases correspond to the areas with the largest error values, and these biases are higher for the SIT2.5 dataset. In both datasets, for about 50% of the data the normalised bias is greater than 1. The large bias at site 12 reflects the incorrect determination of α_P when distortion is added, since the regional data does have a well-determined α_P, which is constant at all periods.
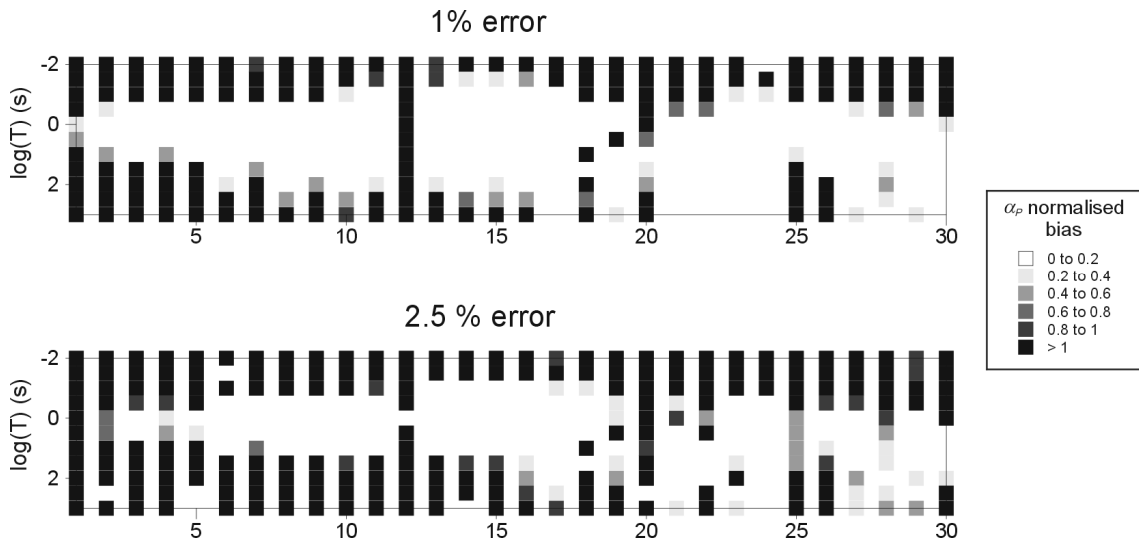
Figure 5.5: Normalised biases of α_P for SIT1 and SIT2.5 datasets. The normalised biased is computed as the difference between the statistical and true values divided by the true value of α_P.

Angle β_P presents values between -4° and 4° for all sites and periods. Both the statistical and true values are similar, and biases between true and statistical values are not significant. The central periods, in the left side of the profile, where β_P has values larger than 3° can be identified as 3D.

The overflows observed at sites 12, 20 and 25 were presumed to be caused by the galvanic distortion added at these sites, given that the noise level is the same for the whole dataset. These sites have shear angle values (φ_s) of 44°, -41° and 49° respectively, the closest to 45° or -45°, compared to the rest of sites.

Figure 5.6 represents, for 1% noise, parameters Φ_{Max}, Φ_{min}, α_P and β_P for each of the 100 realizations generated at T=1 second at sites 12 (φ_s = -44°) and 14 (φ_s = -5°), which have a similar geoelectric structure below but different distortion characteristics. Since the computed parameters should not be affected by distortion, and given the proximity between both sites and the same noise level, one would expect a similar behaviour for these parameters, but site 14 is highly stable whilst 12 is not. This observation reinforces the fact that, under extreme distortion conditions, in addition to noise effects, the phase tensor parameters become unstable and the distortion-invariance property is not valid.
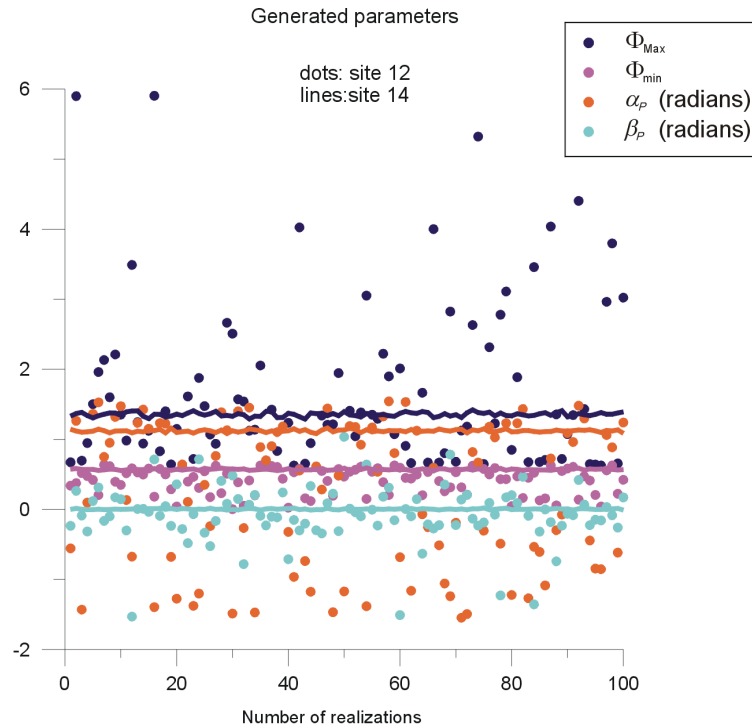
Figure 5.6: Values of phase tensor parameters for the 100 realizations obtained at site 12 and site 14 at T=1 s, with 1% error.

This first dataset allowed the characterization of the phase tensor under different conditions of distortion and noise. The parameters are highly sensitive to the errors and also to the type of dimensionality (e.g. α_P is highly scattered in 1D cases), and the effects of noise and distortion in the data lead to important differences with respect to the regional data.

5.2.2 The COPROD2 dataset: site 85_314

Figure 5.7 displays phase tensor representations of site 85_314 along the registered periods. It follows a simple pattern: circles for periods shorter than 10s, and ellipses with an approximated 60° inclination for the long periods (excluding the longest one). The values of β_P are small (<3°) for the whole range of periods, with the exception of the longest one. Hence, it agrees with the description of the data representing a 1D dimensionality at short periods, 2D at the long ones with a 60° strike and 3D at the longest.
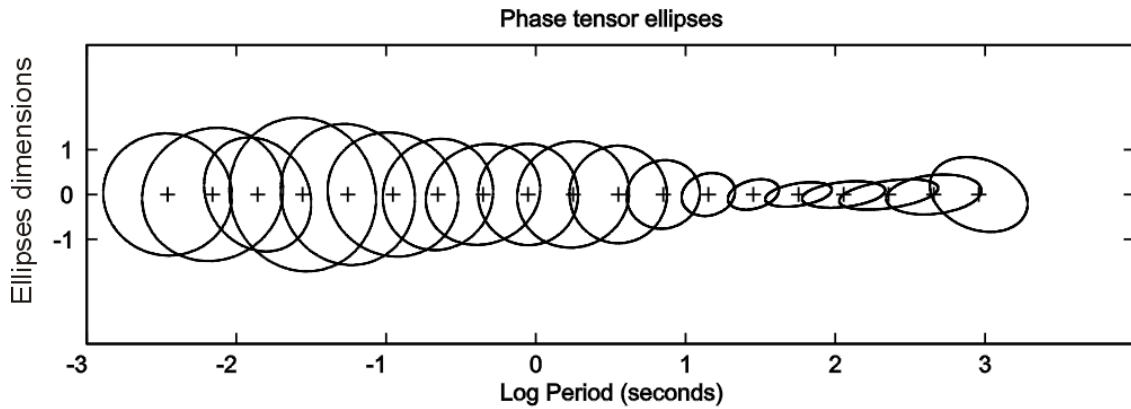
Figure 5.7: Phase tensor ellipses plotted for site 85_314 from COPROD2 dataset, for the different periods registered.

5.2.3 The BC87 dataset

The data corresponding to the BC87 profile was used to compute and analyse the phase tensor general features. Site 4 was also taken to study it in more detail.

Phase tensor parameters and errors were estimated using Random Gaussian Noise generation (as in the synthetic model dataset). No significant differences were found between the true and statistical values.

Phase tensor parameters Φ_{Max}, Φ_{min} were converted into their related phases, φ_{Max} and φ_{min} (equation 2.34). These phases are expressed in the first quadrant, so it must be taken into

account that one of these is in fact φ-180°, such as to agree with a 2D representation. Figure 5.8 presents the cross sections of φ_{Max} and φ_{min}, α_P and β_P. φ_{Max} and φ_{min} have values between 45° and 90°, and their differences (φ_{Max} - φ_{min}) are appreciable, but not too large. On the contrary, the supposed strike direction, given by α_P, changes abruptly for differing periods and from site to site. The angle β_P presents low values, except for long periods in the eastern part of the profile and middle periods in the western part.

In general, the phase tensor related angles are consistent with a 2D behaviour of the data. However, the abrupt changes in angle α_P and the local increases of β_P make it difficult to find a suitable strike direction to make a 2D interpretation of the profile.
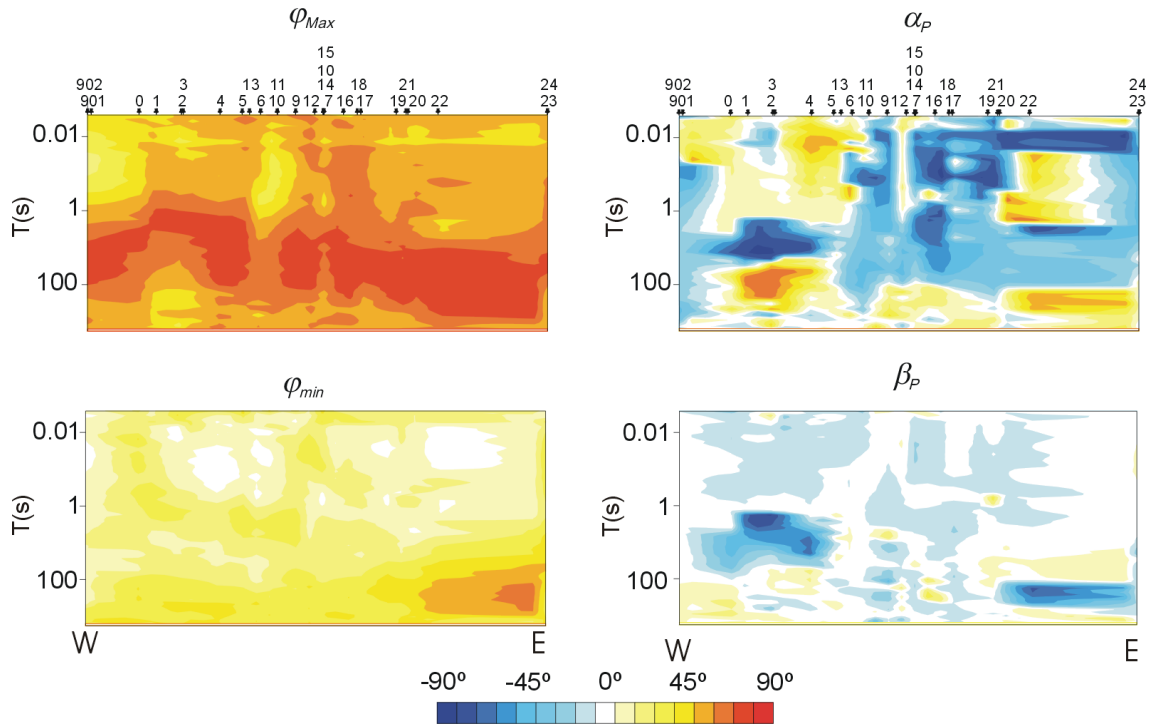
Figure 5.8: Cross sections of phase tensor related angles plotted along BC87 profile and the registered periods. φ_{Max} and φ_{min} are the arctangents of parameters Φ_{Max} and Φ_{min}.

Site 4, located over the Nelson Batholith, was studied in more detail. Figure 5.9 plots the phase tensor ellipses for the range of periods registered together with the direction given by angle α_P. If this direction differs from the maximum axes of the ellipse, a 2D interpretation is not possible, even if Φ_{Max} and Φ_{min} have different values.

Up to 2 s, the major axes of the ellipses coincide with α_P direction, which increases gradually from 45° to almost 90°. Hence, those periods in which the difference between Φ_{Max} and Φ_{min} is not meaningless can be interpreted as 2D (or 3D/2D).

From 2 s to 100 s, the major axes of the ellipses present large values (which mean large values of the phases, close to 90°), with clear divergences between the ellipse orientation and the direction given by α_P. At the longest periods the size of the ellipses decreases and Φ_{Max} and Φ_{min} are still clearly different but their orientation, however, still does not provide the direction of the strike. Consequently, for periods longer than 2s, the data must be treated, in general, as 3D.
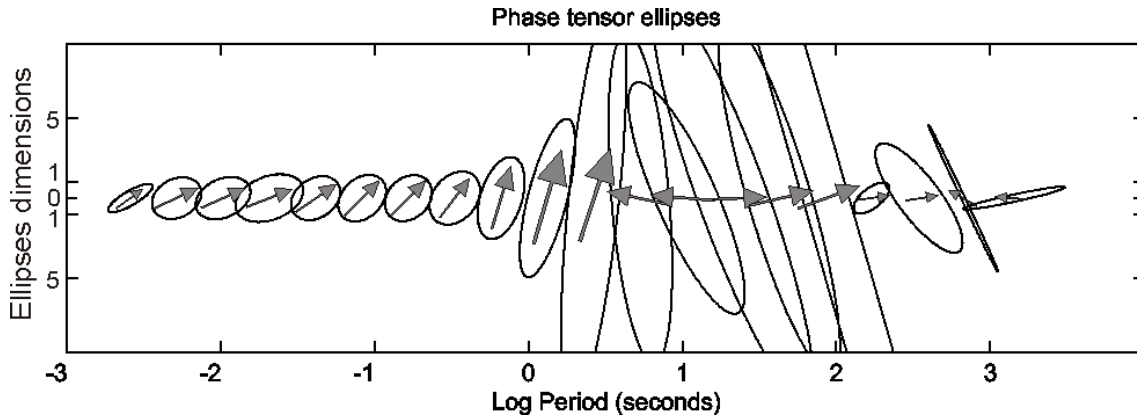
Figure 5.9: Phase tensor ellipses plotted for site 4 from the BC87 dataset for the different periods registered. Arrows indicate the direction given by angle α_P.

Figure 5.10 plots phase tensor angles φ_{Max}, φ_{min}, α_P and β_P with their error bars for site 4. The values of the parameters quantify and reinforce the description provided by the phase tensor representation.

The errors of φ_{Max} and φ_{min} are small, except for periods longer than 100s, although their error bars never cross, so they do not become significant. Errors in the direction angles, α_P and β_P, are small for the shortest periods, in which a 2D strike direction can be defined. These errors become important from T=2s onward, which agrees with a 3D description of the data, without any prevalent strike direction.
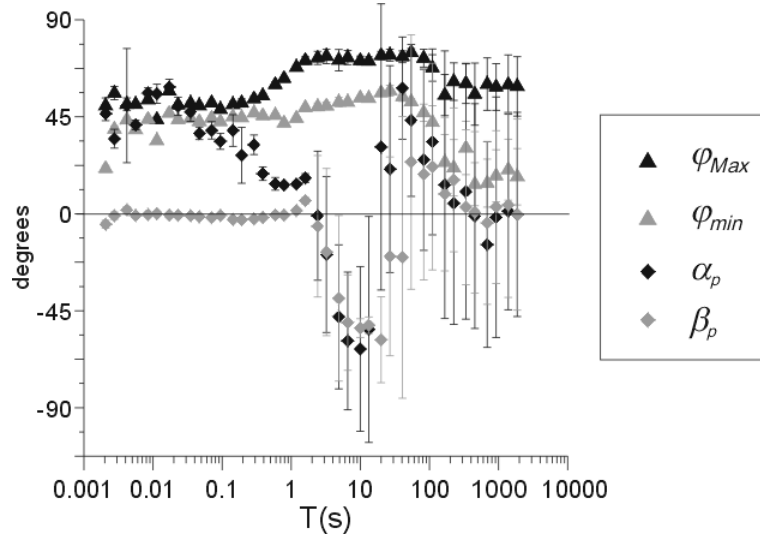
Figure 5.10: Plots of φ_{Max}, φ_{min}, α_P and β_P with their error bars for the registered periods of site 4 from the BC87 dataset.

5.3 Comparison with the WAL Method

The equivalences and differences between the characterisation of the dimensionality from WAL invariants and the phase tensor have already been seen from the theory (section 2.6 and Caldwell *et al.*, 2004) and the examples used.

This section presents the main results of the comparison between the phase tensor and WAL invariants, using the data from section 5.2. This comparison focused on finding new equivalences between both methods and on the determination of the corresponding parameters, under noise and distortion conditions. Another study on the comparison between WAL and the phase tensor can be found in Weaver *et al.* (2003).

For the datasets from the synthetic model, SIT, SIT1 and SIT2.5, WAL and phase tensor parameters and the strike directions obtained from each method were computed and compared.

The cross-sections of Φ_{Max} - Φ_{min} and invariant Q for the SIT dataset (Figure 5.11) show a certain degree of proportionality between both parameters, both dimensionless. A second comparison between φ_{Max} - φ_{min} (the difference between the angles related to Φ_{Max} and Φ_{min}) and invariant Q shows the same values for both parameters (Figure 5.12a), even though φ_{Max} - φ_{min} is an angular magnitude, expressed in radians.

This similarity disappears when distortion is added (Figure 5.12b), since $\varphi_{Max} - \varphi_{min}$ is distortion invariant (with some exceptions due to the overflows caused by some distortion parameters), whereas Q is not invariant under distortion and its value changes.
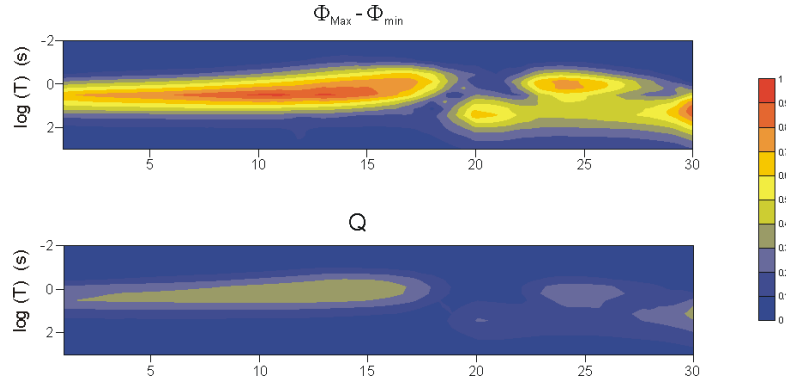
Figure 5.11: Cross-sections of $\Phi_{Max} - \Phi_{min}$ (from the phase tensor) and WAL invariant Q, for the registered periods along the SIT dataset profile.
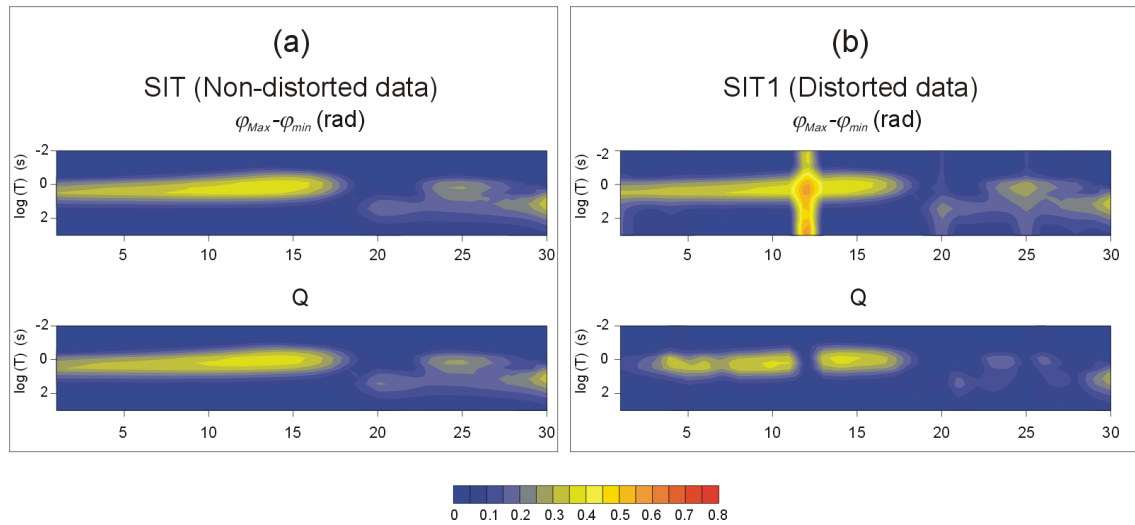
Figure 5.12: Cross-sections of $\varphi_{Max} - \varphi_{min}$ (in radians, from the phase tensor) and WAL invariant Q, for the registered periods. a) SIT dataset (non-distorted data), b) SIT1 dataset (distorted data with 1% error added).

All the examples of section 5.1, to which distortion was added, confirmed this equivalence between Q and $\varphi_{Max} - \varphi_{min}$ for non-distorted data.

For the real data from site 85_314 (COPROD2) and site 4 (BC87) the coincidence and non-coincidence between Q and φ_{Max} - φ_{min}, depending on data being affected of not by distortion, is less clear (Figure 5.13).

Up to 10 s, where according to the WAL and Bahr-Q methods the dimensionality is 1D for site 85_314 and 3D mixed with 3D/2D for site 4 (see Chapter 4, section 4.6), Q and φ_{Max} - φ_{min} have similar values, with the exception of some scattered points for site 85_314 and between 1s and 5s for site 4. For 10s and longer periods (2D at site 85_314 and again 3D mixed with 3D/2D at site 4), the difference between both parameters becomes larger, although at site 85_314 both follow the same trend, whereas at site 4 the differences are more irregular. In the first site, the differences may be attributed to noise effects, whereas in the second, these may be, in fact, due to the distortion.

This coincidence between Q and φ_{Max} - φ_{min} when data are not distorted is an important result, since it opens a new method for identifying galvanic distortion, even in 3D cases. Moreover, it has been tested successfully in synthetic data, where the distortion was important.
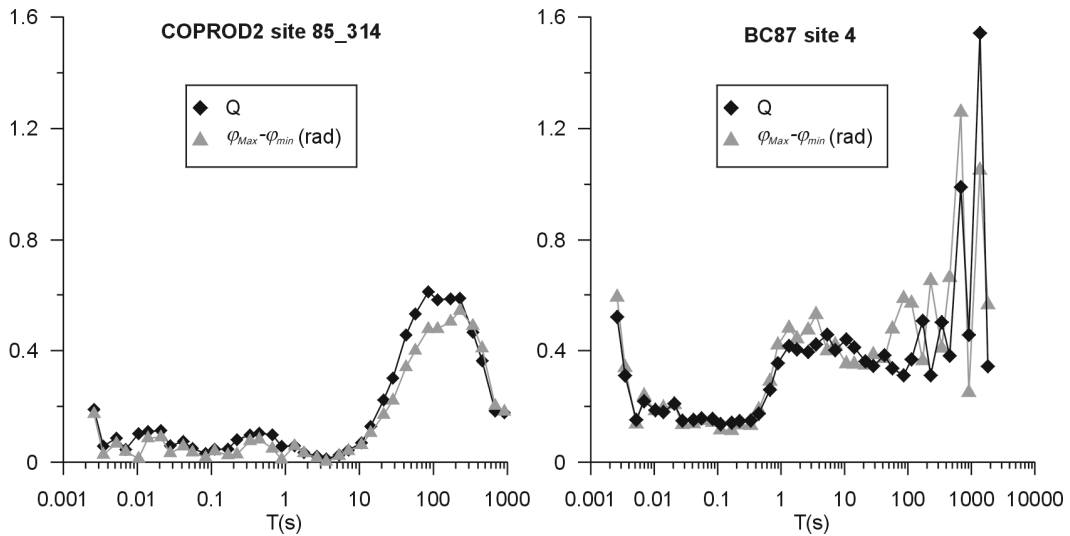
Figure 5.13: Graphical representations of Q invariant (from WAL) and φ_{Max} - φ_{min} for site 85_314 from the COPROD2 dataset and site 4 from the BC87.

In order to compare the determinations of the strike using both approaches, the strike angles were estimated for the SIT1 and SIT2.5 datasets as α_P -β_P from the phase tensor, and θ_3 (chapter 2, equation 2.23) from the WAL method. In both cases Random Gaussian Noise generation was applied. For each dataset, similar values of the strike directions were obtained. The main differences are in the errors, which are larger in the strike directions determined from

WAL parameters. This is a consequence of the different expressions of the strike angles, which leads to different error estimations.

5.4 Comparison with Groom and Bailey Decomposition

A comparison between the phase tensor and Groom and Bailey (G&B decomposition) (Groom and Bailey, 1989) was performed, using site 4 from BC87. Two G&B decompositions of this site are available from Jones *et al.*, 1993.

The first analysis, a) was performed assuming a 2D dimensionality, without distortion. The strike angle obtained is 45° up to 1 s and decreases towards 0° at the longest periods. φ'_{yx} reaches values greater than 90° at the longest periods, and the errors are large (Figure 5.14a).

Analysis b) assumed a 3D/2D dimensionality, with a 60° strike. Both φ'_{xy} and φ'_{yx} phases can be represented in the first quadrant, although a large difference between them is observed at periods from 1s to 10s. Distortion parameters show two different behaviours: twist and shear close to zero from 0.01 to 1s, and increasing to $\theta_t = 20^{o}$ and $\theta_e = -35^{o}$ at the longest periods. Current channelling is important at all periods. According to the errors, which are smaller than in analysis a), a 3D/2D description is more appropriate than a 2D one (Figure 5.14b).

A third analysis c) was performed in this thesis, leaving all parameters and angles free. The strike direction obtained was between -30° and -45° for the short periods (up to 1 s) and around 45° from 1s onward. Twist and shear angles presented sharp variations, particularly the shear. The phases obtained were $\varphi'_{xy} \approx 50^{o}$, and φ'_{yx} varied from -135° (0.01 s) to 90° (1000 s), reaching greater values at the longest periods (Figure 5.14c).

The decomposition obtained from the phase tensor (Figure 5.10) has, up to 2 s, the same phase values as the 2D description given in analysis a), although with different strike directions. For T>2 s, the phase tensor exhibits 3D effects (β_P different from zero). However, for T>10 s, the strike angles are similar to those obtained from analysis a) and c), but not the phases, since those obtained from the phase tensor are arranged in the first quadrant and do not show if the phases are greater than 90°. As it is expected, the phase tensor and G&B decomposition only lead to comparable results when the data can be described as 2D or 3D/2D. Even in these cases, the phase tensor analysis arranges all the phases in the first quadrant, and it is not possible to detect phases outside of the quadrant, as with the G&B analysis.

(a)
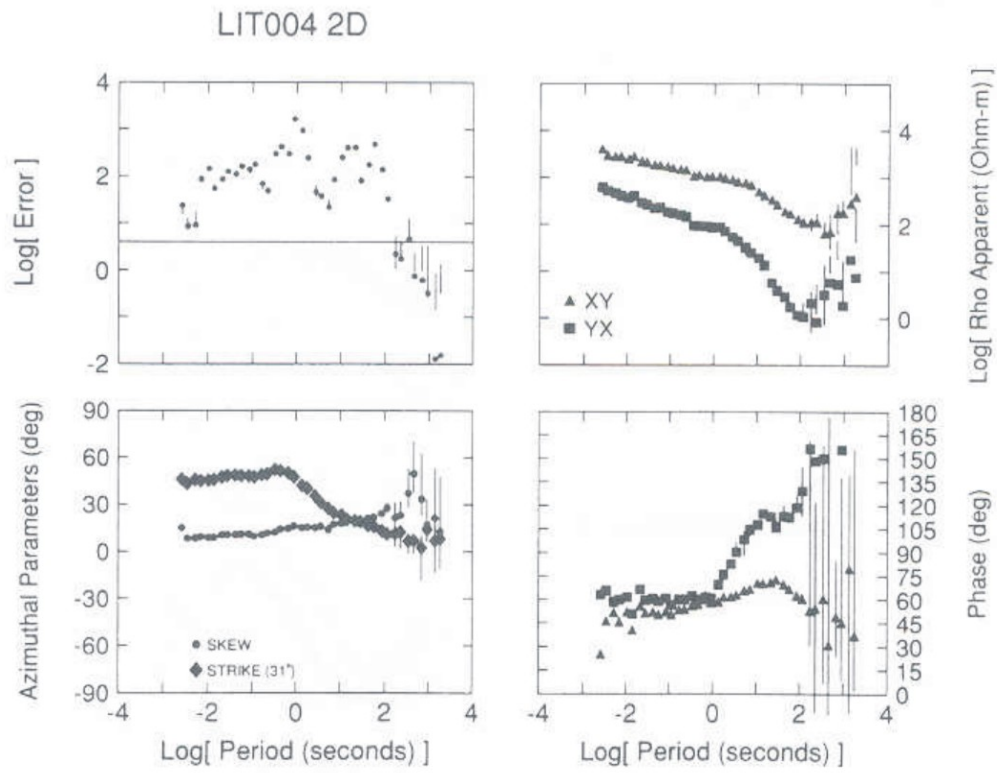
(b)
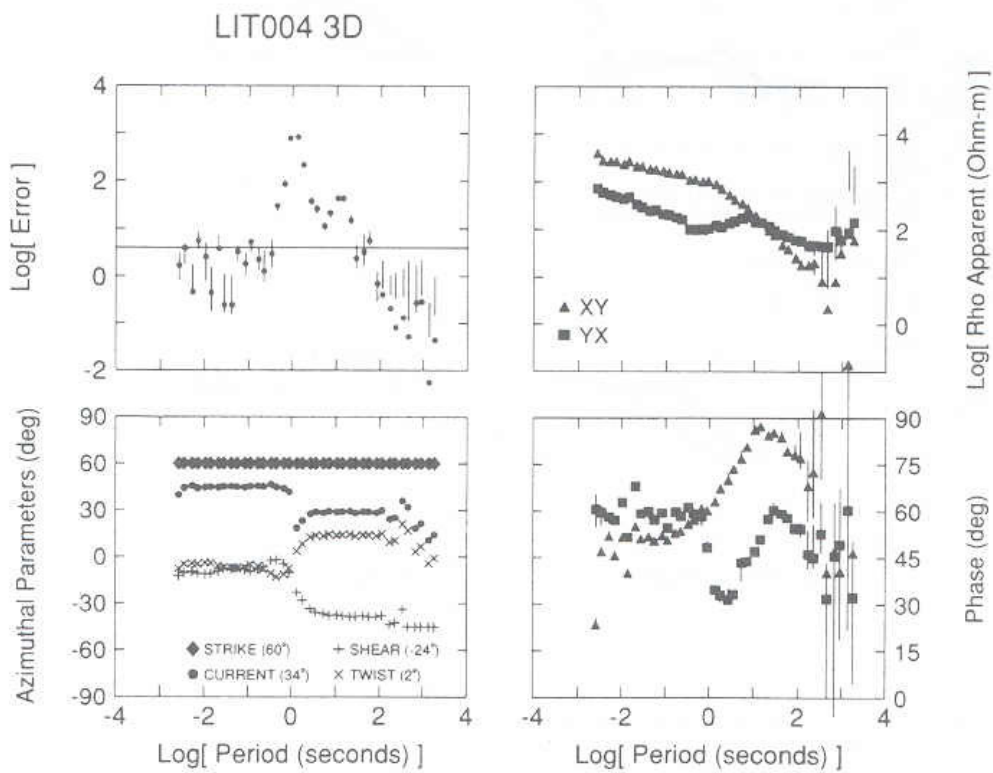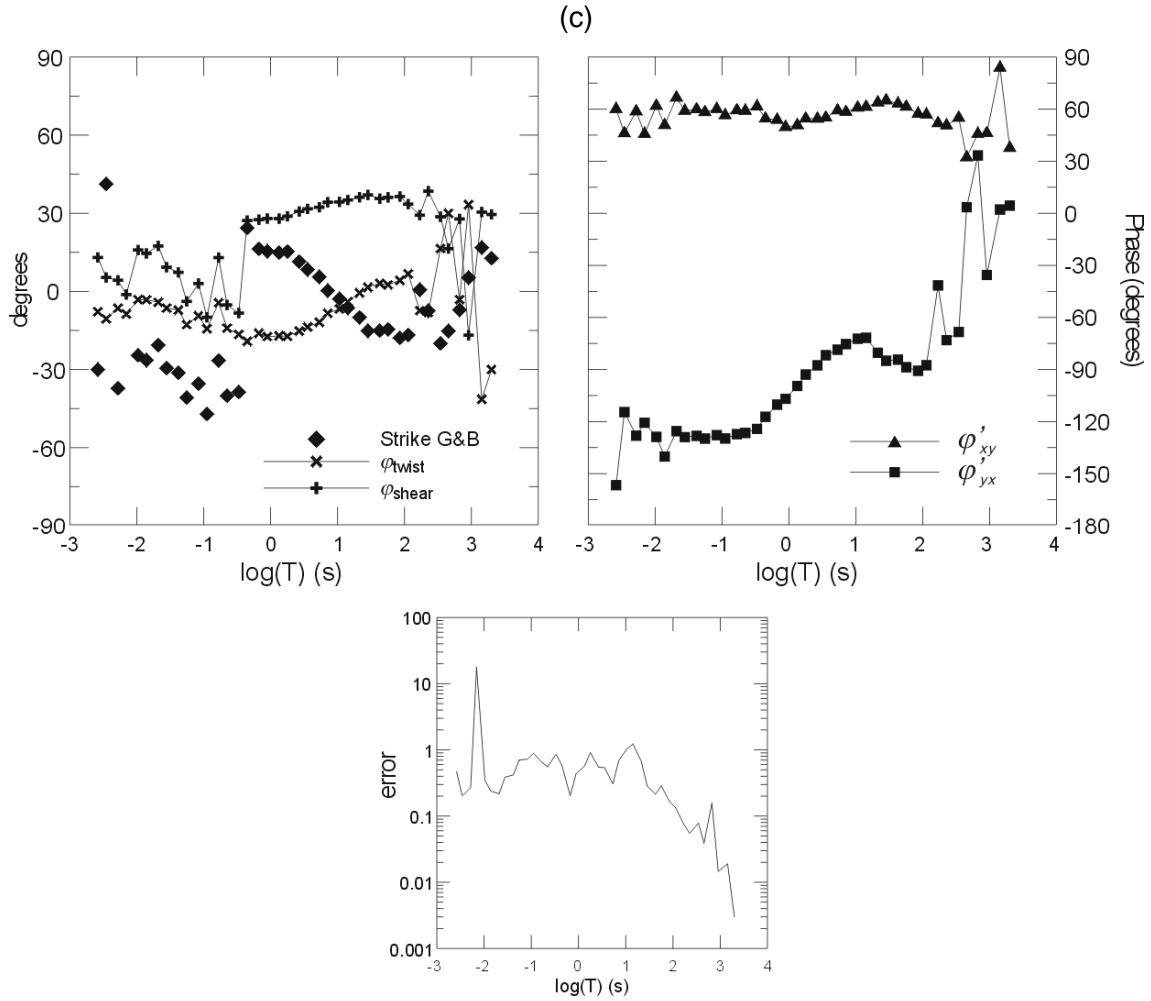
Figure 5.14: Groom and Bailey decomposition parameters using different analysis, corresponding to site 4 from BC87 dataset.   (a): Non-distortion: data rotated to the direction that minimises diagonal components of the MT tensor (Jones *et al.*, 1993). (b): G&B decomposition, allowing galvanic distortion, rotating the data 60° (Jones *et al.*, 1993). (c): G&B decomposition, allowing all parameters free.

5.5 Fitting the Phase Tensor Data to a 2D Model

This section presents an approach to obtain a 2D description of the data, by fitting the measured phase tensor to that corresponding to a 2D model. Contrary to the Multisite Multifrequency Strike code (Strike, McNeice and Jones, 2001), which uses the MT tensor, the proposed approach does not provide distortion decomposition, since the phase tensor does not include this information.

The process of fitting the phase tensor observed data to a 2D phase tensor model was done by minimizing a misfit function between the observed and model parameters of the phase tensor:

$$\gamma^2 = \sum_{k=1}^{N \cdot S} \left(\sum_{i=1}^{4} \left(\frac{\Phi_{iobs} - \Phi_{i\,\mathrm{mod}}}{\sigma_i} \right)^2 \right), \tag{5.1}$$

where N·S is the number of phase tensors included in the process: N, the number of frequencies and S, the number of sites.

$\Phi_{i\,obs}$ and σ_i (i=1 to 4) are the 4 observed components of the phase tensor and their standard deviations.

$\Phi_{i\,\mathrm{mod}}$ (i=1 to 4) are the components that one should obtain for a 2D description of the data, which make a total of 2·N·S+M parameters: N·S·φ_{Max}, N·S·φ_{min} and M·α (different strike directions considered):

$$\Phi_{1\mathrm{mod}} = \Phi_{Max} \cdot \cos^2 \alpha + \Phi_{min} \cdot \sin^2 \alpha, \tag{5.2}$$

$$\Phi_{2\mathrm{mod}} = \Phi_{3\mathrm{mod}} = \left(-\Phi_{Max} + \Phi_{min} \right) \cdot \cos \alpha \cdot \sin \alpha, \tag{5.3}$$

$$\Phi_{4\mathrm{mod}} = \Phi_{Max} \cdot \sin^2 \alpha + \Phi_{min} \cdot \cos^2 \alpha. \tag{5.4}$$

Thus, in the case that each site and each frequency could have a different strike direction, the fitting process would imply N·S different functions, each with 4 data and 3 parameters to fit. If all frequencies in every site had a common strike, there would be S different functions to fit, each one with 4·N data and 2·N+1 parameters to fit. Finally, if a common strike was considered for all data, the fitting would use 4·N·S data and there would be 2·N·S+1 parameters to fit.

The minimisation method employed is the same used in the Strike code (McNeice and Jones, 2001), using a Taylor expansion of the γ^2 function with the Jacobian and Hessian matrixes for the 1st and 2nd derivatives.

Furthermore, the fitting process also needs a set of initial parameters, as well as a convergence parameter or, alternatively, a maximum number of iterations to stop the minimisation.

The code created was tested using a subset of the BC87 dataset, referred to as line BC87c. It includes 10 of the western sites, 902, 0, 1, 3, 4, 5, 006, 11, 15 and 17. This subset was chosen because the information from G&B decomposition, using the Strike code with a strike direction of 18º for the period range from 0.01 to 10s, was available for comparison (Jones, pers. comm.). The hypothetical strike values, α_P-β_P, obtained from the phase tensor, compared to the 18º of the G&B decomposition, are displayed in (Figure 5.15), showing broad variations.
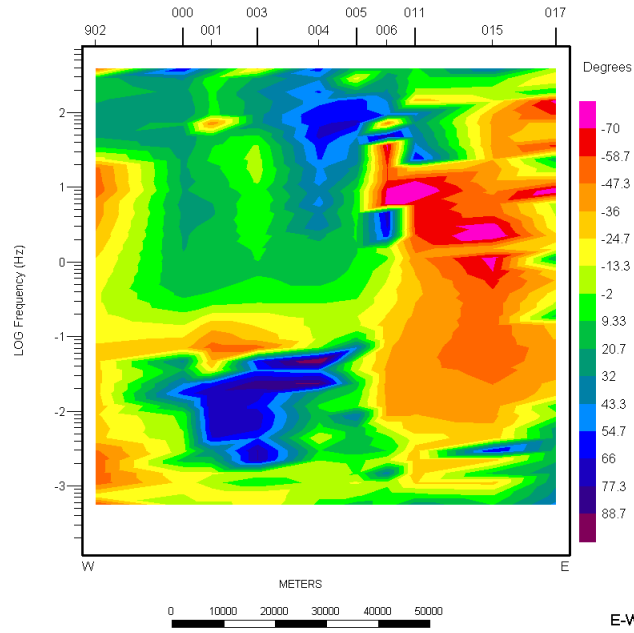
Figure 5.15: α_P-β_P directions obtained along line BC87c from the phase tensor data. ■: 18° (Strike used in the Groom and Bailey decomposition).

A first test was done by trying to adjust all frequencies in each site to the same strike direction. Hence, one function was fitted for each site, with 2·N +1 parameters each. The maximum number of iterations allowed was 100, otherwise, the process stopped when the change in the misfit function between two iterations was less than 10^{-10}. A set of initial parameters was also defined. In general, the final result was independent of the initial parameters. However, in some cases, the final parameters were the same as the initial ones, and any parameter led to the same value of the misfit function, which was notably high. This means that these data cannot, in fact, be adjusted to a 2D model with a unique strike direction. Combining the frequencies into smaller groups made the misfit function smaller, although there were some groups for which the misfit function did not decrease and the iterative process stopped after the 100 iterations.

Three different fitting processes were performed for the BC87c line. The results from site 001, compared to G&B decomposition with an 18° strike, show the following:

1) All parameters free: different strike for every frequency. The aim of this inversion was to check if, even without constraints, there is a predominant strike direction in the final parameters obtained. The strike directions obtained present smooth variations around 0°, but clearly different to the 18° obtained from G&B decomposition. The corresponding phases are similar to those of G&B for the shorter periods. The misfit function is large and converges after 10 iterations.

2) A common strike for every 4 frequencies. The strike directions and phases obtained are similar to those of misfit 1), where these changed smoothly with the period.

3) A common strike for all frequencies. The strike direction obtained was approximately -13°, and the phases similar to 1) and 2).

Although the three inversions led to similar results, these differ significantly from the results of the Groom and Bailey decomposition. For the rest of the sites in this dataset, it was observed that, even if the strike pattern is very different in 1), 2) and 3), the phases are similar, and different to those obtained with Groom and Bailey decomposition.

This small variation of the phases in the strike direction would indicate one-dimensionality, which is not the case. Working only with the phases, and not with the resistivities, is an important limitation. Further tests and research on this minimisation process are necessary to lead to satisfactory results.

5.6 Conclusions

A summary of the phase tensor obtained from synthetic MT tensors has been presented to illustrate its features and graphical representation for different types of dimensionality.

The phase tensors computed from the responses of a synthetic model showed the effects of noise and distortion: the errors lead to wrong interpretations of the dimensionality, and, under extreme distortion conditions, the phase tensor is not distortion-invariant.

The comparison between the phase tensor parameters and WAL invariants allowed the identification of a relationship between φ_{Max} - φ_{min} (difference between the maximum and minimum phases obtained from the phase tensor) and the WAL invariant Q. These magnitudes have the same values when data are not affected by distortion, which introduces a new way to identify distortion even if data are 3D. With regard to the strike angles computed from the phase tensor and from the WAL method using the same data, the errors of the latter are greater.

A comparison of the phases and strike directions obtained from the phase tensor and from the Groom and Bailey decomposition showed significant differences due to the hypothesis of 2D dimensionality that applies in the second, and the use of only the phases information in the phase tensor.

Finally, a code was developed to fit the phase tensor data to a 2D model. The results were quite inconsistent, however, because of few data to work with: 4N data to fit 2N+1 parameters, compared to Groom and Bailey, 8N data and 4N+3 parameters.

Part III. Magnetotelluric Study of the Central Betics Crustal Structure

Chapter 6: Geological and Geophysical Settings

This chapter presents the main geological description and geophysical features of the Betic Chain and the Alboran Basin, with the further purpose of constraining the interpretation of the magnetotelluric data recorded in the Central part of the Betics.

6.1 Geological Setting

The Betic Chain (Betic Cordillera or Betics) (Figure 6.1) is a WSW-ENE oriented Alpine Chain, located in the western end of the Mediterranean. It extends along the southern part of the Iberian Peninsula from the Gulf of Cádiz to Cape de la Nao and continues northeastward towards the Balearic Islands.

The Betics, together with the African Rif Chain, comprise an arc shaped orogenic belt, surrounding the present Alboran Basin, which was formed as a consequence of the convergence between the African and Iberian plates since the Late Cretaceous (60 My) (Platt and Vissers, 1989; García-Dueñas *et al.*, 1992; Azañón and Crespo-Blanc, 2000).

The formation of this arc and its inner Alboran Basin occurred in three main phases:

a) A Late Triassic – mid-Cretaceous extensional stage, related to the significant African plate left-lateral motion relative to a fixed Iberia (Dewey *et al.*, 1973; Rosenbaum *et al.*, 2002; Schettino and Scotese, 2002). During this stage, the area in question was affected by rifting processes that resulted, from the Liassic, to the Tethyan Oceanic accretion between the Iberian and African plates (García-Hernández *et al.*, 1980; Favre and Stampfli, 1992).

137

Figure 6.1: Simplified tectonic map of the Western Mediterranean region with the main Alpine compressive chains and Neogene extensional basins (Roca, 2004).

b) A Late Cretaceous-Middle Oligocene stage, characterised by the beginning of a relatively fast NE-SW to N-S convergence between Iberia, Eurasia and Africa (Dewey *et al.*, 1989; Mazzoli and Helman, 1994; Rosenbaum *et al.*, 2002). This convergence resulted in the development of an orogen from subduction and orogenic wedging between Africa and Iberia, which constituted what is known as the Alboran Domain (Balanyá and García-Dueñas, 1987).

c) An Oligocene-Miocene stage of strong tectonic activity which developed during a slowing of the N-S convergence between Eurasia and Africa (Dewey *et al.*, 1989; Mazzoli and Helman, 1994). During this stage, back-arc extension processes related to N-dipping subduction of the African slab below the Alboran Domain (Rehault *et al.*, 1984; Frizon de Lamotte *et al.*, 2004) resulted in the opening of the Alboran Basin and the outward migration (mainly to the West) of the Gibraltar Thrust (outer limit of the Alboran Domain). This migration thrust, during the Miocene, collided with the passive paleomargins of Africa and Iberia, inducing the development of fold-and-thrust belts (Rif and Betic chains) in the sedimentary materials settled during the former stage (Balanyá and García-Dueñas, 1987). At the same time, the thrust belt previously formed in the Alboran Domain continued in an extensive regime with the formation of low angle faults, which lead to a 13 km - 20 km crustal thinning of the Alboran basin.

In relation to this geological evolution, the Betic Chain has been traditionally divided in two stratigraphically and structurally well-differentiated zones: the External Zone and the Internal Zone (Figure 6.2).
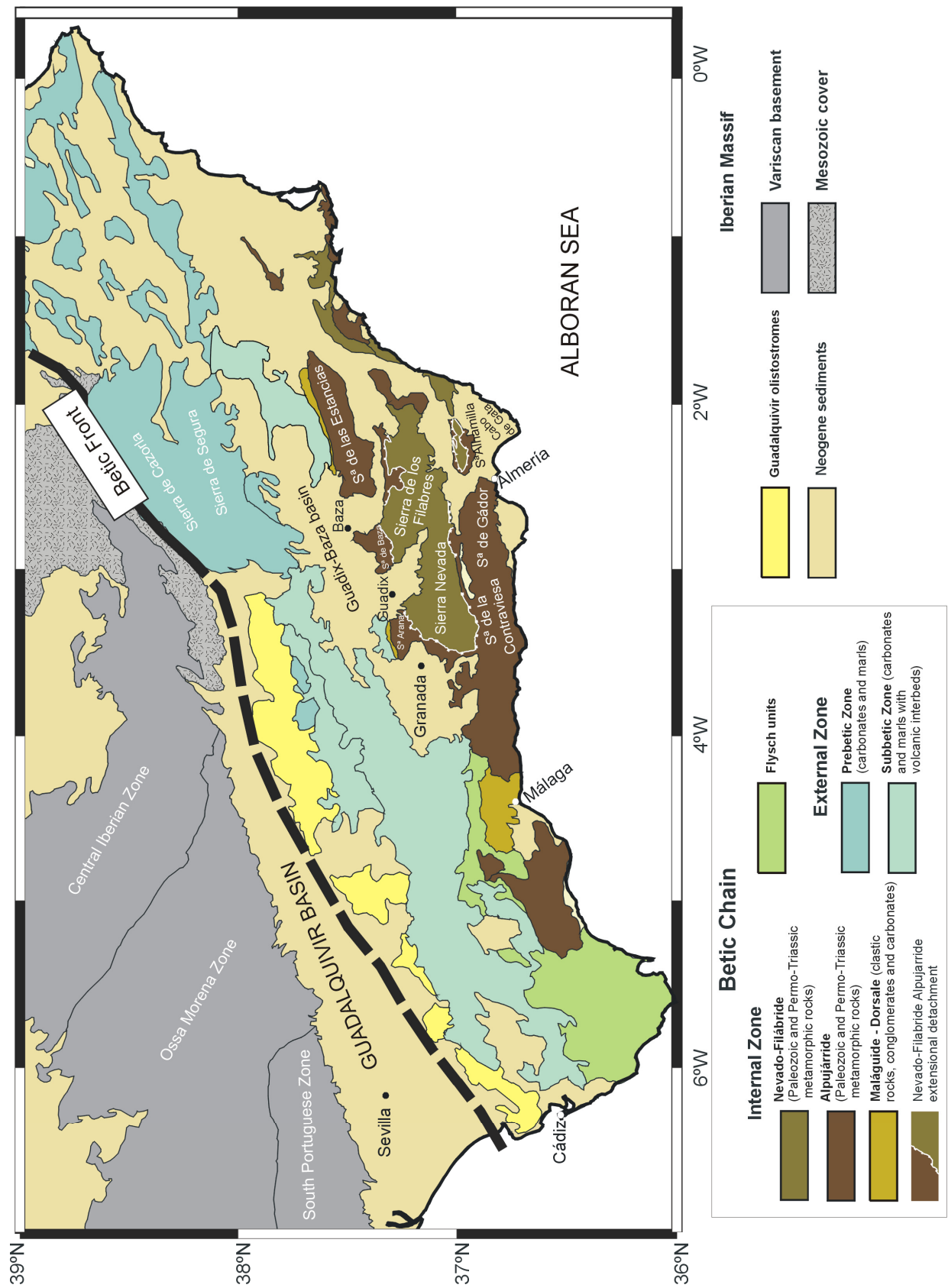
Figure 6.2: Geological sketch map of the Betic Chain.

The **External Zone** is derived from the Mesozoic sedimentary cover of the South Iberian paleomargin of the Tethys (García-Hernández *et al.*, 1980) and crops out in the Northwest of the Chain. It comprises the *Prebetic* and *Subbetic* zones, both formed by non-metamorphosed rocks (mainly carbonates and marls) of Triassic to Neogene age. The *Prebetic Zone* is characterised by shallow-water facies, as opposed to the *Subbetic Zone*, where pelagic facies prevail with some mafic volcanic and subvolcanic interbeds. Both *Prebetic* and *Subbetic* zones are defined as an ENE to NE-trending fold-and-thrust belt with the main transport direction towards the NNW.

Between the External and Internal zones, are the *Flysch units*. These are deformed deep-water sediments, Cretaceous to Miocene in age, which are interpreted as the former sedimentary cover at the paleomargins of the westernmost part of the Tethys Ocean. Hence, the *Flysch units* are structurally below the Internal Zone, with some exceptions, as observed near Ronda and Antequera (Azañón *et al.*, 2002; Frizon de Lamotte *et al.*, 2004).

The **Internal Zone**, in the Southeast, is formed by metamorphic rocks from the Paleozoic and locally from the Mesozoic belonging to the Alboran Domain (Balanyá and García-Dueñas, 1987). The interior structure of the Internal Zone is highly complex, with several stacked thrust sheets emplaced before the Miocene that were affected and cut by low angle normal faults during the latest Oligocene-Miocene opening of the Alboran Basin. These extensional faults determine the present-day structure of the Internal Zone and are associated with the development of several intramontane basins filled with continental and marine Neogene and Quaternary sediments (Sanz de Galdeano and Vera, 1992). The innermost of these basins (e.g., Cabo de Gata) include widespread calc-alkaline Neogene volcanic rocks (López Ruiz *et al.*, 2004). The whole area is deformed and uplifted due to Late Tortonian E-W folding. As a consequence, the lowest sequence materials crop out in the cores of the anticlines (Azañón *et al.*, 2002).

According to their stratigraphic signatures and metamorphic conditions, the stacked thrust sheets of the Internal Zone have been grouped into three nappe complexes, separated by major low angle faults. From lower to upper, these nappes are: the Nevado-Filábride complex, the Alpujárride complex and the Maláguide-Dorsale (Figure 6.3).

The *Nevado-Filábride Complex* is the lowest metamorphic complex and crops out in the Sierra Nevada, Sierra de los Filabres and Sierra de Alhamilla. It consists of three major thrust units (García-Dueñas *et al.*, 1988) containing a thick Paleozoic graphitic schist and quarzite series, Permo-Triassic metapelites and metapsammites and a calcite and dolomite marble formation, Triassic to Cretaceous (?) in age. All rocks of this complex were affected by high pressure – low temperature (HP-LT) metamorphic conditions (Monié *et al.*, 1991).

The *Alpujárride Complex* overthrusts the Nevado-Filábride, although its present boundary corresponds to a Serravallian to Early Tortonian extensional detachment. This

complex is also mainly made up of Paleozoic schists, graphitic micaschists and quartzites, Permo-Triassic metapelites and metapsammites, and calcite and dolomite marbles, Middle to Late Triassic in age (Braga and Martín, 1987; Azañón and Crespo-Blanc, 2000). In the western Betics, this complex includes slices of peridotites and granulites representative of sub-continental lithospheric mantle (Ronda massif). All these rocks were affected by low temperature and medium-high pressure metamorphic conditions during the Paleogene and were later deformed by folds and a penetrative foliation.

The *Maláguide-Dorsale Complex* belongs to the uppermost unit. It contains Paleozoic sedimentary clastic rocks, Middle Triassic continental red conglomerates and an upper succession of carbonate rocks, Middle Triassic to Paleogene in age. The Paleozoic rocks retain Variscan orogenic features (folding and low-grade metamorphic foliation), whereas its Mesozoic to Paleogene cover did not suffer pervasive deformation nor metamorphism (Azañón *et al.*, 2002).

The geometry of the boundary between the Internal and External zones (IEZB) varies from West to East (Frizon de Lamotte *et al.*, 2004). In the western part, the Internal Zone thrusts over the Subbetic zone and the Flysch units (e.g. Platt *et al.*, 2003). In the central and Eastern Betics, the Internal Zone structurally crops out below the Subbetic zone, which is interpreted as a wedge-shaped indentor (Banks and Warburton, 1991; Platt *et al.*, 2003).
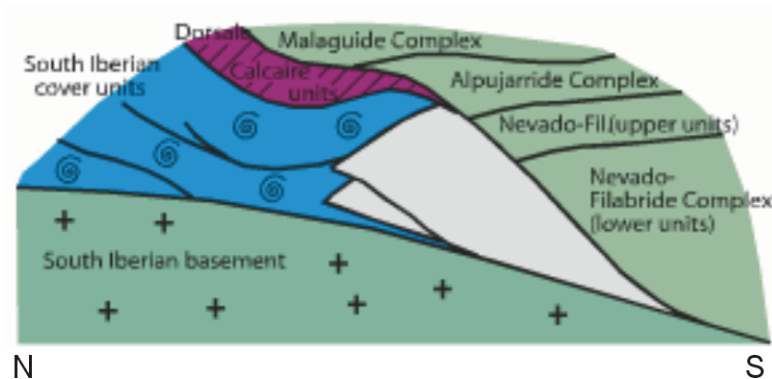
Figure 6.3: Sketch of the relationships between the Internal and External (South Iberian cover) zone units and the Iberian Massif basement in the Central Betics. The scheme proposed is a hybrid solution between the different geometries from West to East. (Modified from Frizon de Lamotte, 2004 with data from Navarro-Vilá and García-Dueñas, 1980 and Balanyá, 1991).

Both Internal and External zones of the Betic Chain overthrust (e.g. Figure 6.3) the Iberian Massif or Iberian Meseta, which near the Betic Chain is overlaid by the Neogene sediments of the Guadalquivir Basin. This basin belongs to the northern foreland basin of the

Betic Chain and is elongated ENE-WSW. It is filled with marine sediments from the Early Miocene up to the present ages (Fernàndez *et al.*, 1998a).

Beneath and North of the Guadalquivir Basin there are Paleozoic and Precambrian rocks of the Iberian Massif. This massif belongs to a portion of the Variscan orogen, formed by sedimentary and volcanic rocks strongly deformed and metamorphosed during the Late Paleozoic. Close to the Betics, it is divided into three NW-SE directed tectonic units with significant stratigraphic and structural features. From NE to SW, these are (Figure 6.2):

- The Central Iberian Zone (CIB), formed by Precambrian and Paleozoic rocks affected by a variable degree of metamorphism with large granitic and granitoid intrusions.

- The Ossa Morena Zone (OMZ), made up of Precambrian to lower Paleozoic sediments, also with a variable degree of metamorphism, and granitoid intrusions.

- The South Portuguese Zone (SPZ), formed by middle to upper Paleozoic rocks, with important sulphur deposits.

The contact between SPZ and OMZ is interpreted as a suture, with basic igneous rock outcrops of oceanic affinity (Pérez-Estaún and Bea, 2004; Ábalos *et al.*, 2002).

6.1.1 Geodynamic Models of the Betic-Alboran-Rif Region

Nowadays it is accepted that the geodynamic evolution of the Betic-Alboran-Rif (BAR) region includes a stage of subduction and orogenic wedging of the Alboran domain, which occurred in an almost constant position; followed by a stage of compression and thrusting along the Gibraltar Arc and coeval extensional opening of the Alboran Basin. However there are two open geodynamic problems in which several hypotheses have been proposed. The first problem is on the state of the initial subduction (stage b), page 132). The second is on the nature of the coeval extension and compression.

With regard to the first problem, two main models have been proposed (Frizon de Lamotte, 2004), to explain the timing of high-pressure events and metamorphic stacking. The first one (e.g. Doglioni *et al.*, 1999) proposes two types of subduction, which acted successively: first, an E to S dipping subduction from the Late Cretaceous to Early Oligocene, which closed a Betic ocean; and a second W to N dipping subduction of the Appeninic-Maghrebian system obliterating the Flysch units from Late Oligocene to Early Miocene (Figure 6.4). The second model suggests a N-dipping subduction which produced a bi-vergent wedge and its progressive roll-back (Jolivet and Faccenna, 2000).
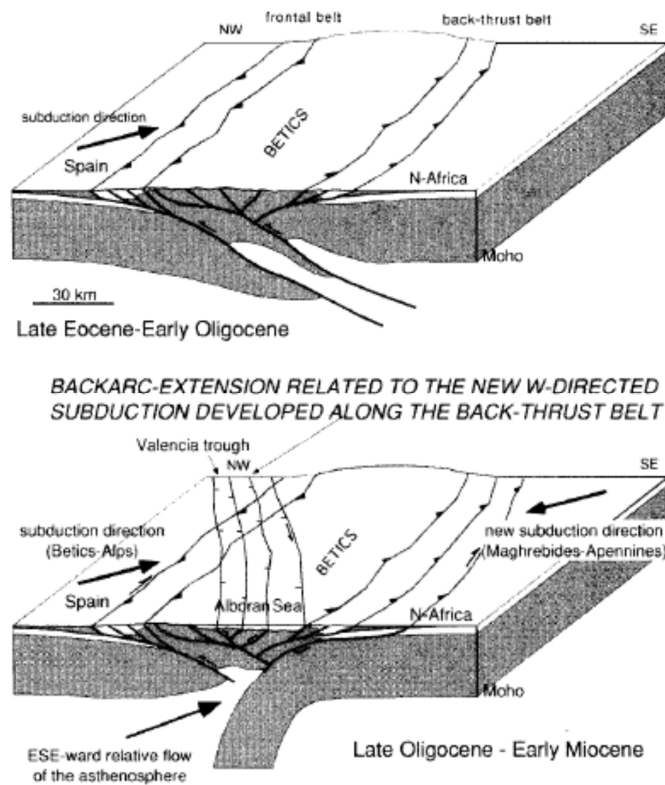
Figure 6.4: Sketch of the superposition of two subduction modes in the formation of the Betic-Gibraltar arc, according to Doglioni *et al.* (1999).

In relation to the coeval thrusting and extension in the BAR region, three main models have been proposed, the last one being the most widely accepted (Figure 6.5):

a) Convective removal of a thickened lithosphere (Platt and Vissers, 1989).

b) Gravitational collapse of a thickened lithosphere (Seber *et al.*, 1996).

c) Westward to southward rollback of an eastward-northward dipping subduction of the African slab that generated back arc extension, which that migrated westward (Royden, 1993; Lonergan and White, 1997; Gutsher *et al.*, 2002).
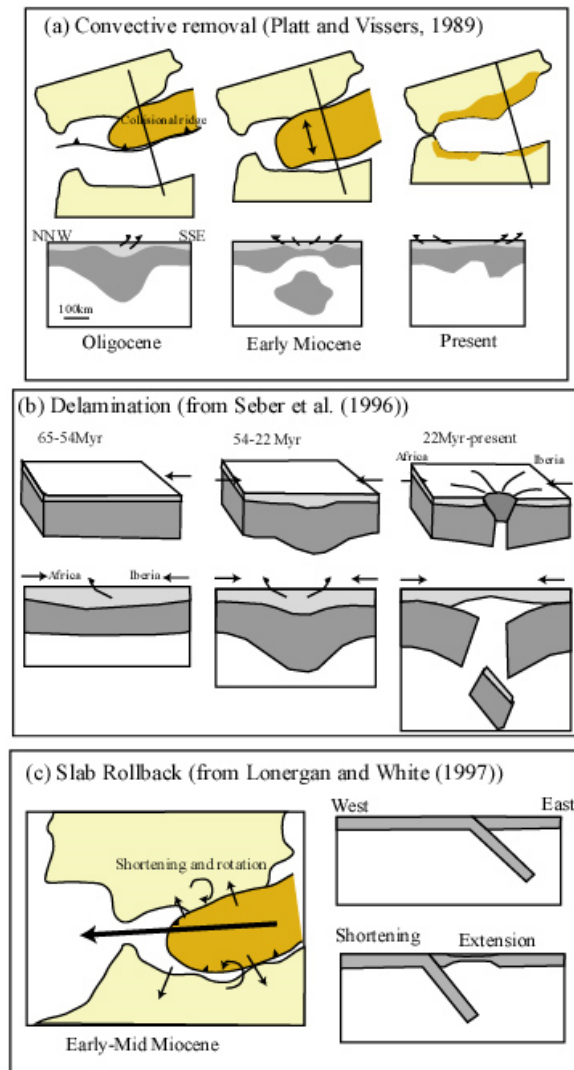
Figure 6.5: Main tectonic models proposed to explain the opening of the Alboran Basin and coeval thrusting and extension along the Gibraltar Arc (Calvert *et al.*, 2000)

6.2 Geophysical Knowledge of the Central Betic Chain

Within this geodynamic framework, as reviewed above, a significant number of geophysical studies performed show that the crustal and lithospheric structure of the Betics is highly complex and difficult to characterise. Thus, the geophysical studies carried out, including gravimetry, magnetism, seismic refraction, reflection and tomography, heat flow and magnetotellurics, have lead to different interpretations for the deep structure of the central Betic Chain.

In the following sections, the main geophysical results and interpretations are presented to summarise the present knowledge of the whole Central Betic crust and upper mantle structures.

6.2.1 Gravimetry

Maps of Bouguer gravity anomalies in the Betics and the Alboran Sea (IGN, 1976; Casas and Carbó, 1990) show a minimum below the Guadiz-Baza basin (-150 mGal), with an ENE-WSW orientation (red area in Figure 6.6), and maximum values of 100 mGal and higher below the Alboran Sea. In the eastern part of the Betics, the gradient between these minimum and maximum values is smooth whereas in the central and western parts this gradient is more abrupt. Towards the North of the minimum, the anomaly increases gradually until reaching values of about –50 mGal, which are common in the Iberian Massif. More locally, positive anomalies are located North of Malaga.

With the exception of these last anomalies, which have been associated with the presence of peridotitic bodies, gravimetric data allow the characterisation of the variations in crustal thickness in the Betics area. Hence, these data indicate a crustal thickening from the Iberian Massif towards the Internal Betics, then a crustal thinning towards the Alboran Sea. It should be also noted that the minimum anomaly values, corresponding to a maximum in crustal thickness (40 km - 45 km), are located in the Guadix-Baza basin and not in Sierra Nevada, which suggests the lack of a significant root below the highest altitudes of the Betics.
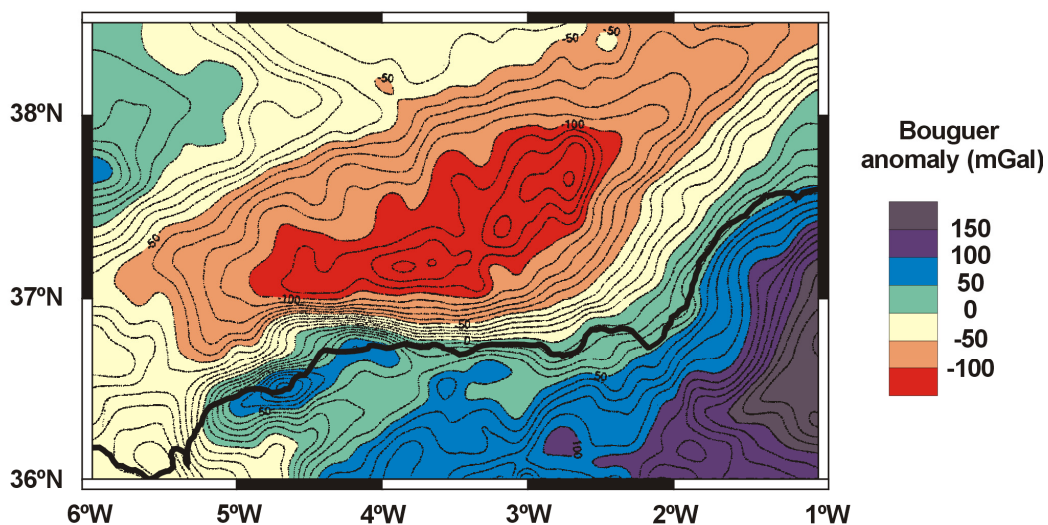
Figure 6.6: Bouguer gravity anomalies map of a Southern sector of the Betics (modified from Torné and Banda, 1992).

6.2.2 Magnetism

The southeastern sector of the 1:1000000 aeromagnetic anomaly map of Spain (Figure 6.7) (Ardizone *et al.*, 1989) shows that in the External Zone the magnetic anomalies are controlled by the crustal structure and not by mesozoic and cenozoic sediments. This crust presents a Variscan structure, which is a continuation of Iberian Massif outcrop materials. For the particular case of the intense NW-SE anomalies that cross from the Iberian Massif to the External Zone, these have been interpreted as igneous rock bodies that outcrop in the Ossa Morena zone, which would continue below the External zone, up to the boundary between the Internal and External zones (Galindo-Zaldívar *et al.*, 1997; Bohoyo *et al.*, 2000). In the Internal Zone, aeromagnetic anomalies are more localised, or have an EW to ENE-WSW orientation. Among these, an ENE-WSW directed anomaly (70 nT and 15 km – 20 km dipole length) is located, east of Guadix, in the Sierra de los Filabres. It was modelled as being caused by Fe-mineralizations in joints of the Nevado-Filabride metamorphic rocks, up to 10 km depth, with a susceptibility value of $\chi=0.005$ (SI) (Galindo-Zaldívar *et al.*, 1997). Other local anomalies are found above the Ronda peridotitic bodies and in the Cabo de Gata volcanic zone.
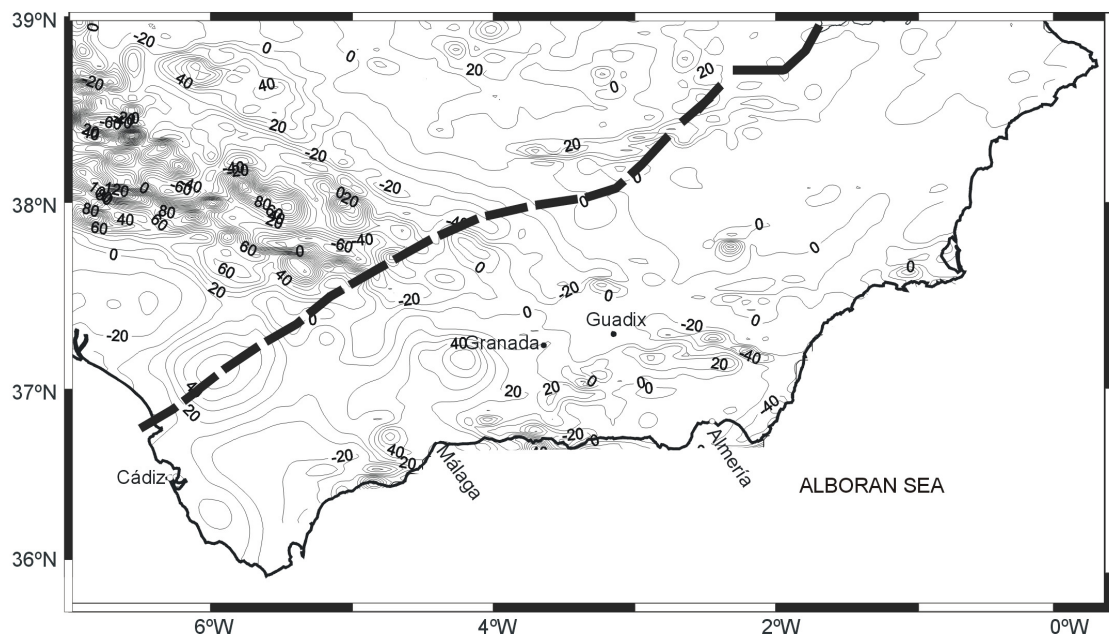
Figure 6.7: Total field magnetic anomalies map (data from Ardizone *et al.*, 1989) of the Betics and southwestern sector of Iberian Massif. Isomagnetic values in nT.

6.2.3 Seismic Refraction Profiles

Refraction seismic profiles carried out in the Betics and the Alboran Sea (Figure 6.8) (Suriñach and Udías, 1978; Banda and Ansorge, 1980; Banda *et al.*, 1983; Medialdea *et al.*, 1986; Banda *et al.*, 1993) made it possible to characterise the Moho depths and intracrustal velocity discontinuities (mainly upper and lower crustal boundaries) in the Central Betics sector.

The interpretation of these profiles shows the following:

- A crustal thickness of 30 km – 35 km in the Iberian Massif.

- Two zones with different crustal structure could be distinguished in the Betic Chain, separated by the Carboneras-Palomares and Alhama de Murcia fault system (Banda and Ansorge, 1980). In the West, the crust can be divided into three layers with different velocities, reaching a total depth of 39 km. In the eastern zone, the crust has two layers and a total thickness of 23 km.

- Towards the South, the crust thins and reaches minimum thicknesses of 13 km to 16 km below the Alboran Sea.

- Both below the Betics and the Alboran Sea, the lower crust is not seismically detected.

- This Southward directed thinning leads to crustal thicknesses along the coast of 23km to 25km.

- SW of Malaga, there is a high velocity body (7 km/s - 7.2 km/s) detected, whose interpretation is speculated on the presence of mantle peridotites, a thinned crust or both (Barranco *et al.*, 1990).
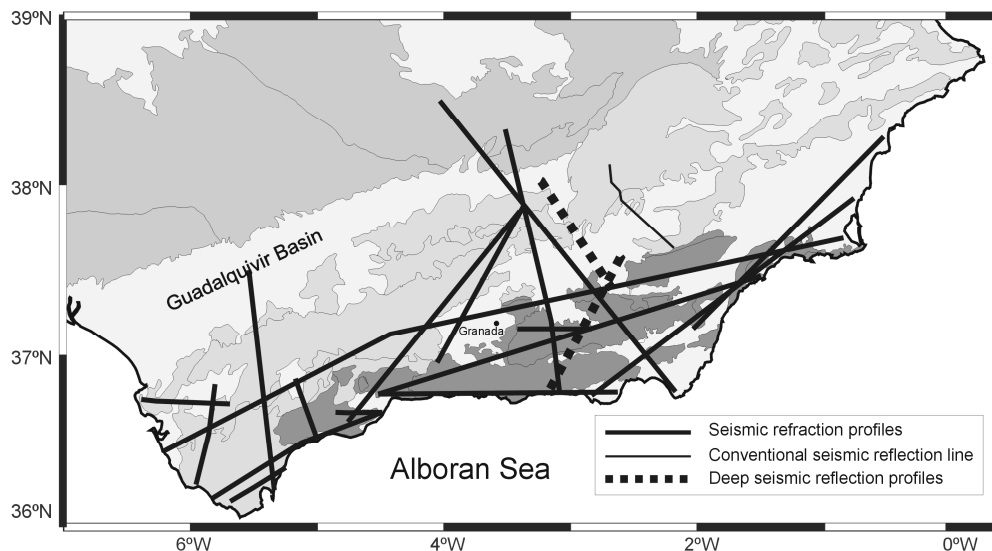
Figure 6.8: Location of seismic refraction and reflection profiles in the Betics.

6.2.4 Seismic Reflection Profiles

Seismic reflection data in the Central Betics is available from multichannel seismic profiles for hydrocarbon exploration and deep reflection profiles.

Among the first, a NW-SE directed profile, BT-3 (Figure 6.8) (Jabaloy *et al.*, 2005), allowed imaging the structure of the contact between the Internal and External zones in the eastern Betics. In this interpretation, the Alpujárride and Maláguide units act as a wedge-shaped indentor between the Prebetic and Subbetic units (Figure 6.9).

Two deep seismic profiles were carried out in the Central Betics: the ESCI-B1, NW-SE directed, that crosses the Guadalquivir Basin and the External Zone; and the ESCI-B2, SW-NE, which, in continuity with the previous profile, crosses the Internal Zones (García-Dueñas *et al.*, 1994) (Figure 6.8).

These two depth converted profiles show:

- The geometry of the Moho, located at 35 km below the External Zone and at a shallower position ($\approx$28 km) below the Internal Zone.

- A well differentiated lower crust with several subhorizontal reflectors and a more or less constant thickness of 15 km – 16 km, and an upper boundary, which is parallel to the Moho at any location below the profiles.

- A transparent upper crust with different features below the External and Internal zones. In the first zone, the upper crust is transparent with a reflective shallow level, with a slightly SE dipping bottom, which corresponds to the Mesozoic and Cenozoic rocks of the External Zone and the Guadalquivir basin. Below the Internal Zone, the upper crust is also transparent, although with the presence of horizontal and dipping bands of reflectors, such as the northeast-dipping UCR. These bands of reflectors follow a dome shape and are interpreted as mylonitic bands. The bands and dome do not affect the lower crust and, consequently, denote a major crustal detachment located at around 10 km – 15 km depth, which corresponds to the Iberian-Alboran domain boundary (Galindo-Zaldívar *et al.*, 1997).
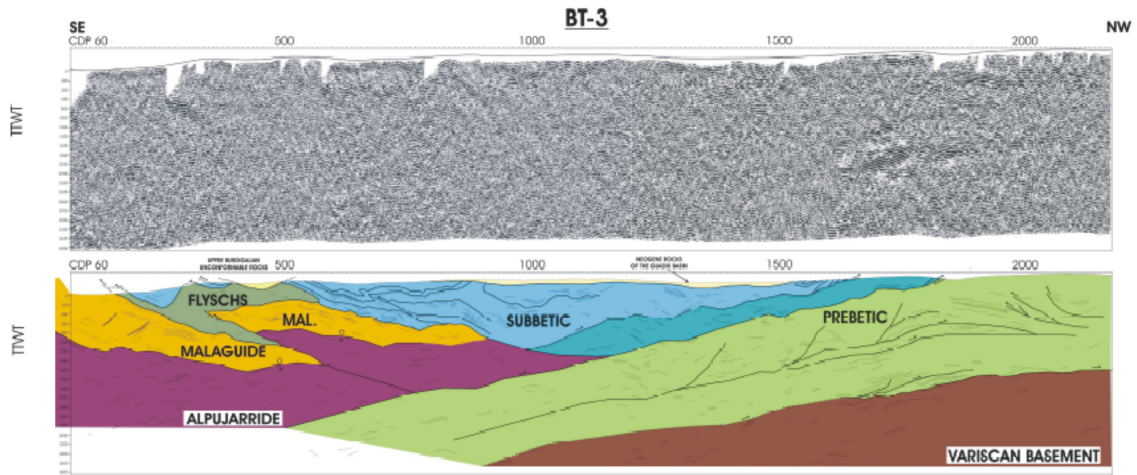
Figure 6.9: Seismic profile BT-3, cross-section and interpretation (Jabaloy *et al.*, 2005).
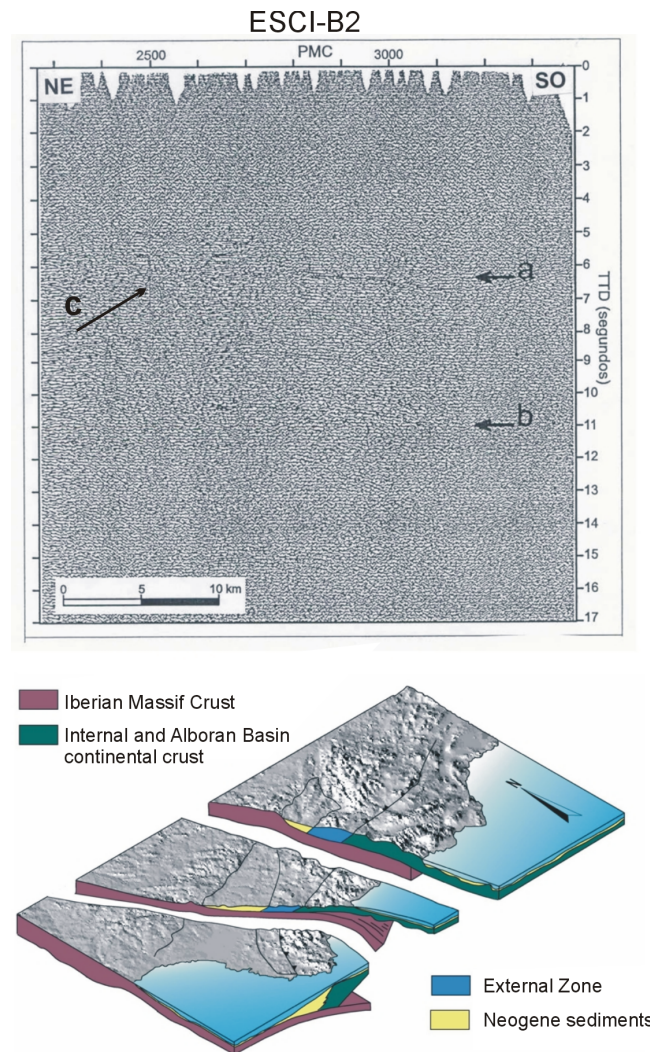
Figure 6.10: Deep seismic profile ESCI-B2. Upper panel: a: upper and lower crust discontinuity. B:Moho. C: Upper Crustal Reflector. Lower panel: sketch of the main crustal structures (modified from Galindo-Zaldívar *et al.*, 2004).

6.2.5 Seismicity and Seismic Tomography

The seismicity of the Betic-Alboran-Rif region is moderate but active (Figure 6.11), with the highest activity located between 3.5°W and 5°W. Earthquakes are mainly produced at mid to low depths, with an important gap between 200 km and 600 km, and some very deep earthquakes which have been recorded (29.3.1954, 30.1.1973, 8.3.1990 and 31.7.1993) under the central and western part of Sierra Nevada, with hypocentral depths > 600 km (IGN, 2001).
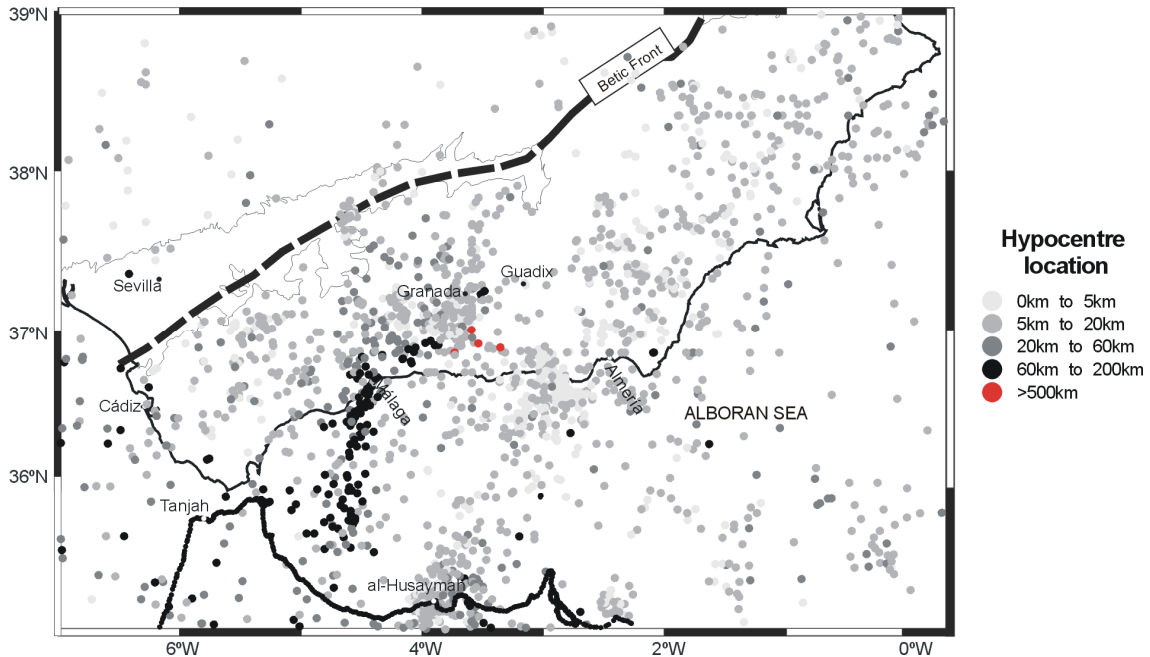
Figure 6.11: Seismicity map of the Betic-Alboran-Rif region. Seismic events from 1950 to 2001 and magnitudes $M_b \geq 3$ have been considered (data from IGN, 2001).

Seismic tomography studies allowed obtaining P-velocity images of the Betics area at crustal - upper mantle levels (Figure 6.12) (Dañobeitia *et al.*, 1998; Serrano *et al.*, 1998).

The results show low velocity zones below the basins, although these continue at lower depths (e.g., 15 km below the Granada Basin, interpreted as fluids along fractures; and 12 km below the Guadix-Baza Basin, suggesting a greater sediment thickness).

At upper crustal levels, high velocity anomalies are found below the Internal and External zones and the contact between them. The anomaly is lower in the External Zone, due to the higher presence of sedimentary materials. At middle and lower crustal levels, these positive anomalies continue below the Internal and External zones, whereas at the contact zone, the velocity is significantly lower.

At the upper mantle, a low velocity anomaly is detected, at the boundary between the Alboran Sea and the Betics.

Lithospheric seismic tomography studies of the Betic- Rif-Alboran region (Calvert *et al.*, 2000) image a high velocity SE dipping body that extends from the Betics to the Alboran Sea, located at depths between 60 km and 400 km, which, followed by a low resolution area, continues up to 650 km.
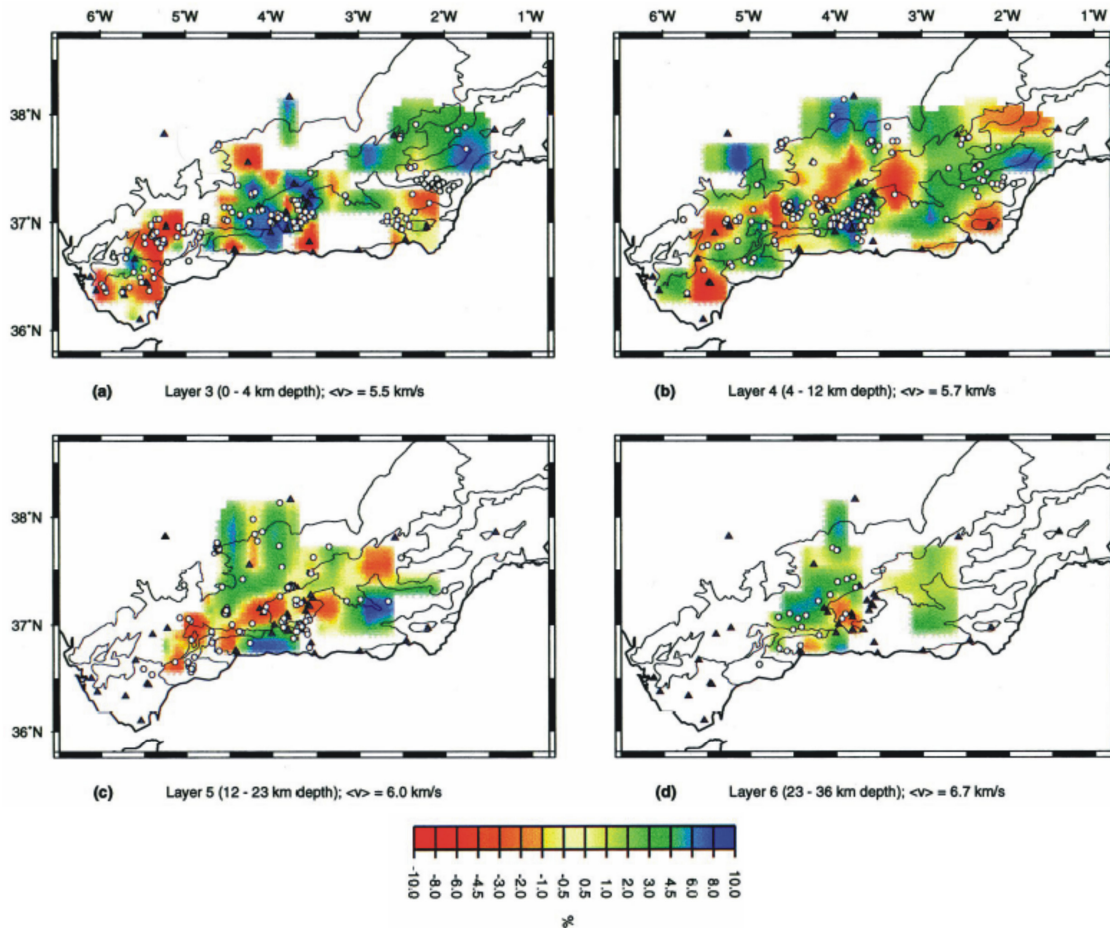
Figure 6.12: Maps of P-velocity anomalies of the Betics crust (after Dañobeitia *et al.*, 1998). Black triangles: station locations. Circles: hypocentral locations within each layer.

6.2.6 Heat-flow

Heat-flow and heat-production maps of the Iberian Peninsula show a rather constant heat-flow value both in the Internal and External zones (60 mW/m^2 – 70 mW/m^2), in continuity with the values obtained from the Iberian Massif and the rest of the peninsula. Towards the South, an abrupt increase of the heat-flow is observed on the coastline, from which it continues increasing until reaching maximum values of 100 mW/m^2 to 120 mW/m^2 in the Alboran Sea

(Fernàndez *et al.*, 1998b). This heat-flow increase has been interpreted as due to the lithospheric thinning from 100 km - 110 km (below the External and Internal zones) to 40 km thick in the Alboran Sea (Polyak *et al.*, 1996).
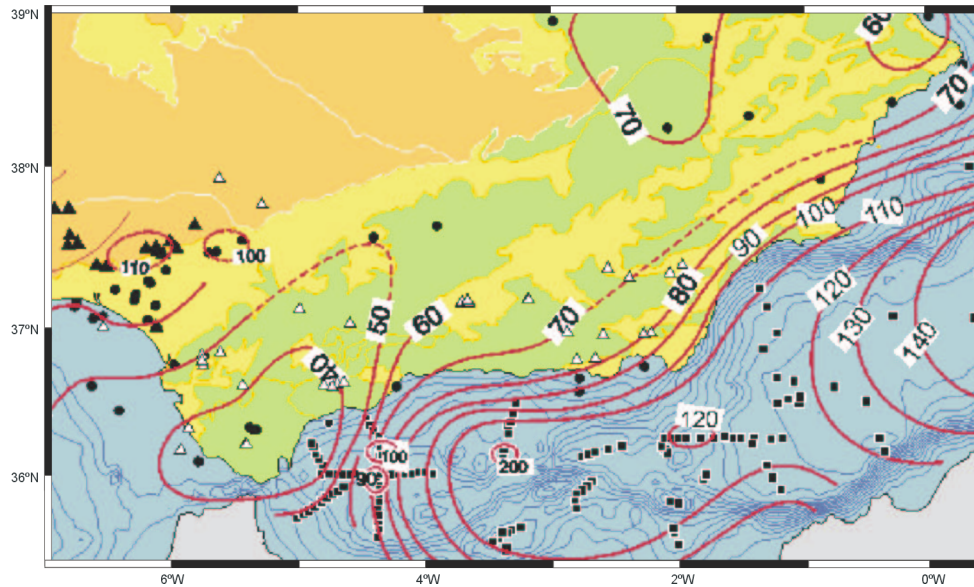
Figure 6.13: Heat-flow map of the Betic-Alboran region. Isolines in mW/m^2. Dots indicate measurements in oil wells; triangles, water and mining exploration wells; and squares, seafloor heat-flow measurements (modified from Fernàndez *et al.*, 1998b).

6.2.7 Magnetotellurics

Previous to the work done in this thesis, a magnetotelluric survey was carried out in the central Betic Chain (Pous *et al.*, 1999). It included 41 sites, with periods recorded from 4ms to 4000s that were acquired between the Iberian Massif and the Alboran Sea coastline.

From this first set of data, a 2D resistivity model was constructed, along a NW-SE strike direction, crossing the Betic Chain from the Guadalquivir Basin to Sierra de Alhamilla (Figure 6.14). The main features of the model are a shallow conductive zone in its northwesternmost part (A); and a shallow resistor, two mid-crustal conductors and a deep conductive body (20 km to 40 km depth) below the Internal Zone.

The main features of the model are three shallow-middle crustal conductors (A, B and D), a shallow resistive zone (C) and a deep conductive body (E), located between 20 km and 40 km depth. The shallow and middle crust conductors have been interpreted as fluid circulation along sedimentary materials (A, Guadalquivir Basin) and along faults (B and D). The shallow resistor C corresponds to metamorphic materials of the Internal Zone. The deep conductive

body, D, located below the Internal Zone, was interpreted as partial melting of the Iberian lower crust under the Alboran Domain.
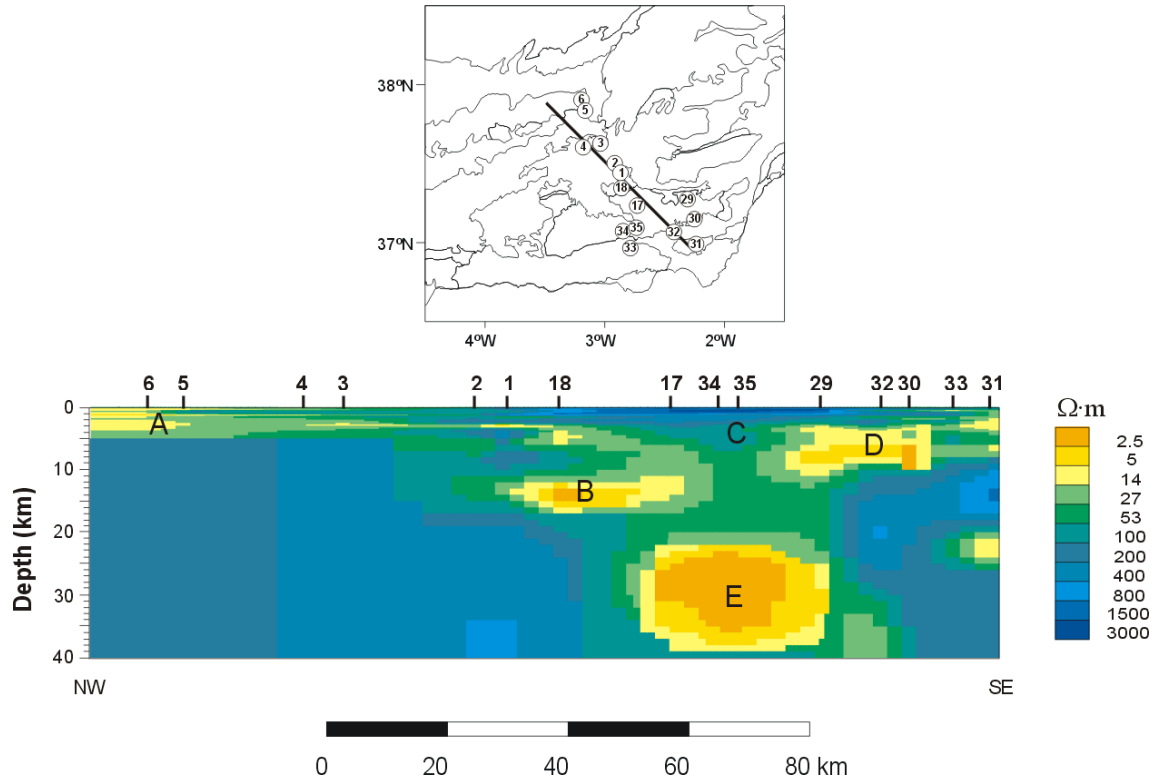
Figure 6.14: Location of MT sites and 2D electrical resistivity model. Circled numbers indicate site locations. A, B, C, D and E are the main conductive structures identified and interpreted.

6.2.8 Summary

The geophysical studies described in the previous chapters allow recognising the main features of the Central Betics inner structure, as have been identified through geophysical disciplinary studies carried out in the last decade (e.g. Galindo-Zaldívar *et al.*, 1997; Carbonell *et al.*, 1998; Morales *et al.*, 1999; Serrano *et al.*, 2002; Frizon de Lamotte, 2004 (Figure 6.15)). The main features are:

- Crustal thickness between 30 km and 40 km below the Internal and External zones, higher on average than those below the Iberian Massif (30 km – 35 km). The maximum crustal thickness, according to gravimetric studies, is located below the Guadix-Baza basin, which indicates the absence of a significant root below the highest elevations of the Betics, in the Sierra Nevada. The crustal thickness decreases towards the coast,

where it reaches values between 20 km and 25 km, and continues decreasing until reaching minimum values below the Alboran Sea (13 km-16 km).

- Continuity of the Iberian Massif below the Betics structure.

- Presence of an anomalous body at lower crustal levels below the Internal Zone, with a low electrical resistivity and low velocities.

- A high velocity slab in the lithospheric mantle below the Internal Zone and Alboran Sea.
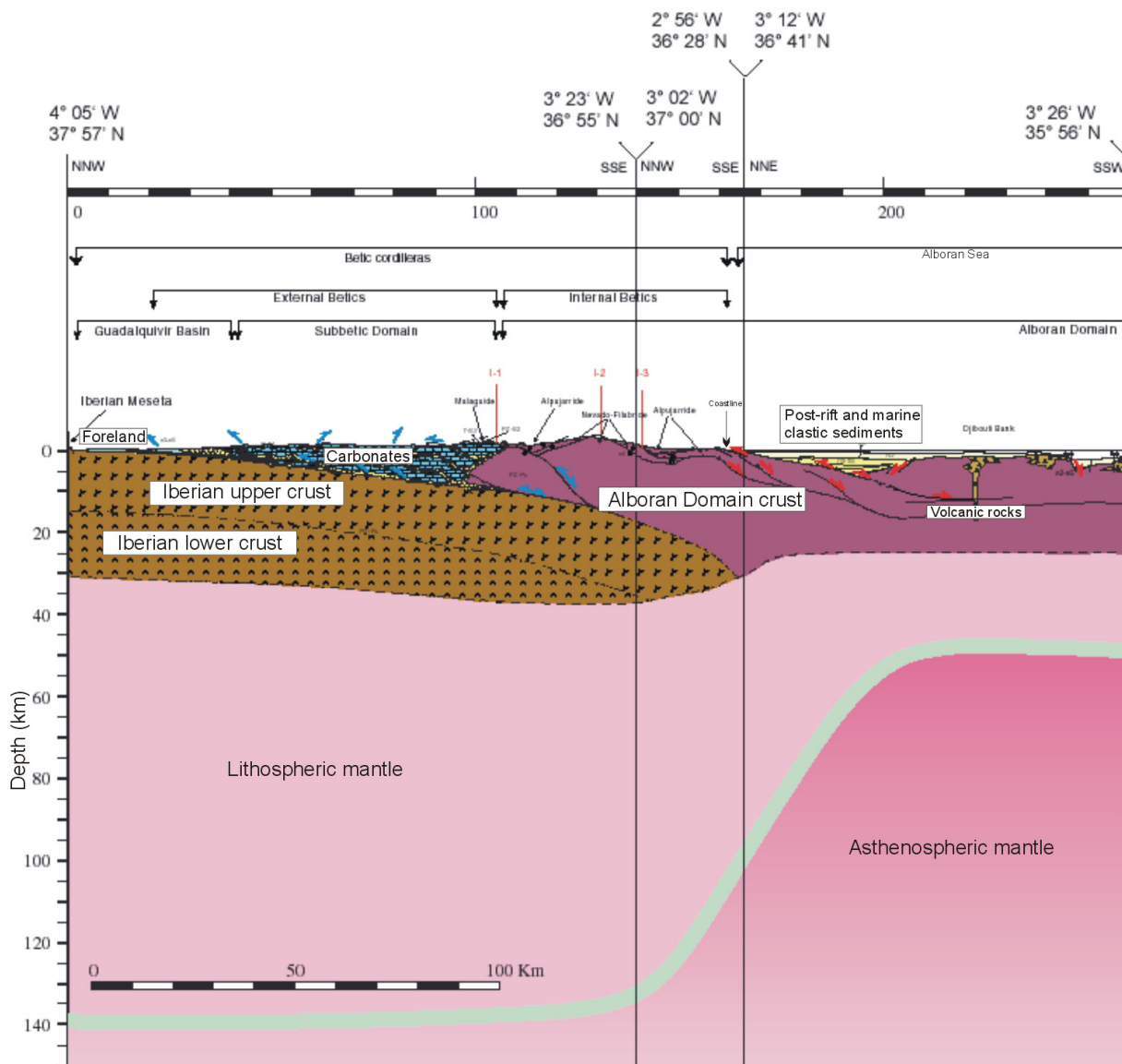
Figure 6.15: Northern portion of TRANSMED Transect I, showing a lithospheric cross-section of the Betic Chain based on geophysical, geological and well data (Frizon de Lamotte *et al.*, 2004).

Chapter 7: Data Acquisition and Processing: Evaluation of MT Responses

The data used in the magnetotelluric study of the Betics were acquired during the former MT survey carried out in 1994-1995, whose data have been processed or reprocessed, as well as in the new survey performed in 2004, for which all the acquisition and processing was done.

In this chapter, the details on how these data were acquired and processed are explained. They are separated into the 94-95 and the 2004 surveys, emphasizing the work done in this thesis. The evaluated responses corresponding to the whole data set are also presented.

7.1 Betics 94-95 Survey

7.1.1 Description

The first magnetolelluric measurements in the Betic Chain were done in the framework of a research project sponsored by the Spanish Education and Science Ministry, with the aim of electrically characterizing the crust in the south Iberian Massif and the Betic chain. The sites were located more or less along a NW-SW profile coincident with previously existing seismic refraction and reflection lines.

The data were acquired in three stages during 1994 and 1995 using three Metronix MS03 instruments, property of the Departament de Geodinàmica i Geofísica of the Universitat de Barcelona (DG-UB).

At each site, the two electric and magnetic horizontal components were registered. The vertical magnetic component was registered only at some sites, given the difficulty of burying the vertical coil in certain terrains. In view of further 2D modelling, the axis orientation of the recorded components at some sites was NE-SW, coincident with the direction of the main outcropping structures of the Betic chain. In total, 41 MT sites, distributed throughout the Central Betics, from the Iberian Massif to the coast, crossing the Internal and External zones and intramontane basins, were acquired (Figure 7.1).

Time series were registered through different bands, with a total duration of three days each. Time series from 21 of the sites were processed using the robust code of Egbert and Booker (1986), resulting in recorded periods ranging from 4 ms to 4000 s.

The sites were labelled as "b" (for "betics") plus an identification number. Part of this dataset was used to create and interpret a 2D model (see chapter 6, section 6.2.7).
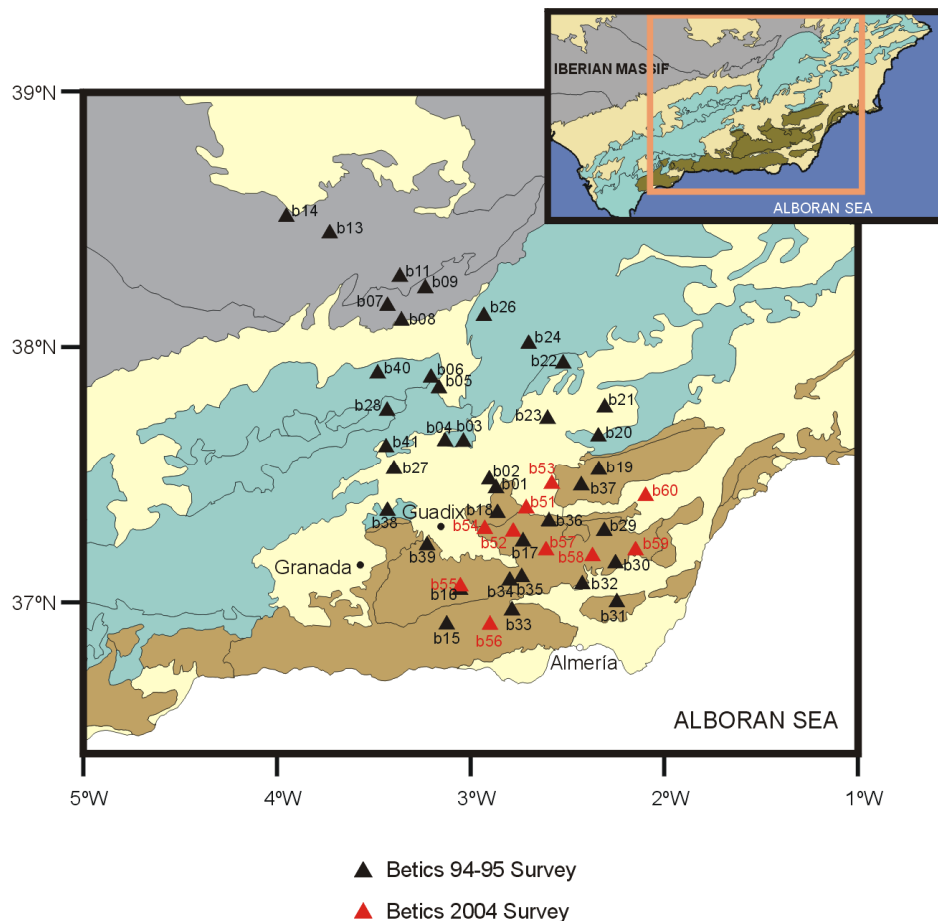
Figure 7.1: Betics sites locations with the corresponding identification, from 94-95 (black) and 2004 (red) surveys.

7.1.2 Time series reprocessing

Although a former dataset with 21 sites from the Betics 94-95 survey existed, reprocessing of the time series and processing of the remaining 20 sites was performed. The aims were to complete the dataset, to obtain a better knowledge of the time series, to have a systematic register of all the processing characteristics and to attempt to improve the quality of the responses, through a careful inspection and selection of the time series segments. Moreover, for further data analysis, especially the dimensionality, it was necessary to establish the same axes directions for all sites, which were set to NS-EW.

The reprocessing consisted of the following five steps, carried out at each site, with the help of specific software provided by Metronix:

1) Restore time series files: Organise time series files in period bands, named band1, band2, band3 and band4 with sampling periods and frequencies: 1 kHz, 32 Hz, 1 s and 32 s respectively (see Table D.2). Band3 and band4 time series can be obtained by resampling the registers of band2 or band3, as long as the recorded ones are not too short and are not low quality.

2) For each band:

a) Visual inspection of the time series and manual selection of the segments (each one containing a determined number of samples) in order to reject contaminated data due to unforeseen incidents (breaking of a wire, digging up an electrode, exhausted batteries…) or to the maintenance of the site. Some indicators of these effects are:
   - Signal amplitudes much greater than the average, which can affect only one channel or all channels simultaneously.
   - Absence of signal for a certain period of time.
   - A period of time with an increase of the oscillation amplitude in all channels.

b) Computation of the MT responses using robust processing (Egbert and Booker, 1986).

c) Data quality check and improvement:
   - Bivariate coherences: low values of $E_x(B_xB_y)$ and $E_y(B_xB_y)$ (below 0.8) indicate poor quality data, with a bad correlation between the measured and the predicted fields. Coherence may be improved by the exclusion of more segments in step a).

- Errors: large error bars in the computed responses are undesirable. They can be reduced by the addition of new segments to the selection made in a), such that the confidence limits of the responses become more restricted.

Obviously, a compromise must be achieved regarding the final number of segments, so that the responses present acceptable coherences and only moderately large error bars.

Alternatives that may work to improve the quality of data from long period bands (band3 and band4):

- Perform time-to-frequency conversion using different segment lengths, in order to dispose of a greater number of segments. However, a consequence of this is that the longest periods cannot be estimated.
- Generate new time series by resampling the time series from shorter period bands (band2 and band3).

3) Attach responses from different bands to construct the complete spectrum.

4) Rotate data to N-S direction for those registered with a 45° orientation.

5) Convert output files to EDI (Electrical Data Interchange) format files, which is the SEG Standard for Magnetotelluric Data.

A worksheet was created to store relevant information about each site:

a) site information and equipment configuration: site location, acquisition date, axes orientations, electrode distances and recorded components.
b) time series: data files, recording lengths and channel amplifications.
c) time series processing: number of selected segments, and name of the output files.

Additional comments, such as problems with the initial files, missing data or particular characteristics of the time series processing were also noted in the worksheet.

As an example, Table 7.1 displays the worksheet corresponding to site b01. At this site, five components were recorded (E_x, E_y, B_x, B_y and B_z), with a NW-SE orientation. Data from all bands were restored directly from the registers, without making any posterior resampling of the longest periods bands.

a) Site information							
	Geographical coordinates						
Site	Latitude	Longitude	Altitude (m)	Acquisition date (day/month/year)	Measurement orientation (x - y axes)	Electrode distances (m)	TIPPER??
b01	+37:26: 31	-2:52:07	1240	31/01/1994 to 02/02/1994	NW-NE	100	YES

b) Time series information			
Time series*.03e files	Recorded bands at each file	Total number of segments at each site	Site gains
_1.03e	1,2,3,4	4650	100
_2.03e	3,4	1990	100
_3.03e	1,2	2995	100
_4.03e	1,2,3,4	5910	100
_5.03e	1,2	3170	100
_6.03e	1,2,3,4	6395	100

c) Time series processing

Number of segments per canal(containing 512 samples each) and total recorded time

Band1	Band2	Band3	Band4
100 (51.008s)	315 (83m 56s)	211 (29h 58m 4s)	14 (30h 9m 4s)

Total selections per canal

Band1	Band2	Band3	Band4
47	85	41	12

Output file: b01ss2t.spe

Table 7.1 Site b01 information stored in the worksheet, as an example of the information entered for all sites.

An important number of segments of the time series recorded at this site exhibited noise effects, as expected due to the proximity to populated areas. After a visual inspection and selection of bands 1, 2 and 3, which originally had a large number of segments, a sufficient number of segments prevailed for the posterior robust processing and estimation of the transfer functions.

The selection for band4, with only 14 recorded segments, was not as accurate and hence, only the 2 worst segments were rejected. Otherwise, there would have not been enough data to process and the error bars would have been even greater than they are (see Figure 7.3). However, it did result in low coherence values.

Figure 7.2 and 7.3 show the bivariate coherences and the non-diagonal resistivity and phase responses estimated for site b01, after a 45º rotation. Coherence values are locally lower

than 0.8 for E_x and for T > 40 s for E_y. Nevertheless, resistivity and phases responses have a smooth behaviour, with the exception of a peak near T=10 s, which is especially evident at the yx phase. Error bars are not significant until T=100 s, when these become important, as a consequence of the lack of enough segments at band4 to make a more accurate estimation of the responses. For further analysis of the data, the peaks in the responses must be removed, which will make the data quality acceptable.
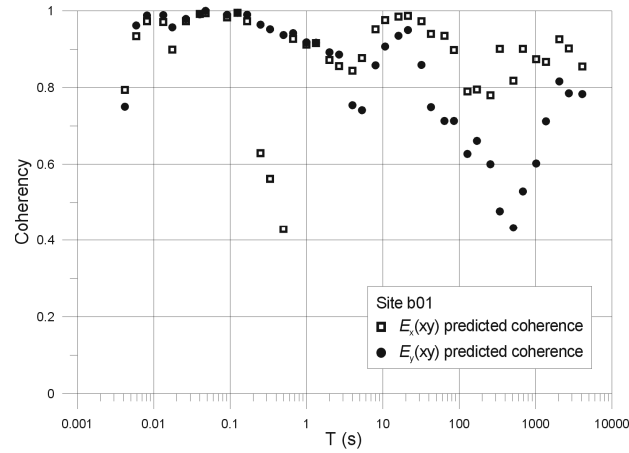
Figure 7.2: Bivariate coherences for the horizontal components of the electric field corresponding to the estimated responses of site b01.
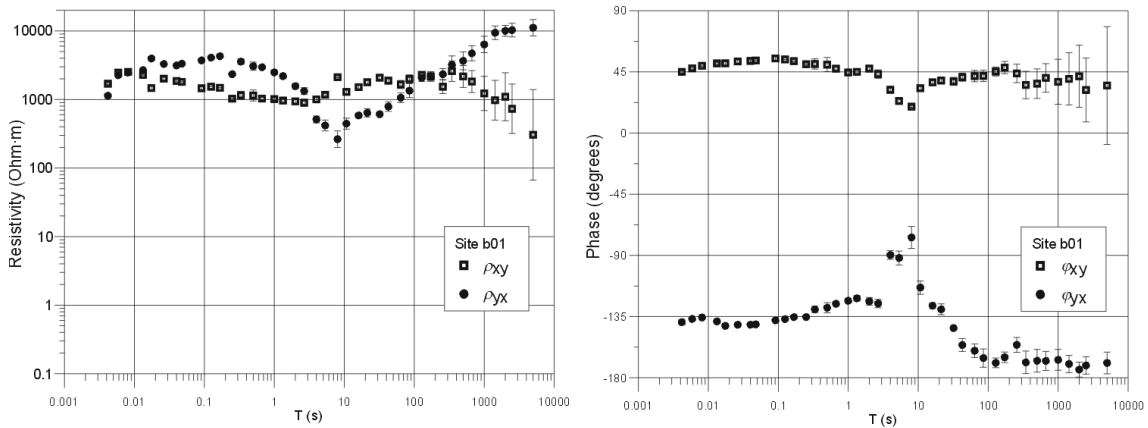
Figure 7.3: xy and yx resistivity and phase responses with their error bars estimated for site b01.

For the remainder of sites, the configuration of the equipment was the same, with the exception of the axes' orientations, the distance between electrodes and the registering or not of the vertical magnetic component. The recording times were similar too, with the time series

displaying the same amount of noise, and in general leading to similar proportions of selected segments. The main differences were in the processing of the longest bands, which in some cases needed different trials regarding the choice of the segments and resampling of the time series, such as to improve data quality. However, at some sites the quality of the data was so low that they had to be rejected from the dataset, which was subsequently reduced to 33 sites.

7.2 Betics 2004 Survey

Given the availability of new MT equipment at the DG-UB, and with the aim of acquiring new data in the study zone, a new MT survey was proposed and executed in the Internal Zone of the Betics during two weeks in the summer of 2004.

7.2.1 Acquisition

The Betics 2004 survey was conducted as a collaboration between the DG-UB and the Departamento de Geodinámica of the Universidad de Granada (DG-UG), using the new Metronix GMS-06 equipment, one belonging to DG-UB and two from the DG-UG.

GMS-06 equipment use the ADU-06 data logger and FMS-06 coils. Compared to the older equipment, ADU-06 allows obtaining high quality data due to 24 Bit Analog/Digital conversion technology, MFS-06 coils are sensitive to a broader range of frequencies (from 0.00025 Hz to 10 kHz) and come with an electronic system to reduce noise levels. This new equipment also permits one to perform remote reference acquisition much more efficiently, due to GPS synchronisation.

The survey area extended from the east of Granada to Almeria, crossing the Nevado-Filábride and Alpujárride complexes, the lowermost of the Internal Zone, and the surrounding basins. Since the area has a marked relief and due to man-made noise, an important task was to carefully locate the sites, to avoid as much as possible the acquisition of noisy data.

The horizontal components of the electric and magnetic fields and the vertical magnetic field (at all except one site) were recorded. The average duration of the registers was two and a half days, in which bands HF, LF1, LF2, Free (with a sampling frequency of 512 Hz) and LF3 were recorded (see chapter 1, Table 1.1, and Table D.2 for comparison with the older system). Band LF4 was obtained from posterior resampling of LF3. At each site, a first test run was performed as a check-up of the equipment. For the shorter bands, HF and LF1, several tests were performed as data backups.

In total, data from 10 sites were acquired (Figure 7.1), identified from b51 to b60. All sites were at new locations, except for b55, which was coincident with the location of a site

from the former 94-95 survey, b16, whose quality was poor with only the short period responses recovered. Apart from improving the information of this site by registering longer time series, the purpose of repeating this measurement was to compare the efficiency between the new and old equipment. The recordings at sites b52 and b57 lasted one week each, in view of using these data for remote reference processing.

Table 7.2 shows part of the worksheet created, containing information on the duration of the recordings at each site, the equipment used and comments on the acquisition runs performed. This table allows one to easily find which of the simultaneous recordings are possible for remote reference processing. Since it was not possible to perform simultaneous recordings of the shorter bands, only LF3 and LF4 could be considered for remote reference. Details of the site coordinates and registered components are also displayed in Appendix D.

Table 7.2: Information on the Betics 2004 survey sites: dates and duration of the recordings, equipment used and comments (only an example from site b60 is shown) on the different acquisition runs and recorded bands. Comments are placed on the triangle marks.

7.2.2 Time series processing

The acquired data were processed using robust processing from the new version of the Metronix processing software, Mapros (Friedrichs, 2003). The scheme followed was similar to the one used in the former survey, with the difference that most of the steps can be performed automatically by the program.

Inspection of the time series segments revealed the presence of noise at some segments. Particularly, the 50 Hz signal from the power lines could be observed at all sites, which was more intense in those data collected on mountainous terrains than in basins. As it has been observed in previous surveys in other zones, it is common that noise is easily transmitted by irregularities in the terrain. The influence of this signal is reduced in the processing.

For each band, the time series processing was performed in various ways, from which the optimum was chosen. These included making a manual selection of the segments or allowing the program to do it automatically, using different segment lengths, which imply obtaining a broader or narrower spectrum of responses, changing parameters of the time to frequency conversion, and, when available, comparing data from different runs.

Although automatic selection of segments is quite accurate, a visual inspection and manual selection of the segments was always performed, which significantly improved the coherence values.

- HF responses presented very low quality at all sites, due to the low intensity of the natural signal; thus, acquisition using Controlled Source would have been preferable. Responses were not smooth along the period and coherences had very low values. For this reason these frequencies were not included in the final responses.

- LF1, Free and LF2 responses are the best quality responses, with coherence values above 0.8 for LF1 and Free and above 0.6 for LF2, with small error bars and smooth curves for all responses.

- The quality of LF3 and LF4 responses changed from site to site. In some of them, these tests were performed in different ways: either to do more accurate selections of segments or change the time window of the segments. However, there was no significant improvement in the results. In general, the coherence values are low, decrease along with the period and error bars become important for band LF4.

- Remote reference processing (RR) was also tested among sites with simultaneous registers of bands LF3 and LF4, the ones that presented worst quality responses. The use of RR improved the smoothness of the responses at band LF3, although coherence values decrease, whereas both band LF4 responses and coherences worsened. This observation suggests that the separation between sites to apply RR was enough in LF3, but not in band LF4, where a greater separation would have been more desirable. Hence, since only the quality of LF3 improved partly, all the final responses used local reference.

As for the sites recorded in both surveys with the same location, b16 and b55, their coherence values are shown in Figure 7.4. b16 responses could only be estimated up to 10 s, since long period bands recordings were too short and highly affected by noise, and presented low coherences. Site b55 recordings were longer and responses were estimated up to 4000 s, although band LF4 responses were rejected for presenting low coherences and large error bars. Coherence values up to 10 s are similar to those of b16. From 10 s to 100 s (band LF3) their values are slightly increasing. The low values of coherences observed in both sites reflect that noise is inherent to the site, as it does not depend on the equipment.
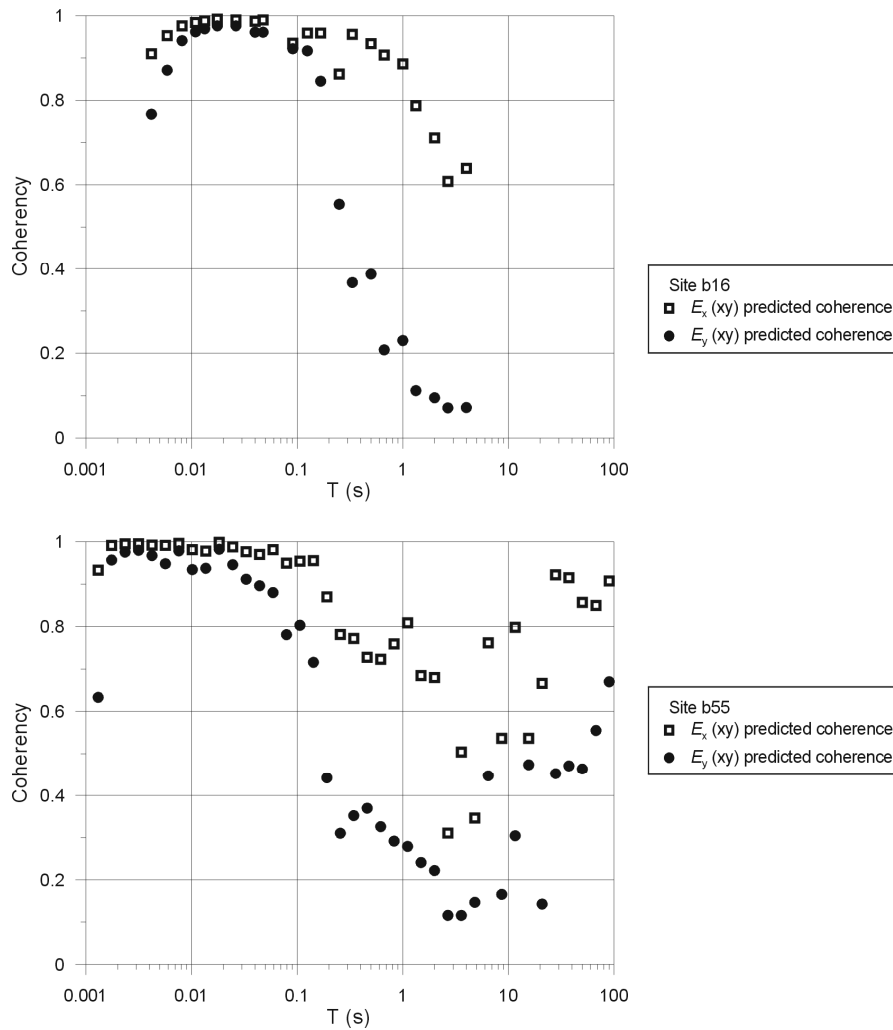
Figure 7.4: Bivariate coherences for the horizontal components of the electric field computed from sites b16 and b55.

7.3 Evaluation of MT Responses

The information about the Betics dataset sites and the MT responses evaluated are displayed in Appendix D (Table D.1 and Figures D.1 to D.9).

The quality of the responses at each site was evaluated following a proposed criterion based on coherences values and errors of the MT tensor components, in the way that high coherence values and small errors are synonymous of good quality.

According to this criterion, there are three sites with poor or very poor quality: sites b09, b38 and b02, the latter due to low coherences, since resistivity and phase curves do not apparently show large error bars. For the rest of Betics 94-95 survey sites, the average qualities are medium and good, and b26 and b30 qualities are very good, as can be seen from the response plots (small error bars).

For sites b51 to b60, with medium and low coherence values, especially for the longest periods, but with moderate error bars, the data quality is regarded from medium to good.

Some of the ρ_{xy} and ρ_{yx} resistivity curves show a displacement, smaller than one decade in value (with the exception of site b52 where it is larger), beginning at the shortest periods. These displacements can be considered static shifts and must be corrected. In general, the variation of the starting resistivity values between sites located over the same area is no greater than one decade.

Apart from the static shifts, it is quite common in the Betics 94-95 sites that the resistivities estimated at the first period present a considerable displacement with respect to the rest of the values. This is a consequence of a problem in the software used on the determination of the responses and, consequently, this period was rejected.

Through an inspection on the shapes of ρ_{xy} and ρ_{yx} plots, which provide a first approach to the variations of underground resistivity with depth, a classification of their morphologies was made, which could be fairly well associated with their locations. The results, in terms of the general behaviour of the different zones, explained from north to south, are:

- Iberian Massif (b14, b13, b11, b09 and b07): smooth resistivity curves for both polaristations, each site with a different constant value, between 10 Ω·m and 1000 Ω·m. The exception is b11 with a drop of ρ_{yx} at the longest periods.
- Guadalquivir basin limits (b08, b06 and b05): split between ρ_{xy} and ρ_{yx} increasing curves.
- Prebetic zone (b26 and b24): constant curves around 100 Ω·m, with a slight drop at intermediate periods.

- Subbetic zone (b40, b03, b20 and b41): b40 and b03 curves have an increasing tendency. b41 resembles more of a basin behaviour, and b20 has a completely different curve, decreasing from 10 $\Omega \cdot$m to 1 $\Omega \cdot$m at 1s, at which point it becomes constant.

- Guadix-Baza basin (b21, b23, b27, b02 and b01): smooth variations of resistivity along a more or less constant curve.

- Internal Zones and surrounding basins (coloured triangles in Figure 7.5): north and south of the Nevado-Filábride complex outcrops (b38, b39, b01, b02, b53, b37, b19, b60, b15 and b32; blue in Figure 7.5), the responses are fairly constant. In the east and west sides of this complex (b18, b30 and b59; yellow in Figure 7.5), the resistivities are increasing at the shortest periods, until reaching a maximum and then drop uniformly. In the NW and SE (b51, b36, b56, b33 and b31; green Figure 7.5) there is a split between xy and yx curves, where ρ_{xy} remains constant and ρ_{yx} decreases. All sites located over the Sierra de los Filabres (b54, b52, b17, b57, b29, b58, b55 and b35; red Figure 7.5) have continuously decreasing resistivity curves. The disposition of the shapes of the resistivity curves around a central part, where a drop in both ρ_{xy} and ρ_{yx} is observed, suggests the existence of a 3D conductive structure confined under the Sierra de los Filabres.
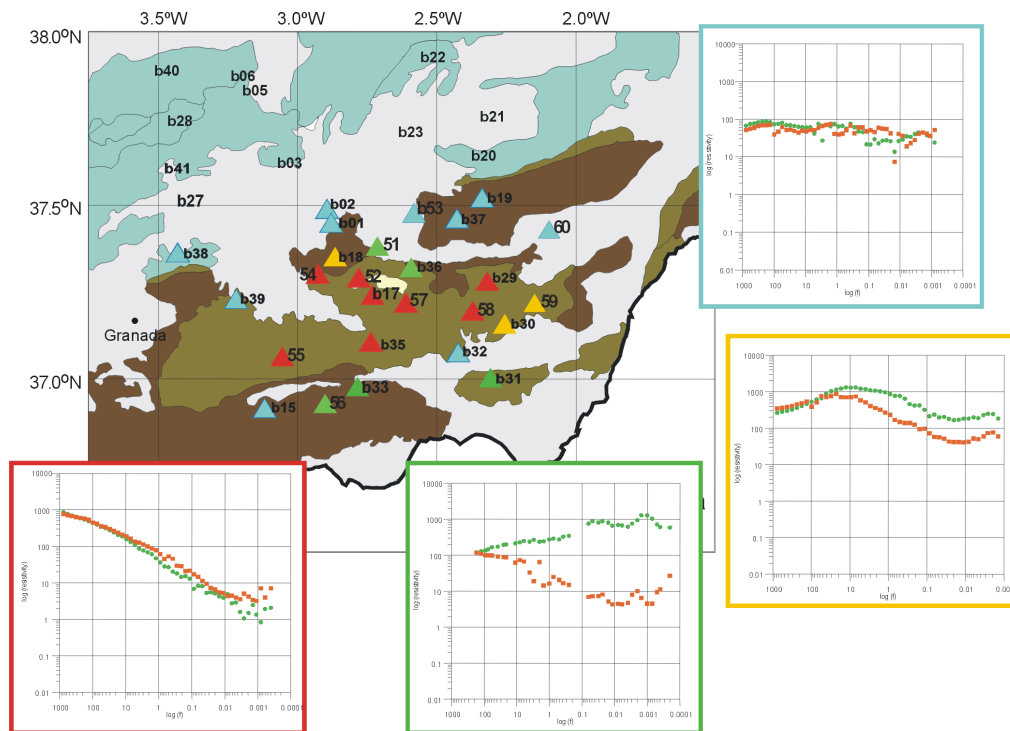
Figure 7.5: Internal Zone and surroundings sites, whose resistivity curves can be classified in four different morphologies, shown in different colours.

The phases corresponding to these curves are consistent with the resistivity variations.

7.4 Conclusions

Betics 94-95 survey data were reprocessed, using a visual inspection of the time series segments. The resulting responses had a range of periods from 4 ms to 4000 s, medium to high coherence values, large error bars at the longest periods and some peaks in the response curves. It resulted in a dataset with 33 sites. The quality was maintained at the sites that already presented good quality and it was improved at sites that presented the lowest coherences and largest error bars.

The new data acquired in 2004 (10 sites) are characterised by high levels of noise, low coherences, but medium to high quality responses, ranging from 1 ms to 1000 s or 4000 s, depending on the sites.

Data from the HF band were not included because of the poor quality of the registers. Remote reference processing was successful for band LF3, but not in LF4, where a larger distance between sites would have been necessary.

The resistivity responses evaluated over the Internal Zone show a central part where both ρ_{xy} and ρ_{yx} decrease, which suggests the presence of a 3D conductive body in depth.

Chapter 8: Geoelectric Dimensionality Analysis of the Betics MT Data

This chapter presents the dimensionality analysis carried out for the Betics MT data. The methodology employed was the WAL invariants criteria, through the WALDIM software developed in this thesis. Taking into account the results of this analysis, an interpretation of the geoelectric structures in depth, and strategies for the further modelling are given.

The results are contrasted with those obtained from two other methodologies, the very commonly used Multisite, Multifrequency Strike code (Strike, McNeice and Jones, 2001), which uses the Groom and Bailey decomposition, and the more recently appeared phase tensor method (Caldwell *et al.*, 2004).

The choice of WAL invariants criteria amongst other methods is due to the fact that it utilises all the information from the MT tensor data and provides a dimensionality description not restricted to a specific model. On the contrary, the phase tensor only utilises half of the information provided by the MT tensor (i.e., the phases). The Strike code searches a 3D/2D description of the data, in view of 2D modelling, although it does provide a misfit that allows one to quantify up to which degree this interpretation is suitable.

8.1 WAL Dimensionality Analysis

Even though all processes in the WALDIM program are performed automatically, this section presents the results obtained for the Betics MT data separated in two steps:

(1) WAL invariant values, errors, and related angles and parameters, at different periods and depths.

(2) Dimensionality analysis results and their interpretation considering other structural knowledge of the crustal structure.

8.1.1 WAL invariants and errors, related angles and parameters

Following the recommendations given in section 3.4, the invariant values were estimated as the true values, and their errors were computed using classical error propagation (approach **a** in section 3.2.1a). Strike directions and distortion parameters were also estimated as true values, whereas their errors were computed using random noise generation (approach **b**, section 3.2.1b).

In order to illustrate the values of the invariants used in the dimensionality determination (I_3 to I_7 and Q) and their variation along the different sites, period and depths, different contour maps were constructed at given periods and equivalent study depths.

Contour maps for constant periods, distributed along the whole spectrum (2 per logarithmic decade) were plotted and analysed. Figure 8.1 shows the invariant maps at four constant periods, whose features are representative of the contiguous ones computed.

T=0.0032 s (Figure 8.1a) is the first period in which almost all sites are represented. I_3 and I_4 have a similar distribution, with broad changes from site to site. I_5 values are in general low, with higher values at the outermost sites, whilst I_6 and Q values are low, the latter implying that I_7 values are considered undetermined. At this period, with $I_3 \neq 0$, $I_4 \neq 0$ and $I_5 \neq 0$, $I_6 \approx 0$ and $Q \approx 0$, the dimensionality is interpreted as 3D/1D2D.

At T=0.1 s (Figure 8.1a), with map appearances representative of the period range from 0.01 s to 1 s, the previous description still holds, although with a notable decrease in all invariants' values. Consequently, the dimensionality is less complex, with mixed 1D and 2D cases.

At T=10 s (Figure 8.1b), invariants I_3 and I_4 follow different values distributions, with higher values than at T=0.1 s. I_5 values become larger at the extremes, but still with a low value zone in the middle. I_6 become larger at the northwesternmost sites, whereas the rest remain low. Q has higher values too, so I_7, with low to moderate values, is not considered undetermined. The exception to this is at the northernmost and southernmost sites, with values larger than 1. At this period, dimensionality increases in complexity, with some 3D cases mixed with 2D cases that are affected by galvanic distortion.

T=1000 s contour maps (Figure 8.1b), with a smaller number of sites, presents a significant change with respect to the rest of period maps. All values are considerably higher than the rest, which indicates an increase in the dimensional complexity, which is mainly 3D.

Contour maps at different study depths were built using "Bostick Modified Depth", h_{BM}, based on the Bostick transform (Bostick, 1977) [1].
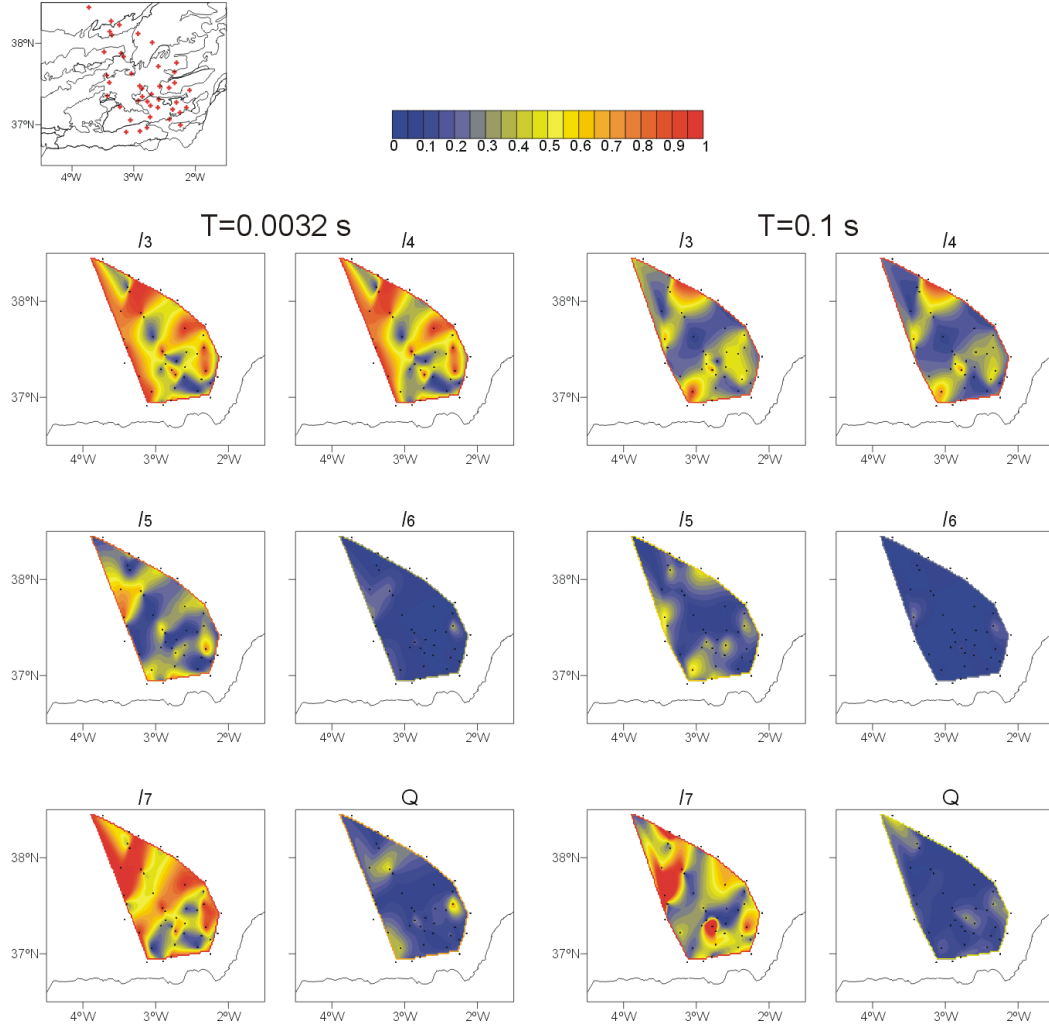
Figure 8.1a: Contour maps of WAL invariants I_3 to I_7 and Q at constant periods T=0.032 s and T=0.1 s. Site locations (black dots) and coastline are given as a reference. Upper left map shows site locations over the main geological features of the study area.

[1] The Bostick transform converts frequency domain resistivity data into a resistivity depth sounding. For each frequency, Bostick resistivity and depth are computed from the apparent resistivity ρ as $\rho_B = \rho \cdot \dfrac{1+M}{1-M}$ and $h_B = \sqrt{\dfrac{\rho}{\omega\mu_0}}$, where M is the slope of ρ in a log-log plot. h_B is $1/\sqrt{2}$ times the skin depth, δ. In a layered Earth, h_B can be interpreted as the "centre of gravity" depth of the in-phase induced current systems studied at a given period.
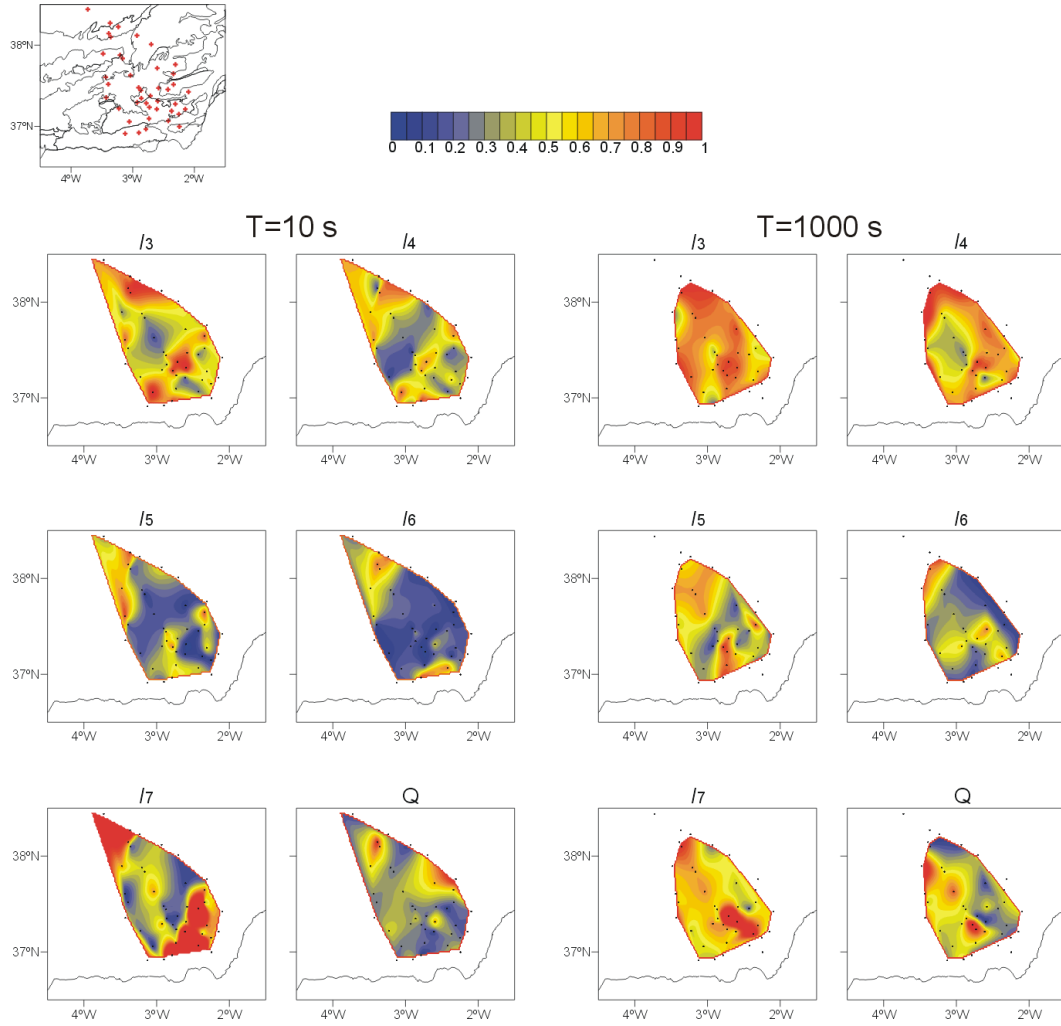
Figure 8.1b: Contour maps of WAL invariants I_3 to I_7 and Q at constant periods T=10 s and T=1000 s. Site locations (black dots) and coastline are given as a reference. Upper left map shows site locations over the main geological features of the study area.

h_{BM} was defined for a given period from the 1D resistivity computed from I_1 and I_2 invariants (eq. 2.20):

$$h_{BM} = \sqrt{\frac{\rho_{1D}}{\omega\mu_0}} = \frac{T}{2\pi}\sqrt{\left(I_1^2 + I_2^2\right)}\,, \tag{8.1}$$

in m, if I_1 and I_2 are expressed in m/s. The choice of this modified depth has the advantage that utilises a rotational invariant resistivity, and allows mapping the dimensionality related invariant values as a function of the two remaining invariants of the WAL set, I_1 and I_2. However, these invariants, as well as the Bostick depth obtained, may be affected by the static shift.

These contour maps were drawn for different intervals of h_{BM} values, since the dependence of h_{BM} on T, I_1 and I_2 resulted in a broad range of values.

Two of these h_{BM} contour maps, at the intervals h_{BM}=100 m to h_{BM}=120 m (named h_{BM}=100 m) and h_{BM}=10000 m to h_{BM}=12000 m (named h_{BM}=10000 m) are displayed in Figure 8.2, as representative of upper and middle depths.
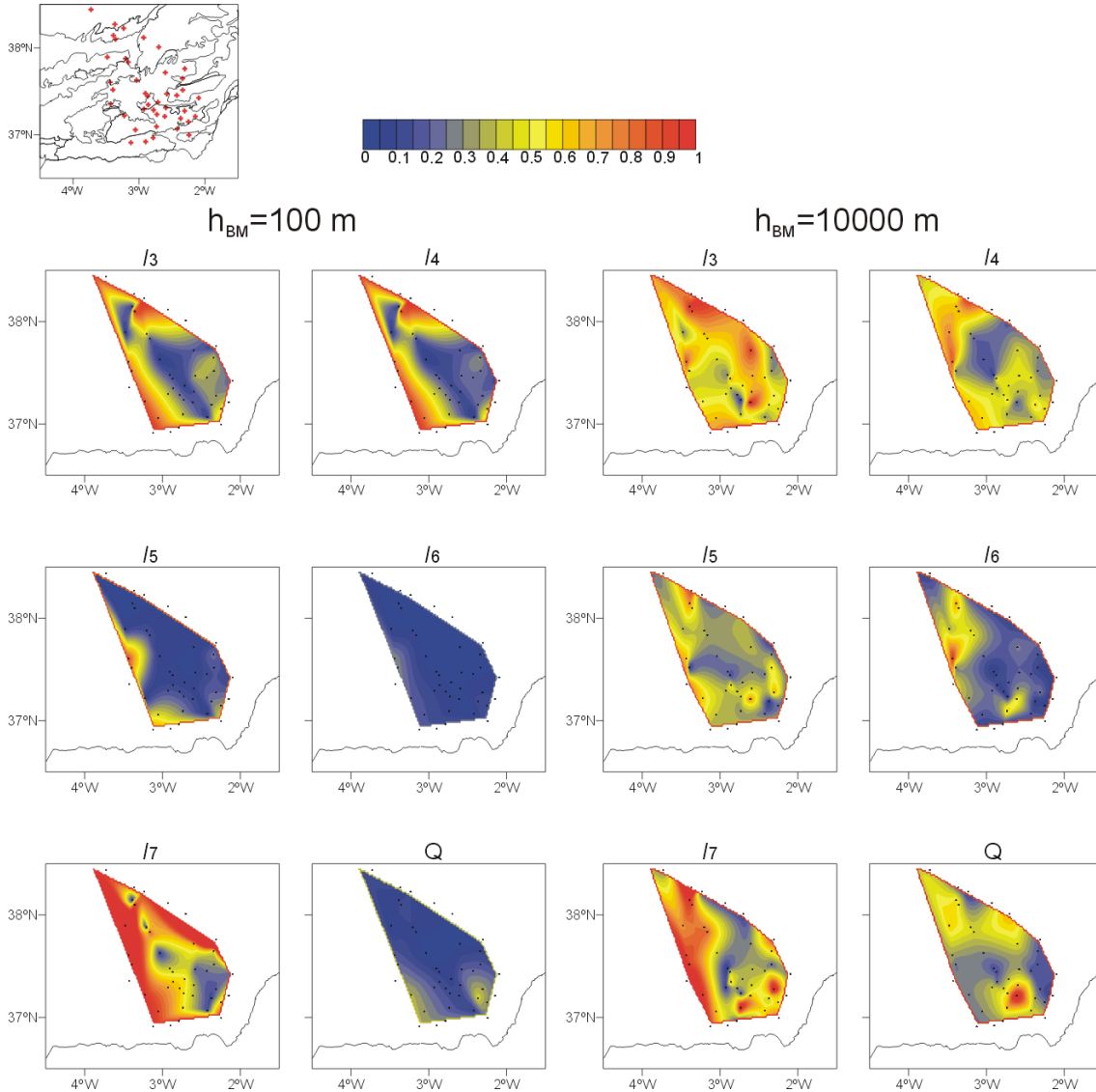
Figure 8.2: Contour maps of WAL invariants I_3 to I_7 and Q at two Bostick modified depths, h_{BM}=100 m and h_{BM}=10000 m. Site locations (black dots) and coastline are given as a reference. Upper left map shows site locations over the main geological features of the study area.

The h_{BM}=100 m map, obtained from 20 sites over two decades (from 0.00175 s to 0.09 s) in general shows similar values of I_3 and I_4, low values of I_5, I_6 and Q; and I_7 is

undetermined, which indicates 1D and 2D dimensionality. However, at the eastern middle and southern edges of the map, I_5 becomes larger, which is interpreted as a twist-distortion; and at the southern part, Q increases, which, together with high values of I_7 indicate three-dimensionality.

The h_{BM}=10000 m map represents 30 sites with an even broader range of periods (between 0.5 s and 1000 s), with most concentrated between 10 s to 100 s. Contrary to the h_{BM}=100 m map, the dimensional complexity is evident, with larger values of all invariants in general, as observed in the middle and long period maps (10 s and 1000 s).

In reference to the errors of WAL invariants, the distribution of the error bars with the period shown at site b23 (chapter 3, Figure 3.3) is in general valid for the rest of the sites. Invariants I_3 to I_6 have error values proportional to the noise level in the MT tensor components, which increase with the period, whereas I_7 and Q errors are large at all periods, especially those of I_7 if Q values are small.

Contour maps of the invariant errors at constant periods follow the above description: up to 100 s, I_3 to I_6 error values are small (<0.1), Q errors are slightly higher (up to 0.4 at some sites and periods) and I_7 errors are large. At longer periods, all errors are large, as it can be seen from the T=1000 s error map (Figure 8.3).

Figure 8.3: Error values of WAL invariants I_3 to I_7 and Q at T=1000 s. Site locations (black dots) and coastline are given as a reference. Left map shows site locations over the main geological features of the study area.
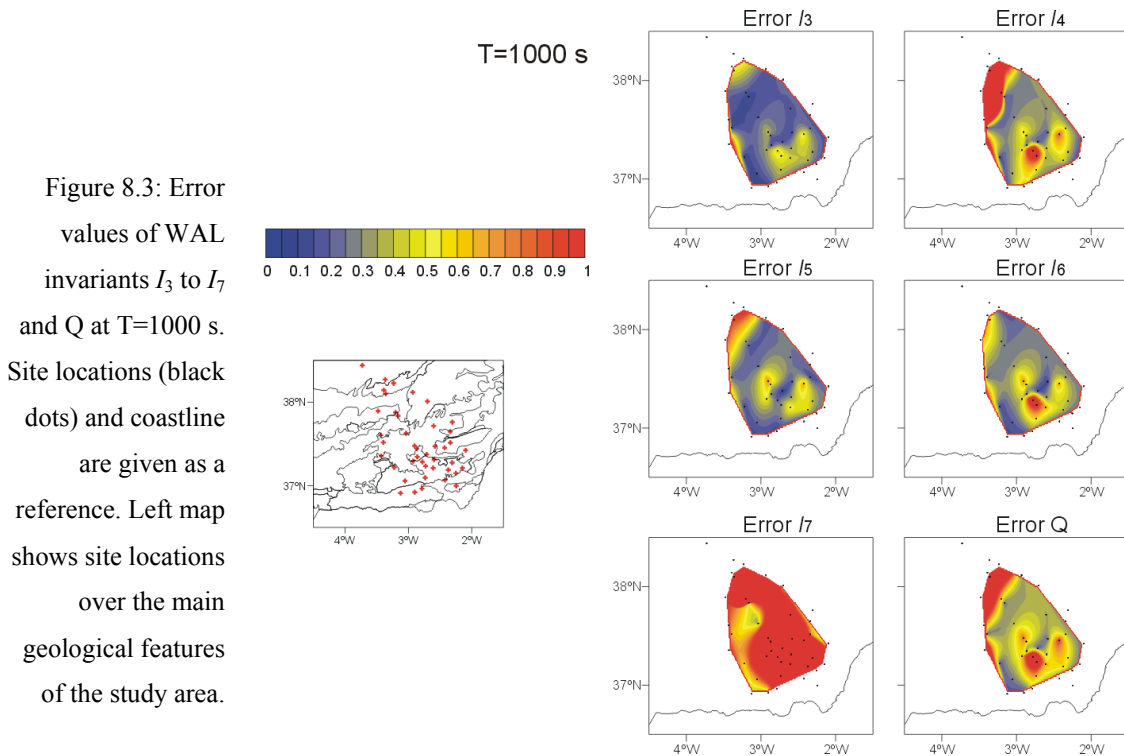
8.1.2 WAL dimensionality analysis of the Betics MT dataset

This dimensionality analysis was carried out for every site and period, using the WALDIM software (chapter 3, section 3.5). The true values of the invariants were estimated and their errors were computed using classical error propagation. For the determination of the dimensionality threshold values $\tau=0.15$ and $\tau_Q=0.1$ were used.

As a preview of the dimensionality results, Figure 8.4 illustrates the dimensionality maps obtained at the same periods used to plot the invariant values (T=0.0032 s, T=0.1 s, T=10 s and T=1000 s). In these four maps there is an ambiguity of 90° in the determination of the strike direction.

At the shortest period, T=0.0032 s, there is a superposition of all dimensionality cases, without a well-defined spatial pattern. This high complexity at a short period could be caused by local shallow bodies that cause distortion in the measured data. It was already observed in section 3.3 (Figure 3.6), in which the shortest periods displayed a complex dimensionality whereas the data at longer periods were 1D or 2D.
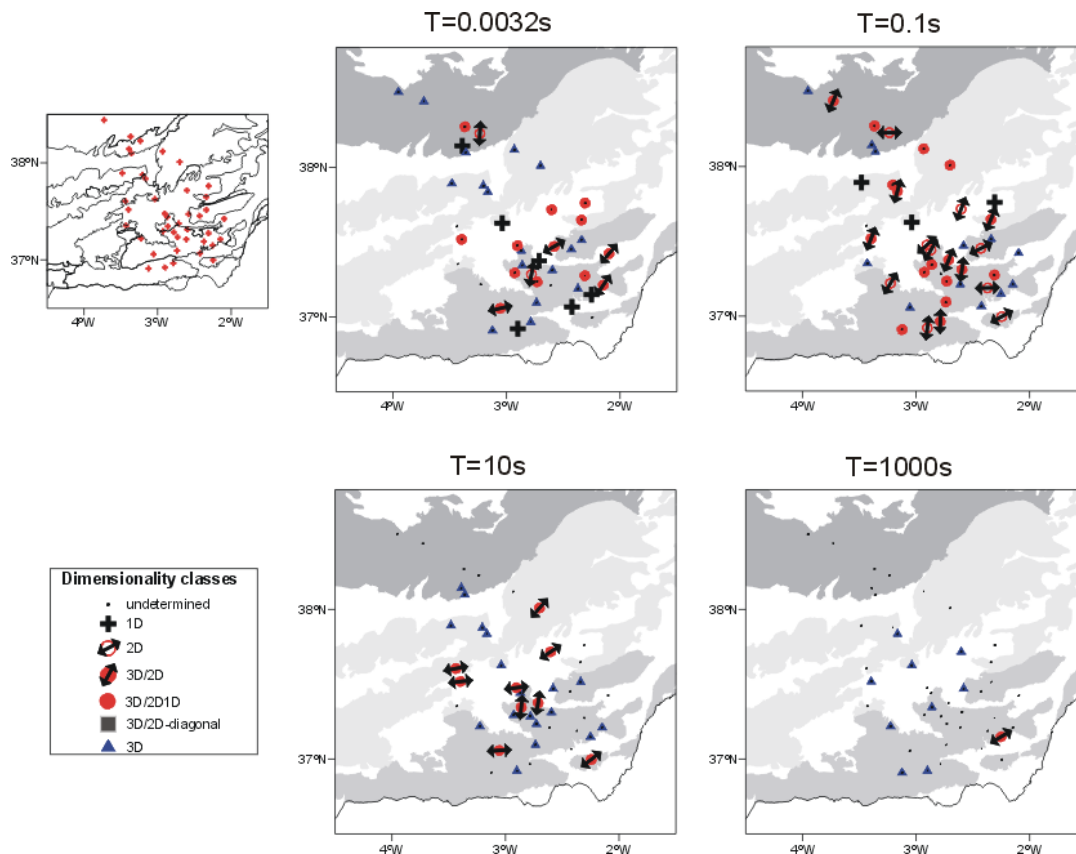
Figure 8.4: Dimensionality distribution according to WAL invariants criteria, for the Betics MT dataset, considering data errors, at four representative periods, T=0.0032 s, T=0.1 s, T=10 s and T=1000 s. Arrows indicate the strike direction, set in the first quadrant. Cases 3D/2Dtwist and 3D/2D are plotted as a single case (3D/2D).

At T=0.1 s, the prevalent dimensionality is 2D, whether affected or not by galvanic distortion, mixed with some 3D/1D2D and 3D cases. Strike directions associated with two-dimensional structures have values around N20°E in the southwesternmost sites and change to values between N60°E and N90°E towards the northeast. The strike determination is good, with small error values (less than 2.5°).

At T=10 s only 3D/2D and 3D cases occur, with an appreciable number of undetermined sites. Strike directions are mainly 0° and N50°E, and the errors are large (up to 20° at some sites).

At T=1000 s, the errors complicate the dimensionality determination, which is reduced to 10 sites, where all but one are 3D.

Considering all periods, the dimensionality could not be determined for thirty percent of the tensors, due to errors, most of them associated with the longest periods.

The dimensionality results (or categories) were grouped at each site in period decade bands (Figure 8.5), in order to represent the prevalent categories and strikes at different penetrations.

The average strike directions with their standard deviations were computed for the bands with 2D and 3D/2D dimensionality. The strike arrows are scaled inversely to the error values. To solve the ambiguity in the determination of the strike direction, the induction arrow information was taken into account when available.

It can be observed (Figure 8.5) that the predominant dimensionality is 3D, with abundant 1D, 2D and 3D/1D2D structures for periods shorter than 1 s and scarcer 3D/2D structures for periods between 1 s and 1000 s.

Up to 1 s (bands 1, 2 and 3, Figure 8.5a to Figure 8.5c), the dimensionality is significantly different between the Iberian Massif, the Betic Chain and the overlying Cenozoic basins. In the Iberian Massif, the structures are 3D and, among these, 2D with strike orientations trending from ENE-WSW to E-W. More to the south, over the Betics, the dimensionality is more complex with 3D/1D2D, 2D, 3D/2D and 3D cases. The bidimensional structures (whether affected or not by galvanic distortion) can be classified into two groups with perpendicular strike directions, one oriented between E-W and WNW-ESE and the other with directions comprised between N-S and NNE-SSW, and a third group, located in the eastern part, with ENE-WSW strike directions. Finally, the sites located over the Cenozoic basins (Guadix and Guadalquivir) are characterised by the presence of 1D cases that are restricted to periods shorter than 0.1 s.

Between 1 s and 10 s (band 4, Figure 8.5d), the structure becomes more 3D. The bidimensional cases are fewer, less precise and located over the Internal Zone of the Betics (southeastern part of the study area) where they also show NNE-SSW and WNW-ESE strike directions.
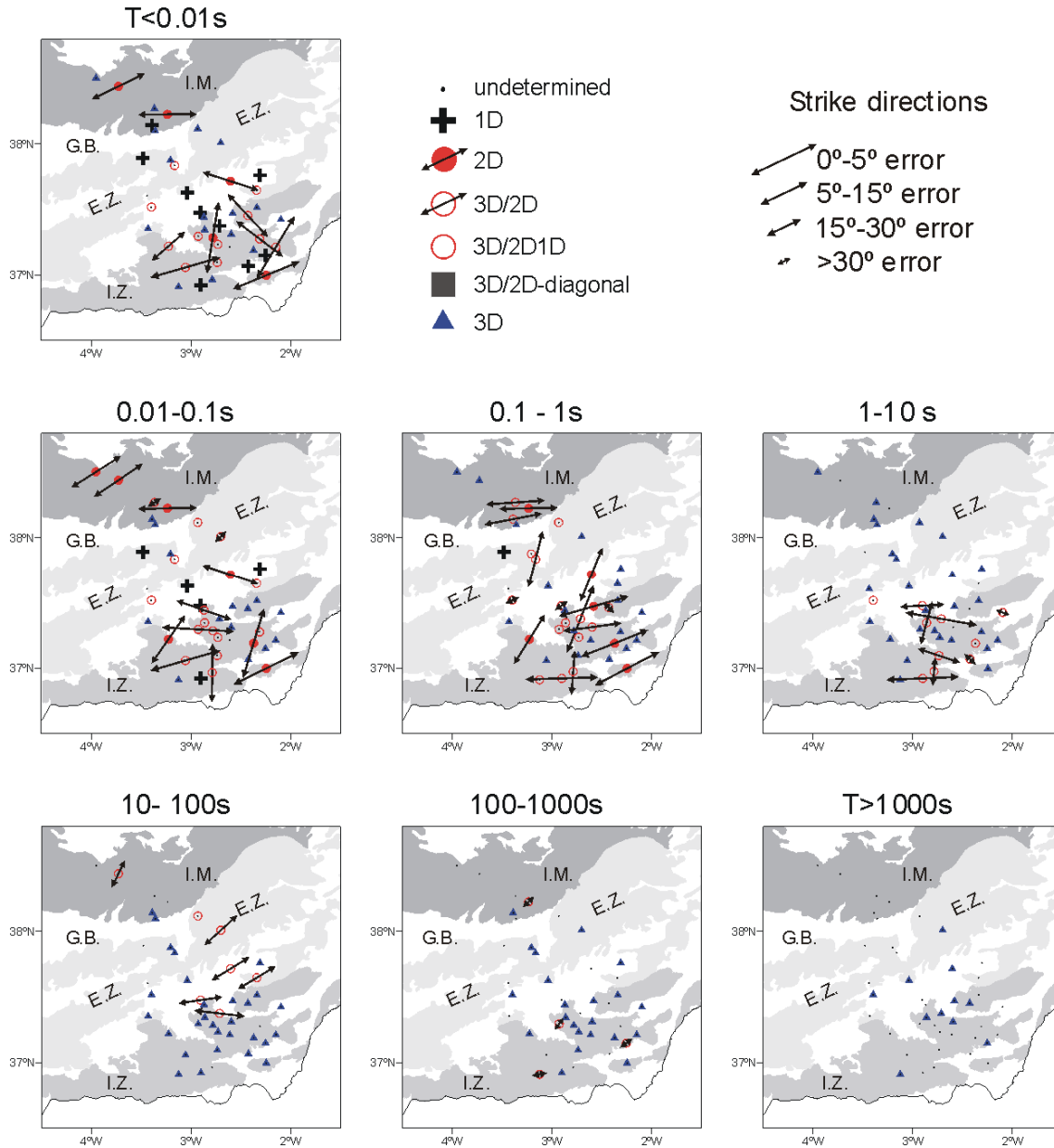
Figure 8.5: Dimensionality results of the Betics MT dataset grouped in 7 period bands. Those cases in which the dimensionality could not be determined are not shown. The arrows indicating the strike directions are scaled by the inverse of the error in the determination of the strike. (a) band 1: T<0.01 s, (b) band 2: 0.01 s – 0.1 s, (c) band 3: 0.1 s –1 s, (d) band 4: 1 s – 10 s, (e) band 5: 10 s – 100 s, (f) band 6: 100 s – 1000 s, (g) band 7: T> 1000 s. I.M.: Iberian Massif, G.B.: Guadalquivir Basin, E.Z.: External Zone and I.Z.: Internal Zone.

These orthogonal bidimensional structures disappear for periods longer than 10 s at the same time that the dimensionality becomes essentially 3D. Despite the predominance of these 3D cases, the presence of periods comprised between 10 s and 100 s (band 5, Figure 8.5e) of relatively abundant bidimensional cases (affected by galvanic distortion) should be noted for the sites located over the Iberian Massif and External Betics. These cases show a strike direction

(NE-SW) which is nearly parallel to that observed for shorter periods in the Iberian Massif. For the longest periods (T < 100 s) (bands 6 and 7, Figure 8.5f and Figure 8.5g), the dimensionality can only be determined at some sites located over the Betic Chain and is in general 3D, with some 2D cases at band 6 (Figure 8.5f) with a high percentage of error.

Discussion

Comparison between the observed geoelectric behaviour and the geological structure of the area denotes a good correlation at upper and middle crustal levels between the changes in the magnetotelluric dimensionality and the kind of deformation affecting the crust. The boundary between the autochthonous Iberian Massif and the allochthonous Betic Chain belongs to a thrust, which dips towards the SSE beneath the Internal Zone and becomes nearly flat at a depth of approx. 5 km beneath the External Zone (Banks and Warburton, 1991). This autochthonous/allochthonous boundary coincides with the most significant change of the dimensionality signature recorded in the analysed data.

Thus, in the allochthonous zones, the dimensionality is highly variable with 2D, 3D/2D, distorted 3D and clearly 3D structures. Further, the strikes show two predominant directions: N-S to NNE-SSW and E-W to WNW-ESE. This signature could be related to the strong Alpine deformation present in this domain which, superimposed upon a previously deformed Variscan basement in the Internal Zone, gave rise to the superimposition of folds and faults of different orientation (Azañón *et al.*, 2002).

Beneath this domain, the upper crustal levels of the autochthonous zone are both 3D and 2D with an ENE-WSW strike. This simpler signature can be correlated with the Variscan structure present in this sector of the Iberian Massif which is characterised by the presence of large E-W to ENE-WSW oriented structural domains (i.e., Ossa-Morena zone) cut by large plutonic bodies with no preferred orientation.

The comparison between this domain and the allochthonous one indicates that the differences of the geoelectrical dimensionality between both domains are related not to the age of deformation but to the major tectonic complexity of the Betic Chain in relation to the Iberian Massif. Whereas the structure of the Iberian Massif is at a large scale mainly bidirectional, the structure of the Betic Chain is characterised by the development of faults and folds which often show changes in direction and are minor in scale.

For the longest periods (> 100 s), in which the inductive length scale is of the same order as the length of the geologic structures, the dimensionality is 3D and it is not possible to distinguish the two domains. The lateral continuity of the conductive body beneath the internal zone in the previous NW-SE 2D model (Pous *et al.*, 1999) is not ensured because the dimensionality obtained is not 2D at a large scale.

8.2 Multisite, Multifrequency Tensor Decomposition Analysis (Strike Code)

Betics MT data were also analysed using Multisite Multifrequency Strike code (McNeice and Jones, 2001). This program performs the Groom and Bailey (G&B) decomposition of the MT tensor data, supported by statistical methods, which can be done in multiple ways: site per site, period per period, for a given group of periods, for a group of sites, fixing some of the parameters or allowing them to be free, etc. In all cases, the strike angle, distortion parameters and the regional tensor (or tensors) are computed. Additionally, a misfit value is given, evaluated from the results and depending on the degrees of freedom of the data considered, which indicates how valid the 3D/2D assumption of the data is.

The final goal of this analysis is to constrain a number of sites within a range of periods in which the data decomposition can be done in view of a 2D model. It means obtaining frequency independent distortion parameters at each site, and a unique strike direction to which to rotate all sites' data. The misfit value is a good tool to determine which these valid sites and period ranges are.

Data analysis using Strike code must be thoughtfully done, as the best fits must be located by the user, supported by the misfit values and other data observations. As an example, site b23 data decomposition was performed, in several ways, and the results compared to those of WAL dimensionality analysis.

In WAL analysis, the error of the MT tensor components was set to a fixed value, to make it comparable to Strike analysis, which utilises a fixed percentage of error in the data instead of using the true data errors. This error percentage was set to 5%. The rest of parameters and options for the WALDIM program were the same as those used in the previous sections.

The Strike program was run with three different settings:

1) Analysis separated in decade period bands, allowing all parameters to be free. Different strike directions and distortion angles were obtained at each band.

2) Analysis of all periods together, all parameters free. One unique strike direction and distortion angles were obtained for the complete period range.

3) Separated analyses in different groups of periods, according to the results from WAL analysis (see Table 8.1, first column):

    a) Up to 1 s (2D according to WAL): assuming a 2D dimensionality, with twist and shear set to zero);

    b) T>1 s (3D/2D, up to 100 s; and 3D, T>100 s): b_1) all parameters free for a single band and b_2) all parameters free, in two groups of periods.

Decomposition results from Strike analysis 1) (Table 8.1) show low misfit values, with the exception of the last band (T>1000 s). The first band (T<0.01 s) has a low misfit, although the strike direction (2°) differs from the direction obtained from WAL (20°) and from the decomposition at the next bands (50° to 60°). From 0.01 s to 100 s, similar values of twist and shear angles are obtained, with low misfit values, which agrees with a 3D/2D description of the data, although strike directions differ up to 10°. From 100 s to 1000 s, misfit values are low, so G&B decomposition is valid, although the strike and distortion parameters differ from those of the previous bands.

Analysis 2) leads to a decomposition with θ=60°, φ_t=0° and φ_e=-11°, similar to the results from WAL and analysis 1) from 1 s to 100 s. However, due to the fact that all periods were considered, the misfit is large, which accounts for the fact that all periods cannot be described as 3D/2D with the same strike direction.

In analysis 3a), a strike angle compatible with WAL analysis is recovered, as expected, in good agreement with a 2D description. In analysis 3b$_1$), which includes all periods from T=1 s to T=100 s, the same strike and distortion angles as in 1) are recovered, once again with large misfit values, due to the longest periods. On the contrary, analysis 3b$_2$) from 1 s to 100 s, the strike and distortion angles are recovered with low misfits, and for T>100 s, a 3D/2D decomposition is obtained, recovering the same parameters as analysis 1) from 10 s to 100 s.

Dimensionality results from site b23 reflected the coincidences and discrepancies between both dimensionality analyses. The Strike program itself showed how it is possible to obtain different decompositions from the same data, since the choice among them depends on a misfit value and not on the real behaviour of the individual MT tensor at each period. At this site, it is not possible to obtain a 2D or 3D/2D description of the data with a unique strike direction. However, when the strike analysis is performed in different bands (e.g. 3b$_2$), the results are compatible with WAL.

The principal difference between both methods is that Strike does a global interpretation of a group of data whereas WAL analysis accounts for each individual MT tensor. An important question remains open, that is, to consider whether trying to fit the data to an a-priory description, or to obtain the exact dimensionality information from each MT tensor, even if it does not have a trivial physical explanation.

Period bands	WAL analysis	Strike analysis				
		1) All parameters free - analysis per bands	2) All parameters free - all periods	3) Two period bands: a) Non distortion b_1) Free – one band b_2) Free – two bands		
				a)		
T<0.01 s		$\theta=2°$ $\varphi_t=-1.5°$ $\varphi_e=9°$		$\theta=18°$		
0.01 s-0.1 s	2D $\theta = 20°\pm5°$	$\theta=50°$ $\varphi_t = 0°$ $\varphi_e = -9°$	$\theta = 60°$ $\varphi_t =0°$ $\varphi_e = -11°$			
0.1 s-1 s		$\theta=60°$ $\varphi_t = -1°$ $\varphi_e = -11°$				
1 s-10 s	3D/2D $\theta = 57°\pm9°$ $\varphi_t =2°\pm0.5°$ $\varphi_e = -9°\pm2°$	$\theta = 59°$ $\varphi_t = -0.5°$ $\varphi_e = -10°$		b_1) $\theta = 57°$ $\varphi_t = 0°$ $\varphi_e = -10°$	b_2) $\theta = 57°$ $\varphi_t = 0°$ $\varphi_e = -10°$	
10 s-100 s	3D/2D $\theta = 59°\pm3°$ $\varphi_t =3°\pm1°$ $\varphi_e = -16°\pm2°$	$\theta = 55°$ $\varphi_t = -0.5°$ $\varphi_e = -9°$				
100 s-1000 s	3D	$\theta = -17°$ $\varphi_t = 15°$ $\varphi_e = 39°$			$\theta = -13°$ $\varphi_t = 12°$ $\varphi_e = 39°$	
T>1000 s	3D	$\theta = -13°$ $\varphi_t = 12.5°$ $\varphi_e = 40°$				

Table 8.1: Results from site b23 WAL analysis (τ=0.15 and τ_Q=0.1) and G&B decomposition, using Strike code: 1) Analysis separated in seven period bands, allowing all parameters free. 2) All periods together, all parameters free. 3) Two different analyses at short and long period bands, according to WAL dimensionality results: a) Short periods, fixing distortion parameters to zero (2D without distortion). b) Long periods, allowing all parameters to be free (b_1: one band, b_2: two bands). Grey backgrounds indicate large misfit values ($\chi^2/\chi^2_{95\%} \geq 1$, poor agreement between the data and a 2D or 3D/2D description).

For all sites of the Betics MT dataset, Strike code was run following this scheme, considering 5% error in the MT tensor components:

1) Analysis site per site, divided into bands containing one or two periods each, obtaining a different decomposition at each band and site.

2) For the sites with a preferred strike direction for all periods obtained in analysis 1), analysis site per site, fitting all the data from each site to the same distortion parameters.

3) Joint analysis of sites with similar strike directions obtained, fixing the strike direction and computing distortion parameters at each site.

Figure 8.6 shows rose diagrams of the strike directions obtained from analysis 1), for eight sites belonging to the different zones of the study area. These plots allow identification of sites that have a prevalent strike direction (or two perpendicular directions) and, consequently, may agree with a 3D/2D description (sites b14, b23, b55, b56 and b58), or may not (sites b24, b40 and b31). From the complete dataset, sites with a preferred strike direction are shown in Table 8.2.
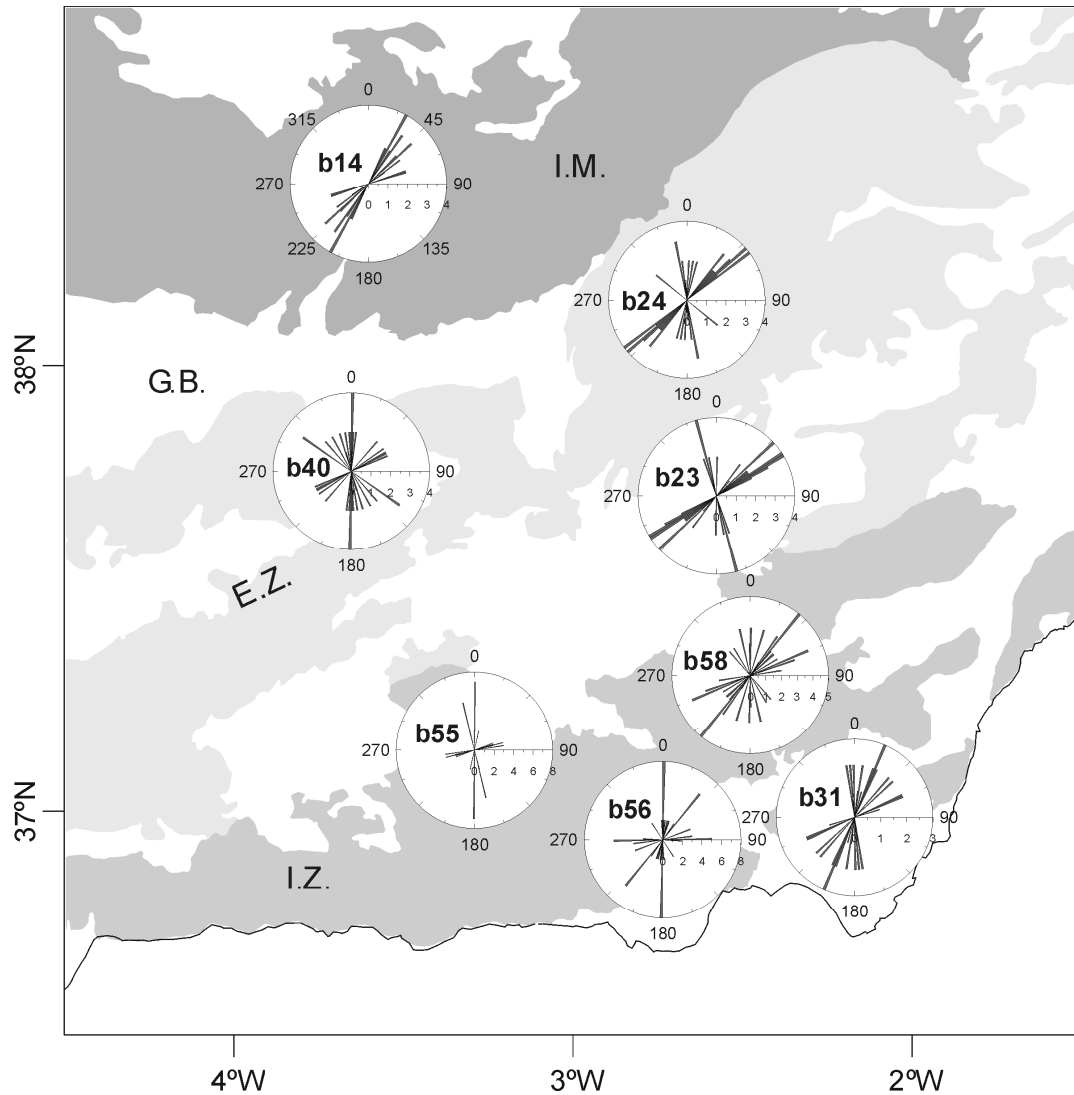
Figure 8.6: Strike directions obtained from Strike analysis 1), for eight sites from the Betics MT dataset, plotted as rose diagrams over the study area.

In analysis 2), the values of the misfits made it possible to corroborate at which sites a 3D/2D assumption is valid (Table 8.2). Only at a few sites is it possible to make a G&B decomposition valid for all periods.

Site	Strike (°)	φ_t (°)	φ_e (°)	$\chi^2/\chi^2_{95\%}$	Decomposition quality ([2])
b31	-5.1 ± 9.6	7.1	-17.1	2	medium
b57	0.0 ± 1.3	6.7	2.3	2	medium
b37	0.0 ± 4.5	6.7	-21.6	1	medium
b01	0.0 ± 5.6	-4.6	-25.0	4	poor
b56	0.0 ± 9.7	0.0	-1.3	3	poor
b08	0.5 ± 7.9	6.5	10.5	2	medium
b35	3.0 ± 9.2	2.7	8.7	6	poor
b39	12.0 ± 2.6	-1.3	-13.2	4	poor
b55	26.0 ± 19.0	-2.0	-33.0	3	poor
b17	28.0 ± 2.0	-7.3	1.7	1	good
b14	34.7 ± 0.3	-3.1	11.0	2	medium
b58	52.0 ± 3.9	1.4	-26.0	0.75	good
b23	57.0 ± 2.0	0.2	-11.0	2	medium
b52	59.0 ± 2.5	1.7	-35.8	0.9	good
b26	62.5 ± 1.0	2.5	-38.8	0.7	good
b20	65.2 ± 10.0	10.0	-17.5	1	good
b09	72.4 ± 0.0	60.0	-42.0	0.025	good
b06	74.0 ± 2.5	-4.5	-25.5	1	good
b19	87.0 ± 1.6	16.0	14.0	3	poor

Table 8.2: Strike analysis 2) results at sites that were identified as possibly 3D/2D in analysis 1). Data has been disposed in ascending Strike value order.

Despite the low misfit values, and given that some of these results indicate a prevalent strike direction (around 0° or its perpendicular, 90°), analysis 3) was performed using sites b01, b08, b31, b19, b35, b37, b56 and b57, while fixing the strike value to 0°, and by separating into period decade bands to obtain the misfit values. The misfit values were substantially greater than in the previous decompositions, given that all sites must fit to the same strike direction, and, since the analysis was performed in period bands, only at a few sites were period independent distortion parameters obtained. Consequently, it seems too restrictive to analyse a

---

[2] The Strike program computes the misfit of the decomposition according to the departure of the individual data from the decomposition parameters, through a χ^2 test. The program outputs provide the χ^2 values that would correspond to 65% and 95% confidence intervals and the χ^2 values resulting from the decomposition. If χ^2 is smaller than $\chi^2_{95\%}$ the assumption is valid. Otherwise, the quality of the misfit is defined in this thesis as medium (if $\chi^2/\chi^2_{95\%} \leq 2$), or poor (if $\chi^2/\chi^2_{95\%} > 2$).

group of sites with a fixed strike value. The analysis of the individual sites showed better fits, with strike values differing up to 3° between them.

8.3 The Magnetotelluric Phase Tensor

The phase tensor (chapter 2, section 2.6) was computed from the magnetotelluric tensors of all the Betics MT dataset, as to provide another representation of its dimensionality.

Figure 8.7 represents phase tensor representations and α_p and β_p angles corresponding to site b01, along the measured periods. At this site, according to WAL (τ=0.15) the dimensionality is 3D, with the exception of the period range 0.01 s to 0.1 s, where it is 2D, with an average strike direction of N60°W (Figure 8.5).

The orientation of the phase tensor ellipses (Figure 8.7a) changes smoothly, pointing from WNW at short periods, almost N at middle periods and WNW again at long periods. Discrepancies of 90° with respect to the strike directions computed from WAL invariants (Figure 3.7) appear, as the phase tensor establishes as strike the direction in which the difference between MT tensor phases is at a maximum. Although not shown, the errors of α_p are moderate at short periods (T < 1 s, σ_{α_P} < 10°), and large at middle and long periods(T > 1 s, σ_{α_P} = 10° - 70°).

A first glance at the ellipses and α_p orientations suggests that the data is 2D, since the ellipses have well distinguishable maximum and minimum axes and are approximately aligned with the direction given by α_p. β_p (Figure 8.7b) has, up to 0.5s, small values and errors, which agrees with a 2D description of the data, with the same strike direction as in WAL (N60°W). At middle and longer periods, β_p is non-zero, with large error bars, which, also taking into account the large errors of α_p, allows one to state that the dimensionality is 3D.

Consequently, to accurately establish the dimensionality using the phase tensor, it is necessary, apart from the analysis of the diagrams, to take into account the values of β_p and the errors.

With the exception of the shortest periods, those up to 1 s, the WAL and the phase tensor descriptions agree well. This discrepancy at the shortest periods lies with the values of I_7, which are not extremely large ($I_7 \approx 0.20$), so a WAL analysis using a slightly larger threshold value would have led to a 2D description (I_5 and I_6 are close to zero), as with the phase tensor description. However, the strike directions θ_1 and θ_2 obtained are significantly different, so a 3D description is more adequate.

(a)

Phase tensor ellipses and α_P

(b)
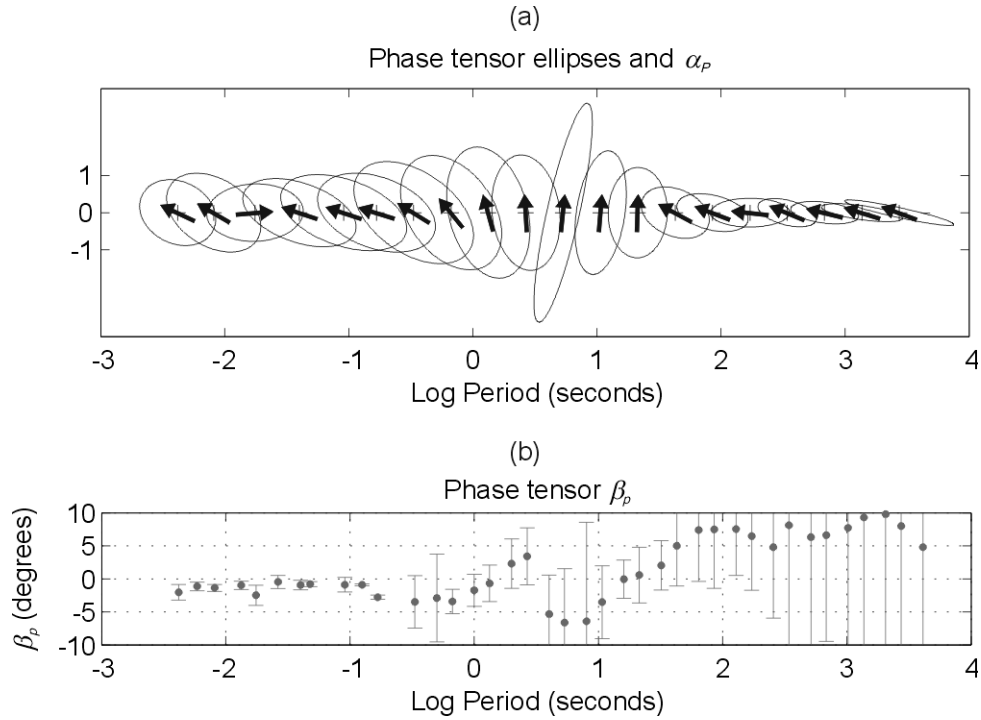
Phase tensor β_p

Figure 8.7: Phase tensor representation for site b01 at different periods. a) Ellipses and α_p directions. b) Values of β_p and errors.

Figure 8.8 presents phase tensor diagrams at different periods, representing different period bands, for all sites. Apparently, similar to what was observed at site b01, there is good agreement between the ellipses and the directions of α_p. However, directions change abruptly from site to site and along the different periods, and in general, values of β_p, as well as their errors, increase with the period. Overall, this map provides an image that validates the high complexity of the data.

8.4 Modelling Strategies

The main purpose of data dimensionality analyses is to precisely identify which type of model is required to attempt to reproduce the geoelectric structures below the study area. As for the Betics MT data, these are interpreted to be 1D and 2D at short and middle periods and generally 3D at the longest periods. Those sites with 2D or 3D/2D dimensionalities generally present period dependent strike and distortion parameters. Strike code provided a period independent decomposition of the data at each site, although with large misfit values. Consequently, the wiser option is to endeavour to do a 3D modelling. Since it must be built by forward modelling techniques, the dimensionality information is fundamental in its

construction, as they allow defining the directionality of conductivity structures at some parts of the models or the complexity of these at a certain depth.

Nevertheless, given the time and computing costs of 3D forward modelling, subsets of the data in which the 2D decompositions are not too large and which have similar 2D strike directions, can be used to perform inversions to obtain 2D models perpendicular to the strike, as previews of the final modelled structures.
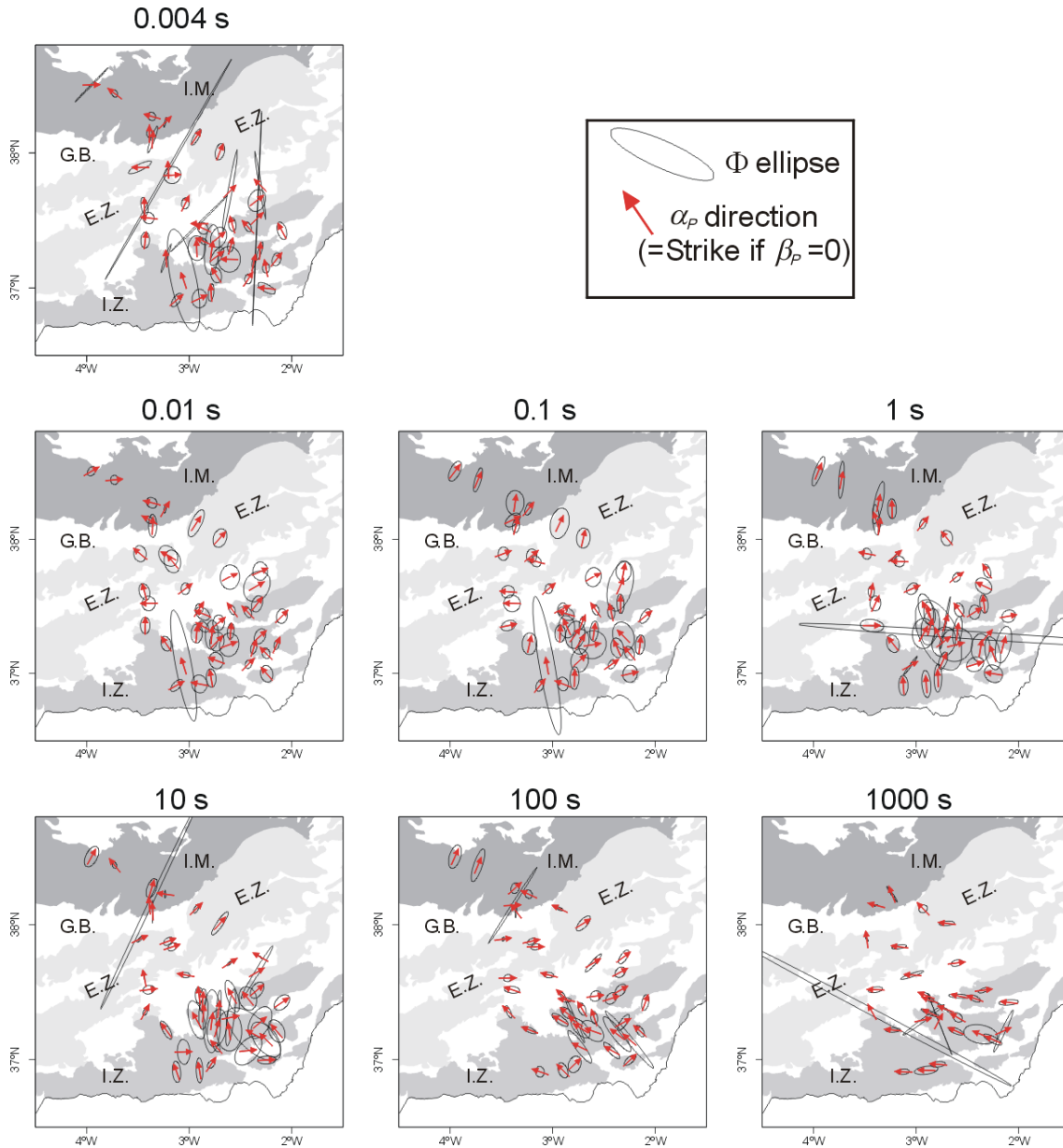
Figure 8.8: Phase tensor maps of the Betics MT data at different periods.

8.5 Conclusions

Dimensionality analysis of the Betics MT data was performed using the WALDIM program based on WAL invariants criteria, taking into account data errors, and with induction arrows complementing the information when available.

The geoelectric structures are mainly 3D, with some 1D cases located over the basins at short periods. Bidimensional structures with N-S to NNE-SSW and E-W to WNW-ESE orientations were found in the allochthonous zones, and with E-W to ENE-WSW orientations in the autochthonous zones. The more complex dimensionality of the Betic Chain is interpreted as being related to the superimposition of processes that took part in its evolution, whereas the Iberian Massif, only affected by the Variscan deformation, shows a simpler dimensionality. The abundance of the 3D structures increases with the period and towards south.

A comparison with other methods showed some similarities but also important discrepancies, a result of the assumptions on which each method is based. G&B decomposition only agrees with the WAL description when this analysis is performed using small subsets of data, and corroborates that the data cannot be described as 2D with a prevalent strike direction. The phase tensor maps of the Betics also confirmed the complex character of the data.

Dimensionality results point at 3D modelling as the best strategy to reproduce geoelectric structures of the Betics, although some 2D models can also be constructed from subsets of the data, which may display a preview of the conductivity structures.

Chapter 9: 2D Modelling

The principal conclusion of the previous chapter is that the dimensionality of the Betics MT data is mainly 3D and that a 3D model is necessary to reproduce the conductivity structures.

However, free 3D inversion software has just been released (Siripunvaraporn *et al.*, 2005, March 2006), and 3D models are still constructed through forward modelling. Meanwhile, 2D inversion is the commonest modelling tool.

In this sense, previous to the 3D modelling, 2D modelling is presented in this chapter. The aims are to do a critical revision of the only prior MT model of the Betics, and also to explore the possibilities of 2D inversion of 3D MT data. In the next chapter, having obtained the 3D model, the limitations of 2D modelling will be demonstrated.

9.1 Sensitivity Study of the Previous 2D Model

The first 2D MT model of the Betics, referred to as MT1 (Pous *et al.*, 1999) was constructed using part of the sites registered in the Betics 94-95 survey (chapter 7, section 7.1), projected over a NW-SE profile. The orientation of the model and the sites to be projected over it were chosen according to the Groom and Bailey decomposition, resulting in a 45° strike, and the induction arrows, which allowed confirmation of the $N45^{o}E$ strike direction and not its perpendicular $N45^{o}W$. Static shift corrections were applied, such that curves of the sites located over the Internal Betics were shifted up to values on the order of 1000 Ω·m at the shortest periods.

TE and TM responses of 15 sites over the profile, with approximately 38 periods each, were inverted through RRI (Smith and Booker, 1991), and the model responses were computed using the code of Wannamaker *et al.* (1987).

The description of the main conductive (A, B, D and E) and resistive (C) structures identified in the model (Figure 9.1) is found in chapter 6, section 6.2.7.

The dimensionality analysis (chapter 8) pointed to a higher complexity of the geoelectric structures. Below the sites located over the MT1 profile (Figure 9.2) the dimensionality is 1D or 2D at the shallowest depths, whereas at middle and lower depths, it is mainly 3D. Furthermore, the 2D resistivity model is the result of an inversion process, so it is not the only possible solution since other models can fit the same data.

Hence, a revision of the model is necessary in order to discern which is the lateral extent of the conductivity structures and up to which degree the 2D assumption is valid. As a first approach, a sensitivity test of the model was performed.

The purposes of the sensitivity test were to evaluate the sensitivity responses of the 2D model and to check which parts of this model are less sensitive to the recorded data, indicating that they have lower resolution, focusing especially on the lower crustal conductor.

Sensitivity tests (Schwalenberg *et al.*, 2002) are performed to determine how well resolved a model is in terms of its resistivity values and structure, and are generally based on forward modelling in a trial and error style. These tests can be broached from linear and non-linear points of view. The former utilises the sensitivity matrix whereas the latter is based on systematic forward modelling studies and evaluations of the misfits. The linear approach is mainly valid for conductive structures, for which MT responses are highly sensitive to small resistivity variations. On the contrary, given the much lower sensitivity of the MT responses to variations in resistive structures, the non-linear approach is necessary when testing such structures, which must be subjected to large resistivity variations.

Since the aim of this test is to focus on the deep conductive structure, the linear approach was followed. This approach utilises a linear approximation of the sensitivity matrix that contains the partial derivatives of the data responses (2 modes of apparent resistivity and 2 modes of phases obtained at each station at each period) with respect to the model parameters (resistivity values of each model element).

To reduce the number of parameters, the sensitivity of each model element is computed from the normalised sum of the column elements of the sensitivity matrix:

$$s_j = \frac{1}{\Delta_j} \sum_{i=1}^{N} \left\| \frac{1}{\sigma_i} \frac{\partial f_i(m)}{\partial m_j} \right\|, \tag{9.1}$$

where Δ_j is the model element size, σ_i is the error of the response (f_i) and m_j is the model element.

The elements with large sensitivity values are better determined by the data, whereas those with lower values are worse determined and could not be relevant when fitting the measured data. Once the sensitivity values are obtained, the validity of the model can be restricted to the elements with higher sensitivity values.
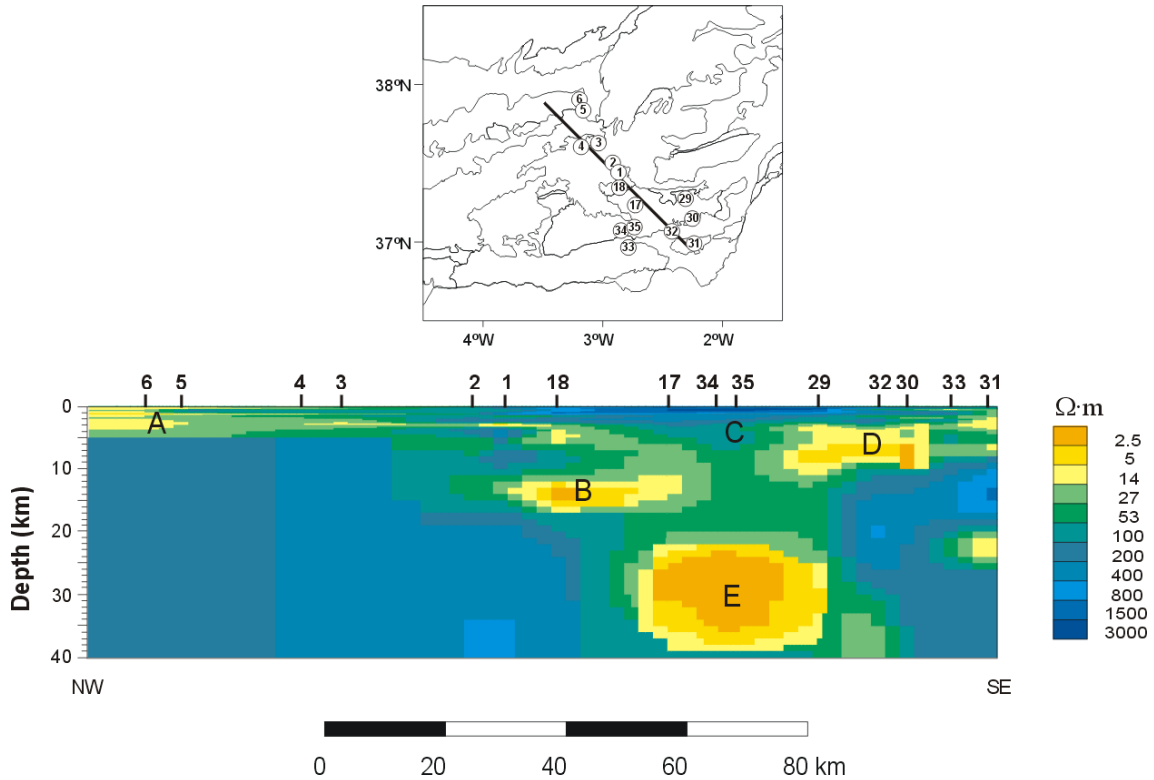
Figure 9.1: MT1 resistivity model. A, B, C, D and E are the main conductive structures identified and interpreted (Pous *et al.*, 1999).
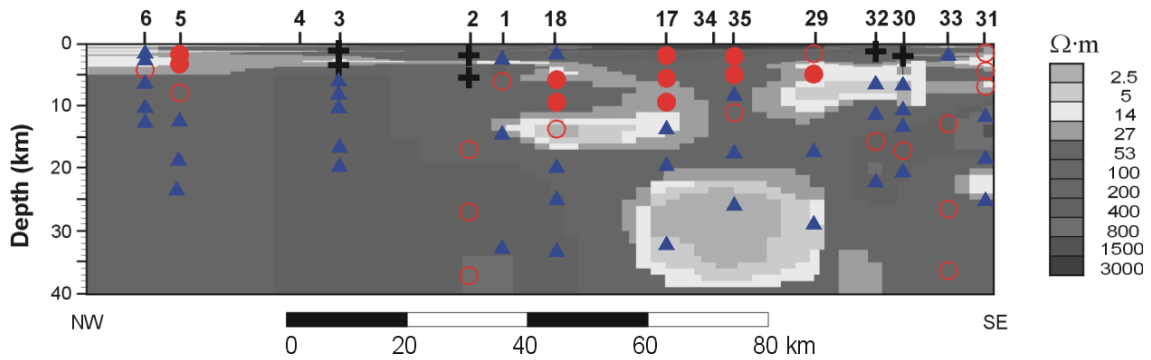
Figure 9.2: Dimensionality of the MT sites along the MT1 profile, displayed over the resistivity model. Dimensionality cases are period-averaged converted into Bostick-depths (see chapter 8, equation 8.1), including the static shift corrections. ✚:1D; ◯: 2D or 3D/2D; ●: 3D/2D and ▲: 3D.

The sensitivity matrices of the studied model were computed for both TE and TM mode responses and for TE and TM modes separately. Two datasets were considered: the one containing all 15 sites used to create the model; and a second set in which the sites located over the deep conductor (17, 34 and 35) were removed. This second dataset was considered in order to determine whether the deep conductor is only necessary to fit the above sites, which would indicate that this is possibly a local feature, or also to fit the lateral ones.

Considering a sensitivity threshold of 10^{-4} (Schwalenberg *et al.*, 2002; Ledo *et al.*, 2004) for all 15 sites, the sensitivity maps (Figure 9.3) show that the model is well resolved up to 30km, for TE+TM modes and for the TM mode alone. For the TE mode, the model is well resolved up to only 20km, with the exception of the deep conductor, which is more sensitive to this mode than TM. TE mode is more sensitive to the finite strikes of 3D structures (Wannamaker *et al.*, 1984) and, since this sensitivity test is based on 2D assumptions, it cannot resolve lateral continuity in the deep conductor.

The removal of sites 17, 34 and 35 from the datasets only modifies significantly the zone below these sites (Figure 9.3), where the sensitivity decreases for all modes, especially at the shallowest depths, coinciding with the resistor C (Figure 9.1). The deep conductor is well resolved too, as expected given the large penetration depths at the resistant body above.
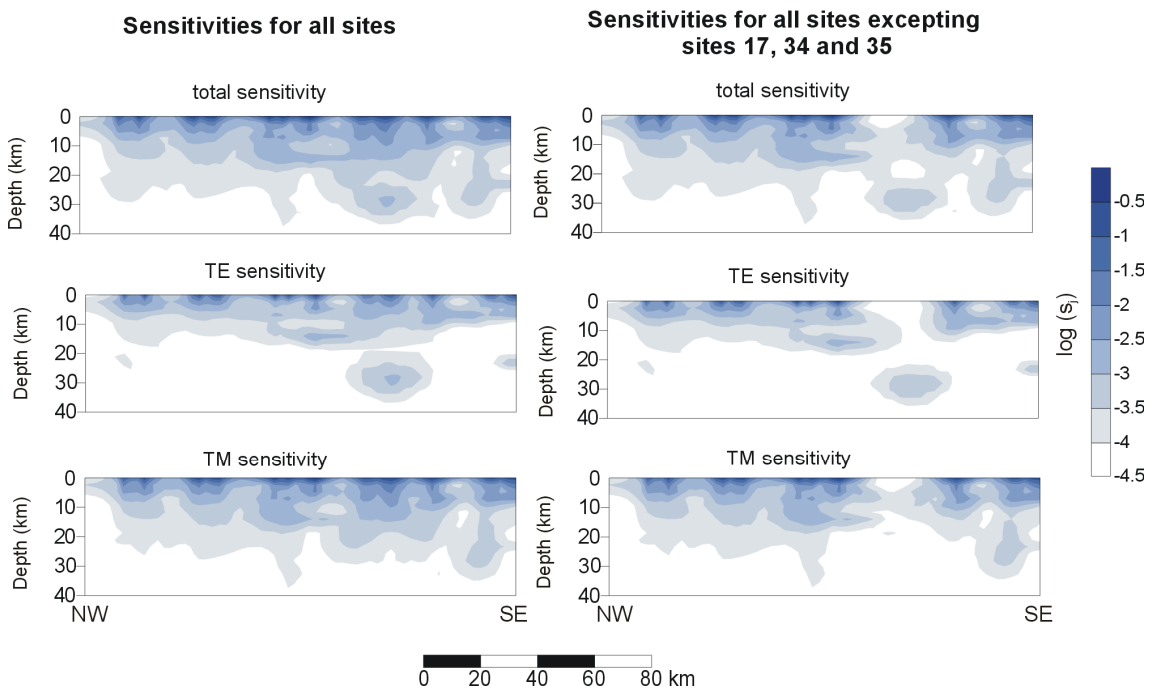
Figure 9.3: Sensitivity values of the 2D model MT1 to the MT responses used in the inversion: TE and TM mode, only TE mode and only TM mode. Left: all sites used in the inversion. Right: all sites but sites 17, 34 and 35 located over the deep conductive body.

The results for both datasets indicate that the presence of the deep conductive body is indeed necessary to fit the data. However, the 3D dimensionality of the data, questions the 2D approach as the most appropriate, and previous studies (Ledo *et al*., 2002) have already demonstrated the problems involved in the 2D interpretation of 3D MT data.

9.2 New 2D Models of the Internal Zones

Using sites from the Internal Zone, the part of the Betics dataset with the highest density of sites, and with more unknowns regarding its conductivity structure (such as the character of the deep conductor) three 2D models were constructed. As already stated, the aims of these 2D models were to obtain a preview of the conductivity structure of the Internal Zone, using inversion techniques, prior to 3D forward modelling.

Three different inversion codes, RLM2DI, REBOCC and DetREBOCC, were used and compared.

9.2.1 Review of inversion codes

RLM2DI code (Mackie *et al.*, 1997) solves the 2D inversion problem using Tikhonov regularization and computes forward responses through finite differences. It allows inverting any of the TE and TM modes resistivities and phases.

REBOCC (reduced basis Occam's inversion) code (Siripunvaraporn and Egbert, 2000) is a variant of the OCCAM algorithm (Constable *et al*., 1987) that allows inverting any of resistivity or phases of TE and TM modes and real and imaginary parts of the Tipper. This code is based on the assumption that MT data are in general smooth and sometimes redundant (if sites or registered periods are too close, although in the Betics dataset this is not the case). Hence, instead of whole datasets, subsets of these are used, which implies a reduction of the size of the sensitivity matrix, without losing details of the model. All these characteristics result in a considerable reduction of memory requirements and computing time.

Pedersen and Engels (2005) propose a routine 2D inversion using the determinant of the impedance tensor, as a variant of REBOCC code, which is here referred to as DetREBOCC. The failure of inverting data that is not truly 2D or that does not have a well-resolved strike direction, decoupled into TE and TM modes, has been largely. Instead, the authors demonstrate that the inversion of the transfer functions (resistivity and phase) related to the determinant of the impedance tensor is a useful tool, as the data are independent of the chosen strike direction, and consequently, of the profile orientation.

The determinant of the impedance tensor is a complex number defined as the square root of the actual determinant (chapter 2, eq. 2.3c, although in that equation it was defined from the MT tensor), thus it has units of impedance (Ω):

$$Z_{DET} = \sqrt{Z_{xx}Z_{yy} - Z_{xy}Z_{yx}} = |Z_{DET}| e^{i\varphi_{DET}} \, , \, ^{(1)} \tag{9.2}$$

and the related transfer functions, determinant resistivity,

$$\rho_{DET} = \frac{1}{\mu_0 \omega} |Z_{DET}|^2 \, , \tag{9.3}$$

and determinant phase, φ_{DET}.

In a truly 2D environment, $\rho_{DET} = \sqrt{\rho_{TE} \cdot \rho_{TM}}$ and $\varphi_{DET} = \frac{1}{2}(\varphi_{TE} + \varphi_{TM})$.

The DetREBOCC code utilises data computed from eqs. 9.2 and 9.3 (using all the components of the impedance tensor), while the inversions are carried out using 2D assumptions.

If static shift was corrected at resistivity TE and TM curves, the following approximation was defined to transfer this correction to the determinant resistivity:

$$\rho'_{DET} \approx \sqrt{s_{TE} \cdot \rho_{TE} \cdot s_{TM} \cdot \rho_{TM}} = \sqrt{s_{TE} \cdot s_{TM}} \cdot \rho_{DET} \, , \tag{9.4}$$

where ´ denotes the corrected value and s is the relationship between corrected and uncorrected resistivities. DetREBOCC code can also invert the tipper component, as in REBOCC.

In any of these three inversion processes, RLM2DI, REBOCC or DetREBOCC, the misfit between data and model responses at each step is computed as the *root mean square* (*rms*), whose minimisation is also searched by the inversion algorithms:

$$(rms)^2 = \sum_{j=1}^{NS} \sum_{i=1}^{NP} \sum_{k=1}^{NVAR} \frac{|p_{k,meas} - p_{k,model}|^2}{|\delta p_k|^2} \, , \tag{9.5}$$

---

[1] $Z_1 = Z_{xx}Z_{yy} - Z_{xy}Z_{yx} = |Z_1| e^{i\varphi_1} \, ; \, |Z_1| = \sqrt{X_1^2 + Y_1^2}$ and $\varphi_1 = arctan(Y_1 / X_1)$

$X_1 = Re(Z_{xx}Z_{yy} - Z_{xy}Z_{yx}) = Re(Z_{xx})Re(Z_{yy}) - Im(Z_{xx})Im(Z_{yy}) - Re(Z_{xy})Re(Z_{yx}) + Im(Z_{xy})Im(Z_{yx})$

$Y_1 = Im(Z_{xx}Z_{yy} - Z_{xy}Z_{yx}) = Re(Z_{xy})Im(Z_{yx}) - Re(Z_{yx})Im(Z_{xy}) - Re(Z_{xx})Im(Z_{yy}) - Re(Z_{yy})Im(Z_{xx})$

$Z_{DET} = \sqrt{Z_1} = |Z_1|^{1/2} e^{i(\varphi_1 / 2)}$

where p_k refers to the variables inverted (*meas*: measured value, model: model response) and δp_k is the error of the variable, *NS*: number of sites used in the inversion, *NP*: number of periods *NVAR*: number of inverted variables. The decreasing rate of the *rms* accounts for the convergence rate of the inversion process.

Commonly, the *rms* corresponding to the final model is given to quantify the quality of the inversion. It can also be computed for a single site, a determined frequency, a range of periods, and it is usually averaged over the total number of data (divided by *NS·NP·NVAR*).

9.2.2 Two-dimensional profiles

Three profiles were chosen to construct the 2D models (Figure 9.4):

- an east-west profile (termed EW), along which sites b55, b54, b52, b35, b17, b57, b58, b29 and b30 were projected.
- a north-south profile (termed NS1), containing sites from the northern boundary and western side of the Sierra de los Filabres, Eastern side of Sierra Nevada and Sierra de Gádor (b53, b51, b52, b17, b57, b35 and b56).
- a north-south profile (NS2), with sites from Sierra de las Estancias and the Eastern part of Sierra de los Filabres (b37, b29, b58, b30 and b32).

Note that some of the sites were projected over two (perpendicular) profiles.
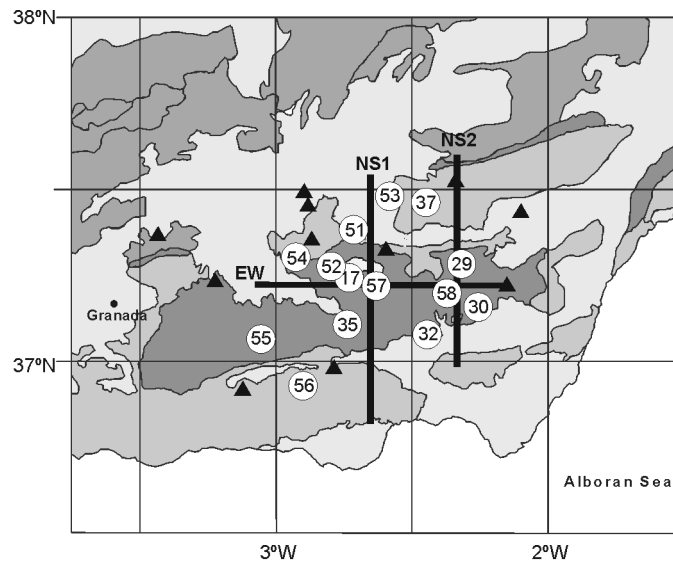
Figure 9.4: Location of Internal Betics MT sites and the 3 profiles, EW, NS1 and NS2 along which the three 2D models were constructed. Numbers in circles are the sites projected over one or two of the profiles.

9.2.3 Data set-up

In order to get the data ready to carry out the inversions, these four steps were conducted:

1) Rotations, identification of TE and TM modes

Since the data sites were projected over EW (i.e. 0° Strike) and NS profiles (90° Strike), the data did not need to be rotated. However in each case TE and TM mode had to be defined according to the alignments of the profiles and hypothetical strike directions (Figure 9.5). In the EW profile, since the strike direction is NS (i.e., along x), xy ≡ TE mode. In the NS profiles, yx is aligned along the strike and yx ≡ TE mode.

If tipper is used in the inversion (e.g., REBOCC and DetREBOCC inversions), only the component aligned with the profile is considered (in the 2D assumption, the other component is zero).
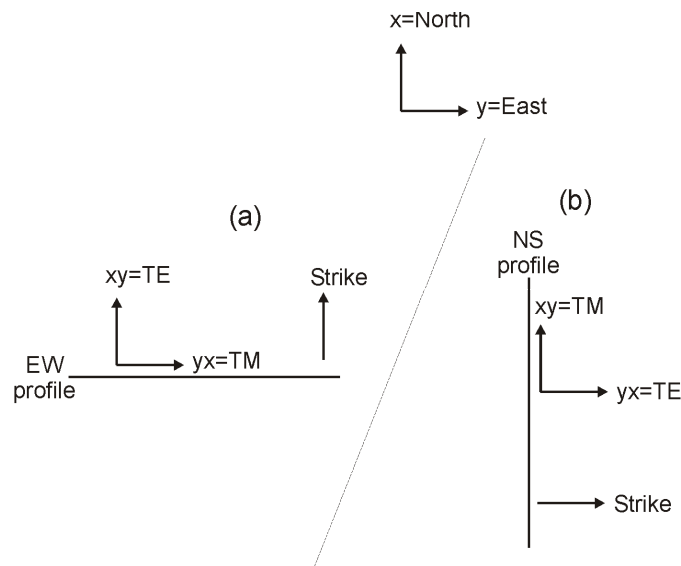
Figure 9.5 Schematic representation of TE and TM modes according to the profile alignment, a) EW and b) NS, using the same reference frame: x=North and y=East. xy ≡ E_x/B_y and yx ≡ E_y/B_x. TE: transversal electric mode: Electric field aligned with the Strike direction. TM: transversal magnetic: Magnetic Field aligned with the Strike direction.

2) Data decomposition

Given the complexity of the data and the presence of galvanic distortion, as obtained from the Groom and Bailey decomposition, data from each profile were decomposed

using the Strike code, to obtain period independent distortion parameters at each site. In this case the strike direction was fixed to 0°.

The resulting distortion parameters were significant (i.e. twist and shear angles in general greater than 5°), with large misfits: considering 5% error, values of $\chi^2/\chi^2_{95\%}$ between 1 (site b37) and 18 (site b30), with an average of $\chi^2/\chi^2_{95\%} = 5$, as expected from the invariants dimensionality analysis.

Final responses were computed by the Strike code as:

$$M_{2D*}(\omega) = C^{-1}M_m(\omega) \,, \tag{9.6}$$

where 2D* refers to the fact that the MT tensor is not 2D, but that the non-diagonal components are assumed to be aligned with the principal directions. From this tensor, the xy and yx resistivities and phases to be inverted were obtained.

3) Static Shift corrections

Data decomposition does not resolve the static shift, which remains unknown. From the processed data (see Appendix D), evidences of static shift are seen as displacements between xy and yx resistivities, starting at the shortest periods, and are in general smaller than one decade.

Static shift was corrected by joining both resistivity curves. The reference resistivity was taken by observing the joining sites curves. This resulted that only yx curves were shifted.

In the inversions, several tests were made using or not using these statics shift corrections.

4) Inactivating periods

Finally, before running 2D inversions, spikes in the curve responses, as well as overly large tipper values were removed to obtain responses as smooth as possible. This was done site by site, by observing all responses' plots. On average, 15% of the data were rejected at each site (see table D.1).

5) Data errors

All data responses to be inverted were assigned an error floor (e_f), i.e., an error level to be taken as the error of a response in the case that its real error is larger than this error floor.

Resistivity and phase error floors were chosen so they have the same weight in the responses, whose relationship is $e_f(\varphi) = \frac{1}{2}e_f(\ln\rho)$.

With regard to the tipper, the recommended error floor, $e_f|\vec{T}| \geq e_f(\ln\rho)\cdot\max|\vec{T}|/2$ (Gabàs *et al.*, 2003) was used.

9.2.4 Inversions and models

For each of the profiles, all the inversions performed departed from an homogeneous model of 100 Ω·m, using a period range from 10^{-3} s to 10^3 s. The details of each inversion and the resulting models are summarised in Table 9.1.

Internal Zone Subset Profiles and projected sites	Inversion code					
	RLM2DI		**REBOCC**		**DetREBOCC**	
EW (90° strike) b55,b54,b52,b35, b17,b57,b58,b29, b30	TM mode Figure 9.7	rms=2.06	TM mode	rms=16.38		
NS1 (0° strike) b53,b51,b52,b17, b57,b35,b56	TM Fig. 9.6 Fig. 9.7	rms=2.14	TM mode Figure 9.8	rms=6.3	only det Figure 9.10	rms=3.23
	TM+TE Fig. 9.6	rms=6.53	TM+tipper Figure 9.9	rms=5.99	det+tipper Figure 9.11	rms=4.19
	TM+TE+ss Fig. 9.6	rms=5.26			det+tipper+ss Figure 9.12	rms=3.97
NS2 (0° strike) b37,b29,b58,b30,b32	TM mode Figure 9.7	rms=5.35	TM mode	rms=4.60	only det	rms=7.48
			TM mode + tipper	rms=2.88		

Table 9.1: Summary of the sites and profiles used to create 2D models from the Internal Zone subset, indicating the inversion code applied, the inverted data (ss: static shift correction), and the rms of the resulting models.

9.2.5 RLM2DI inversions results

For each of the three profiles over the Internal Betics (Figure 9.4), inversions of TM modes and TM+TE mode were carried out using resistivity and phases responses, before and after static shift corrections.

The same model mesh was considered at each profile to perform the different inversions. Experience with the forward estimation of the responses from synthetic models and inversion have demonstrated that it is necessary to run RLM2DI inversions with as regular a mesh as possible is necessary. Model meshes were extended laterally away from the profiles and to depths of up to 100 km to ensure the stability of the responses.

Models obtained from both TM and TE mode inversions presented large misfit values, as one would expect since TE mode is largely affected by 3D effects, whereas in the inversion models these effects as structures below the profile.

The fact of considering static shift corrections or not implies a significant change in the position, extent and conductivity value of the modelled structures. Below some of the sites, after inverting using static shift corrections, large conductivity contrasts with extreme values appear. This suggests a revision of the corrections already made.

In particular, three different inversions were performed for the NS1 profile: one using TM mode data and two using TE+TM data, before and after static shift corrections. Only one inversion was performed using TM mode data alone, because these were not corrected from static shift (only yx (TE) curves were shifted).

All the resulting models (Figure 9.6) have two resistive structures in the northern and southern parts of the models, and three conductive bodies, in the central and southern parts. However, it is evident that there are differences in their positions, shapes and conductivity values. The model using only TM data (upper panel) shows the simplest structure, with a small extent of the conductivity bodies and not particularly low conductivity values. The models from TE+TM mode inversions have a more complex structure (middle and lower panels), and a new shallow conductive body appears at the northern part of the model. Without static shift corrections (middle panel), all the structures appear at shallower depths and the conductive bodies increase in extent and conductivity. In the last model, after the static shift corrections (lower panel), all the conductive bodies increase in extension, depth and conductivity and have different shapes too.
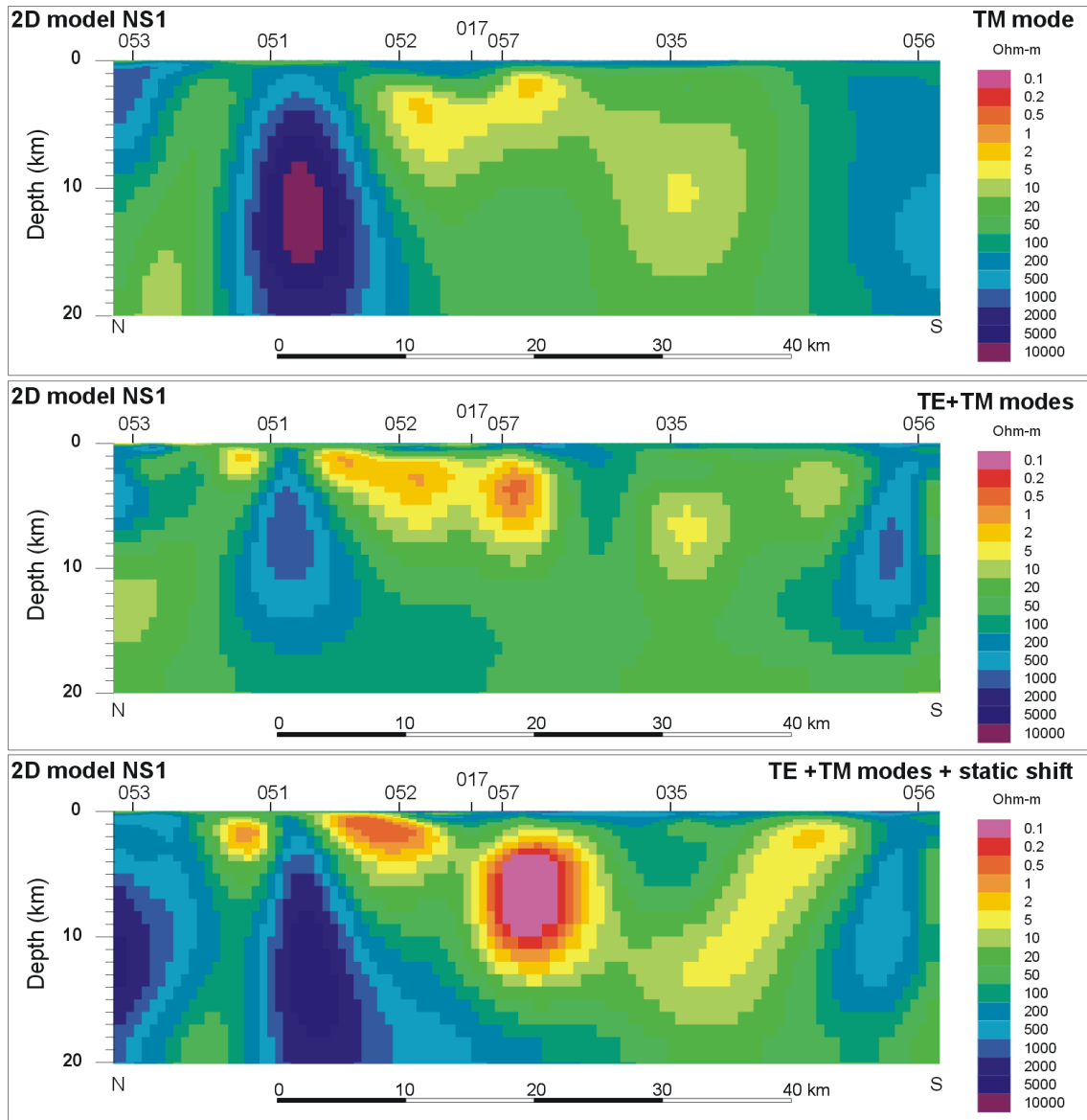
Figure 9.6: Comparison of NS1 profile inversion results, using TM data (upper panel) and TE+TM data, without (middle panel) and with (lower panel) static shift corrections. rms values: 2.14, 6.53 and 5.26 respectively.

For all the profiles, inversions using RLM2DI were performed considering TM modes, without static shift corrections (Figure 9.7). The resulting misfits are low (see figure captions).

Model EW (mesh of 135x50 elements) (Figure 9.7, middle panel) presents structures with well-defined contrasts and a lateral alternation of conductive and resistive bodies. Some interpretations may depict this as anisotropy. In this case it is a consequence of having inverted a profile along a hypothetical strike direction, as all the curves along the profile have similar decreasing resistivity curves. The central conductivity body, below sites 17 and 57, has a vertical extent from 2km-3km to 18km.

Model NS1 (127x50 elements) (Figure 9.7, upper panel) presents highly resistive bodies located under very thin conductive layers, at the northern side below sites located over the Guadix-Baza basin. Between sites 51 and 53, a moderately conductive zone appears at lower depths. The central part of the model, corresponding to the Nevado-Filábride unit (sites 52, 17, 57 and 35) is the most conductive, with a shallow resistive layer on top. The conductor reaches a maximum depth of 9km in its central part, and 15km (10 $\Omega \cdot$m) below site 35.

Model NS2 (74x60 elements) (Figure 9.7, lower panel), located 50 km East from NS1, shows a conductive structure similar to that of model NS1, which can be interpreted as the continuity of the first conductive zone along the Sierra de los Filabres.
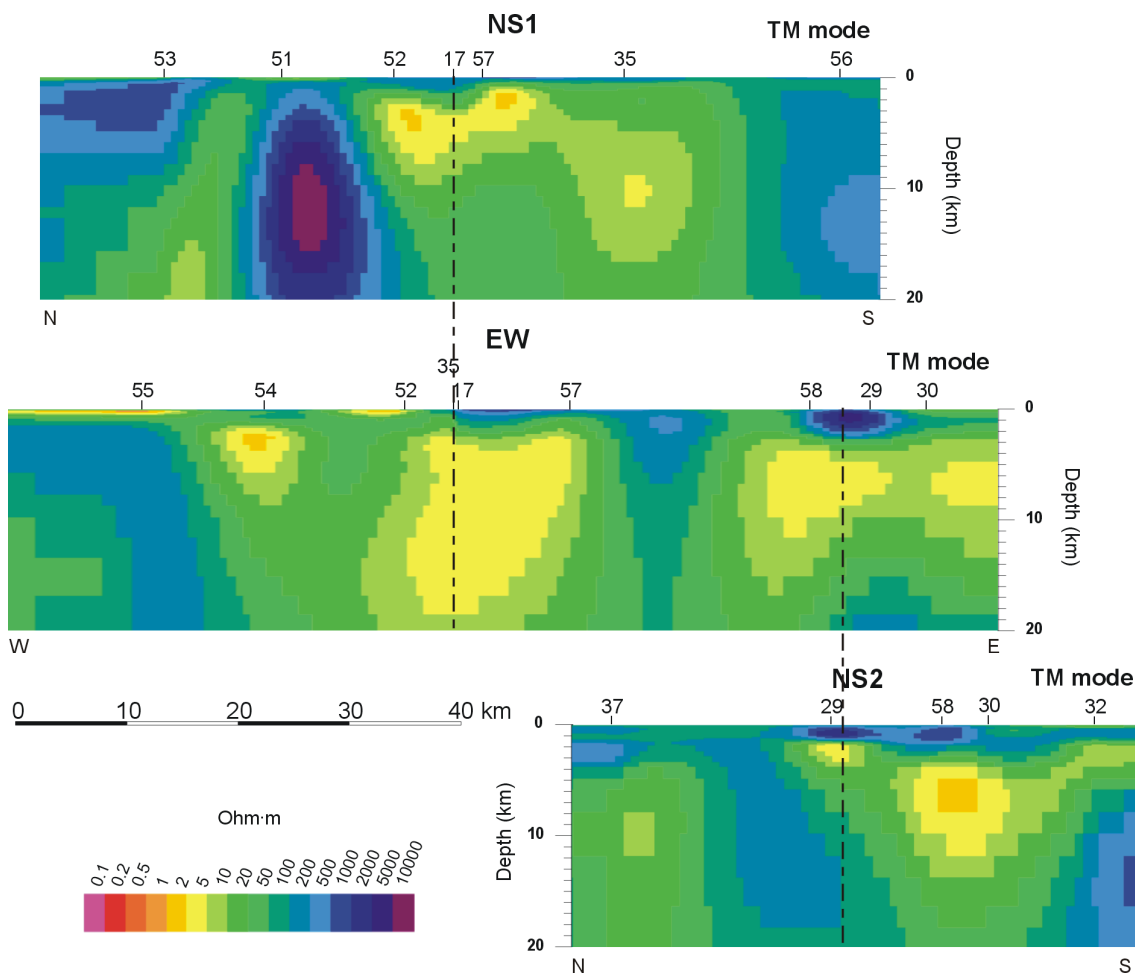
Figure 9.7: 2D models resulting from RLM2DI inversions of TM data, for the three profiles in the Internal Betics. Upper panel, model NS1 (rms=2.14, 57 iterations); middle panel, model EW (rms=2.06, 57 iterations); and lower panel, model NS2 (rms=5.35, 26 iterations). Dashed lines indicate the approximated tie points.

In the Northern side of this body (below sites 58 and 29), its base dips towards the south. Its limit with the underlying resistive structure can be interpreted as the base of the Nevado-Filábride complex.

Below the same sites, the structures depicted from EW and NS directed models are different, since different data polarizations were taken for each direction.

9.2.6 NS1 profile inversions using REBOCC and DetREBOCC codes

As an alternative to the inversions performed and as an opportunity to invert tipper data, REBOCC and DetREBOCC codes were applied to the three profiles.

Using these two codes, inversions from EW profiles showed very poor misfits, even when only considering TM data, since data from these profiles were far from 2D dimensionality with a NS directed strike. The models obtained from NS2 data showed better fits, but very simple structures. Hence, the following description focuses only on the NS1 profile.

A first inversion of the TM mode resistivity and phase data was performed using REBOCC code, to be directly compared to the RLM2DI code (Figure 9.8). Mesh size was set to 104 x 57 elements. The REBOCC model has smoother resistivity contrasts and a lower resolution in depth. REBOCC code has a much faster convergence rate (Siripunvaraporn and Egbert, 2000), although in this case the final *rms* values are higher than those using the RLM2DI code, one of the reasons being the lack of a conductive body below site b35.
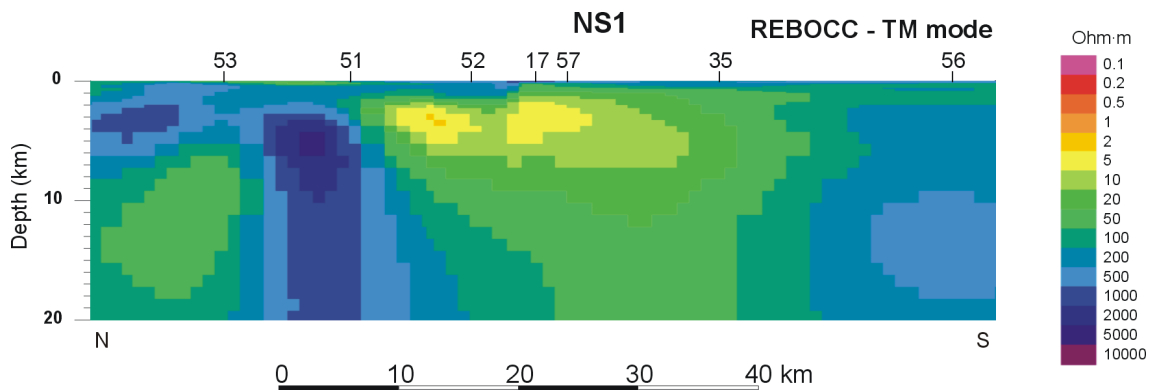
Figure 9.8: Model NS1 from REBOCC inversion of TM resistivity and phase data. (*rms*=6.3, 10 iterations).

The model obtained from joint inversion of TM mode and tipper data (Figure 9.9) presents similar features to the previous one. However, the conductor below Sierra de los Filabres has a larger extent below sites b57 and b17, and the conductor between sites b51 and

b53, already imaged using RLM2DI inversion, appears at a shallower depth, with a lower resistivity value.
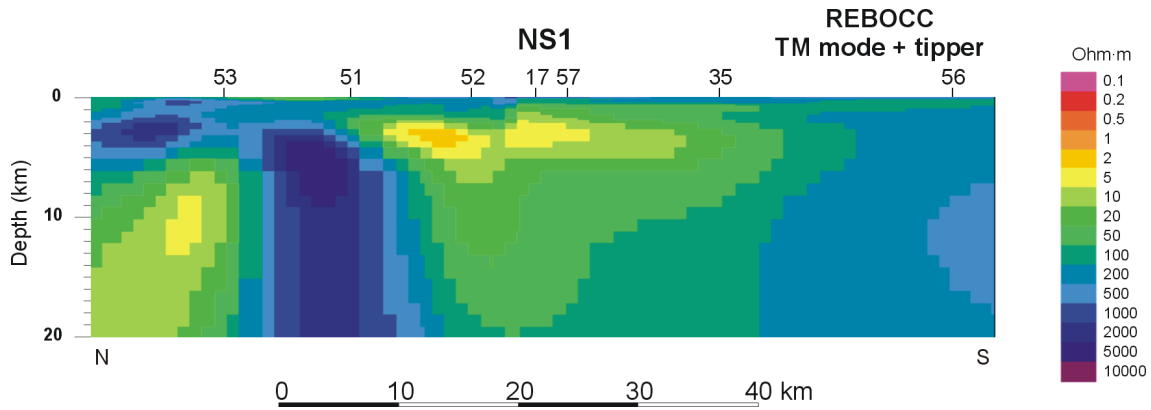
Figure 9.9: Model NS1 from REBOCC inversion of TM resistivity and phase and real and imaginary Tipper data. (*rms*=5.99, 10 iterations).

The DetREBOCC code was used to invert only the determinant data (computed as in eqs. 9.2 and 9.3, using all MT tensor components) (Figure 9.10), including the tipper data (Figure 9.11) and only the determinant data corrected from static shift (eq. 9.4), which resulted in an increase of the determinant resistivity values (Figure 9.12).

The first model (only determinant data, Figure 9.10) shows a conductivity distribution much different from the previous inversions. The conductive body located at the center of the profile, below Sierra de los Filabres, reaches larger depths (up to 20km). Its upper part presents a double-wedged shape, towards sites b52, with extremely low resistivity values, and b57. The inclusion of tipper data (Figure 9.10) allows better resolution of the modelled structures, without major changes, except for a conductive structure that appears at the northern part of the model.

The model obtained from the inversion of the determinant data corrected from static shift (Figure 9.12) presents similar features to the previous ones, especially that which included the tipper. The effects of the static shift correction are not as evident as those observed when inverting the TE mode, since in the present case, the corrections are averaged within the determinant.
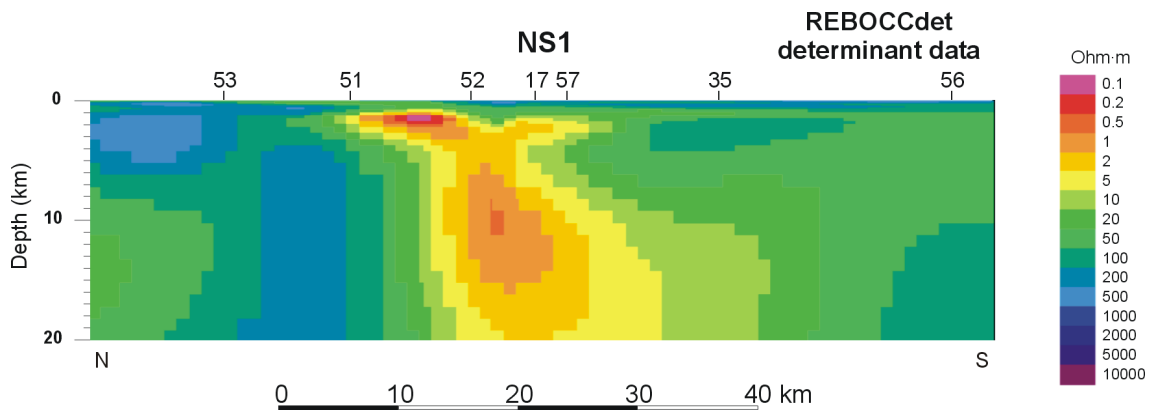
Figure 9.10: Model NS1 from DetREBOCC, inverting determinant data (*rms*=3.23, 10 iterations).
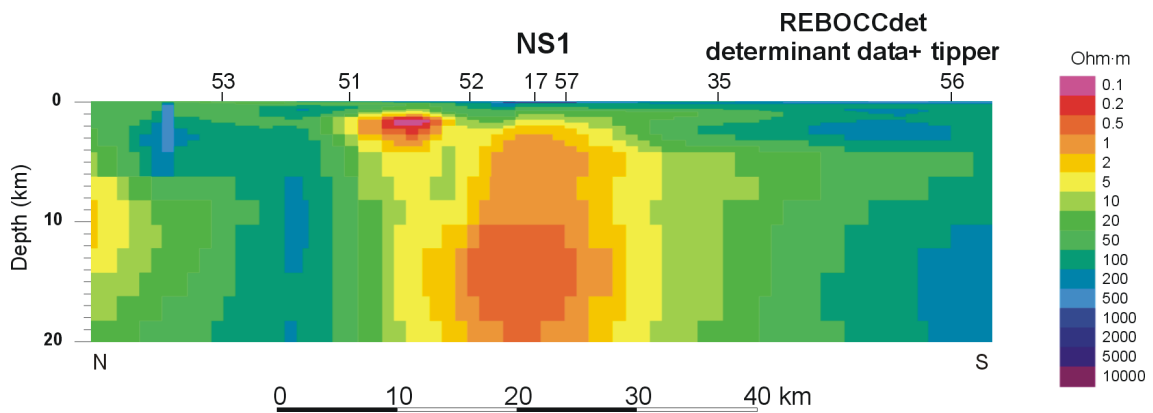
Figure 9.11: Model NS1 from DetREBOCC, inverting determinant data and tipper (*rms*=4.19, 10 iterations).
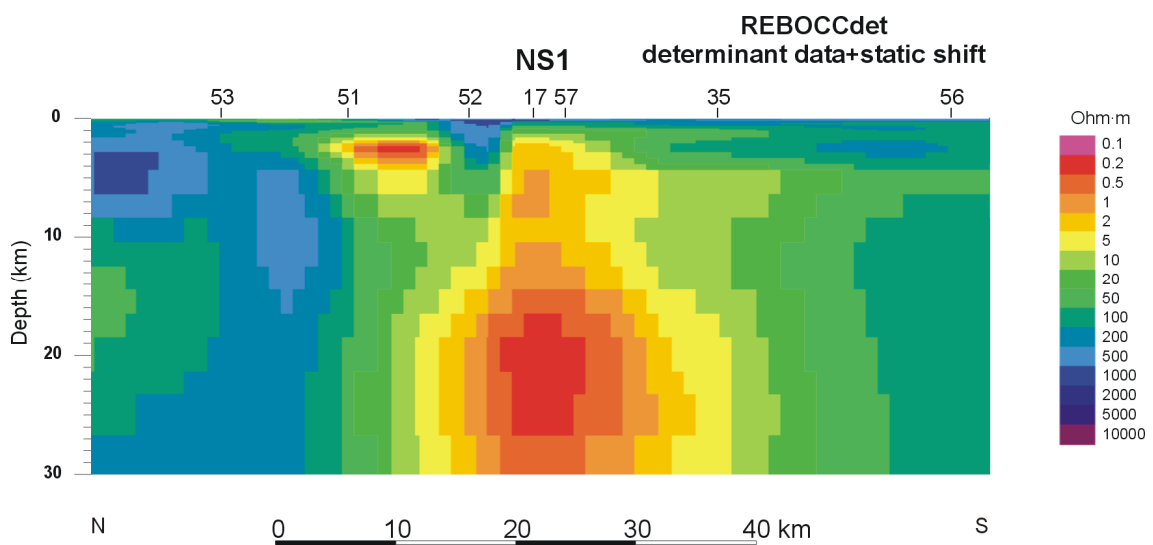
Figure 9.12: Model NS1 from DetREBOCC, inverting determinant, and after static shift corrections (*rms*=3.97, 10 iterations).

Although not shown here, all the models obtained from DetREBOCC inversions of profile NS2 present a differentiation between a shallow conductor located in the Northern part of Sierra de los Filabres and a central and much deeper one, with a variable depth, and a base located between 20 and 30km.

Further 3D modelling of the data should reveal the exact position and geometry of these conductive bodies, in which the sites are not projected over a certain profile.

The use of DetREBOCC code has produced models with very low misfits with respect to the data, and fast convergence rates. The inversion process considers the same amount of information as inverting only TM or TE modes, but, as the data are not truly 2D, the determinant contains information from the full impedance tensor.

9.3 Conclusions

The previous NW-SE 2D resistivity model of the central Betics, which showed a deep conductive body, was revised and a sensitivity test was performed to obtain the resolution at different parts. From this test it can be said that the model is well resolved at shallow depths, whereas resolution is lost in depth. The model responses are sensitive to the deep conductor, although, from the dimensionality results, its lateral continuity is not ensured.

Three 2D models over the Internal Zone, EW, NS1 and NS2, along and across the Nevado-Filábride unit were built as a preview of the 3D model, using RLM2DI inversion code.

The weak point of these inversions is that the data are not truly 2D, and the sites have been displaced and projected over very hypothetical strike directions. Hence, some local conductivity structures are extrapolated to the whole model.

The effects of both the inverted modes and the static corrections are observed in the shapes and resistivity values of the modelled structures, whereas, with some exceptions, these structures are common for all the inversions.

The model EW showed an alternation of conductive and resistive bands, a consequence of inverting data along an approximated strike direction. The largest of these conductors reaches a depth of 18km. NS1 and NS2 models show a conductive body, located below the Nevado-Filabride complex outcrops, which reaches a maximum depth between 10km and 15 km, much shallower than the body imaged in the previous NE-SW model.

The NS1 model was compared with the results from inversions using codes REBOCC and DetREBOCC, which allowed inverting the tipper. With only small variations, all the resulting models presented a conductive body with its base located at 20km depth.

Among the different codes, for the data inverted in this chapter the inversion of the determinant seems to be the most reasonable, because it inverts a response that contains information of the full tensor and is less influenced by the strike direction.

The use of the determinant data in further 3D modelling seems to be a good tool as well, which has the advantages that the sites would not be projected over any particular profile and structures could be imaged in their real positions.

Chapter 10: 3D Modelling of the Central Betics Geoelectric Structure

In this chapter, the modelling of the geoelectric structure of the central Betics crust is presented. Provided that the dimensionality of the data is mainly 3D, with superposition of 2D and 1D cases at particular period ranges, 3D modelling is the only one that has the potential to reproduce the geoelectric structure that best fits all data responses.

The proposed 3D model was constructed from an initial model, and later modified through a trial and error process. In this process, model responses were computed using Mackie *et al.* (1993) forward modelling code. The details of this 3D modelling process, the final model, its misfits, the sensitivity tests and the interpretation of the model features, are addressed below.

10.1 Data Set-Up

Data set-up consisted of arranging the measured data to make them comparable with the model responses, including the following steps:

- Set all the data with the same axes orientations: in this case, x=NS and y=EW, which, as will be seen, coincides with the model orientation.
- Static shift corrections: shifts between xy and yx resistivity curves, and between the resistivity curves at nearby sites, were corrected, in the same way as explained in the 2D modelling data set-up (chapter 9, section 9.2.3). This procedure is justified by the fact that, after several tests, the 3D model responses did not show any

significant separation between the resistivity responses, and hence would not be comparable to the data if it were not corrected from static shift.

- Rejecting data: all site responses were reviewed to inactivate periods with data spikes and ranges of periods with uncommon curve shapes (steep slopes and discontinuities). This lead to the rejection of site b09 (see curves in Appendix D) for having resistivity curves with slopes greater than 45° and phases out of the expected quadrants. As a consequence the final dataset used in the modelling consisted of 42 sites.

The final dataset, compared to the dataset inverted to create the 2D MT1 model of the central Betics (Pous *et al.*, 1999), shows different resistivity curves shapes, and lower resistivity values at some of the common sites of both datasets. This is due to: 1) in this data set-up, where no information is available, the curves were not significantly displaced from their original values; and 2) the data utilised in the MT1 inversions had been rotated and corrected from galvanic distortion assuming a 3D/2D behaviour.

10.2 Model Mesh and Initial Model

A preliminary model mesh with an initial conductivity distribution was constructed from Occam's 1D inversions (Constable *et al.*, 1987) of determinant resistivity and phase at each site. Through an interpolation of horizontal and vertical resistivity values, it resulted in a NS-EW oriented model. The horizontal model mesh was regular, in which sites were relocated at the centre of the cells. The vertical mesh had cell thicknesses increasing logarithmically, with depths from hundreds of metres to tens of kilometres.

The mesh of this preliminary model was extended horizontally (50 km towards south and east) to ensure stability of the responses and to include part of the adjoining Alboran Sea, to model the sea effects. Cells were also split or combined at zones where sites were too close or too distant, respectively. Vertically, the first layers of the mesh were split to gain resolution at the shortest periods. After these modifications, the model mesh considered in our modelling consisted of a rectangular prism with a size of 270(NS)x220(EW)x100(z) km, made up of 50x50x25 cells (Figure 10.1). It extends over the Central part of the Internal and External zones, and includes the eastern end of the Guadalquivir Basin, part of the southern Iberian Massif and a strip of 35 km of the Alboran Sea.

The resistivity distribution of the preliminary model, with a high conductivity zone in its southeastern part, extending in depth from ten to seventy kilometres, was modified in order to be consistent with the static shift corrections applied to the data. On the other hand, specific

conductivity values obtained at the first layers below certain sites were extended towards zones not covered by data, following the distribution of the surface geological units. Hence, low resistivity values (5 Ω·m) were introduced beneath the Cenozoic basins, high values beneath the Internal Zone metamorphic units (200 Ω·m and 500 Ω·m) and Iberian Massif (500 Ω·m), and low to intermediate values beneath the External Zone (50 Ω·m and 100 Ω·m).

In the Alboran Sea, water depth was included in the model, with a resistivity value of 0.5Ω·m and the resistivity of the underlying materials fixed to 50 Ω·m. Below, a relative conductive zone (20 Ω·m) was modelled from 50 km downward, to reproduce the inferred presence of asthenospheric material (e.g. Polyak *et al.*, 1996; Torné *et al.*, 2000; Frizon de Lamotte *et al.*, 2004). This simple lithospheric resistivity model was imposed since there is neither MT data coverage over the Alboran Sea nor a good knowledge of the crustal structure of this area.
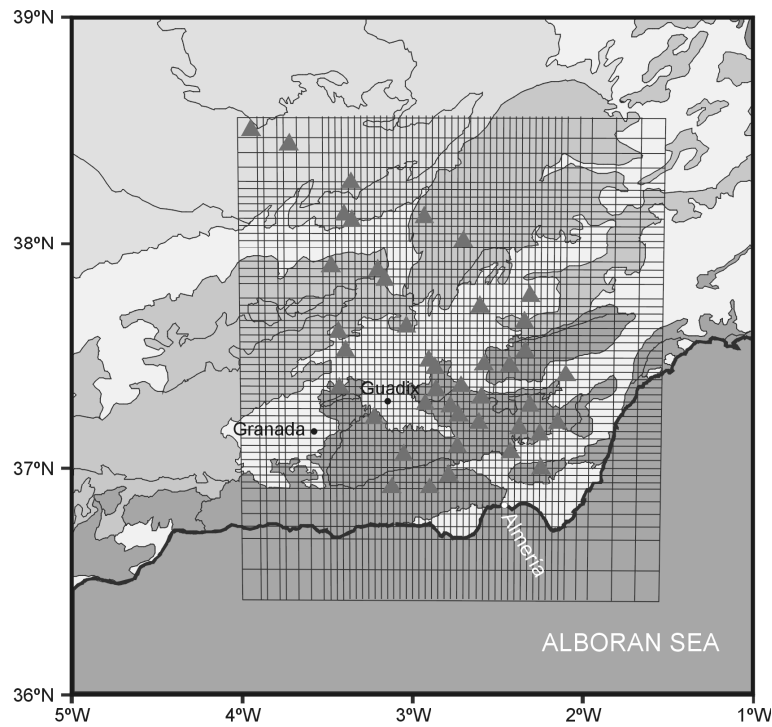
Figure 10.1: Horizontal 2D mesh utilised to construct the initial 3D model, superimposed over the geological units and MT site locations.

The model, result of applying all the previously explained mesh and resistivity distribution modifications is shown in Figure 10.2 and constituted the initial model upon which further models were built.
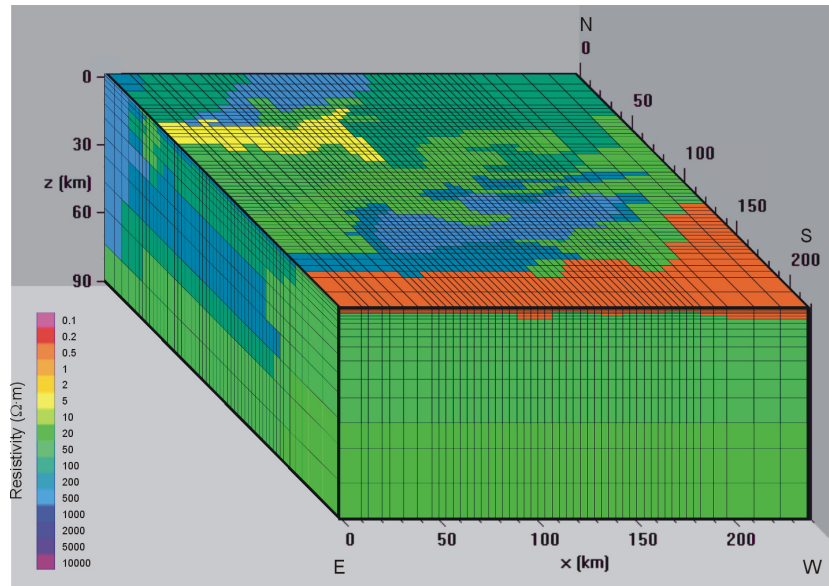
Figure 10.2: 3D view of the initial model and mesh, modified to include the Alboran Sea (0.5 Ω·m) and to reproduce the main geological features.

10.3 Trial and Error Process

Departing from the initial model, successive 3D models were obtained through a trial and error process, which included forward modelling comparisons of responses and model transformations.

The 3D forward modelling was computed using the Mackie *et al.* (1993) code, which was run for 24 periods from 10^{-3} s to 10^3 s. For the mesh considered (50x50x25 elements), each run took approximately 30 minutes using an Intel Pentium4 (3.0 GHz) processor.

From the electric and magnetic fields obtained from each run, the model responses and related parameters (xy and yx resistivities and phases, determinant responses, WAL invariants and dimensionalities) were computed at MT site positions. Their values were compared with the data responses. The misfits between both responses were analysed using pseudo-sections of the responses plotted at constant periods and were quantified using the rms (eq. 9.5). This allowed identifying the zones of the model with poorer fits and modifying the model accordingly.

Once a satisfactory model was obtained, some very local features non-identifiable with geological structures or bodies were removed, in what was called the smoothing of the model. This smoothing was only considered valid if successive forward modelling steps showed no significant changes in the model responses.

10.4 Final Model

After 140 trial and error steps, a satisfactory model (bet3D-140) was obtained, regarding both data fits (explained in section 10.5) and model smoothness. The most relevant features of this model are shown in the horizontal slices at Figure 10.3 (pages 214 and 215) up to 40 km. Below this depth, the recorded data do not allow constraining any geoelectrical structure and hence, the corresponding slices are not shown.

Apart from the Alboran Sea, the model denotes that, up to 40 km depth, the Central Betics and adjoining areas are relatively resistive (mainly 50 $\Omega \cdot$m to 100 $\Omega \cdot$m) with high conductive bodies located at the uppermost crustal levels (<5 km) in the External betics and both uppermost to middle crustal levels (<17.5 km) in the Internal Betics. It also shows that the conductivity distribution is more complex at upper crustal levels beneath the Betic Chain. This fact is explained by the higher density of sites over this zone and the loss of the model resolution in depth.

Next, the detailed geoelectric features of the final model are described from northwest to southeast, perpendicular to the main trend of the Betics structures. In this description the model has been divided following the surface distribution of the main Alpine geologic units recognized in the area. This division facilitates the description of the model, but has the inconvenience that the boundaries between these geological units are not vertical but tilted or even near horizontal (unconformities, thrusts, etc.), and therefore, that bodies as structures of different units could be and indeed are present beneath the outcropping ones. Consequently, deep geoelectrical features observed below an outcropping unit could be not related to this unit but instead to another geological unit that is present at depth.

The main resistive and conductive zones of the model were identified as **R** (resistive) and **C** (conductive), plus the site number or acronym of the geological region beneath which these are located, and an additional number in case there is more than one resistor or conductor in the same area (e.g.: **CF1**, **CF2** and **CF3** are the three conductive bodies located below the Sierra de los Filabres).

- **Iberian Massif** (northwestern side of the model, sites b14, b13, b11, b07 and b08):

At all modelled depths, the resistivity is moderate to high, with a general decrease of the resistivity values from NW (200$\Omega \cdot$m to 2000$\Omega \cdot$m, identified as **RIM**) to SE (20 $\Omega \cdot$m to 50 $\Omega \cdot$m).

Within this resistor **RIM**, however, some relative conductors have been identified. One of them (**CIM**, 50 $\Omega \cdot$m) is a band located at depths between 2.15 km and 17.5 km (Figure 10.3i to Figure 10.3o) that cuts NE-SW across the resistive zone **RIM**. The

other two conductors are narrower and restricted to the SE areas where a Mesozoic cover overlies the Variscan basement: the **C7-8** conductor (10 Ω·m) located between 900 m and 1.2 km, and the conductor named **C-11** (Figure 10.3h), recognised between 1.6 km and 2.8 km.

- **Guadalquivir Basin:**

Beneath the outcropping sediments of this basin, the model reproduces a superficial conductor (**CGB**) up to 350 m depth that depicts a general E-W orientation. This conductor appears again, more localised, between 650 m and 900 m (Figure 10.3e). Below, the resistivity increases with depth, reaching similar values to those described in the Iberian Massif (100 Ω·m – 500 Ω·m).

- **External Zone**-**Prebetics** (sites b26 and b24):

This part of the model is characterised up to 2.15 km by moderate resistivity values (20 Ω·m – 50 Ω·m); bounded beneath by resistivity values ranging from 100 Ω·m to 500 Ω·m, which are also similar to those described in the Iberian Massif. At site b26, and at a depth between 350 m and 650 m, the model also shows the presence of a conductive body which is a continuation of the conductor **CGB**, recognised in the Guadalquivir Basin.

- **External Zone**-**Subbetics and Guadiz-Baza basin** (sites b40, b06, b05, b41, b03, b27, b23, b21, b38 and b20):

The resistivity pattern of the model beneath the outcropping Subbetics is similar to that described in the Prebetics. There is an upper body (up to 1.2 km) of moderate resistivities (10 Ω·m – 50 Ω·m) and a deeper resistor with values similar to those of the Iberian Massif (100 Ω·m – 200 Ω·m). Locally between these two bodies, in the northern part of this zone, there is a 2 Ω·m – 5 Ω·m conductor which is a continuation of the **CGB** conductor of the Guadalquivir Basin. However, the model shows that there are remarkable differences between the geoelectric features of the upper body in both External Zone domains: Whereas in the Prebetics the resistivity is rather homogeneous, in the Subbetics the model records two well differentiated zones: a moderate resistivity zone that coincides at surface with outcropping rocks of the outer Subbetic domain; and a conductive zone restricted to the southeast and formed by two isolated conductors (**C20** and **C27-38**). **C20** crops out at surface east of the Guadix-Baza Basin in the areas where pelagic rocks of the inner Subbetics appear at surface, and it is also present

beneath site b23 from a depth of 350m. This is a conductor with resistivity values between 1 Ω·m and 5 Ω·m that reaches depths from 900 m below site b23 to 7 km below site b20. Therefore, it is a conductor bounded downwards by a south dipping surface. Towards the south, it is bounded by a near vertical E-W oriented surface. The other conductor, **C27-38**, is also located beneath the Guadix-Baza Basin, near the southern boundary of the Subbetics but it does not crop out at surface. The top of this conductor appears at a depth of 900m, and its bottom reaches a maximum depth of 2.8 km.

In relation to the conductor **CGB** located between the upper body and the deeper one, the model shows that the conductor in the Guadalquivir Basin continues southwards beneath the resistive rocks of the external parts of the Subbetics. With values ranging from 2 Ω·m to 5 Ω·m, this conductor appears beneath sites b40, b05 and b06, where its bottom is located at greater depths than in the Guadalquivir Basin: 1.2 km beneath site b40 and 5 km beneath sites b05 and b06.

Finally, it should be noted that the Guadix-Baza basin infill is not well reproduced by the final resistivity model.

- **Internal Zone** (sites b53, b37, b19, b02, b01, b51, b36, b60, b32, b30, b59, b54, b18, b52, b17, b57, b35, b58, b29, b15, b56, b33 and b31):

As already stated, this zone of the model is characterised by its high complexity, with well-differentiated resistors (**RI**) and conductors (**CE**, **CF1**, **CF2**, **C31**, Figure 10.4 and **CF3**, Figure 10.5). Up to 13.5 km depth, in the north and above the top of conductor **CF3** in the central and southern parts of this zone, the crust is characterised by moderate to high resistivity values (**RI**, Figure 10.3a-n), comprised between 200 Ω·m and 1000 Ω·m, with areas of moderate resistivity values (20 Ω·m – 100 Ω·m). Among these, high conductivity zones appear at different position and vertical extents.

In relation to the conductors, the conductor **CE** (2 Ω·m – 5 Ω·m) (Figure 10.3g-i) has a vertical extent from 1.2 km to 2.8 km, west of the Sierra de las Estancias. Conductors **CF1** and **CF2,** located beneath the Sierra de los Filabres (Figure 10.3h-j), have the same resistivity values as the conductor **CE** and have a vertical extent from 1.6 km to 3.8 km. In the southeastern part of the model, below Sierra de Alhamilla, conductor **C31** (5 Ω·m) appears, with a vertical extent between 500 m and 2.15 km (Figure 10.3d-h). Below **CF1** and **CF2**, conductor **CF3** (1 Ω·m – 5 Ω·m) is the largest conductor and the most striking feature of the model (Figure 10.3k-o). It has a WNW-ESE orientation and its top is located at 3.8 km depth. The bottom of this conductor ranges between 5 - 7 km

in the southeastern part, 9 km in the northwestern part, and 17.5 km in the central part (Figure 10.5).
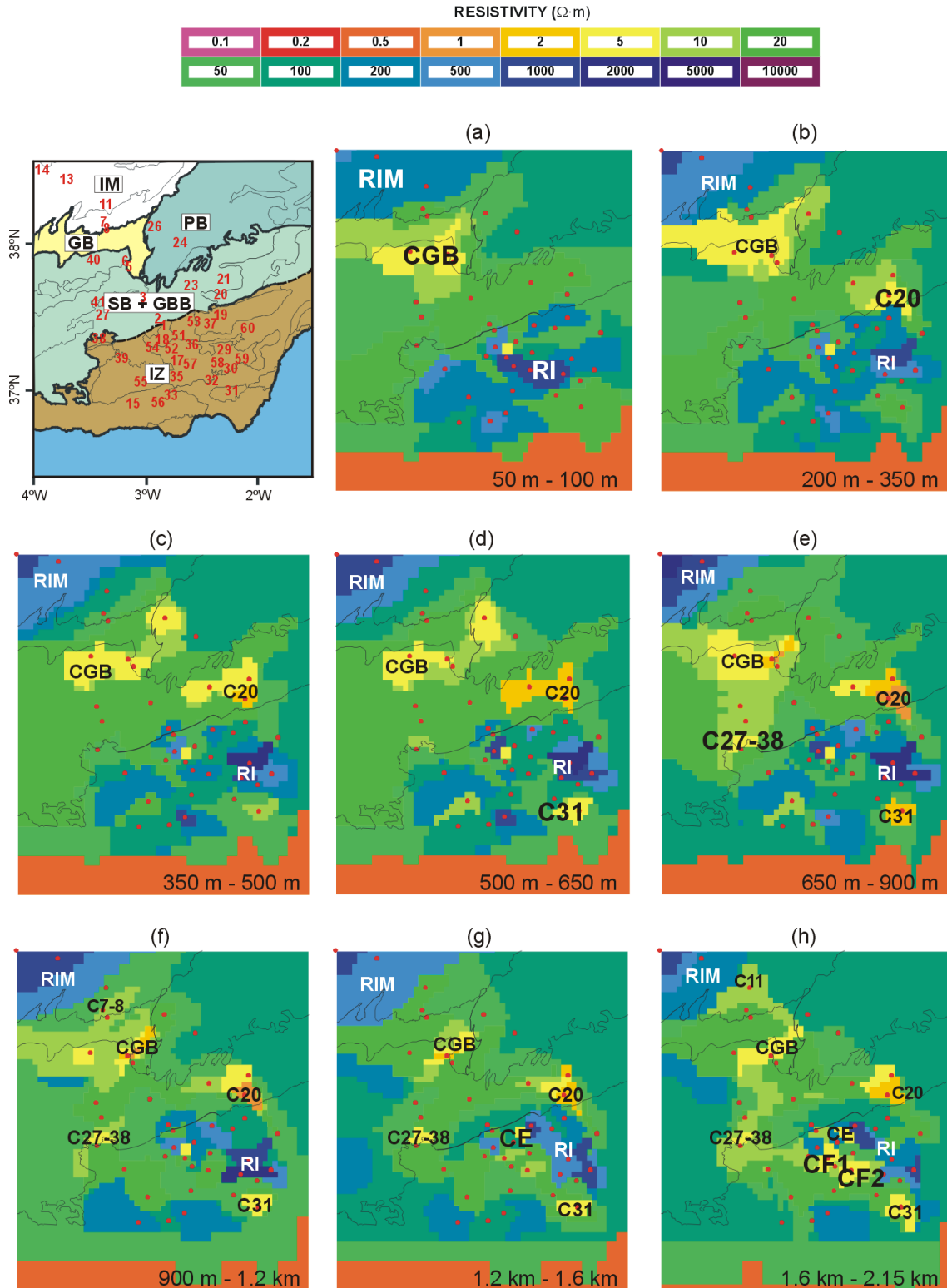
Figure 10.3: Situation map and horizontal cross-sections of the most relevant layers of the final 3D model. Situation map: Site locations in red; main geologic zones used in the model description, separated by wide black lines : IM (Iberian Massif), GB (Guadalquivir Basin), PB (Prebetics), SB+GBB (Subbetics + Guadix-Baza Basin) and IZ (Internal Zone). Cross-sections: red dots indicate site locations; narrow lines mark the geological divisions; the depth range of each layer is indicated in the lower-right;

abbreviations correspond to the main conductors and resistors described in the text, which are indicated in a larger font at its upper position. C: Conductors R: Resistive.
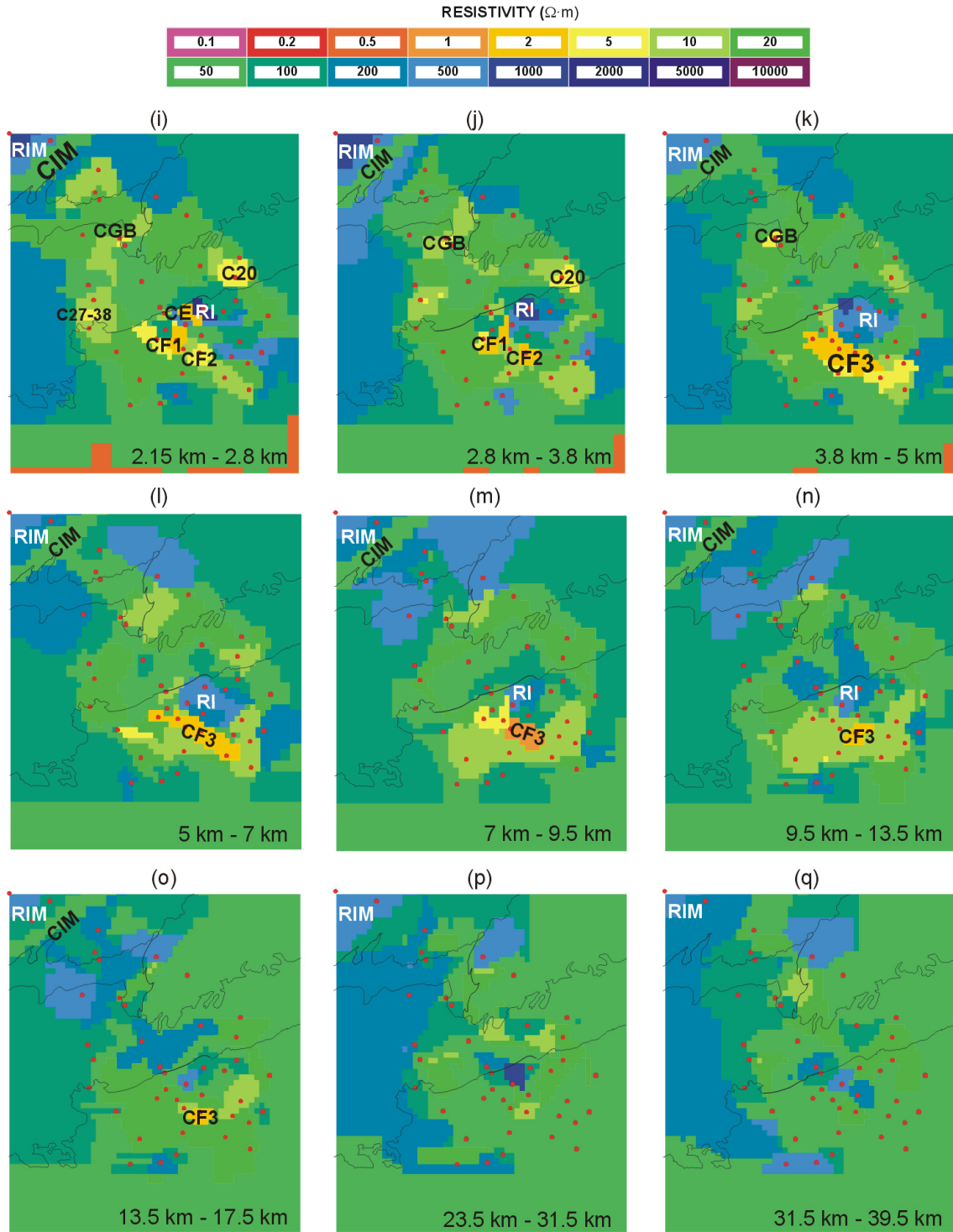
Figure 10.3 (cont.)

Beneath the resistive zone **RI** and the deep conductor, **CF3**, i.e., at depths greater than 13.5 km to 17.5 km, the model shows moderate resistivity values, similar to those

observed in the deeper Iberian Massif and External Zone domains. Nevertheless, locally, beneath site b51 a highly resistive zone (2000 Ω·m) appears between 17.5 and 31.5 km.
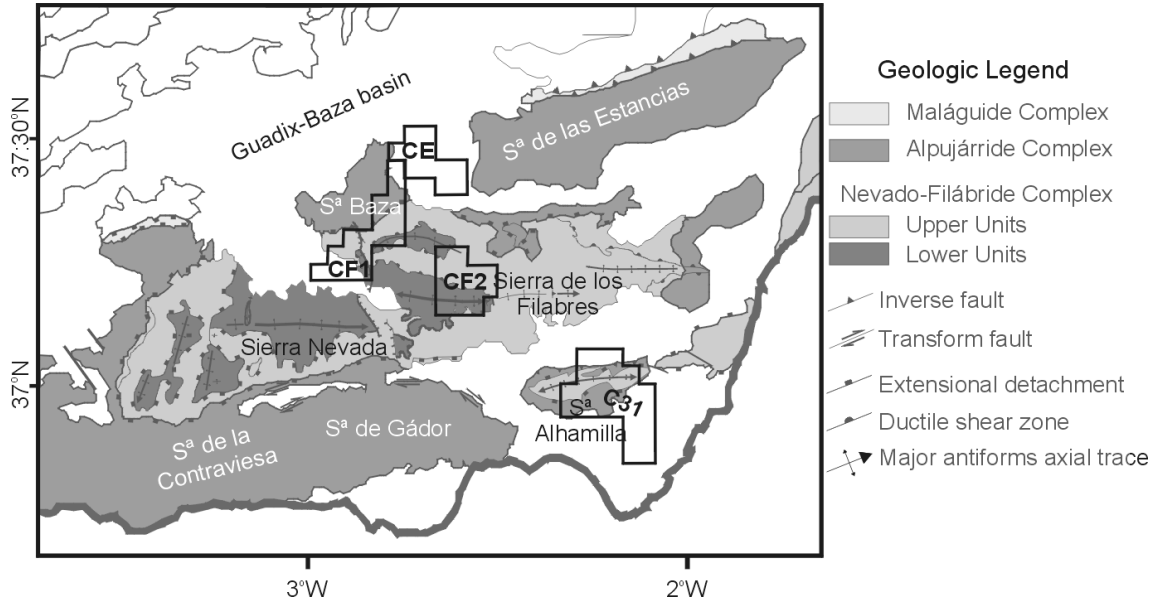
Figure 10.4: Geologic map of the central sector of the Betics Internal Zone, with the locations and shapes of the main shallow conductors imaged in this area. The shapes of these conductors are those of its maximum horizontal extension.

10.4.1 Comparison with 2D conductivity models

Vertical sections of the 3D model bet3D-140, coincident with the 2D conductivity models NS1, NS2 and EW, exposed in chapter 9 (see profiles locations in Figure 9.4) are displayed in Figure 10.6. Comparing the vertical sections of the 3D model with the 2D models, significant differences appear:

The three sections (Figure 10.6) differ significantly from the corresponding 2D models (chapter 9, Figure 9.7). The conductor beneath sites b58, b29 and b30 shown in the 2D model EW disappears; and the deep conductor present beneath the Nevado-Filábride complex has a higher conductivity in sections EW and NS1 but is lower in section NS2. Also, it reaches lower depths in profile NS1, whereas in the profile NS2 it is clearly shallower.

Since the same data sites and static shift corrections have been used in the 3D and 2D approaches, the differences between the three models and sections can be attributed only to the modelling approach, e.g. to the fact of projecting the data sites or not to a profile. In this case, sites have been projected up to 30 km, which is significant given the complexity of the area.

Hence, in the 3D model, the conductive and resistive bodies are more local, such as the deep conductor that is not shown in the 3D section of NS2. In general, the 3D model images some conductive and resistive structures similar to the 2D, although with different positions, sizes and resistivity values.
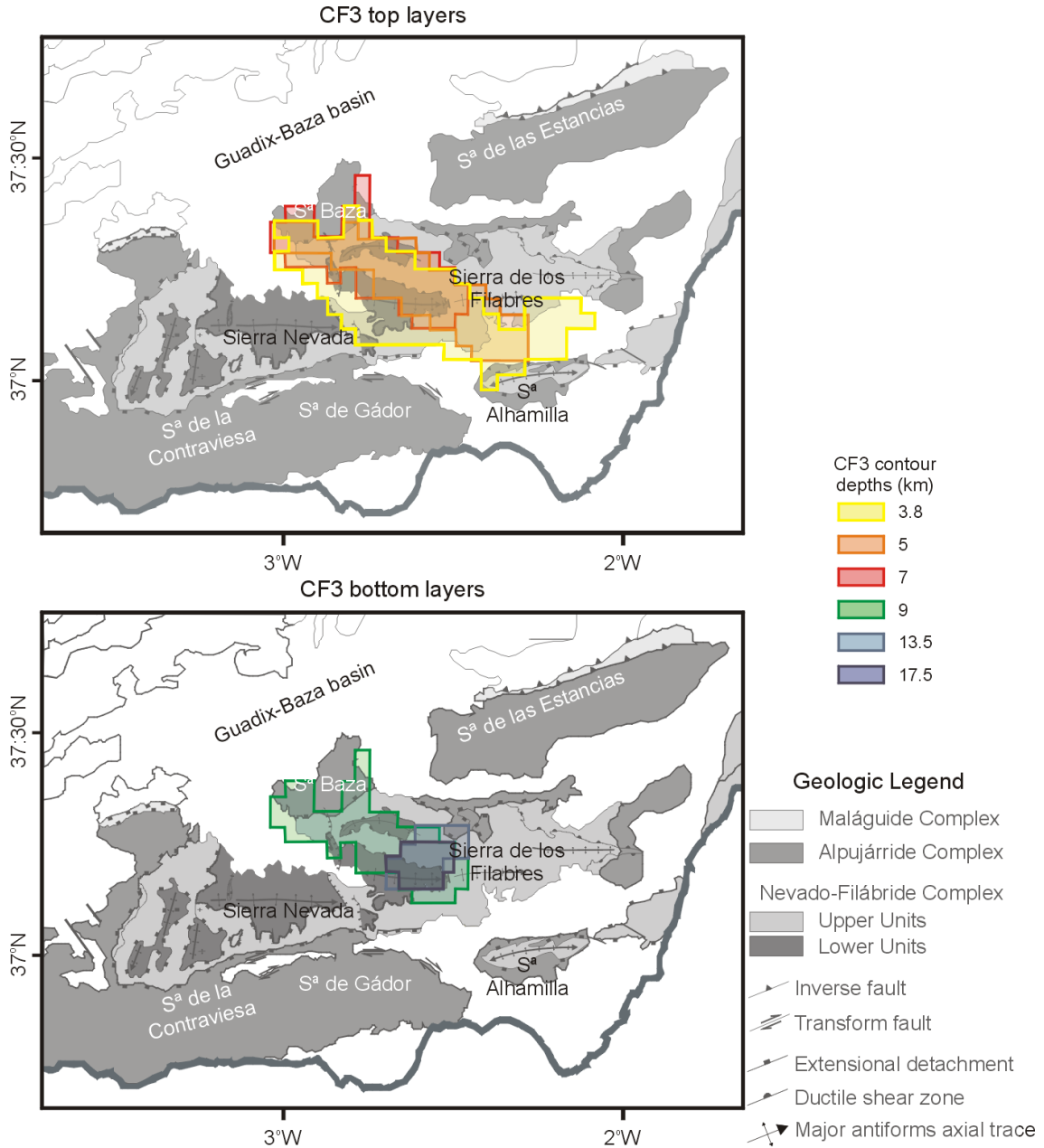
Figure 10.5: Geologic map of the central sector of the Betics Internal Zone, and contours of the top (upper panel) and bottom (lower panel) of conductor CF3.
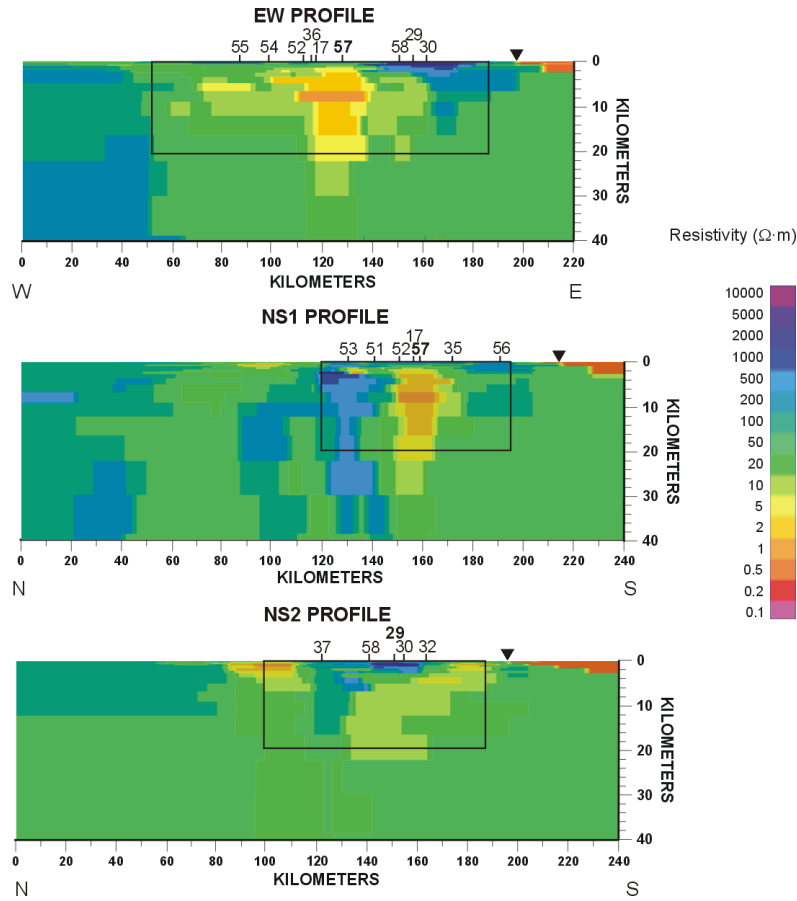
Figure 10.6: Vertical sections of the 3D model bet3D-140 along the NS1, NS2 and EW profiles (see Figure 9.4 for locations). Numbers on top indicate site locations projected over the vertical section. Sites located on the profile trace are in bold. Inverted triangle: coast line. Framed areas indicate the extent of the 2D models.

10.5 Comparison of Responses and Misfits

Data and model bet3D-140 determinant resistivity and phase responses (Appendix E) present a good fit at all sites, except at site b26. At this site, it was not possible to fit data and model responses at periods longer than 1s. Hence, this site was not considered in the computation and analysis of misfit values and further sensitivity tests.

At the other sites, considering an error floor of 10% in the resistivities and 2.9^o in the phases, the total rms values are rms(ρ_{DET})= 4.08 and rms(φ_{DET})=2.32. Short period data (up to 1s) are well fitted by model responses, presenting low rms values (rms(ρ_{DET})= 2.94 and rms(φ_{DET})=1.85), whereas for periods longer than 1s, the model does not reproduce so well the data responses (rms(ρ_{DET})= 5.11 and rms(φ_{DET})=2.65) (see Figure 10.10).

Maps of the total rms values at each site averaged over all periods are plotted in Figure 10.7. They show a broad variation of the determinant resistivity misfits (rms(ρ_{DET})) along the different sites locations compared to the misfits of the determinant phases (rms(φ_{DET})), which are more uniform. Higher values of rms(ρ_{DET}) (>5) are present over the Internal Betics and over sites b14 and b40. The high rms values over the Internal Betics are caused by the high density of sites, with different responses, and the difficulty to fit all them jointly. However, at sites b54 and b57, the high rms values are due to the difficulty of fixing the pronounced negative slope at the middle and long periods (>10 s). Similarly, the high rms values observed at sites b14 and b40 are also caused by the longest periods.

In relation to the determinant phases, the misfits are generally low with values comprised between 1 and 3. The only exception is site b08, which shows a significantly higher value (rms(φ_{DET})=6), a consequence of the proximity to site b07, with significantly different resistivity responses.
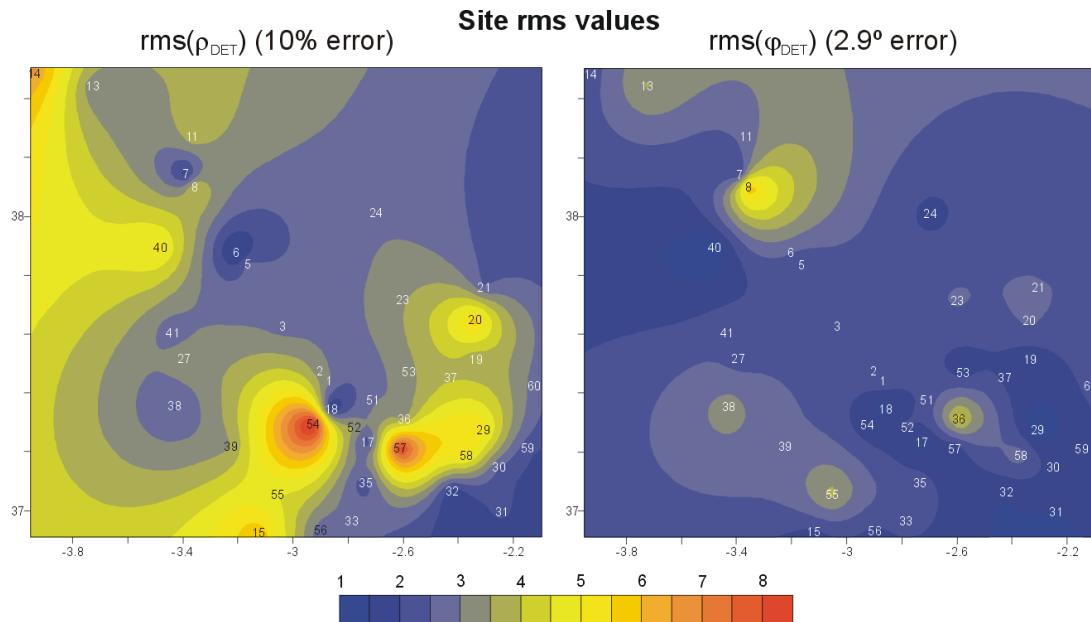
Figure 10.7: Rms maps of the determinant resistivities and phases of the Betics MT sites in reference to bet3D-140 model responses. Numbers on the map indicate site locations.

The rms values of the WAL invariants between data and model responses were also computed, a 10% error. I_1 and I_2, related to the magnitude of resistivity and phase, present low rms values (rms(I_1)=2.87 and rms(I_2)=2.51). For the rest of invariants, although both in the data and model responses are increasing along with the period, the rms values are significantly higher (rms(I_3)=10.84, rms(I_4)=21.56, rms(I_5)=31.09, rms(I_6)=144.53, rms(I_7)=124.76 and

rms(Q)=13.40). Nevertheless, it must be noted that, as already shown in chapter 8, the errors of the Betics dataset invariants are in general higher than 10%. The reasons for these elevated values of the rms stand on the difficulty on jointly fitting all these six invariants and on the lack of errors and/or geologic noise effects in the invariants computed from the ideal model.

10.5.1 Dimensionality of the 3D model

WAL dimensionality analysis of the model bet3D-140 was carried out at the data sites locations (Figure 10.8). Given that it was performed on model responses, not affected by either statistical or geologic noise (i.e., ideal data), a small value of the threshold was used (τ_W=0.01). Although the results do not coincide with the dimensionality obtained from the data at most of the sites, these show how the model complexity increases with the period, and towards the south, as obtained from the data analysis.
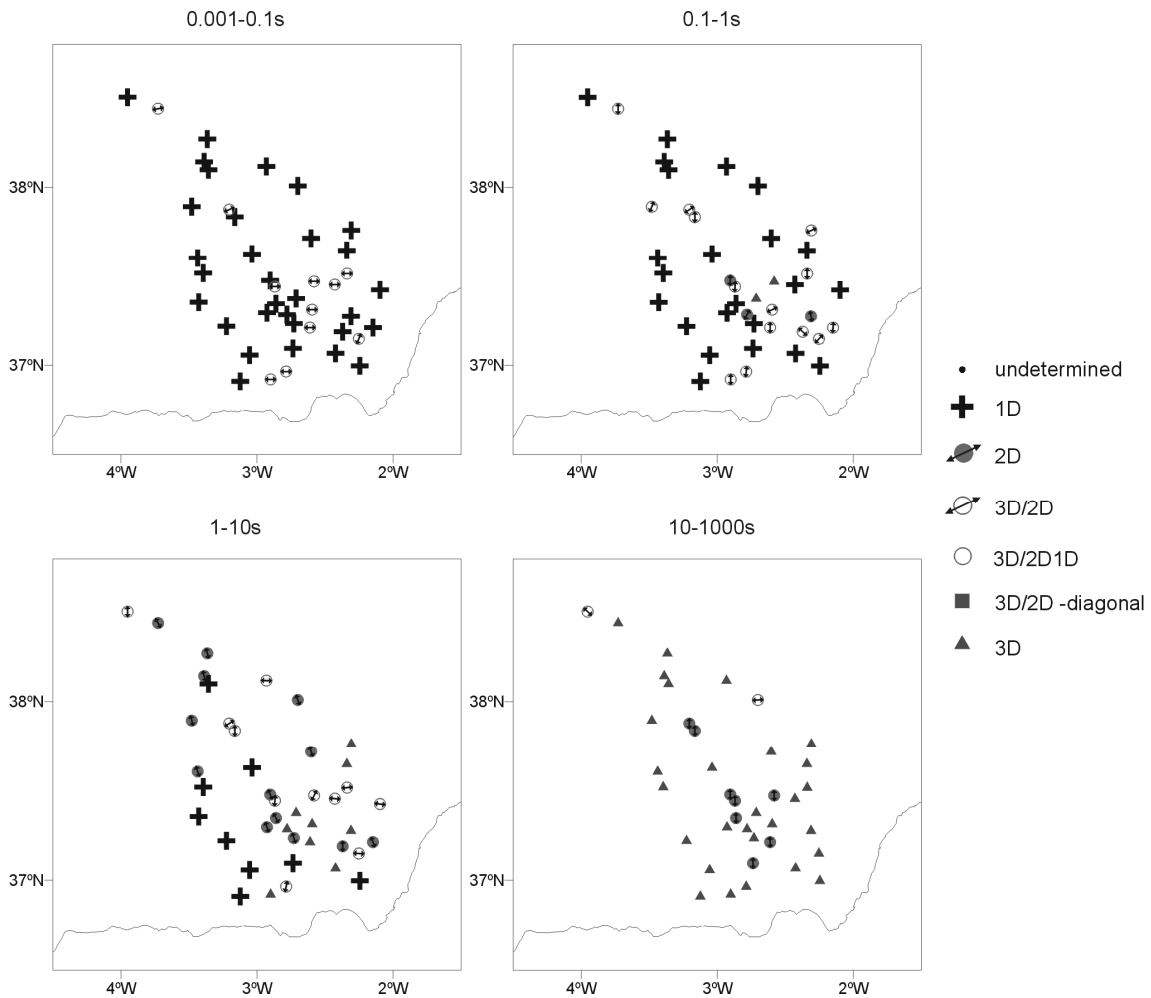
Figure 10.8: Model dimensionality using WAL criteria, using τ=0.01 and τ_Q=0.1.

10.6 Sensitivity Tests

The low and moderate values of the rms obtained between the data and model apparent resistivities and phases allow one to consider the model bet30-140 as valid. However, in order to determine how well defined is the structure shown by the model, sensitivity tests were performed. These deal with: 1) model mesh and 2) position and size of the conductor **CF3** (Figure 10.3k, page 205) located below the Sierra de los Filabres.

Among the sensitivity tests, none were carried out on the resistivity values. It was not considered necessary since along the different steps in the construction of the model, resistivity values were well contrasted. Resistivity values of the model are very sensitive to the static shift correction carried out in the data, and had these corrections been different, other resisitivity values in the model would have been obtained. However, this was outside the scope and time constraints needed to perform such different corrections and to verify them.

10.6.1 Model mesh

With the aim of checking the adequacy of the mesh used to construct the 3D model (50x50x25 elements), the model mesh was resized to 80x80x40 elements. Using this new mesh, the computed forward responses resulted in an increase of the resistivity rms values (Table 10.1). This increase is mainly caused by site 14 (rms$(\rho_{DET})_{bet30-140}$=6.08 and rms$(\varphi_{DET})_{resized}$=22.29), located at the NW edge of the model, and is attributed to the new boundary conditions, which were not inspected in detail. At the rest of sites, no significant changes in the responses were observed. Consequently, it can be stated overall that the model responses converge and are stable with the mesh size.

Rms/model	Model bet3D-140	Resized mesh model
rms(ρ_{DET}) 10% error	4.08	4.38
rms(φ_{DET}) 2.9^o error	2.32	2.38

Table 10.1: rms values of the determinant resistivity and phase between data responses and the original model (bet3D-140) and resized model responses.

10.6.2 Position, extension and size of the conductive body CF3

The presence of a large conductive body at mid crustal levels below the Internal Zone is one of the most striking results obtained from the MT study performed in the Betics.

Consequently, several tests were performed to infer the extension and position of the conductor **CF3** and also to check whether the overlying conductors **CF1** and **CF2** can be considered part of **CF3** or not.

CF3 body extension tests:

To test the horizontal extension of the conductor **CF3**, two new models were constructed (Figure 10.9). In the first one, conductor **CF3** is located only below sites b17 and b57 (bet3D-1757), and in the second, the conductor is extended towards the southwest (bet3D-ext). The conductor was not extended towards other directions, as the surrounding sites indicate that it is not present beneath them.
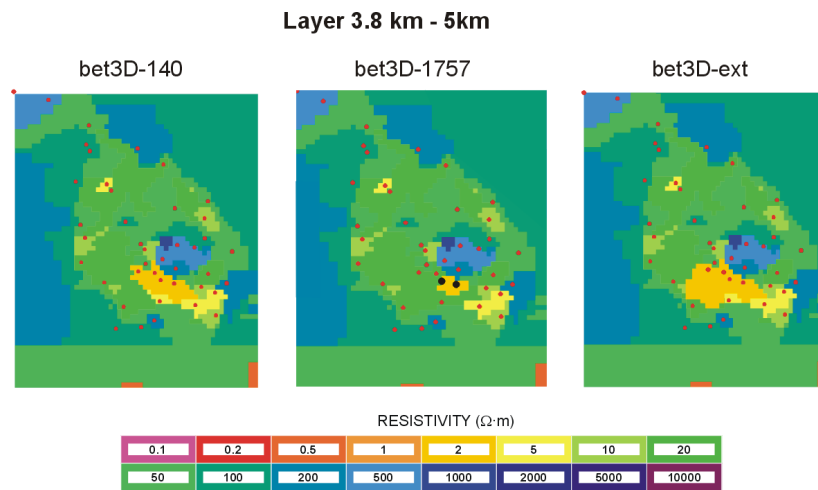
Figure 10.9: Horizontal representation of the 3.8 km – 5 km layer corresponding to bet3D-140 model and the two models testing the extension of conductor **CF3**. In the test model bet3D-1757, the extension of **CF3** reduced to just beneath sites b17 and b57 (locations indicated as black circles on the plot). In the test model bet3D-ext, the conductor **CF3** is extended towards the southwest.

Comparing the rms values corresponding to the determinant responses of these two models with those of the original model (bet3D-140) it can be observed that these changes in the model extension only affect the longest periods (Figure 10.10). Moreover, the resistivity rms values of the sites located above and around the areas are affected by the modifications in the conductor extension (framed region in Figure 10.11).

In the model bet3D-1757, the resistivity rms increases, for periods longer than 50s, in the west and central parts of the framed region (sites b54, b18, b52, b17 and b35), and there is no part of the rms map where this value decreases. Consequently, this model is not considered valid.
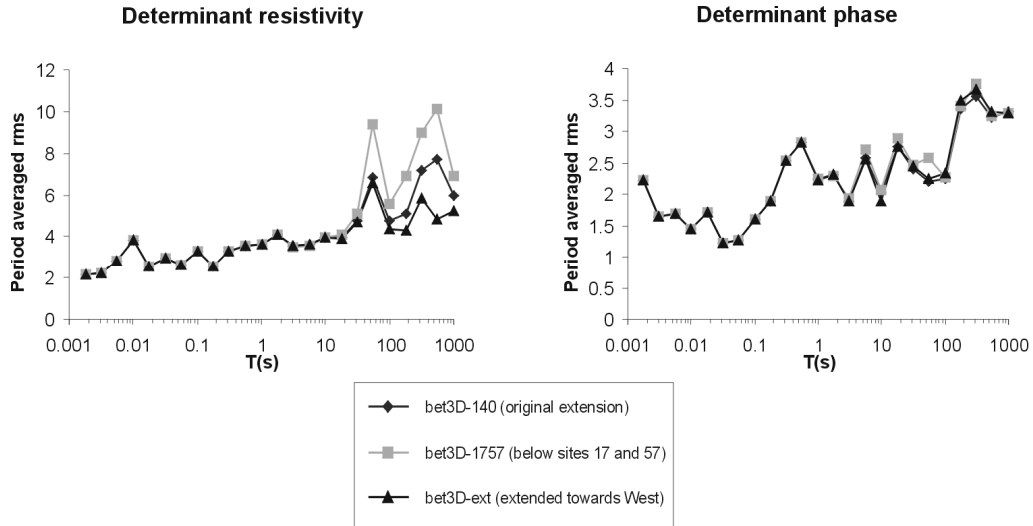
Figure 10.10: Period averaged determinant rms values corresponding to 10% error in the resistivities and 2.9° in the phases, calculated for the three models with different extensions of the conductive body **CF3**. Final model bet3D-140, model bet3D-1757, with the conductor confined below sites b17 and b57; and model bet3D-ext, with the conductor extended towards the southwest.
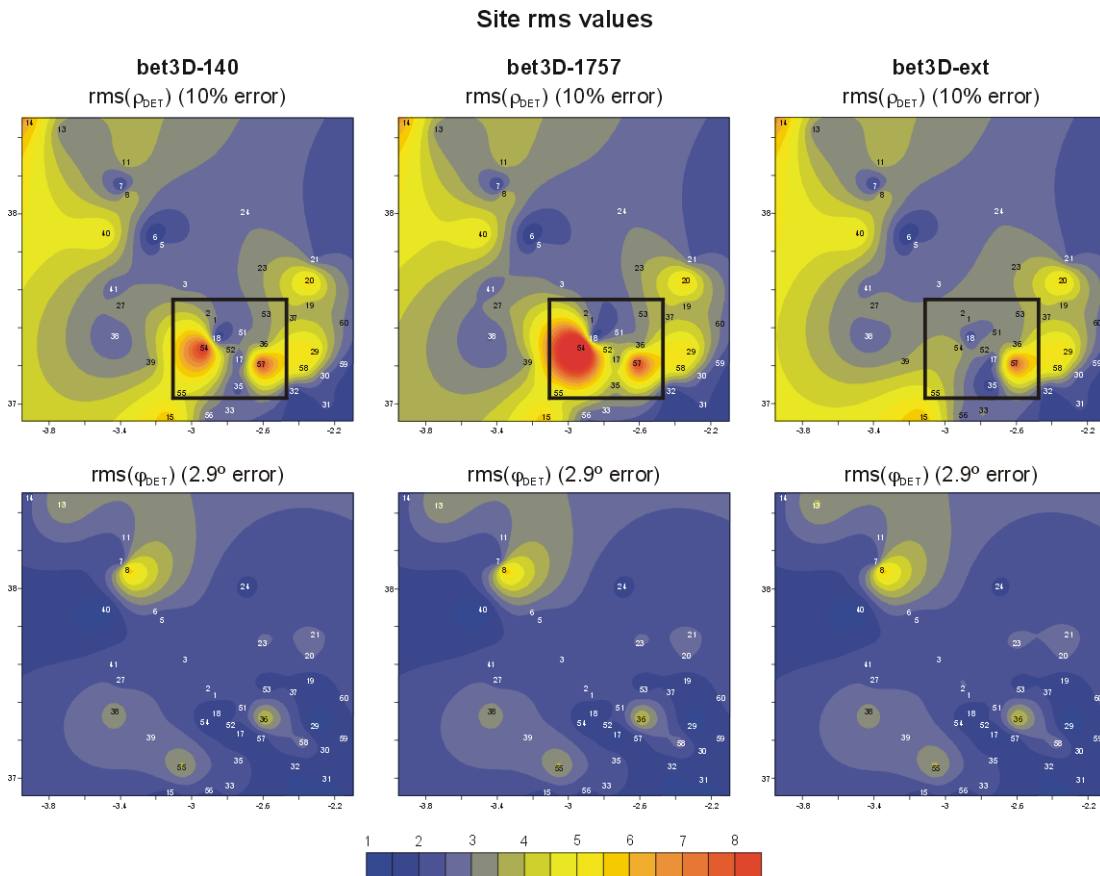
Figure 10.11: Rms maps of the determinant resistivities and phases of the Betics MT sites with respect to models bet3D-140 (original), bet3D-1757 (conductor located below sites b17 and b57) and bet3D-ext (conductor extended towards southwest) models. Numbers on the maps indicate site locations. Frames in resistivity maps show the areas of significant differences between the three models.

As for the model bet3D-ext, the rms values of the determinant resistivity are in general smaller (Figure 10.10). Although in the north-central part of the framed area, it has a slight increase, the rms values decrease drastically at site b54 and, to a lesser degree, at sites b17 and b35. Hence, the model det3D-ext, with the conductor body **CF3** extended towards the west and with an E-W orientation is also compatible with the data responses.

CF3 body depth tests:

The original model, with conductor **CF3** extending vertically from 3.8 to 17.5 km, was modified, in five new models, through changes in the depth positions of the conductor top and bottom (Figure 10.12).
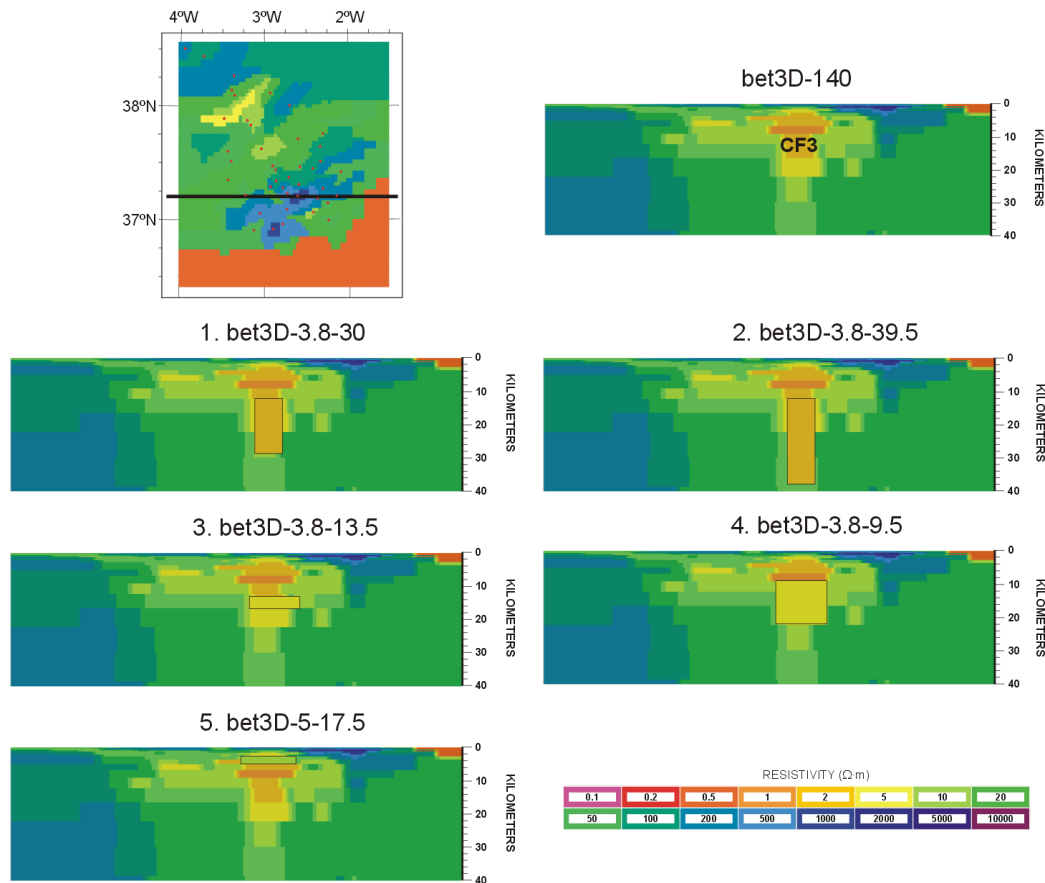
Figure 10.12: Vertical sections of the models created to test the depth sensitivity of the **CF3** conductor. Top: section of the original bet3D-140 model. 1, 2, 3, 4 and 5: sections of the modified models. Numbers in the model names refer to the top and bottom of the modified conductor **CF3** (e.g. 1: top 3.8 km, bottom 30 km). Framed areas in the model sections indicate modified conductivity zones. Location of the vertical sections is indicated in the plan view of the bet3D-140 model (top left corner).

The comparison between the different models only shows significant changes in the values of the rms(ρ_{DET}), and not in the rms(φ_{DET}) (Table 10.2). If the top of the conductor is fixed, the rms values are similar if its bottom is displaced by up to 39.5 km (models 1, 2 and 3), and increases if the bottom is located at an upper position (model 4). On the other hand, changes in the top of the conductor show that its top cannot be at lower depths, given the considerable increase of the rms when the top is located at 5 km depth (model 5). Hence, the conductor **CF3** must have a top located at 3.8 km and a bottom position that may vary from 17.5 km to 30 km depths.

Rms/ model	bet3D-140 (3.8 km-17.5 km)	1. det3D-3.8-30	2. det3D-3.8-39.5	3. det3D-3.8-13.5	4. det3D-3.8-9.5	5. det3D-5-17.5
rms(ρ_{DET})	4.08	4.07	4.08	4.15	4.33	5.38
rms(φ_{DET})	2.32	2.32	2.33	2.32	2.33	2.37

Table 10.2: rms values of the determinant resistivity and phase between data and model responses of bet3D-140 and the 5 models with modifications in the vertical extent of the conductive body, CF3.

Continuity between CF3 and CF1 and CF2 conductors:

In order to test if the conductor **CF3** is in fact connected to the overlying conductors **CF1** and **CF2**, or if, on the contrary, it is separated from them by a relatively resistive zone, two new models were created. Both models include a moderate resistive layer (20 Ω·m) located over the top of the conductor **CF3**. One with the top located at 2.8 km, and a thicker one with the top located at 2 km (Figure 10.13).

Rms(ρ_{DET}) values in both cases are significantly larger than in the original model (Table 10.3). This increase is rather proportional to the separation between **CF1**-**CF2** and **CF3**. Hence, it can be stated that these conductors are vertically connected, or, if they are separated, it is by a thin resistive layer (<400 m).
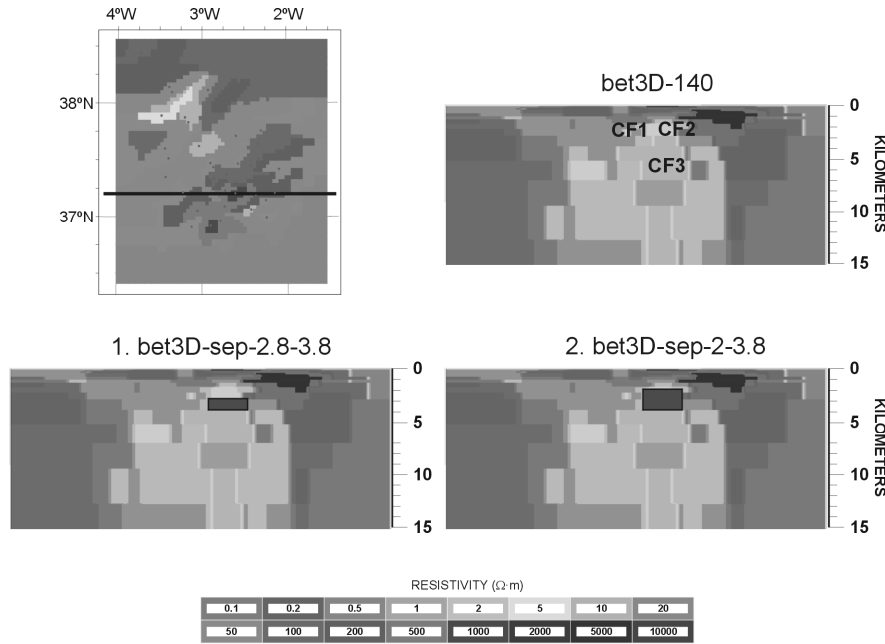
Figure 10.13: Vertical sections of the models created to test the sensitivity of the separation between CF1, CF2 and CF3 bodies. Top: section of the original model bet3D-140 model. 1 and 2: sections of the modified models. Numbers in the model names refer to the top and bottom of the zone where conductivity values were replaced by resistivive ones (black zones, 20 $\Omega \cdot$m). Location of the vertical sections is indicated in the plan view of the bet3D-140 model (top left corner).

Rms/ Model	bet3D-140 (no separation)	bet3D-sep-2.8-3.8	bet3D-sep-2-3.8
rms(ρ_{DET})	4.08	4.51	4.99
rms(φ_{DET})	2.32	2.33	2.37

Table 10.3: rms values of the determinant resistivity and phase between data and model responses of bet3D-140 and those of models bet3D-sep-2.8-3.8 and bet3D-sep-2-3.8, introducing a separation between CF1, F2 and CF3 bodies.

10.7 Model Evaluation

The comparison between data and model responses shows that the model bet3D-140 is consistent, given the low and medium values of the rms observed in the determinant resistivities and phases. However, three main weak points of the model can be stated:

The first one is the difficulty to fit all MT tensor components, as has been reflected in the large rms values of the WAL invariants. Such a problem can be attributed to the limited possibilities in the trial and error modelling process and to the complexity of the area.

The second is the large variation in the rms value among different sites, attributed to the difficulty to fit data from close sites with significantly different responses. Then, one must bear

in mind that the parts of the model below isolated sites with low rms values are not better imaged than those parts below a high density of sites and a high rms value.

The third is the loss of resolution at depth, as reflected by the increase of the rms values with the period. This fact is more important below conductive zones, where the skin depth is shorter.

All these problems could be improved by the acquisition of a denser site distribution and longer time series to obtain longer period data and the use of inversion procedures.

With regard to the sensitivity tests performed, these have corroborated the validity of the model and its most significant features. The model shows to be stable to the mesh size, with the exception of site 14 due to boundary problems.

In relation to the conductivity body **CF3**, detailed sensitivity tests denote that:

1) This needs a maximum top depth of 3.8 km, which can be separated by up to 400 m from the upper bodies **CF1** and **CF2**.

2) Its orientation can vary from WNW-ESE to E-W, given the compatibility between the original model and the model with the conductor extended towards the west.

Although other models with a larger extension and depth of the conductor **CF3** have been shown to be valid, bet3D-140 is considered in the interpretation. This is the one that presents a minimum acceptable structure, and, as it will be shown in section 11.9, it has been considered very difficult to interpret a conductive body reaching depths of 30 km, where the model lacks resolution.

10.8 Comparison with other Geophysical Data

The comparison between the 3D model obtained from MT data (bet3D-140) and the available geophysical data in the study area, allows inference of the following:

The Moho and the boundary upper and lower crust (ULCB) depicted from seismic refraction and deep reflection profiles ESCI-B1 (only the Moho) and ESCI-B2 cannot be equally identified in the MT model (Figure 10.14). Thus, it is neither possible to detect the presence of a crustal root below the Internal Zone, as indicated by gravimetric data. The non-identification of these two limits may be because they cannot be distinguished electrically and hence cannot be correlated with the seismic reflectors (e.g. Holmes's Curious Dog, Cook and Jones, 1995), or in the case of the Moho, to a lack of resolution at these depths.

The bottom of the shallow conductor **CGB**, located where the Guadalquivir Basin infill outcrops with continuation towards the Prebetic and Subbetic zones, is coincident with the reflector observed in the seismic reflection profile ESCI-B1 and with a sudden variation in the velocity (refraction seismology). This velocity change and the presence of the reflector are

interpreted as the base of the Guadalquivir Basin, i.e., the top of the Variscan basement (Galindo-Zaldívar *et al.*, 1997).
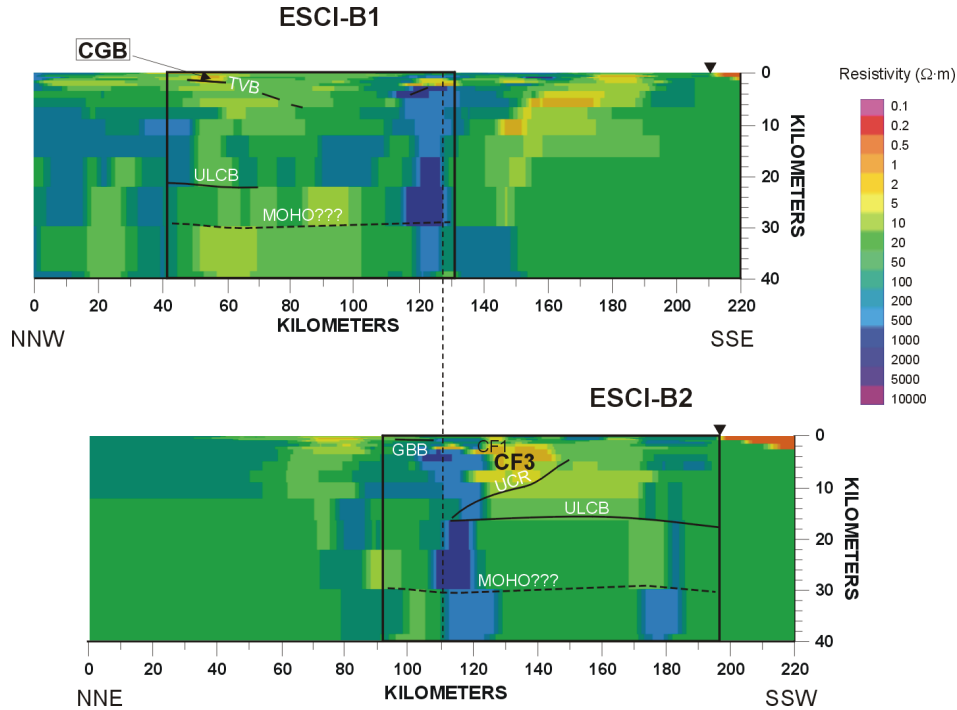
Figure 10.14: Cross sections of 3D conductivity model bet3D-140 along ESCI-B1 and ESCI-B2 seismic reflection profiles with the main interpreted reflectors and conductors. Framed areas indicate the areas covered by these two seismic profiles. White names identify reflection lines, black letters, conductive bodies. Vertical discontinuous line is the tie line. Inverted triangles: coast line. TVB: top of Variscan Basement reflector; ULCB: upper-lower crust boundary reflector; GBB: Guadix-Baza Basin reflector; UCR: upper crust reflector; CGB: Guadalquivir Basin conductor; CF1 and CF3: Filabres conductors.

The conductor **CF3** located beneath the Internal Zone is located slightly SW of a strong magnetic anomaly located at the NNW part of the Sierra de los Filabres (Figure 10.15). This anomaly has a maximum amplitude of 70nT and a dipole length of 15 km – 20 km, which is not incompatible with being caused by the conductor body **CF3**, if it had the required magnetic characteristics.

Along the seismic reflection profile ESCI-B2, the SSW limit of this conductor agrees with the location of the UCR reflector. Yet, there is no significant change in the gravimetric, heat flow and seismic tomography data that could be correlated with the presence of the conductor **CF3**.

Finally, there is no direct correlation between the geoelectric structures, the seismicity and the seismic tomography. However, over and surrounding the conductive body **CF3**, at

depths between 5 km and 17 km, the seismicity is relatively low (Figure 10.16) and this conductor is located over a broader area with relatively high seismic v_p values (Figure 10.17).
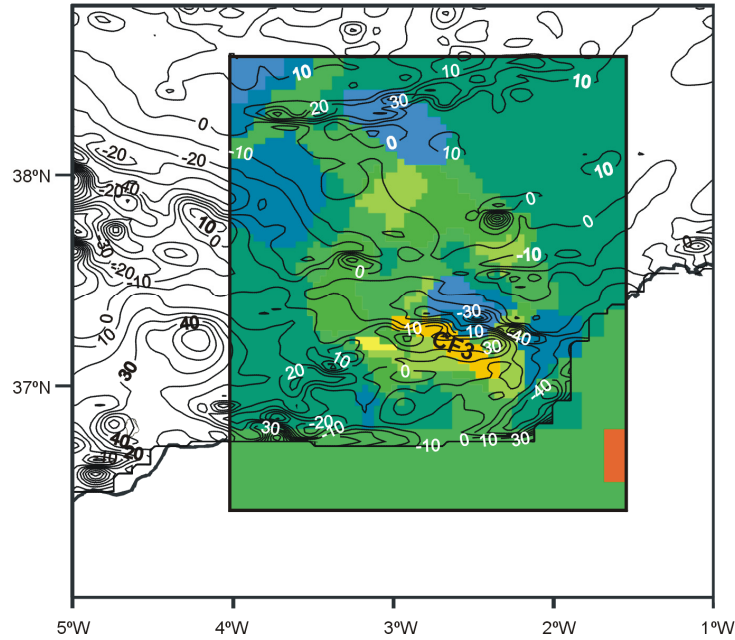
Figure 10.15: Superposition of the total magnetic anomaly map (see chapter 6, Figure 6.7) with layer 5 km-7 km (Figure 10.2l) from model bet3D-140. Isomagnetic anomaly values are in nT.
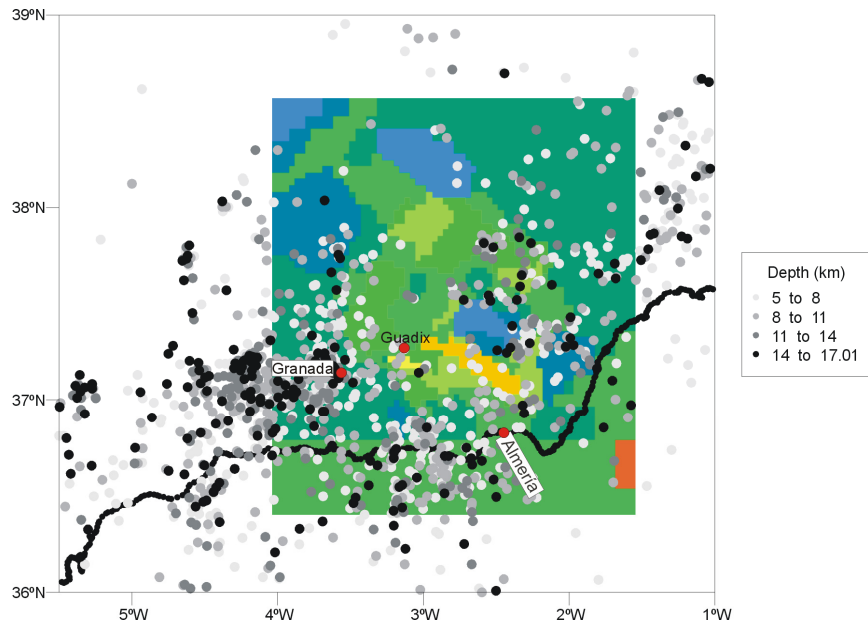
Figure 10.16: Seismicity map of the 3D model area and surroundings, showing only the seismic events from 5 km to 17 km. The coloured background represents the layer 5 km to 7 km of the 3D model bet3D-140.
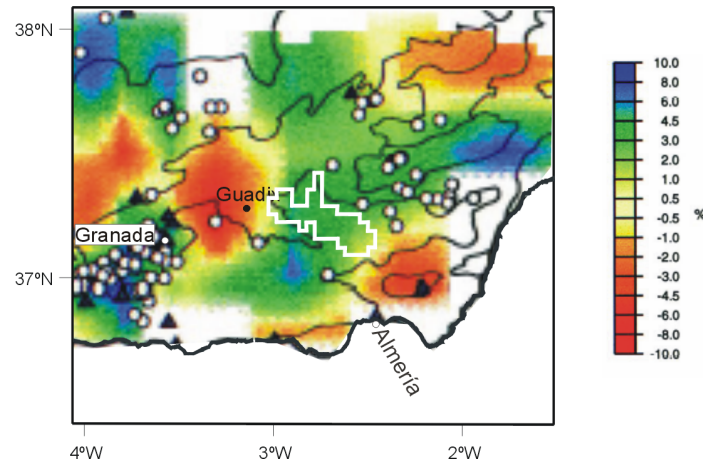
Figure 10.17: Tomographic P-velocity anomalies map corresponding to layer 4 km - 12 km ($<v_P>$ = 5.7 km/s). The white outline represents the layer 7 km – 9 km of the conductive body CF3.

10.9 Interpretation

The comparison between the geoelectric structures imaged in the 3D model and the available geological and geophysical information allowed proposing the following interpretation of the main resistors and conductors recognised in this 3D model.

This interpretation is described in the same order as in the model description (section 10.4) and includes a specific subsection with the discussion of the high conductive body **CF3**, located below the Internal Betics.

Iberian Massif:

This part of the model is characterised by a moderately high resistive zone (**RIM**), with a relatively conductive zone (**CIM**) between 2.15 km and 17.5 km, overlain at the southeast by two shallow conductors, **C7-8** and **C-11**.

Considering the outcropping materials and their structure, the resistive zone **RIM** can be associated with the Variscan basement formed by metamorphic and granitic rock. The relatively high conductivity of **C7-8** (Figure 10.3f, page 214) and **C-11** (Figure 10.3h, page 215), located from 1 km to 2 km depth, which is coincident with the bottom of the Mesozoic cover that overlies the Variscan basement next to the Guadalquivir Basin. This high conductivity is interpreted as due to fluid circulation through the detrital sediments of the base of this cover.

With reference to the NE-SW oriented conductor **CIM**, it does not crop out at the surface and it is not parallel to any of the geologic structures observed at surface, which are mainly NW-SE. Lacking more information, it is proposed that it may be associated with a

lithologic change. In this sense, it may be noted that 200 km towards the west, MT studies (Muñoz, 2005) show even more conductive bodies (5 Ω·m) at similar depths that have been related to the graphite rich Precambrian Serie Negra rocks. Their elevated conductivity has been attributed to the interconnection of graphite grains. These rocks are present in all the Central Iberian Zone, and hence, in the study area as well, although given their higher resistivity values, with a lower content and/or lower interconnectivity.

Guadalquivir basin:

The model shows a shallow E-W oriented conductive body, **CGB**, decreasing in extension with depth that overlies a moderately resistive zone with similar values as in the Iberian Massif.

The coincidence between the shape of the **CGB** conductor at the surface and the outcropping infill of the Guadalquivir Basin, denotes that this conductor is related to this infill, and therefore reproduces its shape (Figure 10.18). Thus, the MT model shows that the maximum depth and thickness of the basin infill increases towards the SE, where it reaches a maximum thickness of 5 km. The high conductivity of the basin infill (5Ω·m) is related to fluid circulation through its poorly consolidated sedimentary layers.
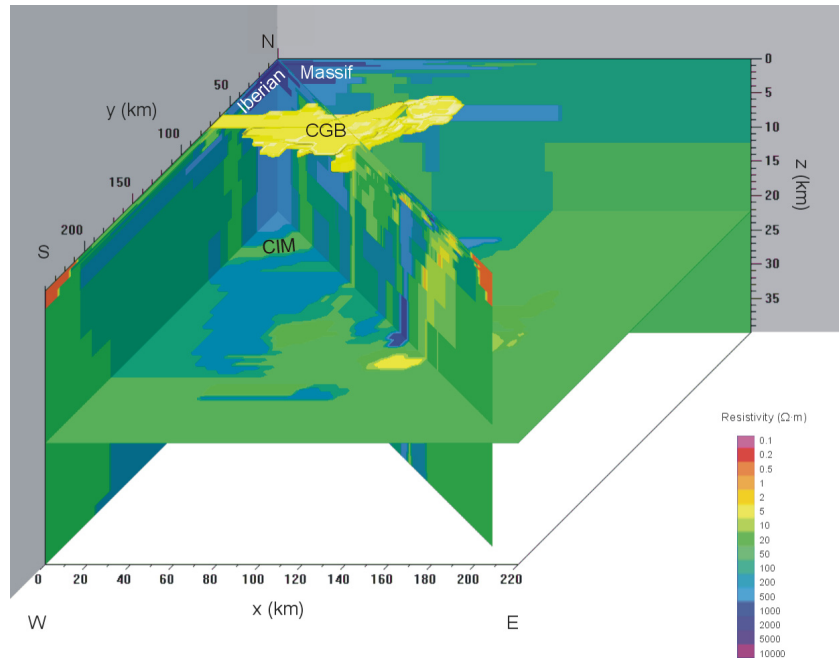
Figure 10.18: 3D view of bet3D-140 conductivity model, in which NS, EW as well as a NW-SE directed vertical slices and a horizontal slice at 22 km are plotted. A 3D view of the 5 Ω·m conductive zone corresponding to the Guadalquivir basin (CGB), and Iberian Massif main features (high resistivity, RIM; and conductive zone CIM) are also plotted.

External Zone:

This zone is characterised by a shallower level (up to 1.2 km - 2.15 km) of moderately resistive values that is more conductive to the south (**C20** and **C27-38**) and overlies a thin conductor, which is in continuity with the conductor **CGB** recognised in the Guadalquivir Basin. Below, in this entire zone there is a relatively high resistive zone.

The elongation in depth of the conductor **CGB** allows delimiting the continuation of this foreland basin below the External Zone, up to 20 km E beneath the Prebetic zone, and up to 30 km S beneath the Subbetics.

The overlying shallow level of moderately resistive values and the conductors **C20** and **C27-38** are associated with the Mesozoic and Cenozoic rocks forming the External Zone of the Betics. The shallow moderate resistivity is related to fluid circulation in carbonated rocks of the Prebetic and outer Subbetic zones; and the conductivity of **C20** and **C27-38** to a major content in shales and the presence of basaltic rocks in the inner Subbetic. The significantly higher conductivity of **C20** indicates that it can be directly attributed to the presence of flysch rocks in this area, which continue NW below the Inner Subbetic materials (Jabaloy *et al.*, 2005) (chapter 6, figure 6.9), below the location of site b20. Differences in the composition and/or porosities between the flysch and inner Subbetic rocks can explain the different conductivity values observed between these two zones.

The continuation of **C20** and **C27-38** below the Internal zone denotes that the External Zone and/or the Flysch units are partially overthrusted by the Internal zone.

Below the conductors and moderately resistive zone of the External Zone and the Guadalquivir Basin, the higher resistivity values are associated with the continuation of the Iberian Massif below the External Zone.

Internal Zones:

This part of the model shows a resistive zone, up to 13.5 km (**RI**), among which several conductors appear as well as a deeper and larger conductor (**CF3**). The shallow conductors appear beneath the Sierra de los Filabres at depths between 1.6 km and 3.8 km (**CF1** and **CF2**), and beneath the Sierra de las Estancias (**CE**) and Sierra de Alhamilla (**C31**), reaching in these cases 2.8 km and 2.15 km respectively. The larger conductor **CF3** has a top that can be more or less variable, depending on whether it includes **CF1** and **CF2** conductors or not. In any case, this top would be situated at depths from 1.6 to 3.8 km in the WNW (or W) part and 3.8 km in the ESE (or E) one. Its base dips from 5 to 9 km (below the NW and SE extremes) to 17.5 km (below the central part of Sierra de los Filabres, i.e., site 57).

The high resistivity values of first layers below the Alpujárride and Nevado-Filábride complexes (**RI**) are caused by metamorphic materials, mainly graphitic schists. Despite its

graphite content, the bulk resistivity of these metamorphic rocks is high, which may be caused by a separation of the graphite films during their uplift (e.g. Mareschal *et al.*, 1992), contrary to the high conductivity observed in the Serie Negra (Iberian Massif), where the graphite films are connected (e.g. Keller and Frischkneht, 1966).
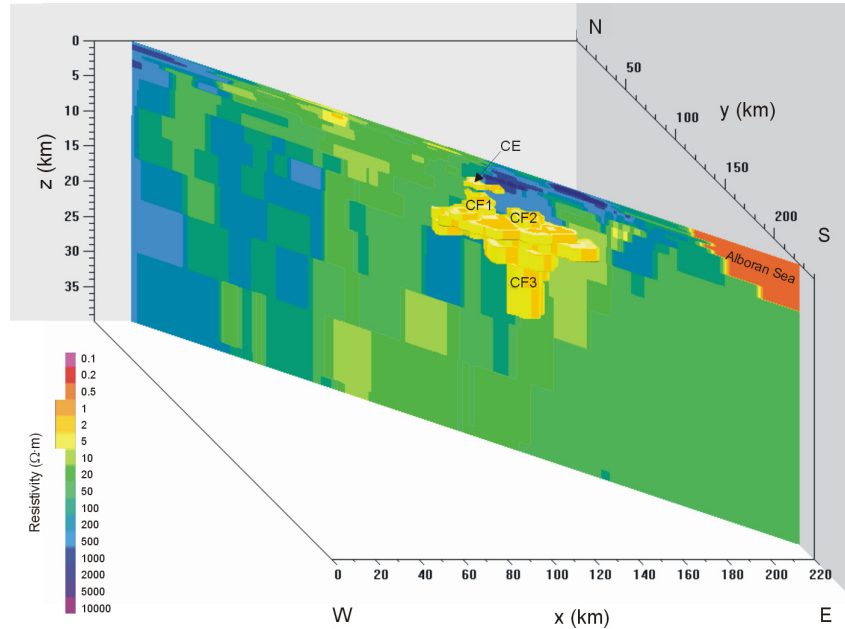
Figure 10.19: N45°W vertical cross section of the 3D model plus a 3D representation of the conductive zones (1 Ω·m, 2 Ω·m and 5 Ω·m) imaged below the Internal Zone.

The size and location of the shallow conductors in the areas affected by folded extensional detachments bounding the Alpujárride and Nevado-Filábride complexes or different Nevado-Filábride units (Figure 10.4) suggests that they are generated by fluid circulation along these fractures.

10.9.1 CF3 high conductivity

The WNW-ESE orientation, parallel to the Variscan structures and tectonic zones, together with the alignment with the conductive Variscan pyrite belt that outcrops NW of the conductor **CF3**, could suggest that this conductor belongs to the Iberian Massif. However, its shallow top makes this interpretation very improbable, as it would imply that the Betics detachment would be located below the Internal Zone at depths of only 3 km -5 km, implying a sudden uplift of such a detachment which, dipping to the SE is located at 10 km depth at the Internal – External boundary zone.

Given its vertical location and extension, the interpretation of **CF3** as belonging to the Alboran domain, seems the more plausible. Under this hypothesis, it is located between the overlying Nevado-Filábride resistive metamorphic rocks (with a total thickness from 1.6 km to 4 km) and the Betics-Iberian crustal detachment level (see NNW-SSE model cross section superposed over Transmed I section, Figure 10.20), in the core of the major antiform that crosses EW the central parts of the Sierra de los Filabres and Sierra Nevada (Figure 10.5).
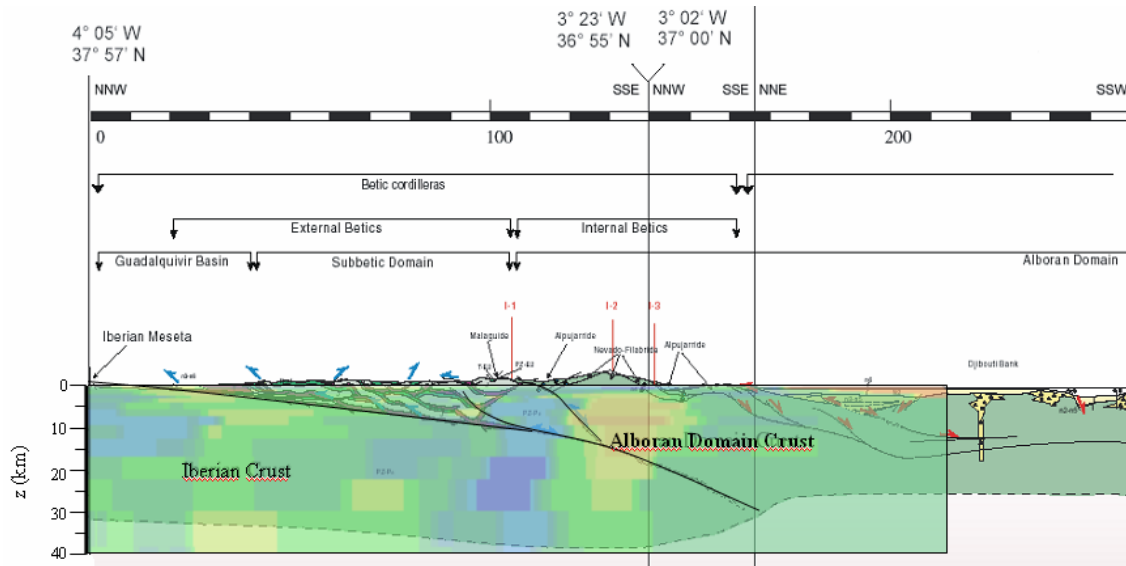
Figure 10.20: Transmed Transect I with a NNW parallel cross section of the 3D model projected.

In this tectonic setting, the conductor is located in an area where available geophysical information shows:

1) A moderately high seismic v_p anomaly between 4 km and 12 km depth (Dañobeitia *et al.*, 1998) (Figure 10.17).

2) Low seismic activity (Figure 10.16).

3) The local coincidence between the location of UCR reflector and the bottom of **CF3** conductive body (Figure 10.14).

4) A magnetic anomaly (-40nT to +30nT) with an almost E-W orientation, with the centre of its western edge coinciding with the WNW edge of the conductor **CF3** (Figure 10.15). This anomaly has been modelled by Galindo-Zaldívar *et al.* (1997) as a 10 km thick magnetic body caused by Fe-mineralisation along joints in the Nevado-Filábride metamorphic rocks, up to a depth of 10 km.

5) High topography (peaks up to 3500 m) located over an area in which the proposed gravimetric models do not show any significant crustal root.

6) Crustal geotherms, calculated for the Betic Chain (Zappone *et al.*, 2000) from available heat flow data (Fernàndez *et al.*, 1998b), estimate a range of temperatures at the depths of **CF3** between 100°C at its top (3.8 km), to 325°C-500°C at its bottom (17.5 km).

In Earth materials, as already seen, high electrical conductivity anomalies can be due to the presence of fluids, partial melting or high conductive mineral phases (e.g. Jones, 1992). In the later, the high conductivity depends on their composition and interconnection level.

With reference to conductive body **CF3**, the presence of fluids alone makes it difficult to explain the large volume of the conductor, its location in the axis of the antiform, the moderately high seismic velocity values and the low seismic activity (the presence of fluids at the considered depths implies elevated pore fluid pressures which decrease the ultimate strength, rupture strength and ductility, Davis and Reynolds, 1996).

The hypothesis of partial melting was rejected too, as it commonly needs minimum temperatures of 700°C (Thompson, 1992), significantly higher than those estimated from heat flow data (see above). Only if **CF3** reached depths up to 30 km, as can be accepted from the sensitivity tests, could partial melting be considered just for the deepest kilometres of the conductor (27 km to 30 km).

Therefore, the high conductivity of the conductor **CF3** seems to be due to the presence of highly conducting mineral phases. According to the geophysical observations the conductor must also be a material with moderately high v_p values, of a ductile nature or mechanically resistant (low seismicity), and likely high density.

As already stated, **CF3**, according to the heat flow data, must have temperatures ranging between 100°C and 500°C. For most materials, these temperatures are below the Curie temperature, and hence, it could explain the westernmost part of the magnetic anomaly observed (Figure 10.15).

Kiss *et al.* (2005) demonstrated the effects of the increase of magnetic susceptibility just below the Curie temperature over magnetic and magnetotelluric data (Hopkinson effect), which is considered more significant than previously thought. If this effect is not considered, magnetic anomalies are interpreted as being caused by large magnetic bodies. Over 2D and 3D MT data, the interpretation results in an ensemble of highly conductive and highly resistive zones. Within the depth range of **CF3**, if the Curie temperature were reached and the Hopkinson effect occurred, it would only involve a layer of a few hundreds of meters. Hence, even if this transition occurred, the whole conductive body **CF3** could not be replaced by a body with lower conductivity values and higher magnetic susceptibilities.

Another geophysical constraint to be considered is the non-existence of a significant crustal root below the highest topography as interpreted (Torné and Banda, 1992) from the Bouguer anomaly map (Figure 7.6). The emplacement of a dense body in the crust below the

high peaks of Sierra Nevada and Sierra de los Filabres, and the addition of a crustal root, is compatible with the observed gravimetric data (e.g. a body with a density $0.1g/cm^3$ higher than the average crustal value will result in a crustal root of 7 km). Hence, the conductive body **CF3** can have a higher density than the average crustal rocks, which would allow for the existence of a crustal root below the Internal Zone.

In order to explain the reasons of the high conductivity of this body, it must be considered how the conducting mineral phases interconnect as to increase the bulk conductivity of a rock. In the case of graphite, it forms thin films that are easily interconnected; whereas other conducting minerals (e.g. pyrite and pyrrhotite) need an additional mechanism to enable their interconnection. This mechanism may be fluids that spread the massive sulphurs forming a matrix allowing for their interconnection. Although these fluids are subsequently released, the interconnected matrix, and hence, the high conductivity prevails.

Considering high seismic velocities, low associated seismicity and high density, the rock hosting these conducting minerals must be a ultrabasic or basic rock, such as ophiolites (e.g. gabbro) or peridotites. In the Betics, rocks of the same type have been observed in the ophiolitic units of the Nevado-Filábride complex, and in outcrops at the western sector of the Betics (Ronda, Alpujárride complex), in some cases partly serpentinized (Zappone *et al.*, 2000). However, especially in the case of ophiolites, the seismic velocity values would be much higher than those estimated, although the v_p values obtained from seismic tomography are averaged over a large depth range. Another possibility is continental lower crustal rocks (amphibolites or granulites). Based on the present geologic and geophysical constraints it is not possible to discern among these hypotheses. Additional petrologic studies and resistivity measurements *in situ* of outcropping materials of the same type as those discussed above, and detailed tomographic and gravimetric studies would provide more constraints on the exact nature of this body.

Summarizing, the highly conductive body has been interpreted as ophiolitic or as lower crustal rocks with some type of mineralization (graphite or pyrite) that enhances the conductivity in a large volume at depths between 4 km and 17.5 km. This differentiated lithologic unit would be located beneath the Nevado-Filábride complex, along the core of the E-W major antiform of the Sierra de los Filabres and Sierra Nevada. This antiform forms a culmination over the conductor **CF3** and plunges east in the east and west in the west. Such geometry, combined with the south-dipping plane of the basal Betic detachment, would explain the disappearance of the conductor east and west of the study area (Figure 10.21). Taking this geometry into account, the conductor would be E-W oriented. In the 3D model, its orientation is WNW-ESE, although, as shown in the sensitivity studies, it can be also E-W, in accordance with the explained geometry.
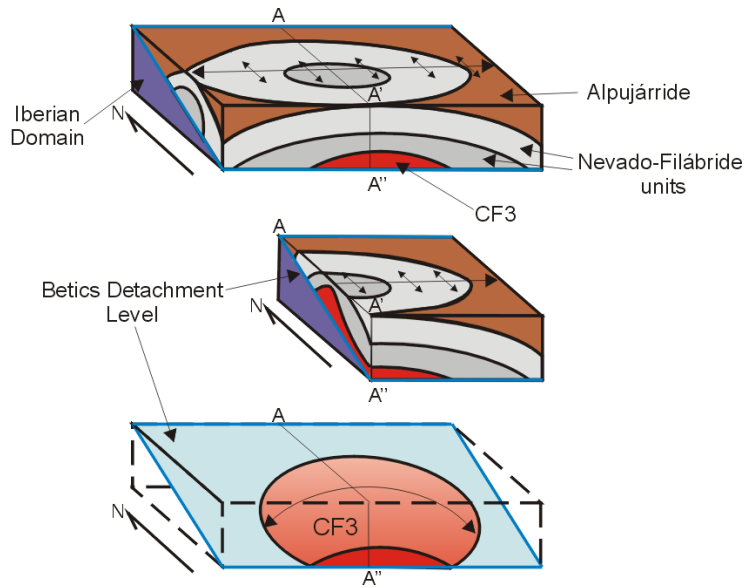
Figure 10.21: Schematic representation of the position of conductor CF3 in the Internal Zone complexes.

10.9.2 Regional geodynamic implications

From the interpretation of the 3D model, the following regional constraints can be added on the geologic and geophysical knowledge of the study area:

- The continuation of the External Zone below the Internal Zone in the Central Betics is only of a few kilometres, as shown by the elongation of the conductive bodies of the External Zone towards the south. Analogously, the conductivity contrast between the Guadalquivir Basin sediments and the External Zone show the continuation of the Guadalquivir basin up to 20 km E beneath the Prebetic zone, and up to 30 km S beneath the Subbetics.

- The emplacement of a differentiated lithologic unit in the core of the main Nevado-Filábride antiform (conductor **CF3**) reinforces the hypothesis that the Internal Betics are formed by an antiformal stack of crustal or even mantle thrust sheets, bounded by a major south-dipping sole thrust. This thrust separates the allochtonous rocks of the Alboran Domain from the authochtonous Iberian plate and belongs to the southern continuation of the sole thrust of the External Betics.

- The presence of mantle or lower crustal rocks below the Central Betics suggests that the mechanism that emplaced peridotitic bodies in some sectors of the western and southern parts of the Gibraltar Arc affected a broader area. This mechanism implied exhumation of mantle rocks at depths of about 180 km.

- The effect of this higher density body opens the door to a new gravimetric model, which would agree with the presence of a crustal root below the Internal Betics.

10.10 Conclusions

This chapter has described the construction of a 3D conductivity model of the Central Betics, from the Iberian Massif to the Alboran Sea, from the first meters to lower crustal levels, the results obtained, how the model was tested and its interpretation, considering other available geological and geophysical information.

A preliminary model was constructed from the extrapolation of 1D models inverted from determinant data at each site, towards a three-dimensional mesh. This initial model was extended towards the Alboran Sea and surrounding areas, whose conductivities were imaged using available surface data. The model mesh consisted of 50x50x25 elements with total dimensions of 270 km(NS) x 220 km(EW) x 100 km(z).

Successive steps to obtain a reliable model consisted of a trial and error process, whose objective was to reach an acceptable misfit between model and data responses.

The final model, termed bet3D-140, was obtained after 140 steps. This model is characterised by average resistivity values between 50 Ω·m and 100 Ω·m. Over this, some resistive zones appear, interpreted as the metamorphic and granitic rocks of the Iberian Massif, and the metamorphic rocks of the Internal Zone. Shallow conductive bodies are associated with the Guadalquivir Basin sediments and with the sedimentary materials of the Subbetic units. In depth, these two conductive regions continue towards the south, i.e., the Guadalquivir sediments below the External Zone, and the External Zone below the Internal Zone.

Among the resistive materials of the Internal Zone, shallow conductors are interpreted as due to fluid circulation along the contacts between the Nevado-Filábride and Alpujárride complexes or different units of the Nevado-Filábride. Below the Sierra de los Filabres, a deep conductor, **CF3**, extends in depth from 4 km to 17.5 km, with resistivities between 1Ω·m and 5Ω·m.

A sensitivity test of the model and its main features was performed, which proved the stability of its mesh, and allowed testing the extension, depth and resolution of the conductive body **CF3**. The main results were that the extension of this conductor could continue some kilometres towards the west, have an orientation from E-W to WNW-ESE and its bottom could also continue up to 30 km depth.

Based on geological and geophysical constraints, the deep conductive body is interpreted as a differentiated lithologic unit formed by ophiolites or lower crustal rocks containing a conducting mineral phase below the Nevado-Filábride complex. This body is located in the core of the main Sierra Nevada – Sierra de los Filabres antiform, and extends in depth up to the Betics detachment level.

Conclusions

Within the framework of the magnetotelluric method, this thesis has been divided into two distinct parts. The first one consisted of an investigation and improvement of the methods used in the dimensionality analysis of MT data. The second part comprised the MT crustal study of the Central part of the Betic Chain. Accordingly, the main contributions and conclusions inferred from each part are presented separately.

Methodological contributions on geoelectric dimensionality

The purpose of this part has been to investigate the main methods used in the analysis of the geoelectric dimensionality from MT, focusing on their applications in real data. These methods have been the WAL (Weaver *et al.*, 2000) rotational invariants criteria, the Bahr invariant parameters (Bahr, 1988) and the phase tensor (Caldwell *et al.*, 2004). These methods have been compared and contrasted, highlighting the strong and weak points of each, and by making some modifications to ensure equivalency. All this work has been done using synthetic examples and real data from the public COPROD2 and BC87 datasets and from the Betics dataset with simple to complex dimensionality and from low to high noise levels.

From the revision of the WAL dimensionality criteria applied to real data and considering situations in which the data do not exactly fit the ideal 1D, 2D and 3D cases:

- The estimation of WAL rotational parameters and their errors has been tested using three approaches: classical error propagation, random Gaussian noise generation and the resampling Bootstrap method. All these lead to similar results, although classical

error propagation has been chosen as the most stable way to estimate the errors of the invariants. The related strike and distortion angles and errors should be estimated using random noise generation, where a minimum value of n=100 is recommended.

- With regard to the threshold value, dimensionality results with the corresponding strike directions and/or distortion angles and errors obtained using different thresholds have been analysed and a range for which these parameters are more stable has been defined. This threshold range has been set to 0.1 to 0.15, valid for medium to high quality data.

- As a product of this study, a program has been created to perform MT dimensionality analysis using WAL criteria while considering data errors. This program (WALDIM) has been successfully applied to several datasets.

From the comparison between the WAL and the Bahr methods, and considering the revision of the latter to make both equivalent:

- The analytical relationships between the WAL and Bahr parameters have been obtained.

- The threshold values defined by Bahr, have been redefined as a function of the WAL parameters, through their analytical relationships.

- A new method has been proposed, termed Bahr-Q, which uses the Bahr parameters and the WAL invariant Q. Using the new threshold values this method is equivalent to the WAL method. Bahr and Q parameters are less affected by noise, and hence, the Bahr-Q method can be considered as more robust than the WAL.

From the study of the phase tensor:

- The phase tensor has been applied to different dimensionality cases, including errors and distortion. It has been shown that, in extreme distortion situations (shear angle close to 45°), the phase tensor is not distortion – invariant.

- When data are not affected by distortion, φ_{Max} - φ_{min} (computed from the phase tensor) and WAL parameter Q have similar values. This allows for the detection of galvanic distortion, even over 3D regional structures.

- The inversion of the phase tensor data to fit a 2D description fails in general because of the use of only half of the information from the impedance tensor.

General conclusions from the first part of the thesis are:

- In the dimensionality analysis, it is always important to consider the errors, since they affect the determination of the dimensionality by any method.

- The best dimensionality analysis is performed using all the available information from the impedance (or magnetotelluric) tensor. Assumptions on a certain type of dimensionality should only be used for hypothesis testing (sometimes these assumptions are made as dimensionality analysis, leading to erroneous interpretations).

- Care must be taken when using methods such as the phase tensor, because they provide a compact description of the dimensionality, but in view of a further modelisation, information on the presence of distortion is not available, and it cannot be corrected.

Magnetotelluric study of the central Betic crustal structure

This part of the thesis has presented a synthesis of the geological and geophysical information of the Central Betics, the reprocessing of previous MT data and the acquisition and processing of new data, from which a more complete dataset to work with has been obtained. From the dimensionality analysis of the data, the 2D and 3D modelling approaches and the model interpretations, the following results and conclusions are highlighted:

- The dimensionality analysis has revealed the high complexity of the MT data, which points to 3D modelling as the best strategy. Furthermore, the pattern of the 2D cases present over the study zone can be related to the different processes which have occurred in the Betics and Iberian Massif: The existence of a more complex pattern over the Betics is related to the superposition of these processes (Alpine orogeny over Variscan materials), whereas in the Iberian Zone, only affected by the Variscan orogeny, a simpler dimensionality is observed.

- The dimensionality and the sensitivity study of the previous NW-SE 2D conductivity model show that lateral extension of the deep conductor is not ensured.

- The three 2D models created from the Internal Betics data show the presence of a conductive body below the Sierra de los Filabres, shallower than the previous 2D model.

- From the comparison of the 2D inversion codes RLM2DI, REBOCC and DetREBOCC, the latter, which inverts the determinant data, has been shown to be very useful when data are not 2D. The use of this response for the 3D modelling should be a good tool as well.

- Finally, a 3D conductivity model of the central part of the Betics crust has been created. Departing from an initial model obtained from the 1D inversion of determinant data and constrained with the geometry of known geologic structures,

this model has been obtained through a trial and error process, through the Mackie *et al.* (1993) code and using the rms to compare different model and data responses.

- The robustness of the main features of the 3D model has been proved through several sensitivity tests. Also, this model shows a pattern that reproduces the main dimensionality features of the data.

- The final model allowed characterization of the following features:

  - In the Iberian Massif, a resistive zone associated with metamorphic and granitic rocks. And within it, a conductive zone (2 km – 17 km depth), interpreted as being interconnected graphite, as observed NNW of the study area in other zones of the same geologic unit. The elongation of the resistive zone below the External Zone confirms the continuation of the Iberian basement below the Betics.

  - A shallow conductor, related to fluid circulation through the sediments of the Guadalquivir Basin. The shape of this conductor shows that the basin infill continue below the External Zone.

  - Moderately low resistivity values in the External Zone, associated with fluid circulation in the carbonate rocks, both in the Prebetic and the Subbetic zones. In the Inner Subbetic, even lower resistivity values are associated with a major content in shales and basaltic rocks, and in the eastern part of this zone, with the presence of flysch rocks.

  - In the Internal Zone, a highly resistive zone (up to 13.5 km) interpreted as being caused by metamorphic rocks from the Nevado-Filábride and Alpujárride complexes, as well as some shallow conductors interpreted as fluid circulation along the contacts between both zones or within the Nevado-Filábride.

  - A large conductive zone, located below the Sierra de los Filabres, from 4 km to 17.5 km. According to the sensitivity tests performed, this body could have an orientation from WNW – ESE to EW, and may reach a maximum depth of 30 km.

- Based on geological and geophysical constrains, the deep conductive body is interpreted as a differentiated lithologic unit formed by ophiolites or lower crustal rocks containing a conducting mineral phase, below the Nevado-Filábride complex. This body is located in the core of the main Sierra Nevada - Sierra de los Filabres antiform, and extends in depth up to the Betics detachment level.

Future perspectives

This thesis, which has solved some of the aspects of the determination of geoelectric dimensionality in MT and has obtained a description of the geoelectric structures of the Central Betics crust, still leaves some open doors to further investigation in these same directions. Next, the future perspectives proposed as a continuation of this thesis are presented:

Regarding the geoelectric dimensionality of the MT data:

- Continue investigating the dimensionality methods based on rotational invariants. Improve the WALDIM program by applying fuzzy logic, instead of a fixed threshold, to discern between dimensionality cases; and allowing for regional averages (along with the present period band averages). Allow for certain hypothesis assumptions, whose validity will be quantified by a misfit value. Finally, include the tipper information to skip the 90° ambiguity of the strike direction.
- Investigate the use of the rotational invariants of the MT tensor in the presence of anisotropy. Decipher if there is a way to identify and characterise this property in the geoelectric structures.
- Optimise the use of the rotational invariants to compare data and model responses.
- Continue investigation of the relationships between the phase tensor angles φ_{Max} - φ_{min} and WAL parameter Q. Establishment of thresholds for the phase tensor parameters to quantify the type of dimensionality.

In relation to the geoelectric structure of the Betics, the main result has been the obtainment of a 3D model of the Central Betics crustal structure and within it, the identification of a conductive body below the Internal Zone located at upper-middle crustal depths. Future MT research in the Betics should focus on improving the knowledge of this body and on the broadening of the study area:

-   Perform a 3D inversion of the Betics MT data using the code of Siripurnvaraporn *et al.* (2005). To this end, the data set up and different tests using the code are presently being performed. Try to improve the fits between the data and model responses, and compare with the present model.
-   Record new data, registering longer periods, to obtain better resolution at depth; and to cover a broader area. Get complementary data to correct the static shift and constrain the conductivity of the first layers.

Due to the increasing interest of this zone, within the PICASSO Research Initiative (Program to Investigate the Cause of the Alboran-AtlaS System convective Overturn) and the research project to be developed under this initiative, the contributions of this thesis (MT dataset, dimensionality characterization and 3D geoelectric model of the Central Betics) provide an update and a departing point to the new MT studies to be made in this complex and wide zone. The main objective of PICASSO is to determine the three-dimensional inner structure of the crust and the lithosphere, with special emphasis on the geometry of the upper mantle in order to image the lithospheric processes that are taking place. Different geophysical data will be collected for an integrated interpretation. As an example, a recent MT survey (February 2006), made as a collaboration between Granada and Barcelona universities, in the north of Morocco, proceeds in this direction. Also, new MT sites at longer periods covering a wider area of the Betics will be collected soon by DIAS and also with the collaboration of UG and UB.

Gràcies…

Finalment puc omplir aquestes darreres pàgines per poder donar les gràcies a totes aquelles persones que heu compartit amb mi aquests anys i heu contribuït a que finalment aquesta tesi s'hagi convertit en una realitat.

Abans que res, agrair sincerament als meus directors, la Pilar Queralt i l'Eduard Roca, per haver-me donat l'oportunitat de realitzar-la, pel temps dedicat, per guiar-me i aconsellar-me, i per tot el que m'heu ensenyat tant de la MT i de la geofísica, com de la geologia.

Gràcies al Juanjo i l'Àlex, pels seus consells, les seves crítiques, i també els seus ànims, que m'han permès aprendre i continuar endavant sabent quina direcció agafar.

Al Jesús Galindo-Zaldívar, del Departamento de Geodinámica de la Universidad de Granada, per col·laborar i participar en la campanya i en totes les idees que ha aportat, i a tota la resta de l'equip que vau aguantar els dies de sol i suor, perquè l'Anna pogués disposar de més dades: la Pilar, la Claudia, la Patricia, el Vicente, el Fernando, el Carlos, l'Antonio i l'Ana. A la Montse Liesa, per aclarir els dubtes petrològics i poder desencallar la interpretació.

A tots aquells amb qui he compartit la oportunitat de formar-me i exercir en la docència: als companys de l'Escola Santa Eulàlia de Cornellà; al Dani, la Trini, l'Eloi i el Pere del grup de física de l'Escola d'Agricultura de la UPC, i als companys de l'Escola Industrial. I als de la UB, amb tantes classes compartides i/o substituïdes amb l'Emma, el Jaume, el Ghia, la Pilar, l'Àlex (també per mentoritzar-me!), la Mireia, el Juanjo, la Berta, la Bea i l'Anna. A tots, per tot el que hem après ensenyant plegats.

A l'Alan G. Jones, per acollir-me a Ottawa i donar-me la oportunitat de treballar amb ell al Geological Survey de Canadà, i endinsar-me una mica més en el món de la MT; també al Jim

Craven, per fer-me sempre un lloc al GSC i convidar-me a participar en els seus projectes, i a la resta de companys del GSC.

Un record molt especial per l'Anna G., amb qui vam començar juntes en el món de la recerca i la geofísica, en els cursos de doctorat, les nostres primeres classes, els projectes de docència, els congressos, per aconsellar-me en tot allò que passa tant dins com fora de la feina, per ser una gran amiga. També a la Bea, entre moltes altres coses, per la teva gran ajuda en les classes, i a la resta de companys del grup de treball, la Claudia, l'Ester, la Mireia, l'Oriol i el Miquel, per les estones bones i no tant bones passades, entre dades, mapes, programes, articles, ajustos i disgustos, formats i deadlines... i també fora d'ell.

A l'Òscar, per ajudar-me en entendre més d'un terme geològic, i per compartir els "fatal errors" del Fortran; i a les noves companyes de despatx, l'Anna C. i la Sara, que també heu viscut el final d'aquesta tesi. Al Gerard i la Wiebke, companys en el món de la MT, per haver-me solucionat algun que altre problema amb el programa dels botonets vermells. I com no, a tots els becaris i becàries del departament de Geodinàmica i Geofísica, pels esmorzars i dinars, que han fet que per una estona ens oblidéssim del que passava a dalt. A l'Héctor, i/o a la comissió de festes i xerinoles, per les escapadetes a la muntanya i pels grans aconteixements gastronòmics. I a la resta de gent del departament, on sempre hi he trobat algú disposat a donar-me un cop de mà.

Als meus pares, per donar-me sempre ànims, i no deixar de sentir-vos orgullosa de mi. Gràcies per deixar-me viure a "Cal Vicencià", per alguna que altra carmanyola furtiva i per les múltiples reparacions. A l'Elena i el David, per estar al meu costat i per comptar amb mi, per les estones passades, i per les rialles. A la iaia Paquita, pels nostres sopars dels dijous, que per molts anys!!!, pels teus consells i històries, i per la teva inesgotable energia, que fa que mai deixi d'admirar-te.

A tots els meus amics i amigues, especialment a la Neus, a l'Anna i l'Emili. A la Marta i el Josep, per les aventures al "pisillu" i per haver viscut de prop els meus nervis i també les alegries, i a tota la colla que ens vam conèixer dalt de l'escenari i que de tant en tant ens trobem al voltant d'una bona taula o fent una llarga passejada per la platja. A l'orquestra de Capellades i als companys del quartet: el Jordi, la Mireia i l'Estefania; als qui més d'un cop he enyorat tot escoltant música mentre intentava fer compilar algun programa.

I a tu, Grant, per estimar-me, escoltar-me i animar-me des de qualsevol costat de l'oceà. Per la teva ajuda en els moments més durs de la tesi, i per fer-me mirar sempre "the whole picture". Gràcies, "language man", per treure tots els "the" de més i canviar tants "make" per "do", i per fer que aquestes línies no necessitin traducció. Per a que puguem escriure el nostre futur plegats.

<div style="text-align: right">

Masquefa-Vilanova-Ottawa, una llarga

tardor i un molt fred hivern, 2005-06

</div>

References

Ábalos, B., Carreras, J., Druguet, E., Escuder Viruete, J., Gómez Pugnaire, M.T., Lorenzo Alvárez, S., Quesada, C., Rodríguez Fernández, L.R. and Gil-Ibarguchi, J.I. (coordinator), 2002. Variscan and Pre-Variscan Tectonics. *In:* Gibbons, W. and Moreno, T. (eds) The Geology of Spain, *Geological Society (London)*, 155-183.

Arango, C., 2005. Estudio Magnetotelúrico de la zona de Lluchmajor (Mallorca): Avances en el proceso de datos y modelo 3D, PhD Thesis, *Departament de Geodinàmica i Geofísica, Universitat de Barcelona.*

Ardizone, J., Mezcua, J. and Socias, I. 1989. Mapa aeromagnético de la España Peninsular, *Instituto Geográfico Nacional*, Madrid.

Azañón J.M., and Crespo-Blanc, A., 2000. Exhumation during a continental collision inferred from the tectonometamorphic evolution of the Alpujarride Complex in the central Betics (Alboran Domain, SE Spain), *Tectonics*, **19**, 549-565.

Azañón, J. M., Galindo-Zaldívar, J., García-Dueñas, V. and Jabaloy, A., 2002. Alpine Tectonics II: Betic Cordillera and Balearic Islands. *In*: Gibbons, W. and Moreno, T. (eds) The Geology of Spain, *Geological Society (London)*, 401-416.

Babu, J.K. and Singh, K., 1983. Inference on means using the bootstrap, *Annals of Statistics*, **11**, 999-1003.

Bahr, K., 1988. Interpretation of the magnetotelluric impedance tensor: regional induction and local telluric distortion, *J. Geophys.*, **62**, 119-127.

Bahr, K., 1991. Geological noise in magnetotelluric data: a classification of distortion types, *Phys. Earth planet. Inter.,* **66**, 24-38.

Balanyá, J.C. and García-Dueñas, V., 1987. Les directions structurales dans le Domaine d'Alborin de part et d'autre du Detroit de Gibraltar. *Comptes Rendus de l'Academie des Sciences de Paris*, **304**, 929-932.

Banda, E. and Ansorge, J., 1980. Crustal structure under the central and eastern part of the Betic Cordillera, *Geophys. J.R. Astron. Soc.,* **63**, 515-532.

Banda, E., Udias, A., Mueller, St., Mezcua, J., Boloix, M., Gallart, J., and Aparicio, A., 1983. Crustal structure beneath Spain from deep seismic sounding experiments. *Physics of the Earth and Planetary Interiors,* **31**, 277-280.

Banda, E., Gallart, J., García-Dueñas, V., Dañobeitia, J.J. and Makris, J., 1993. Lateral variation of the crust in the Iberian Peninsula, New evidence from the Betic Cordillera, *Tectonophysics*, **221**, 53-66.

Banks, C.J. and Warburton, J., 1991. Mid crustal detachment in the Betic system of southeast Spain, *Tectonophysics*, **191**, 275-289.

Barranco, L., Ansorge, J. and Banda, E., 1990. Seismic refraction constraints on the geometry of the Ronda peridotitic massif (Betic Cordilera, Spain), *Tectonophysics*, **184**, 379-392.

Bendat, J.S. and Piersol, A.G., 1971. Measurement and Analysis of Random Data, *John Wiley and Sons*, New York.

Berdichevsky, M.N. and Dmitriev, V.I., 1976. Basic principles of interpretation of magnetotelluric curves, in *Geoelectric and Geothermal Studies*, pp. 165-221, ed. Á. Ádam, *KAPG Geophysical Monograph*, Akademiai Kaido, Budapest.

Bohoyo F., Galindo-Zaldivar J. and Serrano I., 2000. Main features of the basic rock bodies of the Archidona Region derived from geophysical data (External Zones, Betic Cordillera), *Comptes Rendus de l'Academie des Sciences. Series IIA: Earth and Planetary Science*, **330** (10), 667-674.

Bostick, F.X., 1977. A Simple Almost Exact Method of MT Analysis, *Workshop on Electrical Methods in Geothermal Exploration*, Snowbird, Utah: U.S. Geological Survey Contract 14-08-001-6-359.

Braga J.C., and Martín, J.M., 1987. Sedimentación cíclica lagunar y bioconstrucciones asociadas en el Trías superior alpujarride, *Cuadernos Geología Ibérica*, **11**, 459-473.

Brigham, E.O., 1974. The Fast Fourier Transform, *Prentice-Hall, Inc*.

Brown, C. 1994. Tectonic interpretation of regional conductivity anomalies. Surveys in *Geophysics*, **15**, 123 - 157.

Cagniard, L., 1953. Basic theory of the magnetotelluric method of geophysical prospecting, *Geophysics*, **18**, 605-635.

Caldwell, T.G., Bibby, H.M. and Brown, C., 2004. The Magnetotelluric Phase Tensor, *Geophys. J. Int.,* **158**, 457-469.

Calvert, A., Sandvol, E., Seber, D., Barazangi, M., Roecker, S., Mourabit, T., Vidal, F., Alguacil, G., and Jabour, N., 2000. Geodynamic Evolution of the Lithosphere and Upper Mantle Beneath the Alboran Region of the Western Mediterranean: Constraints from Travel Time Tomography, *Journ. Geophys. Res.*, **105**, 10871-10898.

Campbell, W.H., 2003. Introduction to Geomagnetic Fields. *Cambridge University Press*.

Cantwell, T., 1960. Detection and analysis of low frequency magnetotelluric signals. Ph.D. Thesis, *Dept. of Geology and Geophysics, M.I.T. Cambridge, MA*.

Carbonell, R., Sallarés, V., Pous, J., Dañobeitia, J.J., Queralt, P., Ledo, J.J. and García-Dueñas, V., 1998. A multidisciplinary study in the Betic Chain. *Tectonophysics*, **288**, 137-152.

Casas, A. and Carbó, A., 1990. Deep structure of the Betic Cordillera derived from the interpretation of a complete Bouguer anomaly map, *Journal of Geodynamics*, **12**, 137-147.

Chave, A.D. and Smith, J.T., 1994. On electric and magnetic galvanic distortion tensor decompositions, *J. Geophys. Res.*, **99**, B3, 4669-4682.

Chave A.D. and Thomson D.J., 2004. Bounded influence magnetotelluric response function estimation. *Geophysical Journal International*, **157**, 988-1006.

Constable, S.C., Orange, A.S., Hoversten, G.M. and Constable, C.G., 1987. Occam's inversion: A practical algorithm for generating smoth models from EM sounding data, *Geophysics*, **63**, 816-825.

Cook, F.A. and Jones, A.G., 1995. Seismic reflections and electrical conductivity: A case of Holmes's curious dog?, *Geology*, **23** (2), 141-144.

Dañobeitia, J.J., Sallarès, V. and Gallart, J., 1998. Local earthquakes seismic tomography in the Betic Cordillera (southern Spain), *Earth and Planetary Science Letters*, **160**, 225-239.

Davis, G.H. and Reynolds, S.J., 1996. Structural Geology of Rocks and Regions, 2nd ed., *Wiley and Sons*, NY.

Dewey, J.F., Pitman III, W.C., Ryan, W.B.F. and Bonnin, J., 1973. Plate Tectonics and the evolution of the Alpine system. *Geol. Soc. Amer. Bull.,* **84**, 3137-3180.

Dewey, J.F., Helman, M.L., Turco, E., Hutton, D.H.W. and Knott, S.D., 1989. Kinematics of the western Mediterranean. In: Coward M.P., Dietrich, D. and Park, R.G. (eds), Alpine Tectonics, *Geol. Soc. Spec. Publ.*, **45**, 265-283.

Doglioni, C., Fernàndez, M., Gueguen, E. and Sabat, F., 1999. On the interference between the early Apennines-Maghrebides backarc extension and the Alps-Betics orogen in the Neogene Geodynamics of the Western Mediterranean, *Boll. Soc. Geol. It.*, **118**, 75-89.

Dupis, A., 1997. 1961-1994: A third of a century of magnetotellurics, *The leading Edge*, **16**, 497-502.

Efron, B., 1979. Bootstrap methods: Another look at the jackknife. *Annals of Statistics,* **7**, 1-26.

Efron, B. and Tibshirani, R. J., 1998: An introduction to the bootstrap. *Monographs on statistics and applied probability*, **57**, Boca Raton, CRC, 436 pp.

Egbert, G.D. and Booker, J.R., 1986. Robust estimation of geomagnetic transfer functions. *Geophys. J. R. Astron. Soc.,* **87**, 173-194.

Favre, P. and Stampfli, G., 1992. From rifting to passive margin: the example of the Red Sea, Central Atlantic and Alpine Tethys, *Tectonophysics*, **215**, 67-97.

Fernàndez, M., Berástegui, X., Puig,C. García-Castellanos, D., Jurado, M.J., Torné, M. and Banks, C., 1998a. Geophysical and geological constraints on the evolution of the Guadalquivir foreland basin, Spain. In: Mascle, A., Puigdefabregas, C., Fernàndez, M. (eds), *Cenozoic foreland Basins of western Europe, Geol. Soc. Spec. Publ*, **134**, 29-48.

Fernàndez, M., Marzán, I., Correia, A. and Ramalho, E., 1998b. Heat flow, heat production, and lithospheric thermal regime in the Iberian Peninsula. Tectonophysics, **291**, 29-54.

Fischer, G. and Masero, W., 1994. Rotational properties of the magnetotelluric impedance tensor, the example of the Araguainha impact crater, Brazil, *Geophys. J. Int*., **119**, 548-560.

Friedrichs, B., 2003. Mapros, Magnetotelluric Processing Software (Metronix) User Manual.

Frizon de Lamotte, D., A. Crespo-Blanc, B. Saint-Bezar, M. Fernàndez, H. Zeyen, and Ayarza, P., 2004. TRANSMED-TRANSECT I [Betics, Alboran Sea, Rif, Moroccan Meseta, High Atlas, Jbel Saghro, Tindouf basin], edited by R. W. Cavazza, F., Spakman, W., Stampfli, G. and Ziegler, P.A., *Springer-Verlag*.

Galindo-Zaldívar, J., Jabaloy, A., González-Lodeiro, F. and Aldaya, F., 1997. Crustal structure of the central sector of the Betic Cordillera (SE Spain), Tectonics, **16** (1), 18-37.

Galindo-Zaldívar, J., González-Lodeiro, F. and Vera, J.A., 2004. Datos de Geología de Subsuelo y relaciones con otros dominios geológicos españoles. In: Geología de España, J.A. Vera, editor, *SGE-IGME*, Madrid, 350-352.

Gamble, T.D., Goubau, W.M. and Clarke, J., 1979. Magnetotellurics with a remote magnetic reference, *Geophysics*, **44**, 53-68.

Garcia, X., Chave, A.D. and Jones, A.G., 1997. Robust processing of magnetotelluric data from the auroral zone, *J. Geomagn. Geoelectr.*, **49**, 1451-1468.

García, X. and Jones, A.G., 1999. Extended decomposition of MT data, in The second international symposium on Three-dimensional Electromagnetics (3DEM-2), Salt Lake City (USA), 27-29 October.

García-Hernández, M., López-Garrido, A.C., Rivas, P., Sanz de Galdeano, C. and Vera, J., 1980. Mesozoic paleogeographic evolution in the External Zones of the Betic Cordillera (Spain), *Geol. Mijnb*, **59**, 155-168.

García-Dueñas, V., Martínez-Martínez, J.M., Soto, J.I., 1988. Los Nevado-Filabrides, una pila de pliegue-mantos separados por zona de cizalla, *II Cong. geol. España*, 17-26.

García-Dueñas, V., Balanyá, J.C. and Martínez-Martínez, J., 1992. Miocene extensional detachment in the outcropping basement of the Northern Alboran basin (Betics) and their tectonic implications, *Geo-Mar. Lett.,* **12**, 88-95.

García-Dueñas, V., Banda, E., Torné, M., Córdoba, D. and ESCi-Béticas Working Group, 1994. A deep seismic reflection survey across the Betic Chain (southern Spain): first results, *Tectonophysics*, **232**, 77-89.

Groom, R.W. and Bailey, R.C.,1989. Decomposition of the magnetotelluric impedance tensor in the presence of local three-dimensional galvanic distortion, *J. Geophys. Res.,* **94**, 1913-1925.

Gutsher, M.A., Malod, J., Rehault, J.P., Contrucci, I., Klingelhoefer, F., Mendes-Victor, L. and Spakman, W., 2002. Evidence for active subduction beneath Gibraltar, *Geology*, **30**, vol. 12, 1071-1074.

Hjelt, S.E. and Korja, 1993. Lithospheric and upper-mantel structures, results of electromagnetic sounding in Europe, *Physics of the Eaarth and Planetary Interiors*, **79**, 137-177.

Huber. P.J., 1981. Robust Statistics, *Wiley*, New York.

IGN, 1976. Mapa de anomalías de Bouguer. Escala 1:500000. Madrid.

IGN, 2001. Catalogo Sísmico Nacional.

Jabaloy, A., Fernández-Fernández, E.M., González-Lodeiro, F. and Sanz de Galdeano, C. 2005. The structure of the Eastern Betic Cordillera (SE Spain), *Joint Earth Science Meeting*, France.

Jiracek, G., 1990. Near-surface and topographic distortions in electromagnetic induction. *Surv. Geophys.*, **11**, 163-203.

Jolivet, L. and Faccenna, C., 2000. Mediterranean extension and the Africa-Eurasia collision, *Tectonics*, **19** (6), 1095-1106.

Jones, A.G. and Jödicke, H., 1984. Magnetotelluric transfer function estimation improvement by a coherence-based rejection technique, 54th Annual International Meeting, *Society of Exploration Geophysicists*, Atlanta, Dec. 2-6, 1984.

Jones, A.G., 1988. Static Shift of Magnetotelluric Data and its Removal in a Sedimentary Basin Environment, *Geophysics*, **53**, 967-978.

Jones, A.G., Chave, A.D., Egbert. G., Auld, D. and Bahr, K., 1989. A comparison of Techniques for Magnetotelluric Response Function Estimation. *Journal of Geophysical Research*, **94**, 14210-14213.

Jones, A.G., 1992. Electrical Conductivity of the Continental Lower Crust. *In:* Continental Lower Crust, edited by D.M. Fountain, R.J. Arculus and R.W. Kay, *Elsevier*, 81-143.

Jones, A.G., 1993. The COPROD2 dataset: Tectonic setting, recorded MT data and comparison of models, *J. Geomag. Geoelectr.*, **45**, 933-955.

Jones, A.G. and Groom, R.W., 1993. Strike angle determination from the magnetotelluric impedance tensor in the presence of noise and local distortion: rotate at your peril!. *Geophys. J. Int.,* **113,** 524-534.

Jones, A.G., Groom, R.W. and Kurtz, R.D., 1993. Decomposition and Modelling of the BC87 dataset, *J. Geomag. Geoelectr.*, **45**, 1127-1150.

Jones, A.G., J. Ledo and I.J. Ferguson, 2005. Electromagnetic images of the Trans-Hudson orogen: The North American Central Plains (NACP) anomaly revealed, *Canadian Journal of Earth Sciences*, **42**, 457-478.

Jones, F.W., Munro, R.A., Craven, J.A., Boerner, D.E., Kurtz, R.D. and Sydora, R.D., 2002. Regional geoelectrical complexity of the Western Canada Basin from magnetotelluric tensor invariants, *Earth Planets Space*, **54**, 899-905.

Junge, A, 1996: Characterization of and Correction for Cultural Noise, *Surveys in Geophysics*, **17**, 361-391.

Kaufman, A.A. and Keller, G.V., 1981. The Magnetotelluric Sounding Method, *Methods in Geochemistry and Geophysics*, **15**. Amsterdam.

Kaufman, A. A., 1988. Reduction of the geological noise in magnetotelluric soundings, *Geodex*, **25**, 145-161.

Keller, G.V. and Frischkenecht, F.C., 1966. Electrical Methods in Geophysical Prospeting, *International Series in Electromagnetic Waves*, vol. **10**, Pergamon Press.

Keller, G.V., 1987. Rock and Mineral Properties. *In:* Electromagnetic Methods in Applied Geophysics – Vol 1. Theory. *Soc. Expl. Geophys.,* Tulsa, OK.

Kiss, J., Szarka, L. and Prácser, E., 2005. Second-order magnetic phase transition in the Earth *Geophysical Research Letters*, **32**, L24310, doi:10.1029/2005GL024199.

Larsen, J., 1977. Removal of local surface conductivity effects from low frequency mantle response curves, *Geodinamica Acta*, **12**, 183-186.

Ledo, J., 2005. 2-D versus 3-D magnetotelluric data interpretation, *Surveys in Geophysics*, **26**, 671-806.

Ledo, J.J., Queralt, P. and Pous, J., 1998. Effects of galvanic distortion on magnetotelluric data over a three dimensional structure, *Geophys. J. Int.*, **132**, 295-301.

Ledo, J., Gabàs, A. and Marcuello, A., 2002a. Static shift levelling using geomagnetic transfer functions. *Earth Planets Space*, **54**, 493-398.

Ledo, J., Queralt, P., Martí, A. and Jones, A.G., 2002b. Two-dimensional interpretation of three-dimensional magnetotelluric data: an example of limitations and resolution, *Geophys. J. Int.*, **150**,127-139.

Ledo, J., Jones, A.G., Ferguson, I.J. and Jones, A.G., 2004. Lithospheric structure of the Yukon, northern Canada Cordillera, obtained from magnetotelluric data, *Journal of Geophysical Research*, **119**, B04410, DOI 10.1029/2003JB002516.

Lezaeta, P., 2002. Confidence limit of the magnetotelluric phase sensitivity skew, *Earth Planets Space*, **54**, 451-457.

Lilley, F.E.M., 1976. Diagrams for magnetotelluric data, *Geophysics*, **41**, 766-770.

Lilley, F.E.M., 1993: Magnetotelluric analysis using Mohr circles, *Geophysics*, **58,** 1498-1506.

Lilley, F.E.M., 1998a: Magnetotelluric tensor decomposition: 1. Theory for a basic procedure, *Geophysics*, **63,** 1884-1897.

Lilley, F.E.M., 1998b: Magnetotelluric tensor decomposition: 2. Examples of a basic procedure, *Geophysics*, **63,** 1898-1907.

Lonergan, L. and White, N., 1997. Origin of the Betic-Rif mountain belt, *Tectonics*, **16**, 504-522.

López Ruiz, J. (coord), Cebrià, J.M., Doblas, M. and Benito, R. 2004: La región volcánica de Almería-Murcia. En: Geología de España (J.A. Vera, Ed.), *SGE-IGME*, Madrid, 678-682.

Lupton, R. H., 1993. Statistics in Theory and Practice, *Princeton University Press*.

Mackie, R.L. and Madden, T.R., 1993. Three-Dimensional Magnetotelluric Inversion using Conjugate Gradients, *Geophys. J. Int.,* **115**, 215-229.

Mackie, R.L., Madden, T.R., and Wannamaker, P. E., 1993. Three-dimensional magnetotelluric modeling using difference equations – Theory and comparisons to integral equations solutions, *Geophysics*, **58**, 215-226.

Mackie, R., Rieven, S. and Rodi, W., 1997. Users Manual and Software Documentation for Two-Dimensional Inversion of Magnetotelluric Data, *GSY-USA Inc. San Francisco* (USA).

Malan, D.J., 1963. Physics of lightning. *English Universities Press. London.*

Mareschal, M., Fyfe, W.S., Percival, J. and Chan**,** T., 1992. Grain-boundary graphite in Kapuskasing gneisses and implications for lower-crustal conductivity, *Nature*, **357**, 674-676.

Marquis, G., Jones, A.G. and Hyndman, R.D, 1995. Coincident conductive and reflective lower crust across a thermal boundary in southern British Columbia, Canada, *Geophys. J. Int.*, **120**, 111-131.

Martí, A., Queralt, P. and Roca, E., 2004. Geoelectric dimensionality in complex geologic areas: application to the Spanish Betic Chain. *Geophys. J. Int.*, **157**, 961-974.

Martí, A., Queralt, P., Jones, A.G. and Ledo, J., 2005. Improving Bahr's invariant parameters using the WAL approach, *Geophys. J. Int.,* **163**, 38-41.

Mazzoli, S. and Helman, M., 1994. Neogene patterns of relative plate motion for Africa-Europe: some implications from recent Mediterranean tectonics, *Geol. Rund.*, **83**, 464-468.

McNeice, G and Jones, A.G., 2001. Multisite, multifrequency tensor decomposition of magnetotelluric data, *Geophysics*, **66**, 158-173.

McPherron, R.L., 2005. Magnetic pulsations: their sources and relation to solar wind and electromagnetic activity, *Surveys in Geophysics*, **26** (5), 546-592.

Medialdea, T., Suriñach, E., Vegas, R., Banda, E. and Ansorge, J., 1986. Crustal structure under the western end of the betic Cordillera (Spain), Ann. Geophys., **4** (B4), 457-464.

Meju, M.A., 2005. Simple relative space−time scaling of electrical and electromagnetic depth sounding arrays: implications for electrical static shift removal and joint DC-TEM data inversion with the most-squares criterion, *Geophysical Prospecting*, **53**, 463-479.

Monié, P., Galindo-Zaldívar, J., González Lodeiro, F., Goffe, B. and Jabaloy, A., 1991. 40Ar/39Ar geochronology of Alpine tectonism in the Betic Cordilleras (southern Spain), *Journal of the Geological Society*, London, **148**, 289-297.

Morales, J., Serrano, I., Jabaloy, A., Galindo-Zaldívar, J., Zhao, D., Torcal, F., Vidal, F., and González-Lodeiro, F., 1999. Active continental subduction beneath the Betic Cordillera and the Alborán Sea, *Geology*, **27**, 735-738.

Muñoz, G., 2005. Estudi Magnetotel·lúric tridimensional de les estructures varisques del SW de la Península Ibèrica, PhD Thesis, *Departament de Geodinàmica i Geofísica, Universitat de Barcelona*.

Navarro-Vilá, F. and García-Dueñas, V., 1980. Geological map, Sheet La Peza 1010, *Instituto Geológico y Minero de España*, Madrid, scale 1:50000.

Newman, G.A, and Alumbaugh, D.L., 2000. Three-Dimensional Magnetotelluric Inversion using Non-Linear Conjugate Gradients, *Geophys. J. Int.*, **140**, 410-424.

Nover, G., 2005. Electrical Properties of Crustal and Mantle Rocks – A Review of Laboratory Measurements and their Explanation, *Surveys in Geophysics*, **26** (5), 593-651.

Ogawa, Y., 2002. On two-dimensional modeling of magnetotelluric field data. *Surveys in Geophysics*, **23**, 99-273.

Padilha, A.L., 1999. Behaviour of magnetotelluric source fields within the ecuatorial zone, *Earth Planets Space*, **51**, 1119-1125.

Palacky, G.J., 1987. Resistivity Characteristics of Geologic Targets. *In:* Electromagnetic Methods in Applied Geophysics – Vol 1. Theory. *Soc. Expl. Geophys.,* Tulsa, OK.

Park, S.K. and Mackie, R.L., 2000. Resistive (dry?) lower crust in an active orogen, Nanga Parbat, northern Pakistan, *Tectonophysics*, **316**, 359-380.

Pedersen, L.B. and Engels, M., 2005. Routine 2D inversion of magnetotelluric data using the determinant of the impedance tensor, *Geophysics*, **70**, G33-G41.

Pek, J. and Verner, T., 1997. Finite-difference modelling of magnetotelluric fields in two-dimensional anisotropic media, *Geophys. J. Int.,* **128**, 505-521.

Pérez-Estaún, A. and Bea, F. (Eds.), 2004. Macizo Ibérico, en: Geología de España (J.A. Vera, Ed.), *SGE-IGME*, Madrid, 19-230.

Pirjola, R., 1992. On magnetotelluric source effects caused by an auroral electrojet system, *Radio Sci.*, **27**, 463-468.

Platt, J.P. and Vissers, R.L.M., 1989. Extensional collapse of thickered continental lithosphere: A working hypothesis for the Alboran Sea and Gibraltar arc, *Geology*, **17**, 540-543.

Platt, J.P., Allerton, S., Kirker, A., Mandeville, C., Mayfield, A., Platzman, E.S. and Rimi, A., 2003. The ultimate arc: differential displacement, oroclinal bending and vertical axis rotation in the External Betic-Rif arc, *Tectonics*, **22** (3), DOI 10.10292001TC001321.

Polyak, B.G., Fernàndez, M., Khutorskoy, M.D., Soto, J.I., Basov, I.A., Comas, M.C., Ye. Khain, V., Alonso, B., Agapova, G.V., Mazurova, I.S., Negredo, A., Tochitsky, V.O., de la Linde, J., Bogdanov N.A. and Banda, E., 1996. Heat flow in the Alboran Sea (the western Mediterranean), *Tectonophysics*, **263**, 191-218.

Pous, J., Queralt, P., Ledo, J.J. and Roca, E., 1999. A high electrical conductive zone at lower crustal depth beneath the Betic Chain (Spain), *Earth and Planetary Science Letters*, **167**, 35-45.

Press, W.H., Flannery, B.P., Teukolsky, S.A., Vetterling, W.T., 1992. Numerical Recipes in Fortran: The Art of Scientific Computing, *Cambridge University Press*.

Radhakrishnamurty, C. and Likhite, S.D., 1970. Hopkinson effect, blocking temperature and Curie point in basalts, *Earth and Planetary Science Letters*, **7***, 389-396.*

Rehault, J.P., Boillot, G. and Mauffret, A., 1984. The western Mediterranean Basin, geological evolution, *Mar. Geol.,* **55**, 447-477.

Romo, J.M., Gomez-Treviño, E. and Esparza, F.J., 1999. An invariant representation of the magnetic transfer function in magnetotellurics, *Geophysics*, **64**, 1418-1428.

Rosenbaum, G., Lister, G.S., and Duboz, C., 2002. Relative motions of Africa, Iberia and Europe during Alpine orogeny, *Tectonophysics*, **359**, 117-129.

Royden, L.H., 1993. Evolution of retreating subduction boundaries formed during continental collision, *Tectonics*, **12**, 629-638.

SAMTEX (Southern African Magnetotelluric Experiment) Workshop on MT data Processing. Dublin Institute of Advanced Physics. March 2004.

Sanz de Galdeano, C. and Vera, J.A., 1992. Stratigraphic record and palaeogeographical context of the Neogene basins in the Betic Cordillera, Spain, *Basin Research*, **4**, 21-36.

Sasaki, Y., 2001. Full 3-D Inversion of Electromagnetic Data on PC, *J. Appl. Geophys.,* **46**, 45-54.

Schettino, A. and Scotese, C. 2002. Global kinematic constraints to the tectonic history of the Mediterranean region and surrounding areas during the Jurassic and Cretaceous. *In:* Rosenbaum, G. and Lister, G. S., Reconstruction of the evolution of the Alpine-Himalayan orogeny, *Journal of the Virtual Explorer*.

Schwalenberg, K., Rath, V. and Haak, V., 2002. Sensitivity studies applied to a two-dimensional resistivity model from the Central Andes, *Geophys. J. Int.,* **150**, 673-686.

Seber, D., Barazangi, M., Ibenbrahim, A. and Demnati, A., 1996. Geophysical evidence for lithospheric delamination beneath the Alboran Sea and Rif-Betics mountains, *Nature*, **379**, 785-790.

Serrano, I., Bohoyo-Muñoz, F., Galindo-Zaldivar, J., Morales-Soto, J., Zhao, D. P., 2002. Geophysical signatures of a basic-body rock placed in the upper crust of the external zones of the Betic Cordillera (Southern Spain), *Geophysical Research Letters*, **29** (11).

Serrano, I., Morales, J., Zhao, D., Torcal, F. and Vidal, F., 1998. P-wave tomographic images in the Central Betics-Alborán sea (South Spain) using local earthquakes: contribution for a continental collision, *Geophysical Research Letters*, **25** (21), 4031-4034.

Simpson, F. and Bahr, K., 2005. Practical Magnetotellurics, *Cambridge Univesity Press*.

Sims, W.E., Bostick, F.X.Jr. and Smith, H.W., 1971. The estimation of magnetotelluric impedance tensor from measured data, *Geophysics*, **36**, 938-942.

Siripunvaraporn, W. and Egbert, G., 2000. An efficient data-subspace inversion method for 2-D magnetotelluric data, *Geophysics*, **65**, 3, 791-803.

Siripunvaraporn, W., Egbert, G., Lenbury, Y. and Uyeshima, M., 2005. Three-dimensional magnetotelluric inversion: data-space method, *Physics of the Earth and Planetary Interiors*, **150**, 3-14.

Smith, J.T. and Booker, J., 1991. Rapid inversion of two- and three-dimensional magnetotelluric data, *J. Geophys. Res*., **96**, 3905-3922.

Smith, J.T., 1995. Understanding telluric distortion matrices, *Geophys. J. Int*., **122**, 219-226.

Suriñach, E. and Udías, A., 1978. Determinación de la raíz de Sierra Nevado-Filabres a partir de sondeos sísmicos profundos y medidas gravimétricas. *In:* Geodinámica de la Cordillera Bética y Mar de Alborán, *Univ. de Granada*, 25-34.

Swift, C.M., 1967. Magnetotelluric investigation of an electrical conductivity anomaly in the southwestern United States, *PhD thesis*, Department of Geology and Geophysics, MIT, Cambridge, MA (reprinted in *Magnetotelluric Methods*, pp. 156-166, ed. Vozoff, K., Geophys. Reprint Ser. No. 5. 1988, SEG, Tulsa, OK).

Szarka, L. and Menvielle, M., 1997. Analysis of rotational invariants of the magnetotelluric impedance tensor, *Geophys. J. Int.,* **129**,133-142.

Szarka, L., 1999. A correction to Bahr's "phase deviation" method for tensor decomposition. *Earth Planets Space*. **51**, 1019-1022.

Thompson, A.B., 1992. Metamorphism and Fluids. *In*: Understanding the Earth, eds. Brown, G.C., Hawkesworth, C.J. and Wilson, R.C.L., *Cambridge University Press*.

Thomson, D.J. and Chave, A.D., 1991. Jackknifed error estimates for spectra, coherences, and transfer functions. *In: Advances in spectrum analysis and array processing* (Shykin, S., ed.), pp 58-113, Englewood Cliffs, NJ: Prentice Hall.

Tikhonov, A.N., 1950. Determination of the electrical characteristics of the deep strata of the Earth's crust, *Dokl. Akad. Nauk.* SSSR, **73**, 295-297.

Torné, M. and Banda, E., 1992. Crustal thinning from the Betic Cordillera to the Alboran Sea, *Geo-Marine Letters*, **12**, 76-81.

Torné, M., Fernàndez, M., Comas, M.C. and Soto, J.I., 2000. Lithospheric structure beneath the Alboran Basin: Results from 3D gravity modeling and tectonic relevance, *Journal of Geophysical Research*, **105**, 3209-3228.

Tournerie, B., Chateau, M. and Marceotte, D., 2004. Estimation and removal of the MT static shift effect using geostatistical methods, *17th International Workshop on Electromagnetic Induction in the Earth.* Hyderabad (India).

Trad, D.O. and Travassos, J.M., 2000. Wavelet filtering of magnetotelluric data, *Geophysics*, **65**, 482-491.

Utada, H. and Munekane, H., 2000. On galvanic distortion of regional three-dimensional magnetotellurics impedances, *Geophys. J. Int.*, **140**, 385-398.

Vera, J.A. (Ed.), 2004. Cordillera Bética y Baleares, en: Geología de España (J.A. Vera, Ed.), *SGE-IGME*, Madrid, 19-230. 347-464.

Vozoff, K., 1972. The magnetotelluric method in the exploration of sedimentary basins, *Geophysics*, **37**, 98-141.

Vozoff, K. 1991. The magnetotelluric method. *In:* Electromagnetic Methods in Applied Geophysics – Vol 2. Applications. *Soc. Expl. Geophys.,* Tulsa, OK.

Wannamaker, P.E., Hohmann, G.W. and Ward, S.H., 1984. Magnetotelluric responses of three-dimensional bodies in layered earths, *Geophysics*, **49**, 1517-1533.

Wannamaker, P. E., Stodt, J.A. and Rijo, L., 1987. A stable finite element solution for two-dimensional magnetotelluric modelling, *Geophys. J. R. Astr. Soc.,* **88**, 277-796.

Wannamaker, P.E., 1999. Affordable magnetotellurics: Interpretations in natural environments, in Three-Dimensional Electromagnetics, eds Oristaglio, M. and Spies, B., *Society of Exploration Geophysicists*, Tulsa.

Weaver, J.T., Agarwal, A.K. and Lilley, F.E.M., 2000. Characterisation of the magnetotelluric tensor in terms of its invariants, *Geophys. J. Int.,* **141**, 321-336.

Weaver, J.T., Agarwal, A.K. and Lilley, F.E.M., 2003. The relationship between the magnetotelluric tensor invariants and the phase tensor of Caldwell, Bibby and Brown, *3DEMIII Workshop*, Adelaide.

Wight, D.E. and Bostick, F.X., 1980. Cascade decimation – A technique for real time estimation of power spectra, Proc. IEEE Intern. Conf. Acoustic, Speech, Signal Processing, Denver, Colorado, April 9-11, 626-629.

Zappone, A., Fernàndez, M., García-Dueñas, V. and Burlini, L., 2000. Laboratory measurements of seismic P-wave velocities on rocks from the Betic chain (southern Iberian Peninsula), *Tectonophysics*, **317**, 259-272.

Zhang, P., Roberts, R.G. and Pedersen, L.B., 1987. Magnetotelluric Strike Rules, *Geophysics*, **52**, 267-278.

Zhang,Y. and Paulson, K.V., 1997. Enhancement of signal-to-noise ratio in natural source transient magnetotelluric data with wavelet transform. *Pure and Applied Geophysics*, **149**, 405-419.

Zhdanov, M.S., Fang, S. and Hursan, G., 2000. Electromagnetic Inversion using Quasi-Linear Approximation, *Geophysics*, **65**, 1501-1513.

Zonge, K.L. and Hughes, L.J., 1991. Controlled Source audio-frequency magnetotellurics. *In:* Electromagnetic Methods in Applied Geophysics-Vol 2. Applications. *Soc. Expl. Geophys.,* Tulsa, OK.

Appendix A: Expressions of the Errors of WAL Invariants and Strike Angles using Classical Error Propagation

To obtain the analytical expression of the errors (δI_k) of each invariant (I_k), classical error propagation was applied to equations (2.10 to 2.18), regarding the errors of the tensor components M_{ij} as statistically independent. The expressions are shown in terms of ξ_i and η_i (see eq. 2.8) and their errors:

$$\zeta_1 = \xi_1 + \eta_1 i = \frac{M_{xx} + M_{yy}}{2}, \tag{A.1a}$$

$$\zeta_2 = \xi_2 + \eta_2 i = \frac{M_{xy} + M_{yx}}{2}, \tag{A.1b}$$

$$\zeta_3 = \xi_3 + \eta_3 i = \frac{M_{xx} - M_{yy}}{2}, \tag{A.1c}$$

$$\zeta_4 = \xi_4 + \eta_4 i = \frac{M_{xy} - M_{yx}}{2}. \tag{A.1d}$$

Since $\delta(\operatorname{Re} M_{ij}) = \delta(\operatorname{Im} M_{ij}) = \delta(M_{ij}) = (\operatorname{var}(M_{ij}))^{1/2}$ (eq. 3.1):

$$\delta\xi_1 = \delta\xi_3 = \delta\eta_1 = \delta\eta_3 = \frac{1}{2}\sqrt{\left(\delta M_{xx}\right)^2 + \left(\delta M_{yy}\right)^2} \ , \tag{A.2a}$$

$$\delta\xi_2 = \delta\xi_4 = \delta\eta_2 = \delta\eta_4 = \frac{1}{2}\sqrt{\left(\delta M_{xx}\right)^2 + \left(\delta M_{yy}\right)^2} \ . \tag{A.2b}$$

Errors of invariants I_1- I_7 and Q:

$$\delta I_k = \sum_{i=1}^{4}\left(\left(\frac{\partial I_k}{\partial\xi_i}\right)^2\left(\delta\xi_i\right)^2 + \left(\frac{\partial I_k}{\partial\eta_i}\right)^2\left(\delta\eta_i\right)^2\right)^{1/2} \ , \tag{A.3}$$

then,

$$\delta I_1 = \frac{1}{I_1}\sqrt{\xi_1^2\delta\xi_1^2 + \xi_4^2\delta\xi_4^2} \ , \tag{A.3}$$

$$\delta I_2 = \frac{1}{I_2}\sqrt{\eta_1^2\delta\eta_1^2 + \eta_4^2\delta\eta_4^2} \ , \tag{A.4}$$

$$\delta I_3 = \frac{1}{I_1^2 I_3}\sqrt{\xi_2^2\delta\xi_2^2 + \xi_3^2\delta\xi_3^2} + \frac{I_3}{I_1^2}\sqrt{\xi_1^2\delta\xi_1^2 + \xi_4^2\delta\xi_4^2} \ , \tag{A.5}$$

$$\delta I_4 = \frac{1}{I_2^2 I_4}\sqrt{\eta_2^2\delta\eta_2^2 + \eta_3^2\delta\eta_3^2} + \frac{I_4}{I_2^2}\sqrt{\eta_1^2\delta\eta_1^2 + \eta_4^2\delta\eta_4^2} \ , \tag{A.6}$$

$$\delta I_5 = \delta s_{41} = \frac{1}{I_1 I_2}\sqrt{\left(\eta_4 - I_5\xi_1\frac{I_2}{I_1}\right)^2\delta\xi_1^2 + \left(\eta_1 - I_5\xi_4\frac{I_2}{I_1}\right)^2\delta\xi_4^2 + \left(\xi_4 - I_5\eta_1\frac{I_1}{I_2}\right)^2\delta\eta_1^2 + \left(\xi_1 - I_5\eta_4\frac{I_1}{I_2}\right)^2\delta\eta_4^2} \ , \tag{A.7}$$

$$\delta d_{ij} = \frac{1}{I_1 I_2}\sqrt{\left(\eta_j - d_{ij}\xi_i\frac{I_2}{I_1}\right)^2\delta\xi_i^2 + \left(-\eta_i - d_{ij}\xi_j\frac{I_2}{I_1}\right)^2\delta\xi_j^2 + \left(-\xi_j - d_{ij}\eta_i\frac{I_1}{I_2}\right)^2\delta\eta_i^2 + \left(\xi_i - d_{ij}\eta_j\frac{I_1}{I_2}\right)^2\delta\eta_j^2} \ , \tag{A.8}$$

$$\delta I_6 = \delta d_{41} = \frac{1}{I_1 I_2}\sqrt{\left(\eta_1 - I_6\xi_4\frac{I_2}{I_1}\right)^2\delta\xi_4^2 + \left(-\eta_4 - I_6\xi_1\frac{I_2}{I_1}\right)^2\delta\xi_1^2 + \left(-\xi_1 - I_6\eta_4\frac{I_1}{I_2}\right)^2\delta\eta_4^2 + \left(\xi_4 - I_{41}\eta_1\frac{I_1}{I_2}\right)^2\delta\eta_1^2} \ , \tag{A.9}$$

$$\delta Q = \sqrt{\sum_{k=1}^{4}\left[\left(\sum_{\substack{ij=12,\\13,24,34}}\frac{\partial Q}{\partial d_{ij}}\frac{\partial d_{ij}}{\partial \xi_k}\right)^2\delta\xi_k^2 + \left(\sum_{\substack{ij=12,\\13,24,34}}\frac{\partial Q}{\partial d_{ij}}\frac{\partial d_{ij}}{\partial \eta_k}\right)^2\delta\eta_k^2\right]}, \qquad (A.10)$$

and

$$\delta I_7 = \sqrt{\sum_{k=1}^{4}\left[\left(\frac{\partial I_7}{\partial Q}\sum_{\substack{ij=12,\\13,24,34}}\frac{\partial Q}{\partial d_{ij}}\frac{\partial d_{ij}}{\partial \xi_k}+\frac{\partial I_7}{\partial d_{41}}\frac{\partial d_{41}}{\partial \xi_k}+\frac{\partial I_7}{\partial d_{23}}\frac{\partial d_{23}}{\partial \xi_k}\right)^2\delta\xi_k^2 + \left(\frac{\partial I_7}{\partial Q}\sum_{\substack{ij=12,\\13,24,34}}\frac{\partial Q}{\partial d_{ij}}\frac{\partial d_{ij}}{\partial \eta_k}+\frac{\partial I_7}{\partial d_{41}}\frac{\partial d_{41}}{\partial \eta_k}+\frac{\partial I_7}{\partial d_{23}}\frac{\partial d_{23}}{\partial \eta_k}\right)^2\delta\eta_k^2\right]},$$

$$(A.11)$$

with:

$$\frac{\partial Q}{\partial d_{12}} = \frac{1}{Q}\left(d_{12}-d_{34}\right) \text{ and } \frac{\partial Q}{\partial d_{34}} = -\frac{1}{Q}\left(d_{12}-d_{34}\right), \qquad (A.12)$$

$$\frac{\partial Q}{\partial d_{13}} = \frac{\partial Q}{\partial d_{24}} = \frac{1}{Q}\left(d_{13}+d_{24}\right), \qquad (A.13)$$

$$\frac{\partial d_{ij}}{\partial \xi_k} = \frac{1}{I_1 I_2}\begin{Bmatrix} \eta_j, k=i \\ \\ -\eta_i, k=j \\ \\ 0 \quad, k\neq i\neq j \end{Bmatrix} - d_{ij}\frac{1}{I_1}\begin{Bmatrix} \xi_k/I_1 ,k=1,4 \\ \\ 0 \quad, k=2,3 \end{Bmatrix}, \qquad (A.14)$$

$$\frac{\partial d_{ij}}{\partial \eta_k} = \frac{1}{I_1 I_2}\begin{Bmatrix} -\xi_j, k=i \\ \\ \xi_i, k=j \\ \\ 0 \quad, k\neq i\neq j \end{Bmatrix} - d_{ij}\frac{1}{I_2}\begin{Bmatrix} \eta_k/I_2 ,k=1,4 \\ \\ 0 \quad, k=2,3 \end{Bmatrix}, \qquad (A.15)$$

$$\frac{\partial I_7}{\partial Q} = -\frac{1}{Q^2}\left(d_{41}-d_{23}\right), \qquad (A.16)$$

$$\frac{\partial I_7}{\partial d_{41}} = \frac{1}{Q} \text{ and } \frac{\partial I_7}{\partial d_{23}} = \frac{-1}{Q}. \qquad (A.17)$$

Strike angles, θ_1 and θ_2, θ_D and θ_3 and their errors, using classical error propagation as well:

$$\theta_1 = \frac{1}{2}\arctan\left(\frac{-\xi_3}{\xi_2}\right) \tag{A.18}$$

$$\delta\theta_1 = \frac{1}{2}\frac{1}{1+\left(-\xi_3/\xi_2\right)^2}\sqrt{\left(\frac{\xi_3}{\xi_2^2}\right)^2\delta\xi_2^2+\left(\frac{-1}{\xi_2}\right)^2\delta\xi_3^2}\,, \tag{A.19}$$

$$\theta_2 = \frac{1}{2}\arctan\left(\frac{-\eta_3}{\eta_2}\right), \tag{A.20}$$

$$\delta\theta_2 = \frac{1}{2}\frac{1}{1+\left(-\eta_3/\eta_2\right)^2}\sqrt{\left(\frac{\eta_3}{\eta_2^2}\right)^2\delta\eta_2^2+\left(\frac{-1}{\eta_2}\right)^2\delta\eta_3^2}\,, \tag{A.21}$$

$$\theta_D = \frac{1}{2}\arctan\left(\frac{\xi_2}{\xi_3}\right), \quad \text{(or using imaginary components } \eta_2 \text{ and } \eta_3) \tag{A.22}$$

$$\delta\theta_D = \frac{1}{2}\frac{1}{1+\left(\xi_3/\xi_2\right)^2}\sqrt{\left(\frac{1}{\xi_3}\right)^2\delta\xi_2^2+\left(\frac{-\xi_2}{\xi_3^2}\right)^2\delta\xi_3^2}\,, \tag{A.23}$$

$$\theta_3 = \frac{1}{2}\arctan\left(\frac{d_{12}-d_{34}}{d_{13}+d_{24}}\right), \tag{A.24}$$

$$\delta\theta_3 = \frac{1}{2}\frac{1}{1+\left(\dfrac{d_{12}-d_{34}}{d_{13}+d_{24}}\right)^2}\sqrt{\left(\frac{1}{d_{13}+d_{24}}\right)^2\cdot\left(\delta d_{12}^2+\delta d_{34}^2\right)+\left(\frac{-(d_{12}-d_{34})}{\left(d_{13}+d_{24}\right)^2}\right)^2\cdot\left(\delta d_{13}^2+\delta d_{24}^2\right)}\,, \tag{A.25}$$

where errors of d_{ij} are those of equation A.8.

The errors of distortion parameters ϕ_1 and ϕ_2 are not shown, given their complex dependence on all the magnetotelluric components and the strike angle (e.g. $\phi_1 = f(M_{xx}, M_{xy}, M_{yx}, M_{yy}, \theta_3)$), and the fact that these errors are better resolved using random gaussian noise generation.

Appendix B: The COPROD2 Dataset: Geological Setting and Responses from Site 85_314

The COPROD2 is an MT dataset collected along a 400 km EW profile in southern Saskatchewan and Manitoba (Canada), at 49^oN, and from 106^oW to 100^oW, crossing the thick Paleozoic sediments of the Willingston basin. Within the basement beneath the sediments lies one of the world's longest and most enigmatic crustal conductivity features: the North American Central Plains (NACP) conductivity anomaly. At the eastern extreme of the profile there is a second basement anomaly (TOBE) interpreted as being associated with the Thompson Nickel Belt at the Superior-Churchill boundary (Figure B.1).

Data have a wide bandwidth (2.6ms to 1820s) and are of high quality (impedance errors typically <2%) (Jones, 1993). These data were made available to the MT community and are commonly used to test and compare 2D inversion codes, as in general these have a 2D behaviour. Presently, these data can be downloaded from the MTNET web page (http://www.mtnet.info).

Site 85_314, which has been used through this thesis to test different methodologies, is located in the central part of the COPROD2 profile. Figures B.2 and B.3 display the MT tensor components, apparent resistivities and phases, with the corresponding error bars, computed at this site.
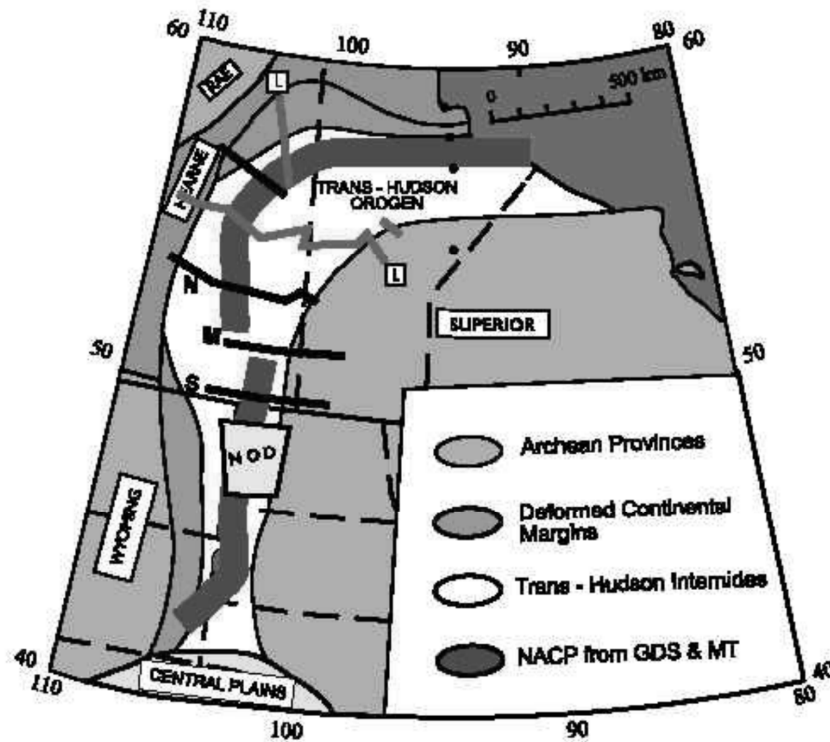
Figure B.1: The North American Central Plains (NACP) anomaly within the Trans-Hudson orogen. Also shown, the locations of the MT surveys. S: Coprod2 profile. (From Jones *et al.*, 2005).
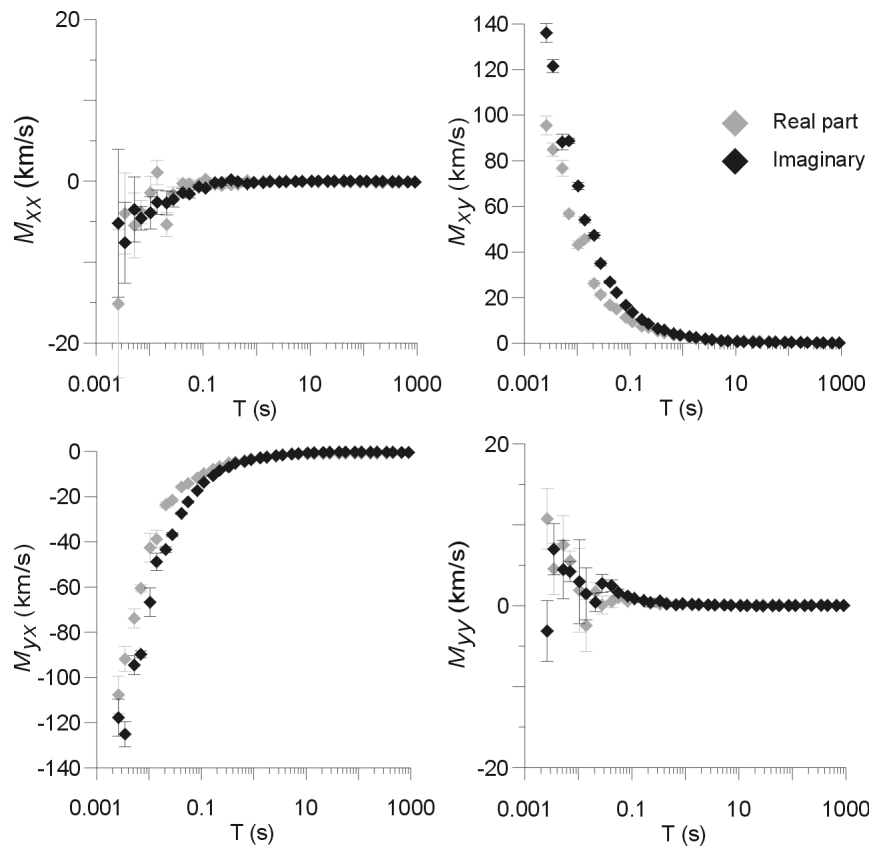
Figure B.2: Magnetotelluric tensor components of site 85_314 from the COPROD2 dataset.

Apparent resistivities and phases

Figure B.3:
Apparent
resistivity and
phase computed
from MT tensor
components of the
COPROD2 site
85_314
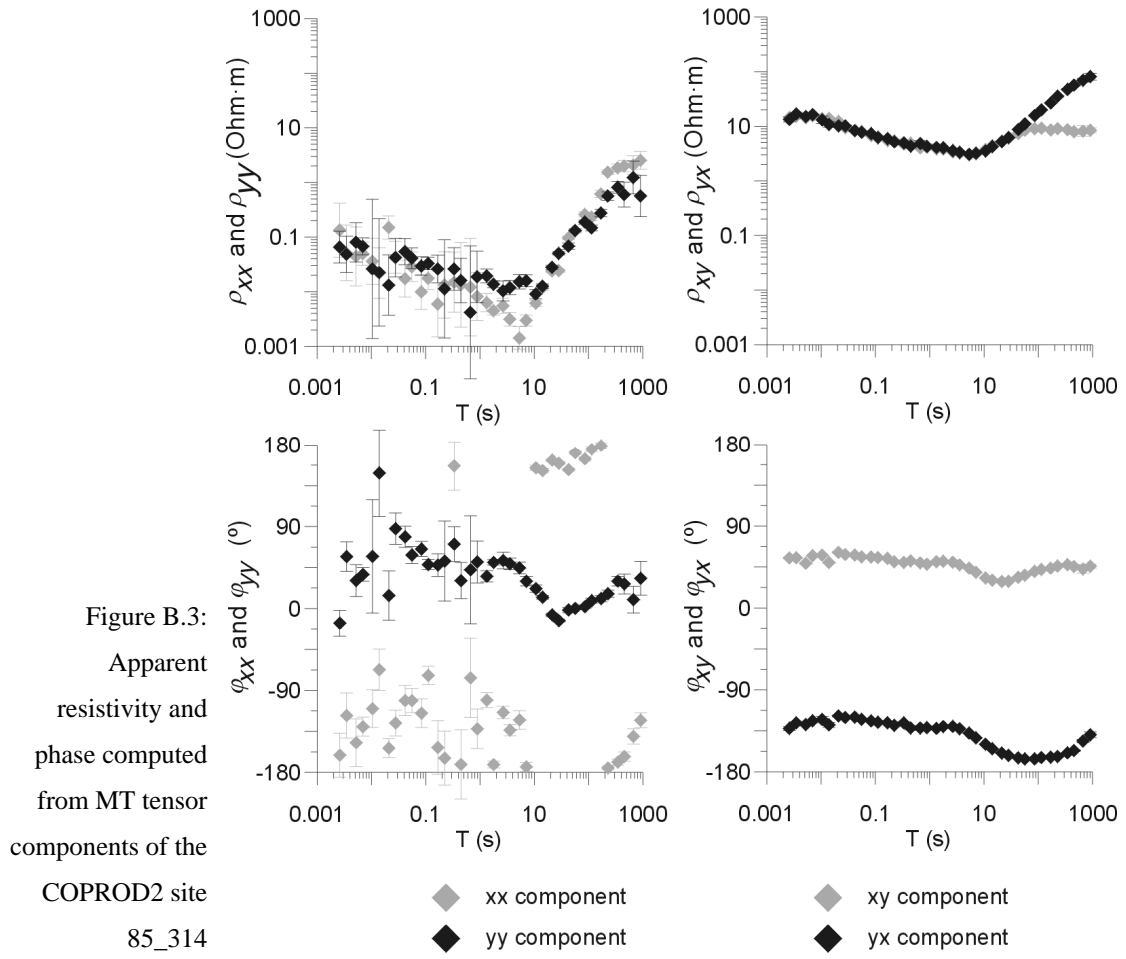
Appendix C: The BC87 dataset: Geological Setting and Main Features of the MT Responses

The BC87 dataset was acquired in southeastern British Columbia as part of the LITHOPROBE project. This dataset is commonly used too to test and compare new methods in analysis and interpretation of MT data (Jones *et al.*, 1993), and especially to show the limitations of 2D interpretation of MT data (Chave and Jones, 1997). It consists of 27 sites along an approximate E-W profile (Figure C.1).
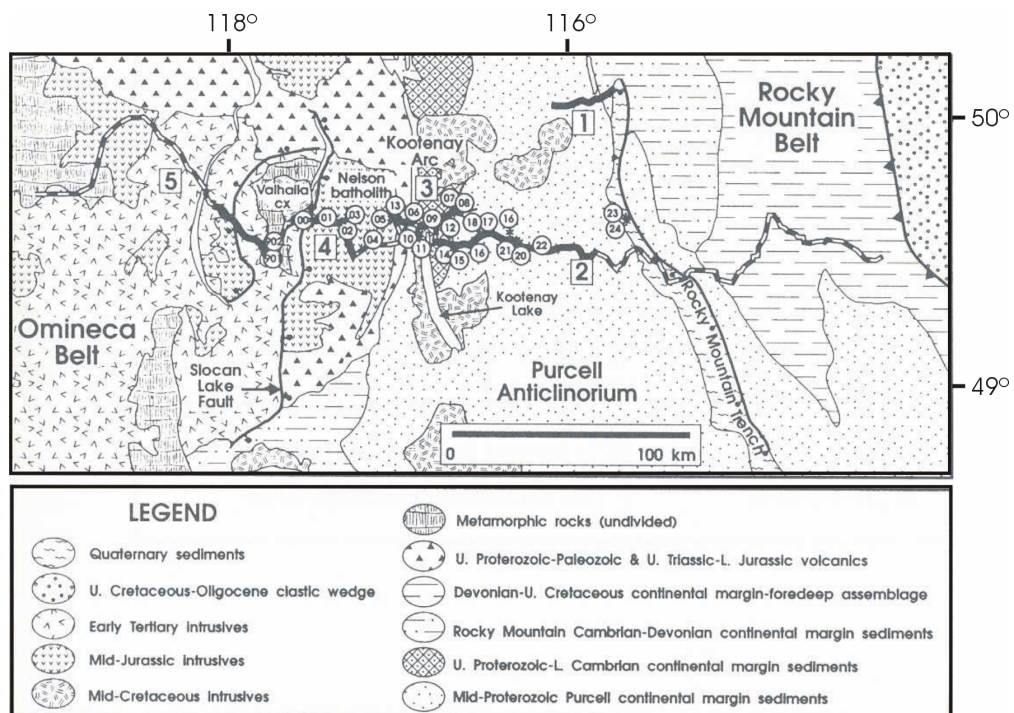
Figure C.1: BC87 geological setting and location of MT sites. Site 4 is located above Nelson Batholith.

Data display complex 3D effects, due both to local effects and the presence of the Nelson Batholith body (western part of profile). Site 4 is located above this body. The responses at this site (magnetotelluric tensor components and apparent resistivities and phases) are shown in Figures C.1 and C.2. Presently, these data are available from the MTNET web page.
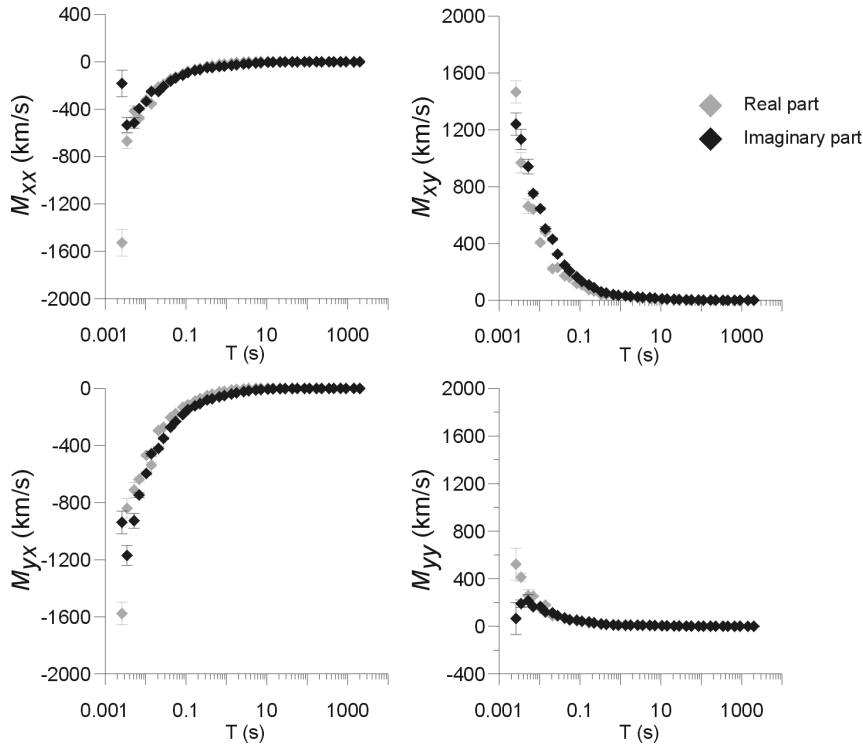
Figure C.2: Magnetotelluric tensor components of site 4 from the BC87 dataset.
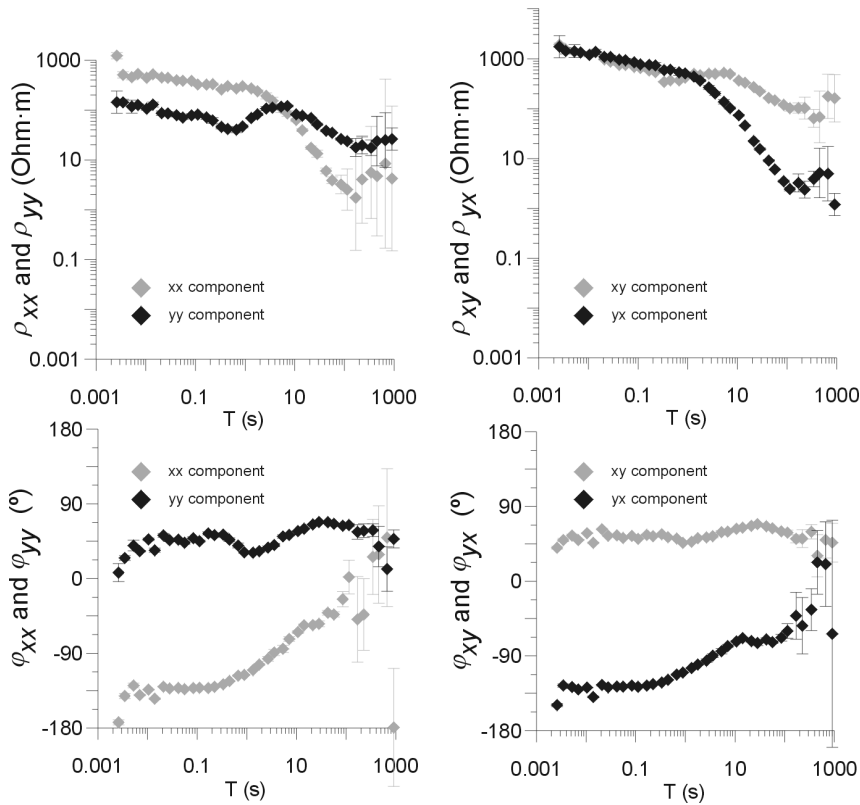
Figure C.3: Apparet resistivity and phases computed from MT tensor components of site 4 from the BC87 dataset.

Appendix D: Betics Dataset Locations and Responses

Site id	Zone	Geographical coordinates		Alt. (m)	Tipper?	# or estimated periods and range	Data quality	% of periods used in modelling
		Latitude	Longitude					
b01	Guadix-Baza Basin - Sª de Baza	+37:26:31	-2:52:07	1240	yes	40 4ms-4000s	GOOD	83
b02	Guadix-Baza Basin - Sª de Baza	+37:28:35	-2:54:13	1050		39 4ms-4000s	POOR	82
b03	Subbetic - Guadix-Baza Basin	+37:37:37	-3:02:14	620	yes	38 4ms-2000s	GOOD	92
b04	Subbetic - Guadix-Baza Basin	+37:37:43	-3:07:57	840				
b05	Subbetic - Guadalquivir Basin	+37:50:09	-3:09:49	520	yes	40 4ms-4000s	GOOD	90
b06	Subbetic - Guadalquivir Basin	+37:52:38	-3:12:16	420		34 4ms-500s	MEDIUM	94
b07	Iberian Massif	+38:08:37	-3:23:20	420	yes	40 4ms-4000s	MEDIUM	75
b08	Iberian Massif - Guadalquivir Basin	+38:05:58	-3:21:25	500		34 4ms-500s	MEDIUM	44
b09	Iberian Massif	+38:13:34	-3:14:03	650		39 4ms-4000s	VERY POOR	0
b11	Iberian Massif	+38:16:15	-3:21:56	550	yes	34 4ms-500s	GOOD	91
b13	Iberian Massif	+38:26:25	-3:43:39	850		34 4ms-500s	GOOD	85

b14	Iberian Massif	+38:30:16	-3:57:06	650		32 4ms-500s	MEDIUM	81
b15	Sª de la Contraviesa (Alpujárride)	+36:54:37	-3:07:24	1160		41 4ms-4000s	GOOD	85
b16	Sª Nevada	+37:03:32	-3:03:10	2160	yes			
b17	Sª de los Filabres	+37:14:04	-2:43:46	1920	yes	34 4ms-500s	VERY GOOD	97
b18	Sª de Baza (nevado	+37:20:44	-2:51:40	1740	yes	40 4ms-4000s	GOOD	100
b19	Sª de las Estancias (Alpujárride)	+37:30:54	-2:20:17	1360	yes	40 4ms-4000s	GOOD	98
b20	Sª de María (Prebetic)	+37:38:51	-2:20:25	1340	yes	32 4ms-300s	MEDIUM	81
b21	Guadix-Baza Basin	+37:45:39	-2:18:27	1100	yes	32 4ms-200s	GOOD	88
b22	Sª de la Sagra	+37:55:56	-2:31:19	1450				
b23	Guadix-Baza Basin	+37:42:59	-2:36:10	860	yes	40 4ms-4000s	GOOD	95
b24	Sª de Segura (Prebetic)	+38:00:34	-2:42:01	1660	yes	40 4ms-4000s	GOOD	98
b26	Sª de Cazorla (Prebetic)	+38:07:05	-2:55:53	1340	yes	40 4ms-4000s	VERY GOOD	93
b27	Guadix-Baza Basin	+37:31:05	-3:23:45	1200	yes	40 4ms-4000s	GOOD	93
b28	Sª Mágina (Subbetic)	+37:44:52	-3:25:52	1640				
b29	Sª de los Filabres	+37:16:31	-2:18:35	1080	yes	32 4ms-300s	MEDIUM	72
b30	Sª de los Filabres	+37:08:56	-2:15:06	700	yes	40 4ms-4000s	VERY GOOD	95
b31	Sª de Alhamilla (Nevado-Filábride)	+36:59:50	-2:14:41	920	yes	29 4ms-300s	GOOD	97
b32	Tabernas Basin - Sª de los Filabres	+37:04:02	-2:25:24	420	yes	32 4ms-300s	MEDIUM	81
b33	Sª de Gádor (Alpujárride)	+37:03:36	-2:15:11	1050		40 4ms-4000s	MEDIUM	80
b34	Sª de los Filabres	+37:04:54	-2:47:53	2000				
b35	Sª de los Filabres	+37:05:42	-2:44:10	1080	yes	35 4ms-500s	GOOD	80
b36	Guadix-Baza - Almanzora Basin (North of Sª de los Filabres)	+37:18:45	-2:35:43	1320		41 4ms-4000s	MEDIUM	88
b37	Sª de las Estancias (Alpujárride)	+37:27:12	-2:25:42	1220	yes	40 4ms-4000s	MEDIUM	93
b38	Sª Arana (Alpujárride)	+37:21:15	-3:25:45	1050	yes	40 4ms-4000s	POOR	73
b39	Sª Nevada	+37:13:10	-3:13:30	1150	yes	41 4ms-4000s	MEDIUM	95
b40	Sª Mágina (Subbetic)	+37:53:36	-3:28:48	440	yes	41 4ms-4000s	MEDIUM	95

b41	Sª Mágina (Subbetic)	+37:36:17	-3:26:12	1100		32 4ms-4000s	GOOD	66
b51	Guadix-Baza Basin	+37:22:30	-2:42:47	1150	yes	51 1ms-4000s	GOOD	82
b52	Sª de Baza (Alpujárride)	+37:17:04	-2:46:48	1950		48 1ms-1000s	MEDIUM	92
b53	Guadix-Baza Basin	+37:28:15	-2:34:51	1100	yes	51 1ms-4000s	GOOD	76
b54	Sª de Baza (Alpujárride)	+37:17:41	-2:55:38	1700	yes	49 1ms-4000s	MEDIUM	90
b55	Sª Nevada	+37:03:27	-3:03:17	2230	yes	39 1ms-100s	MEDIUM	77
b56	Sª de Gádor (Alpujárride)	+36:55:16	-2:54:01	1680	yes	50 1ms-2000s	MEDIUM	88
b57	Sª de los Filabres	+37:12:42	-2:36:39	2000	yes (LF1 and LF2)	50 1ms-2000s	MEDIUM	100
b58	Sª de los Filabres	+37:11:19	-2:22:15	900	yes	49 1ms-2000s	MEDIUM	90
b59	Tabernas Basin - Sª de los Filabres	+37:11:38	-2:08:53	650	yes	50 1ms-2000s	GOOD	90
b60	Almanzora Basin (East of Sª de los Filabres)	+37:25:24	-2:05:48	610	yes	48 1ms-1000s	MEDIUM	81

Table D.1: Betics MT dataset site information: Site identification, geographic and geologic location, geographical coordinates, altitude and whether tipper was recorded or not. Evaluated responses: # of periods estimated and period range used in the dimensionality analysis; data quality (see forthcoming text) and % of periods used in modelling. Grey: sites rejected due to the impossibility of doing adequate data processing (not enough long time series, highly contaminated segments or extremely low coherence values).

Sites	Band names and sampling frequencies (or periods)					
b01-b41		band1 (1kHz)		band2 (32Hz)	band3 (1s)	band4 (32s)
b51-b60	HF (40960 Hz)	LF1 (4096 Hz)	Free (512 Hz)	LF2 (64 Hz)	LF3 (2 Hz)	LF4 (T=16s, from LF3 resampling)

Table D.2: Band names and sampling frequencies of periods employed in data acquisition using Metronix MS-03 (sites b01 to b41) and Metronix MS-06 (sites b51 to b60) systems. Bands from both systems are aligned according to their sampling frequencies proximity.

A quality parameter of the data was evaluated based on the average coherence values and relative errors at each site:

$$Q_D = \frac{\overline{coh} + \left(1 - \overline{\varepsilon_M}\right)}{2}, \qquad (D.1)$$

where $\overline{coh}$ is the average of bivariate coherences of one site,

$$\overline{coh} = \frac{\sum_{i=1}^{nfreq}\left(coh(E_x)_i + coh(E_y)_i\right)}{2 \cdot nfreq}, \tag{D.2}$$

and $\overline{\varepsilon}$ is the average of the relative errors of all MT tensor components of one site:

$$\overline{\varepsilon} = \frac{\sum_{i=1}^{nfreq}\left(\varepsilon_{rel}(M_{xx}) + \varepsilon_{rel}(M_{xy}) + \varepsilon_{rel}(M_{yx}) + \varepsilon_{rel}(M_{yy})\right)}{4 \cdot nfreq}. \tag{D.3}$$

The quality is then classified according to the criterion displayed in Table D.3, which was established from a comparison between Q_D values and a visual inspection of Betics dataset data.

$Q_D > 0.9$	VERY GOOD
$0.8 < Q_D < 0.9$	GOOD
$0.6 < Q_D < 0.8$	MEDIUM
$0.5 < Q_D < 0.6$	POOR
$Q_D < 0.5$	VERY POOR

Table D.3: Quality data criterion according to Q_D, which considers coherence values and data errors.

The following figures present all the magnetotelluric responses, resistivities, phases and tipper components, with their error bars, and induction arrows corresponding to the tipper real part, obtained at all sites. These are raw curves, referenced to NS-EW orientation axes. With the exception of the induction arrows, all estimated periods are displayed.
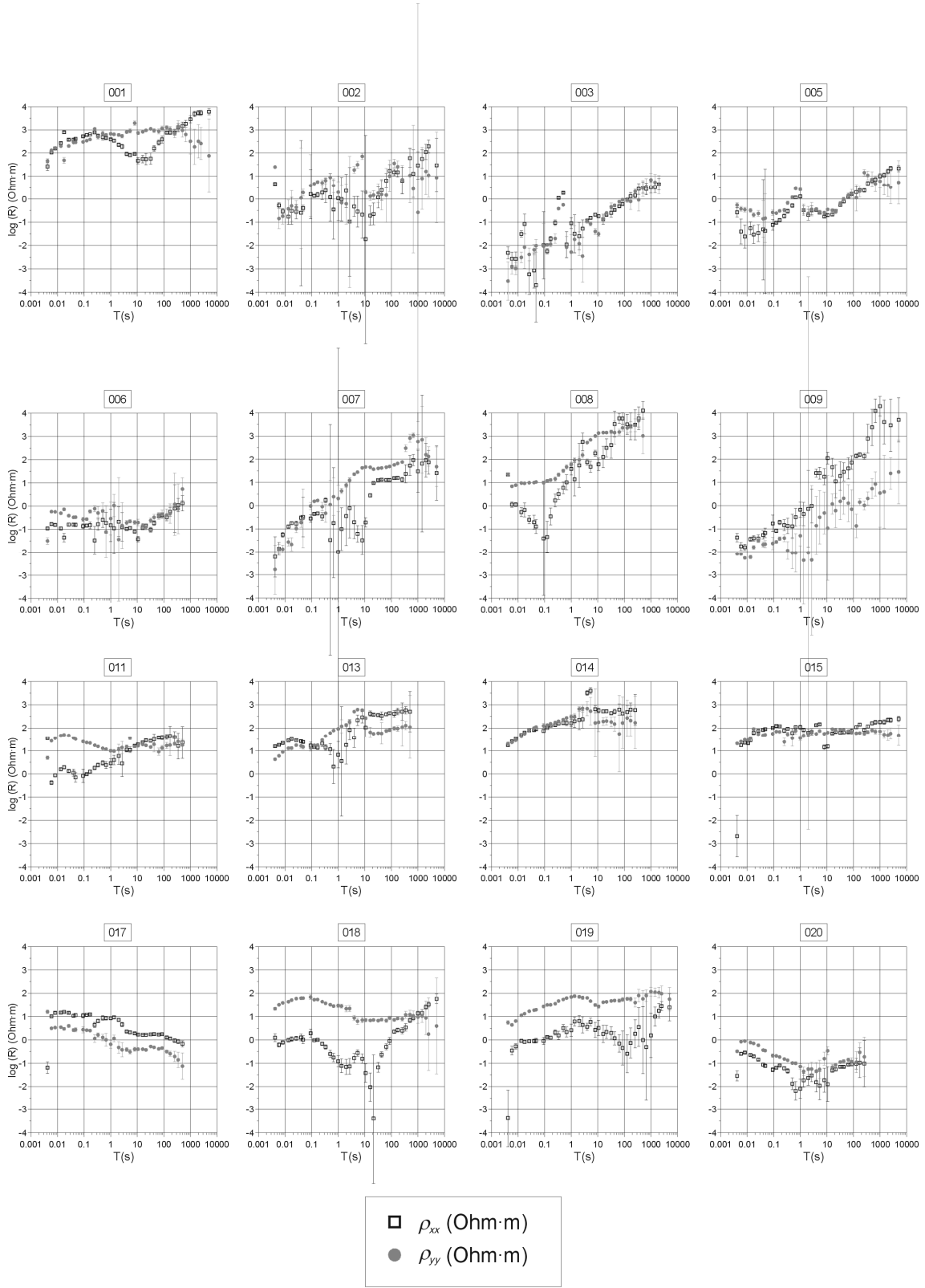
Figure D.1: Resistivity responses (ρ_{xx}, ρ_{xy}, ρ_{yx} and ρ_{yy}) with error bars for sites 001 to 020 from the Betics MT dataset.
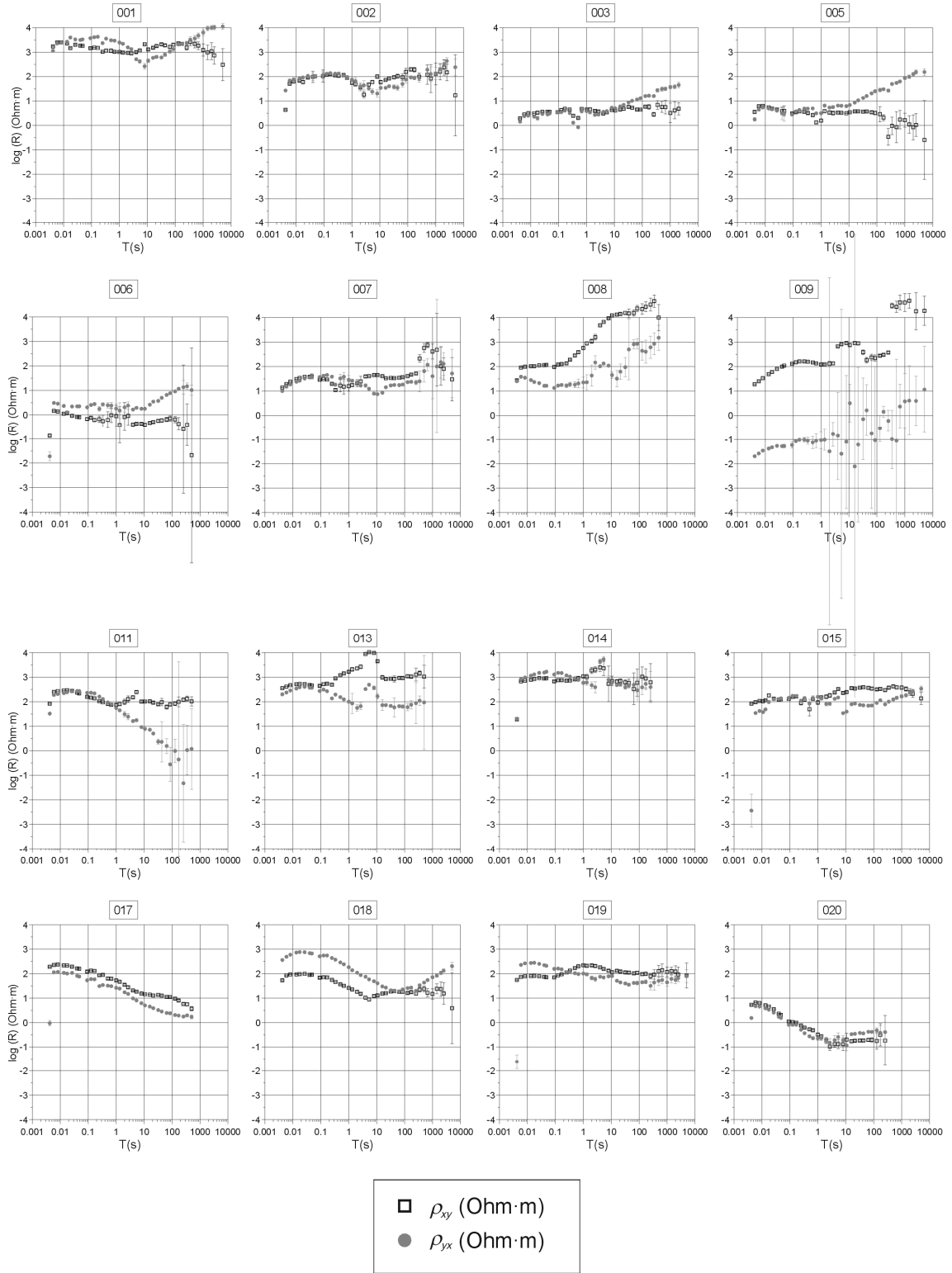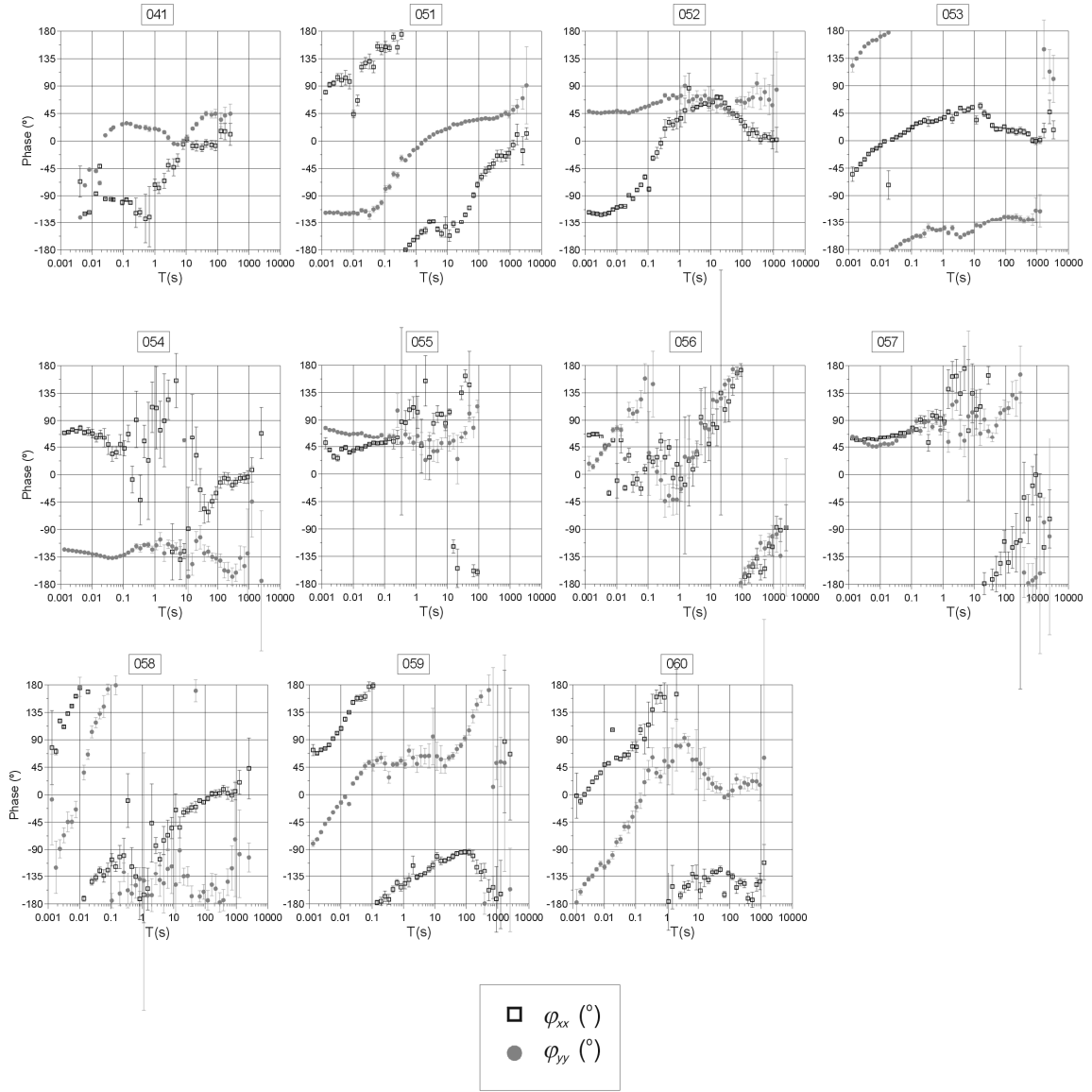
Figure D.1 (cont.)
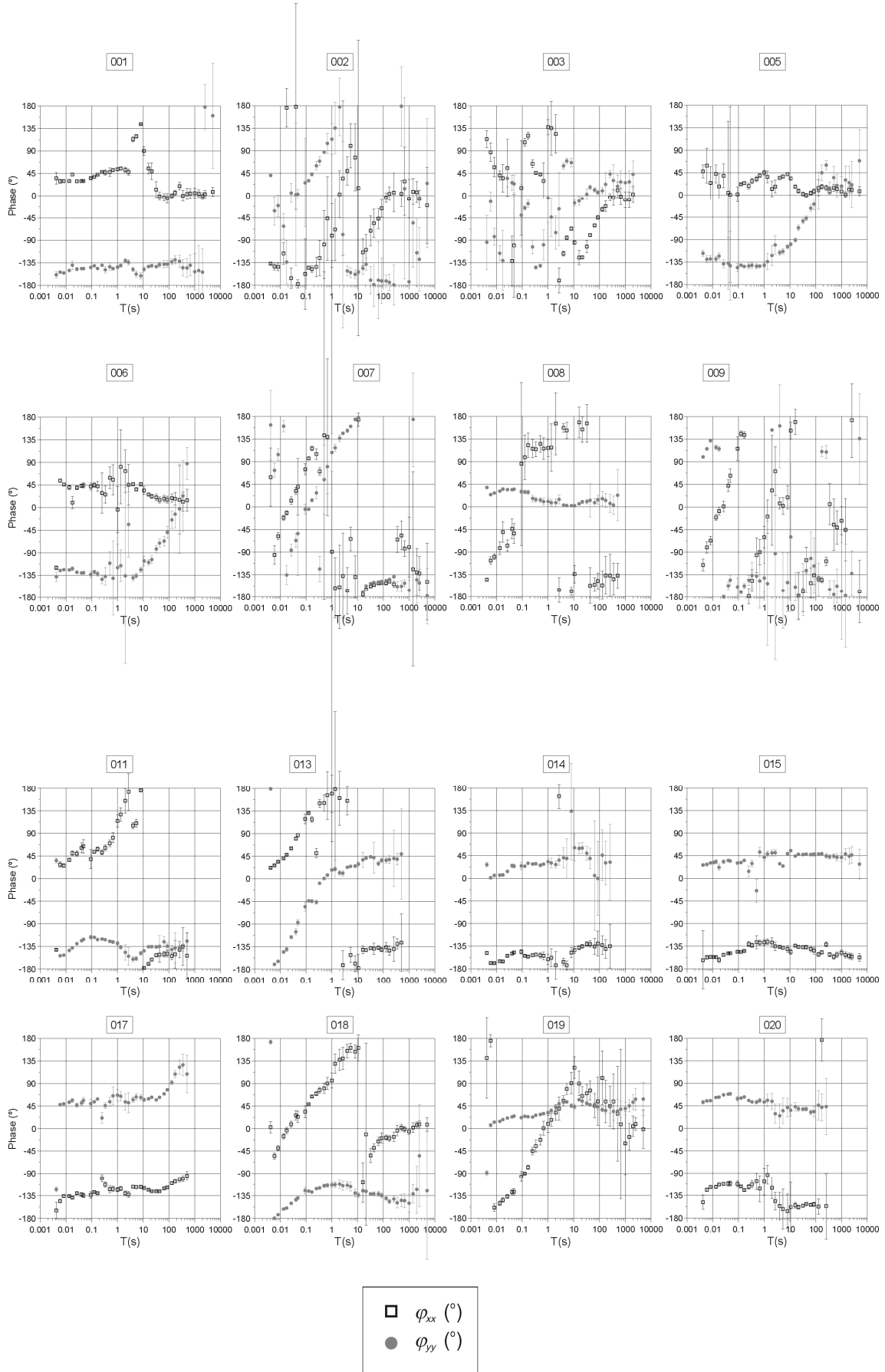
Figure D.2: Phase responses $(\varphi_{xx}, \varphi_{xy}, \varphi_{yx}$ and $\varphi_{yy})$ with error bars for sites 001 to 020 from the Betics MT dataset.
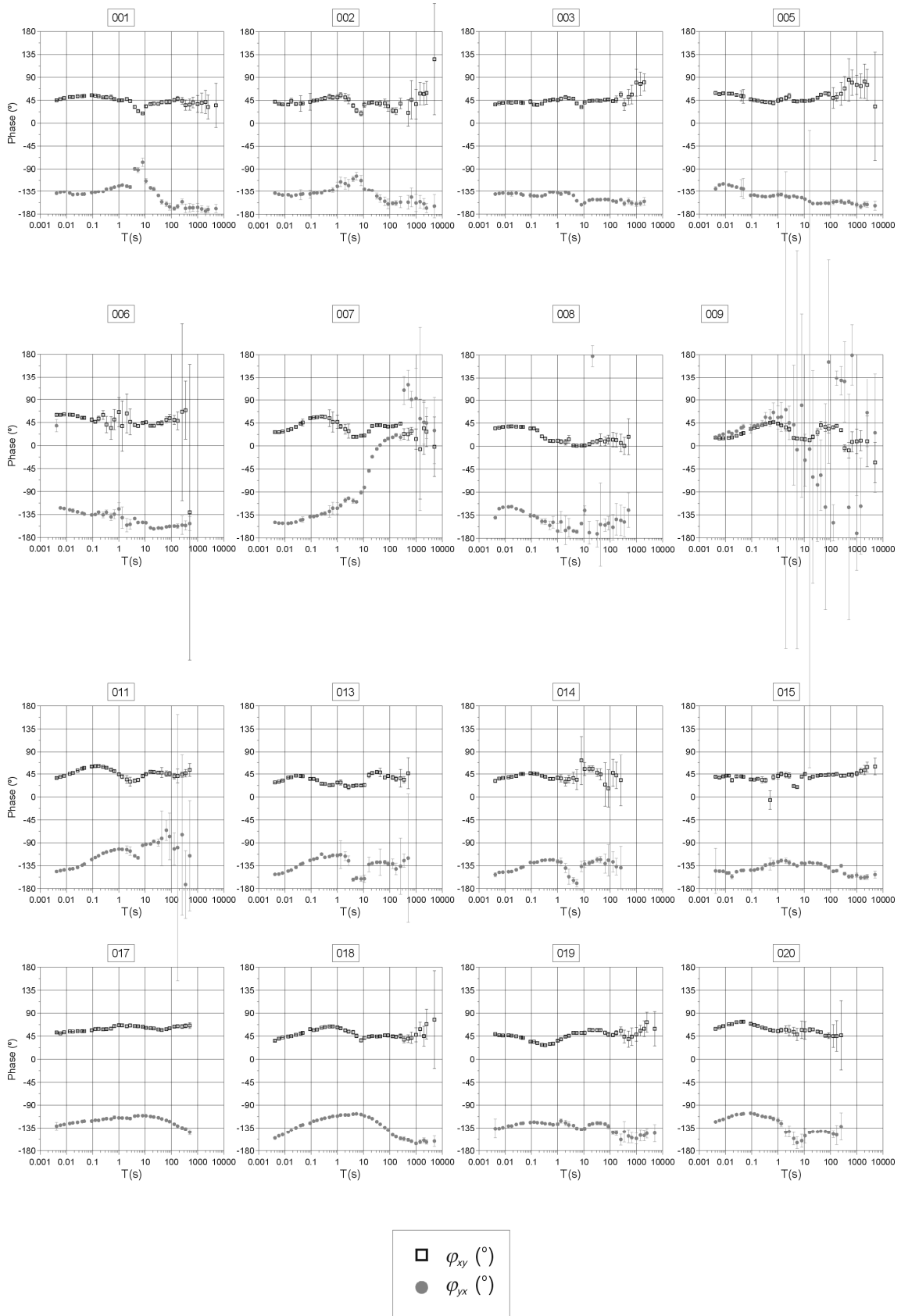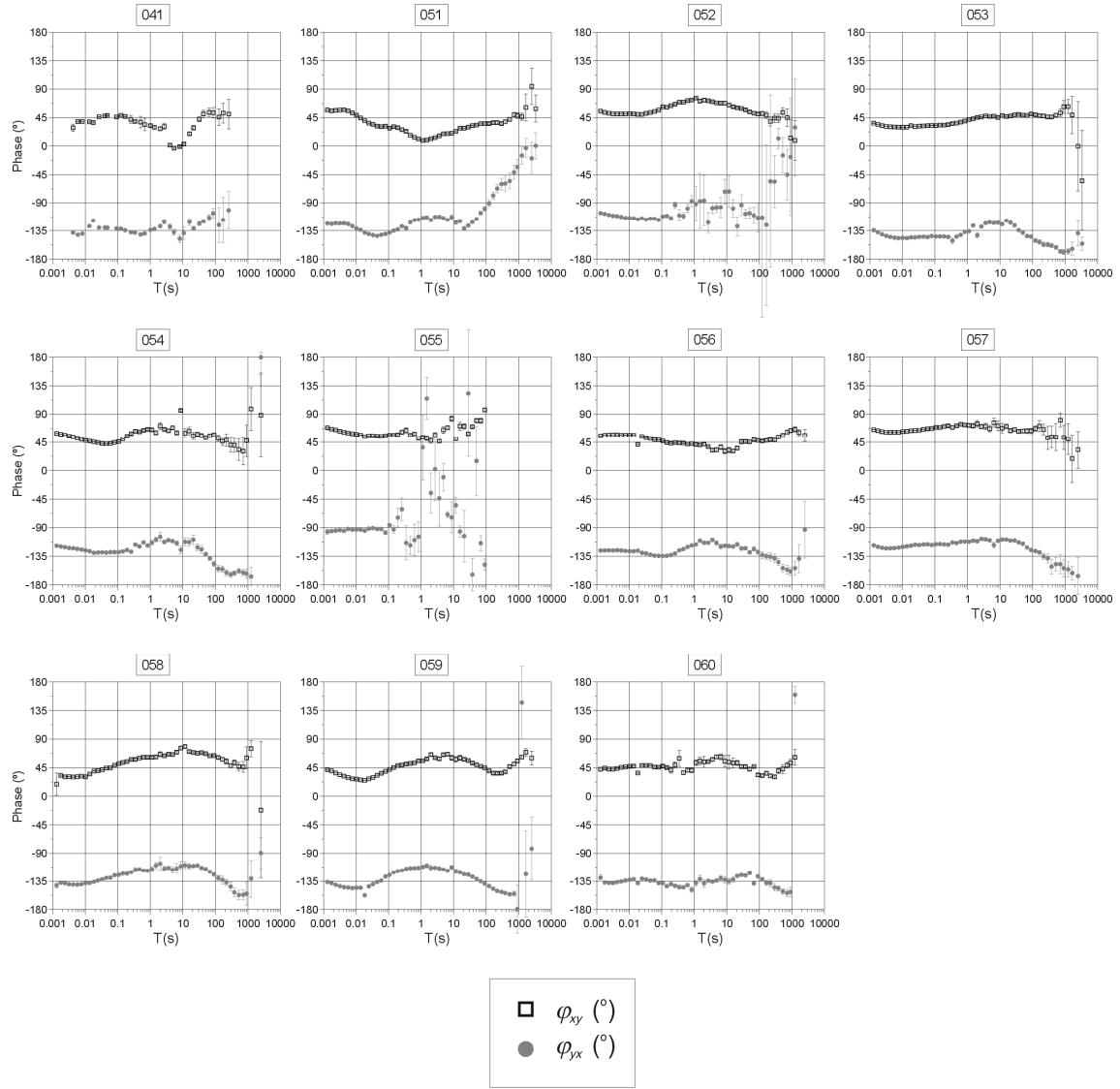
Figure D.2 (cont.)
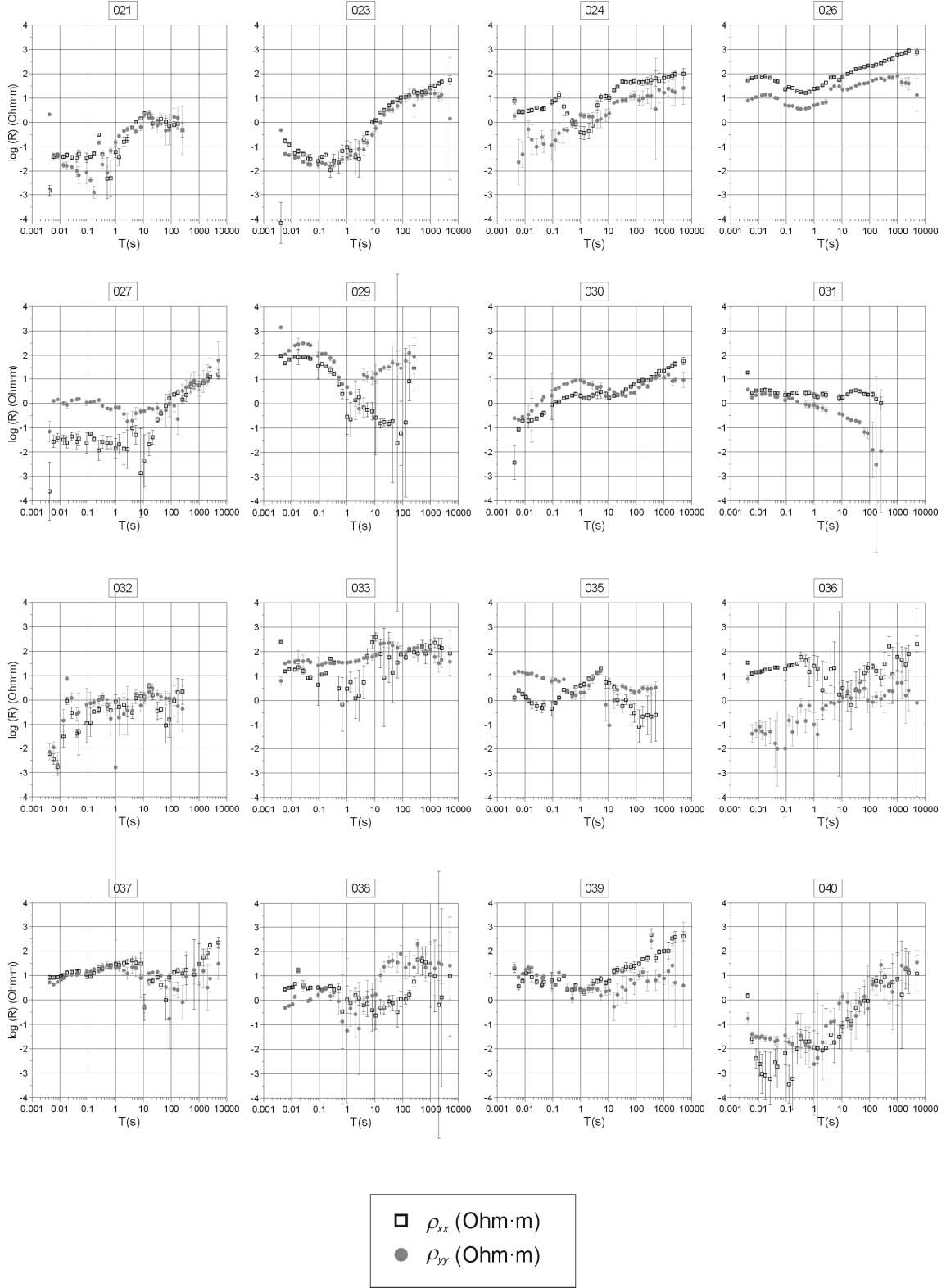
Figure D.3: Resistivity responses (ρ_{xx}, ρ_{xy}, ρ_{yx} and ρ_{yy}) with error bars for sites 021 to 040 from the Betics MT dataset.
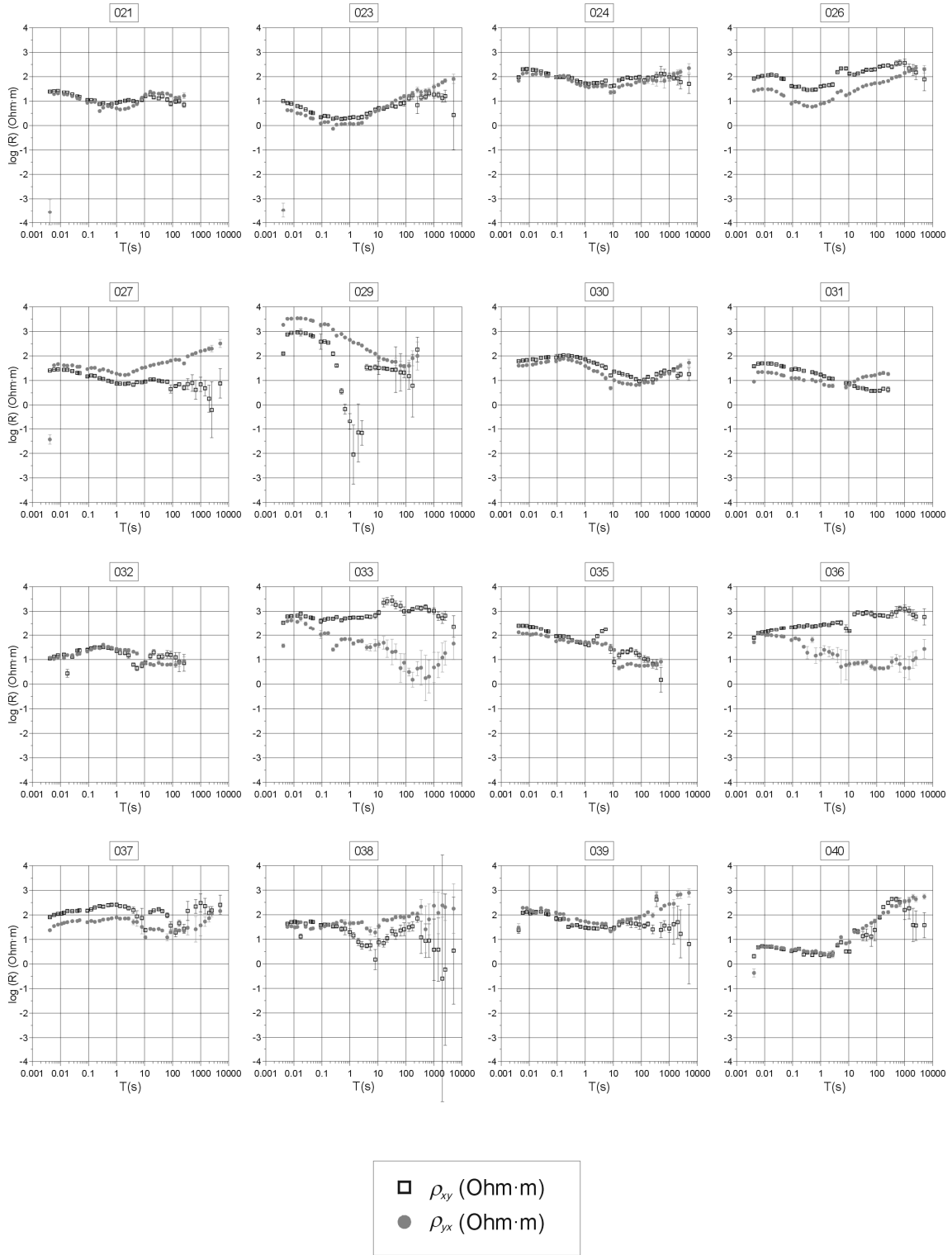
Figure D.3 (cont.)
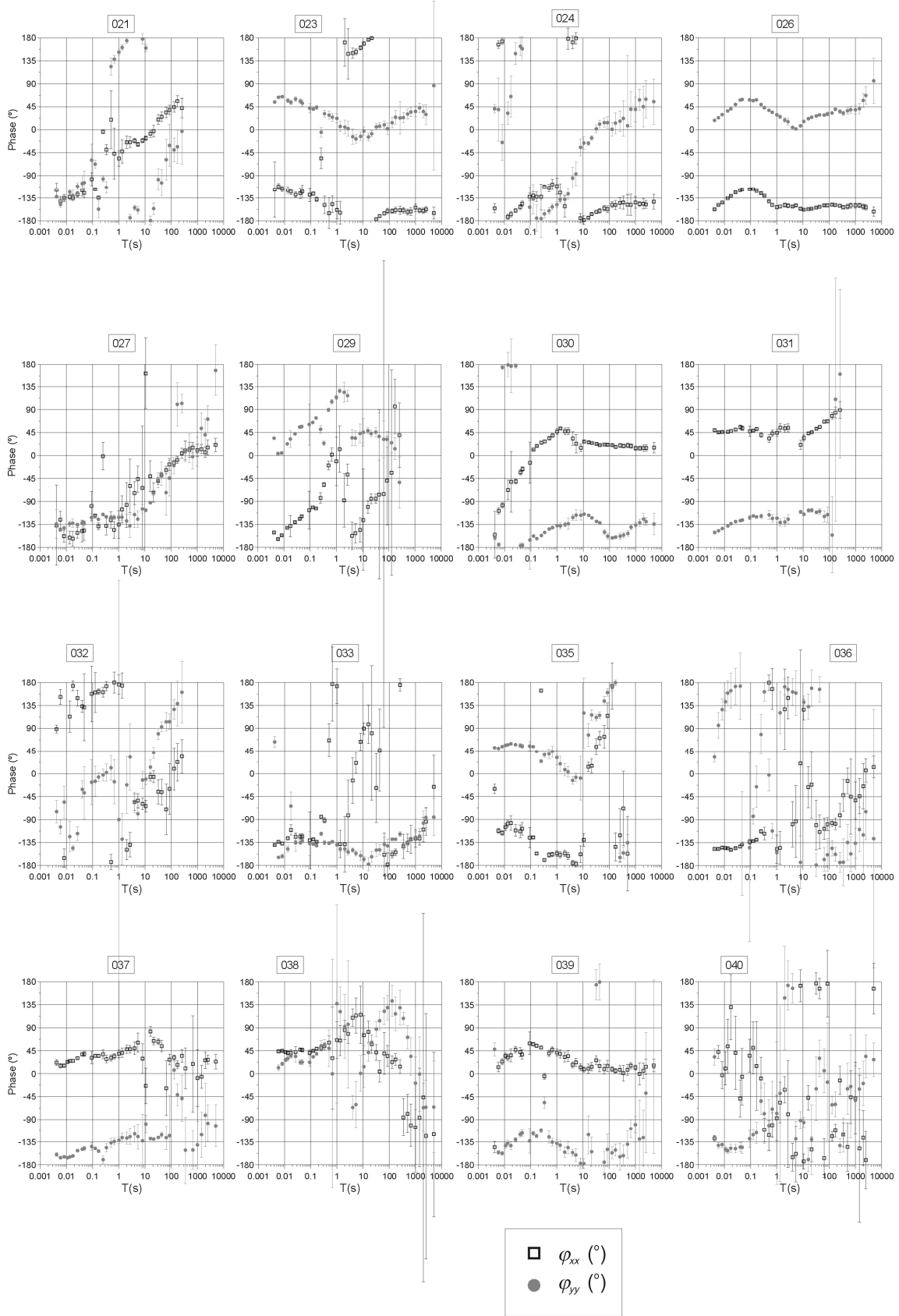
Figure D.4: Phase responses (φ_{xx}, φ_{xy}, φ_{yx} and φ_{yy}) with error bars for sites 021 to 040 from the Betics MT dataset.
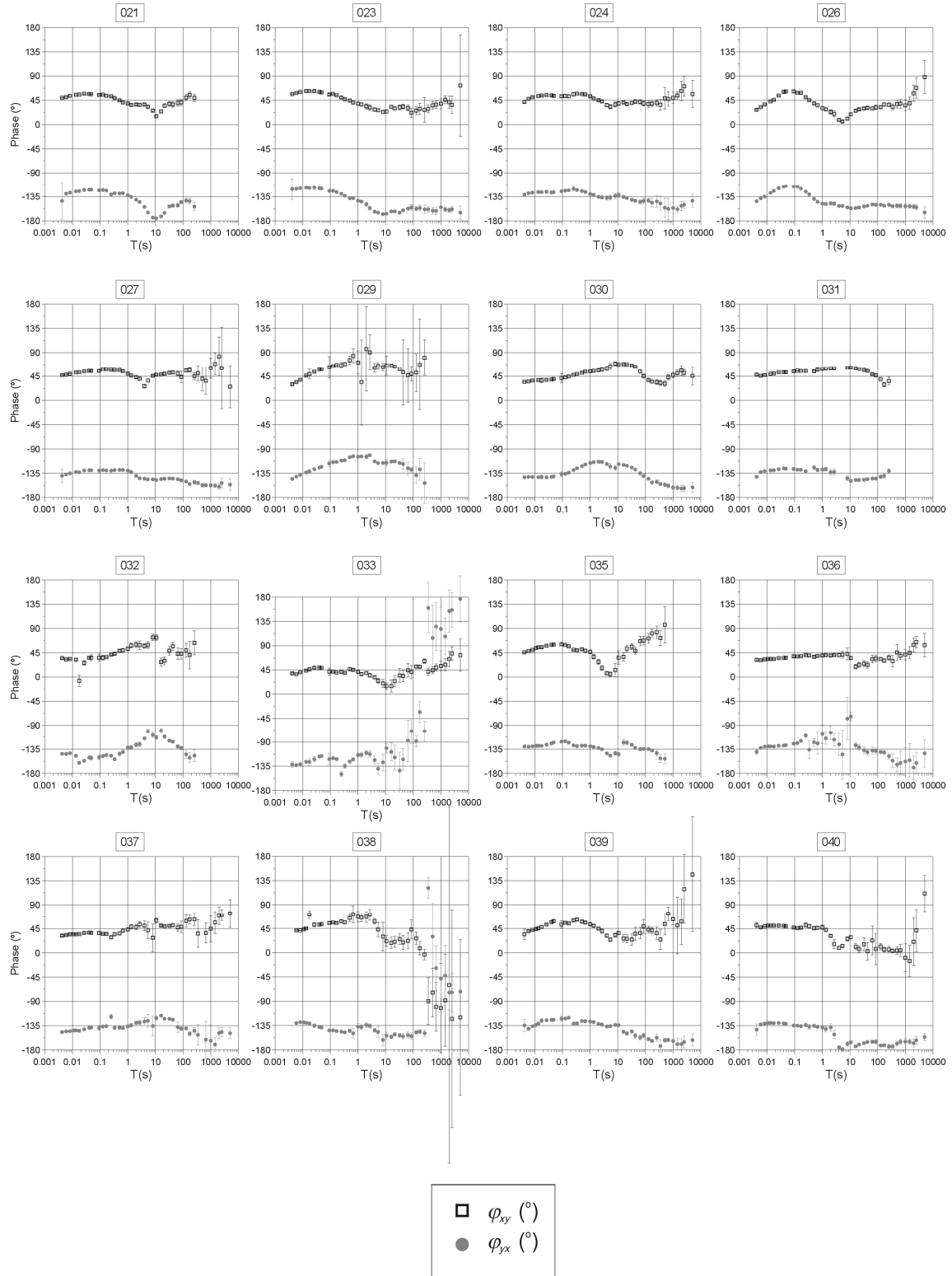
Figure D.4 (cont.)
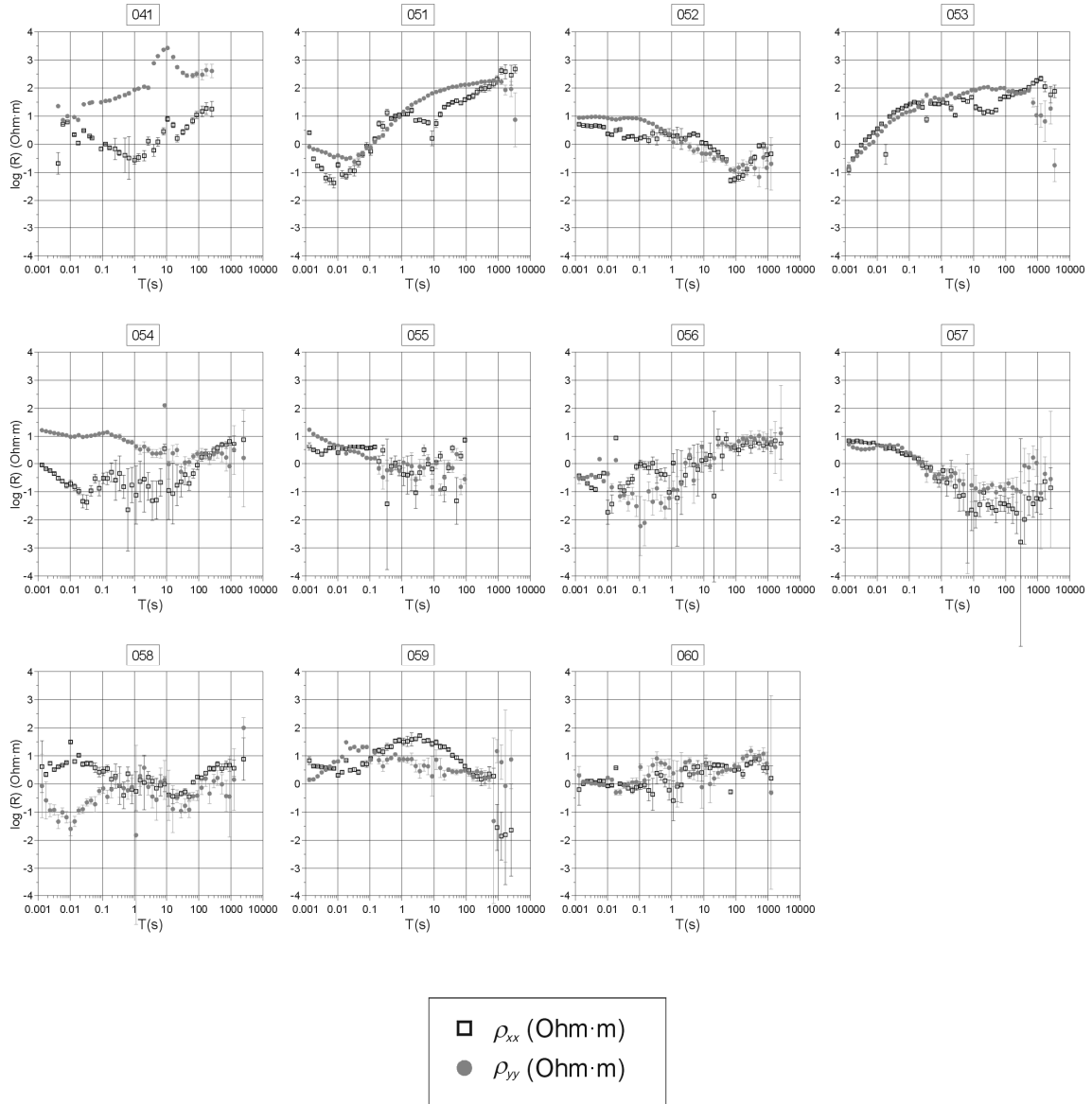
Figure D.5: Resistivity responses (ρ_{xx}, ρ_{xy}, ρ_{yx} and ρ_{yy}) with error bars for sites 041 to 060 from the Betics MT dataset.
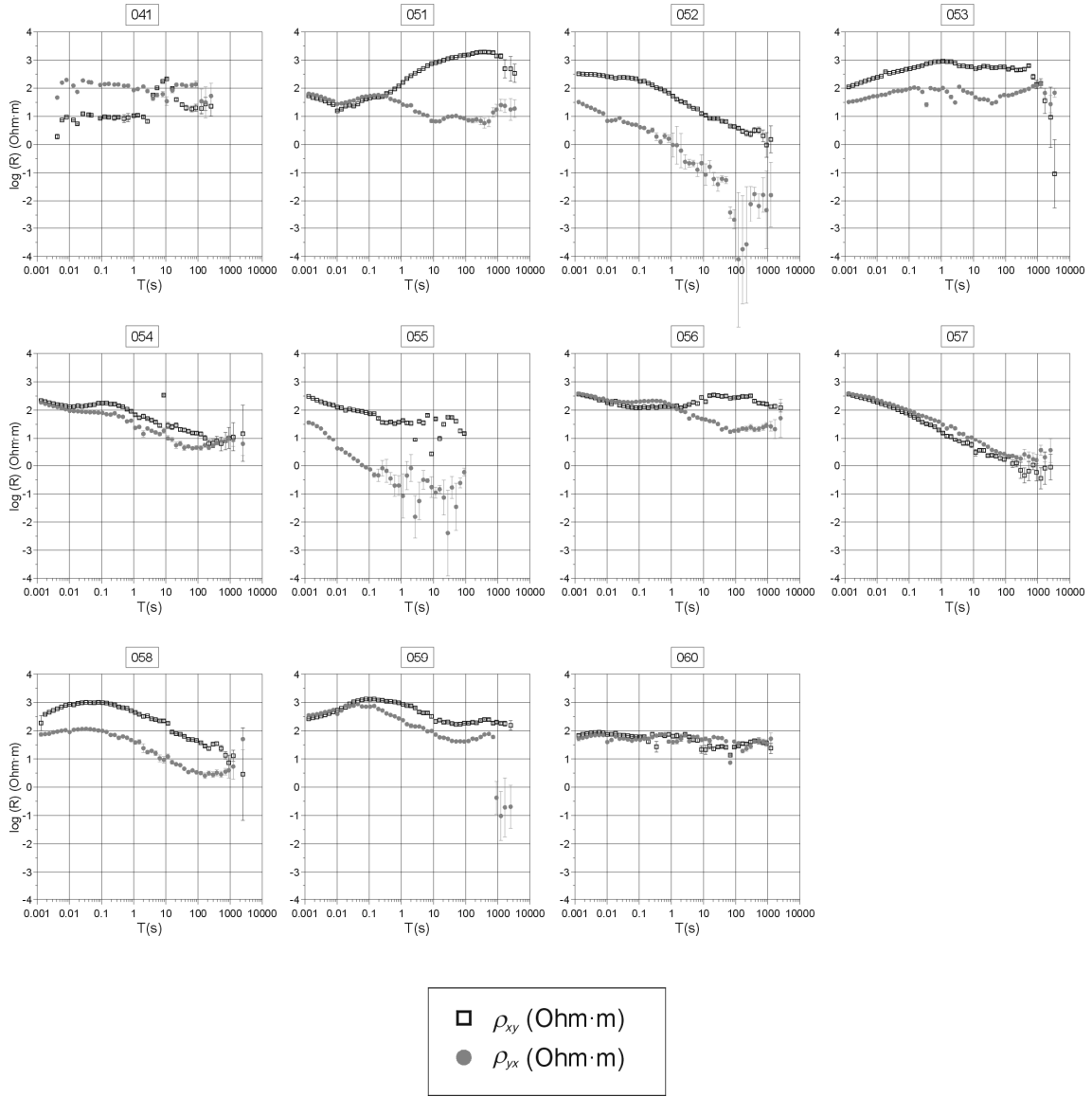
Figure D.5 (cont.)

Figure D.6: Phase responses (φ_{xx}, φ_{xy}, φ_{yx} and φ_{yy}) with error bars for sites 041 to 060 from the Betics MT dataset.

Figure D.6 (cont.)
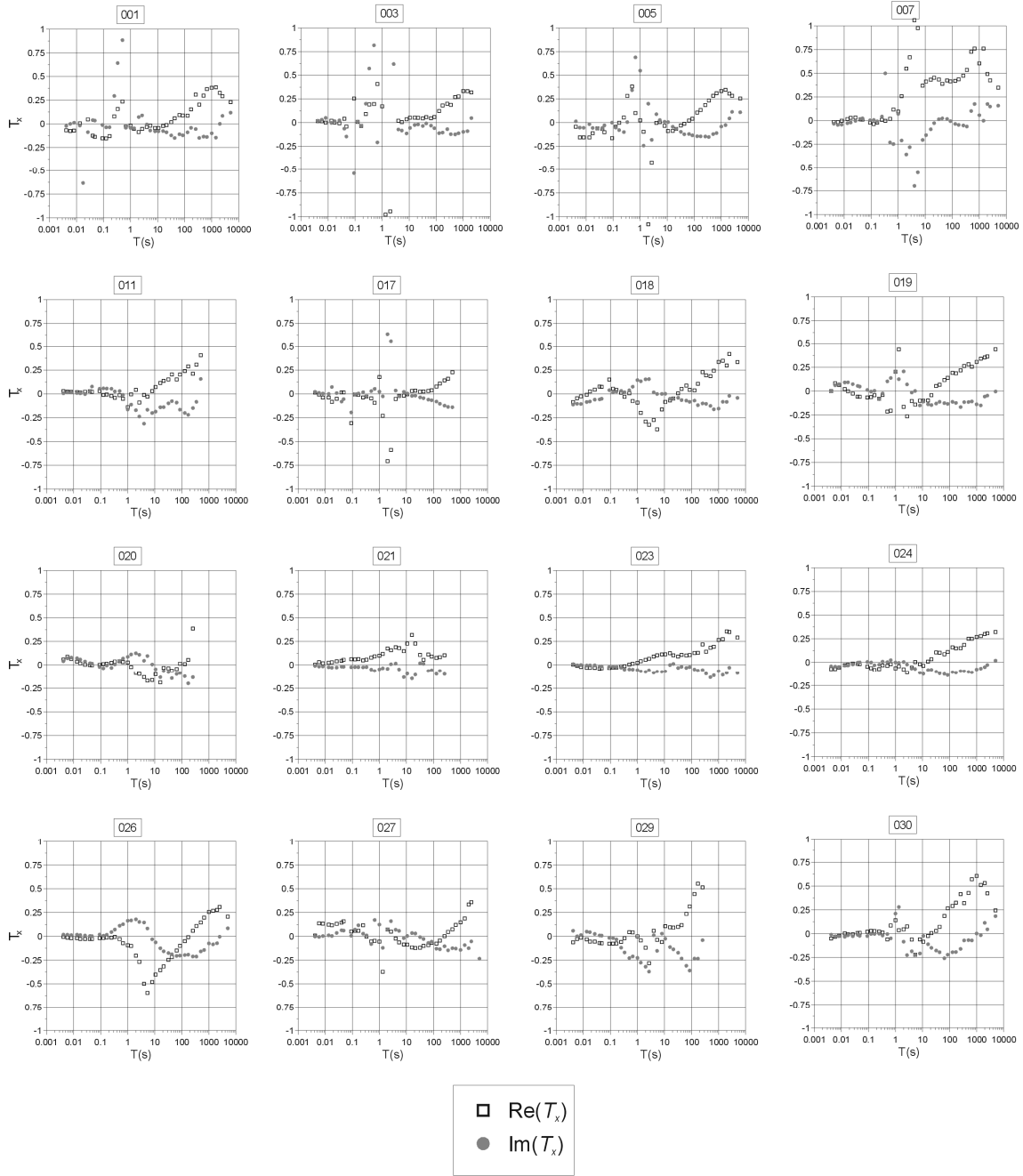
Figure D.7: Real and imaginary parts of x and y tipper components (Re(T_x), Im(T_x) and Re(T_y), Im(T_y)) for sites 001 to 030 from the Betics MT dataset in which the vertical magnetic component was registered.
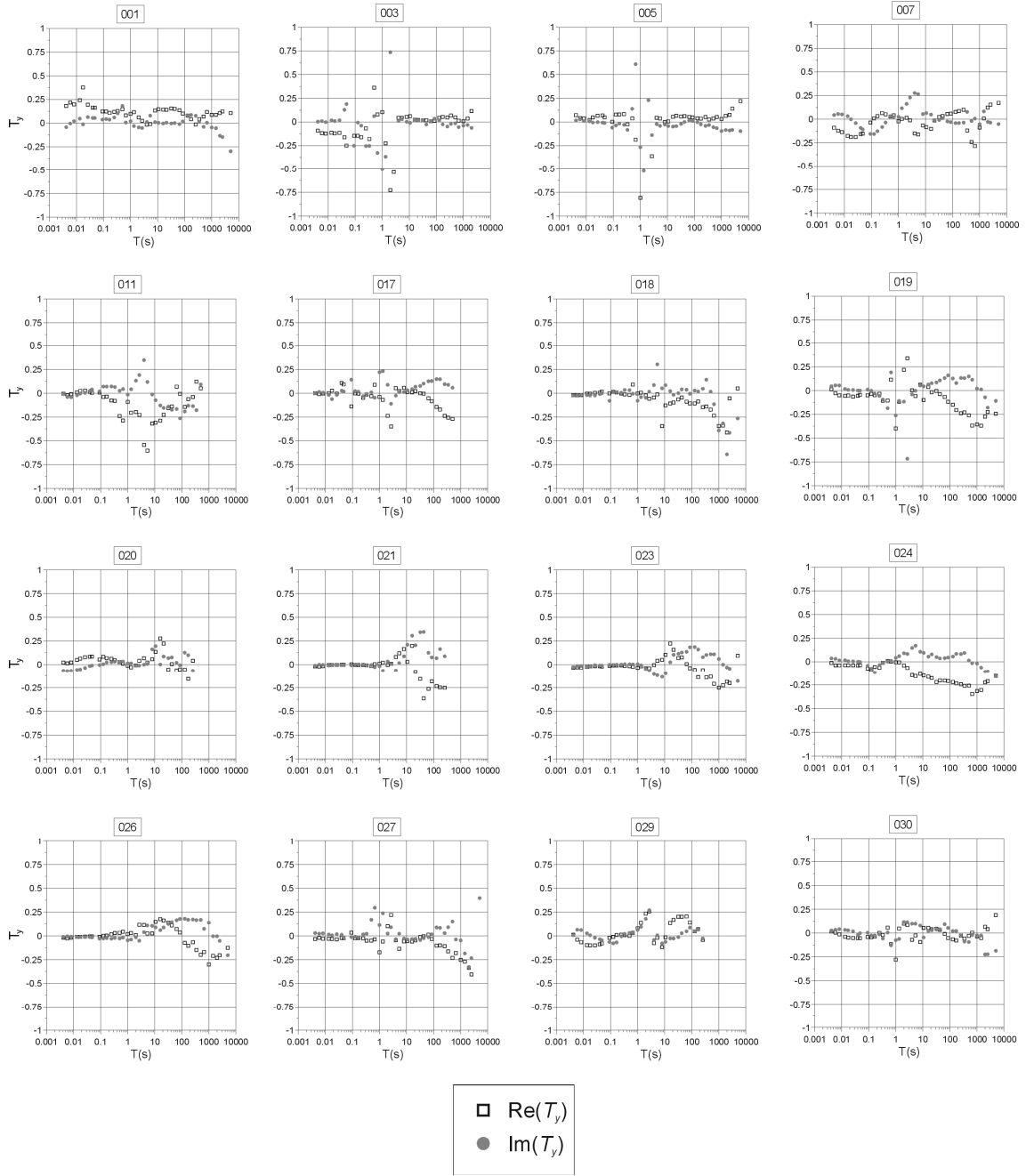
Figure D.7 (cont.)
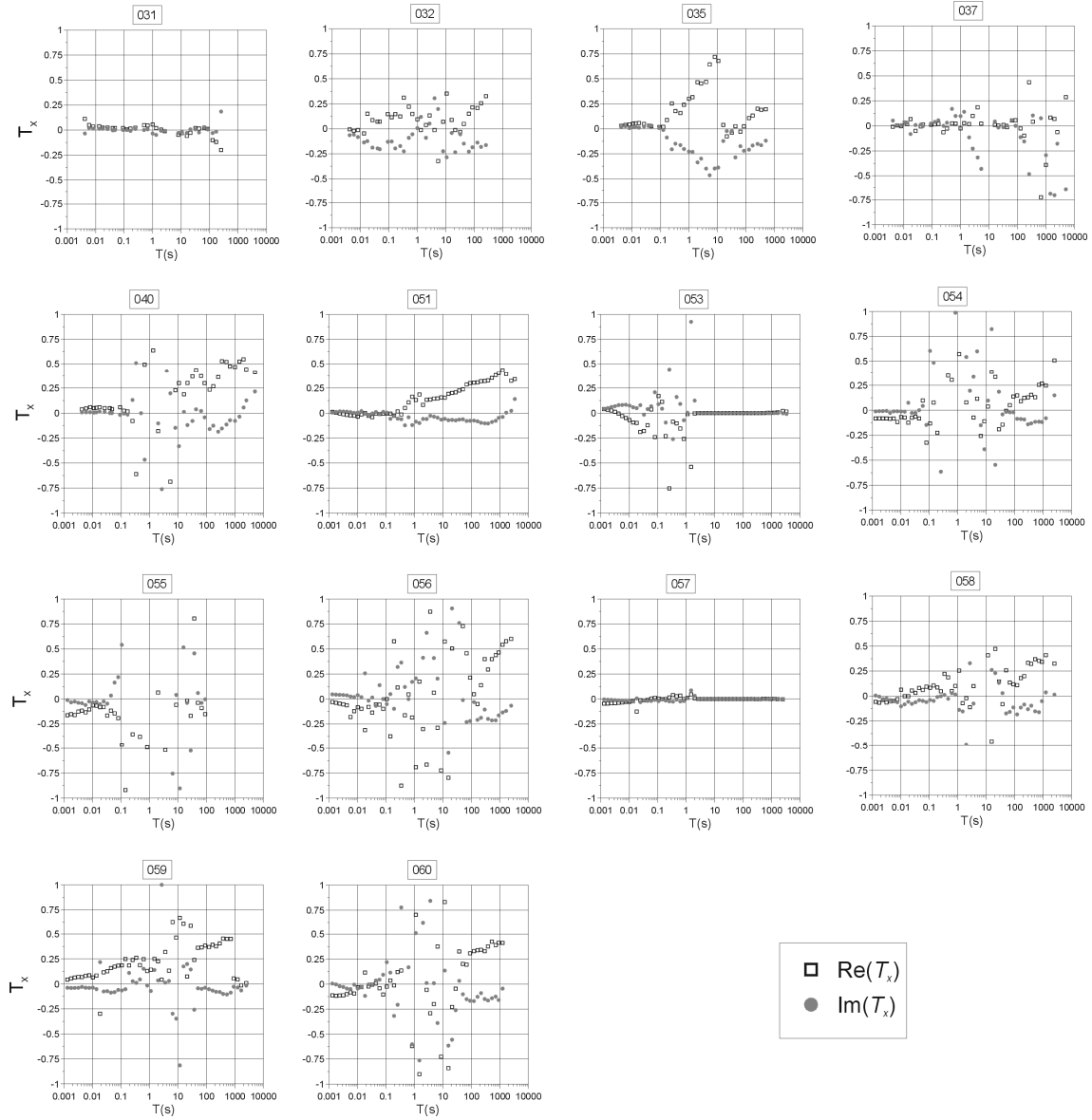
Figure D.8: Real and imaginary parts of x and y tipper components (Re(T_x), Im(T_x) and Re(T_y), Im(T_y)) for sites 031 to 060 from the Betics MT dataset in which the vertical magnetic component was registered.
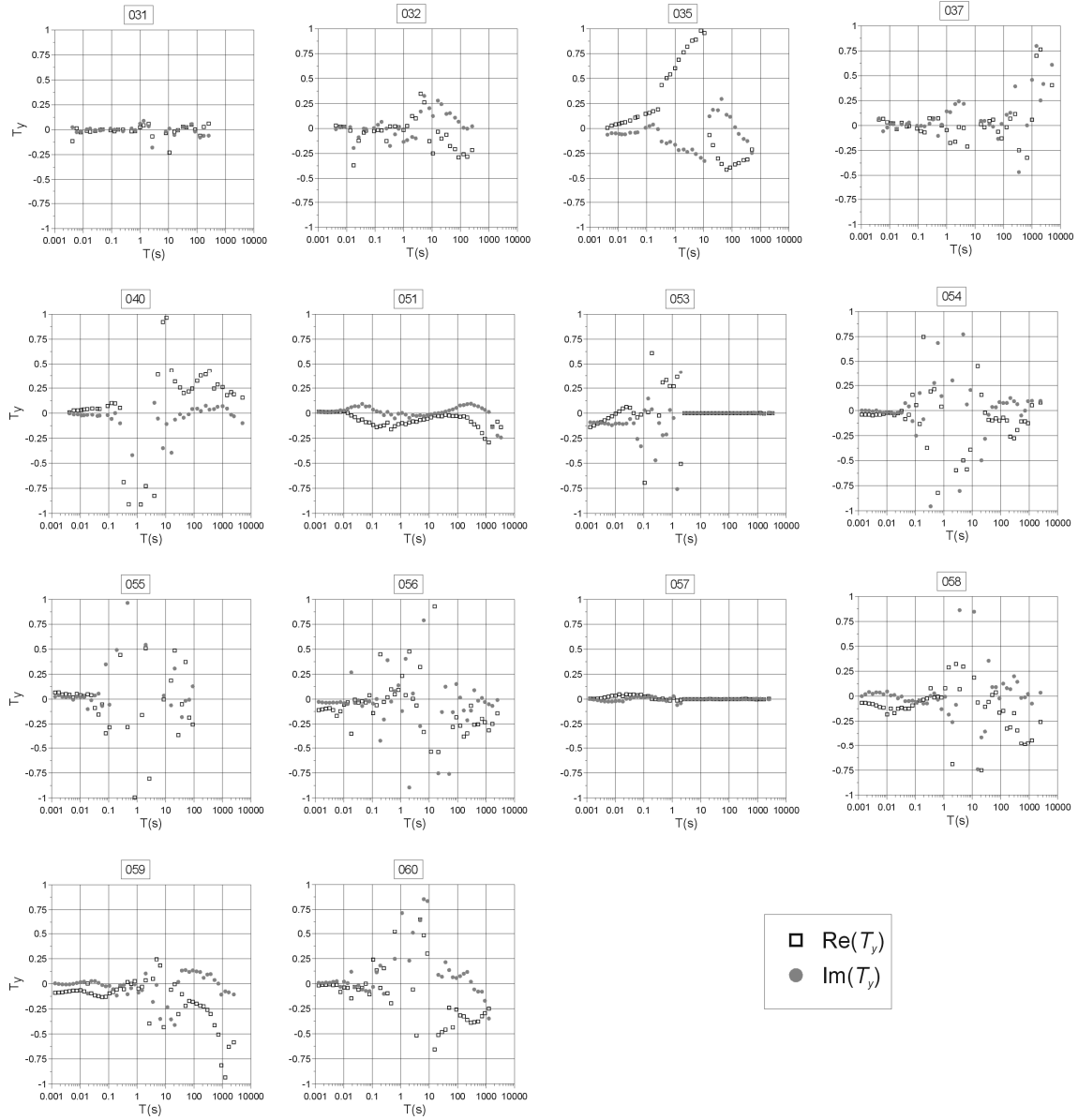
Figure D.8 (cont.)
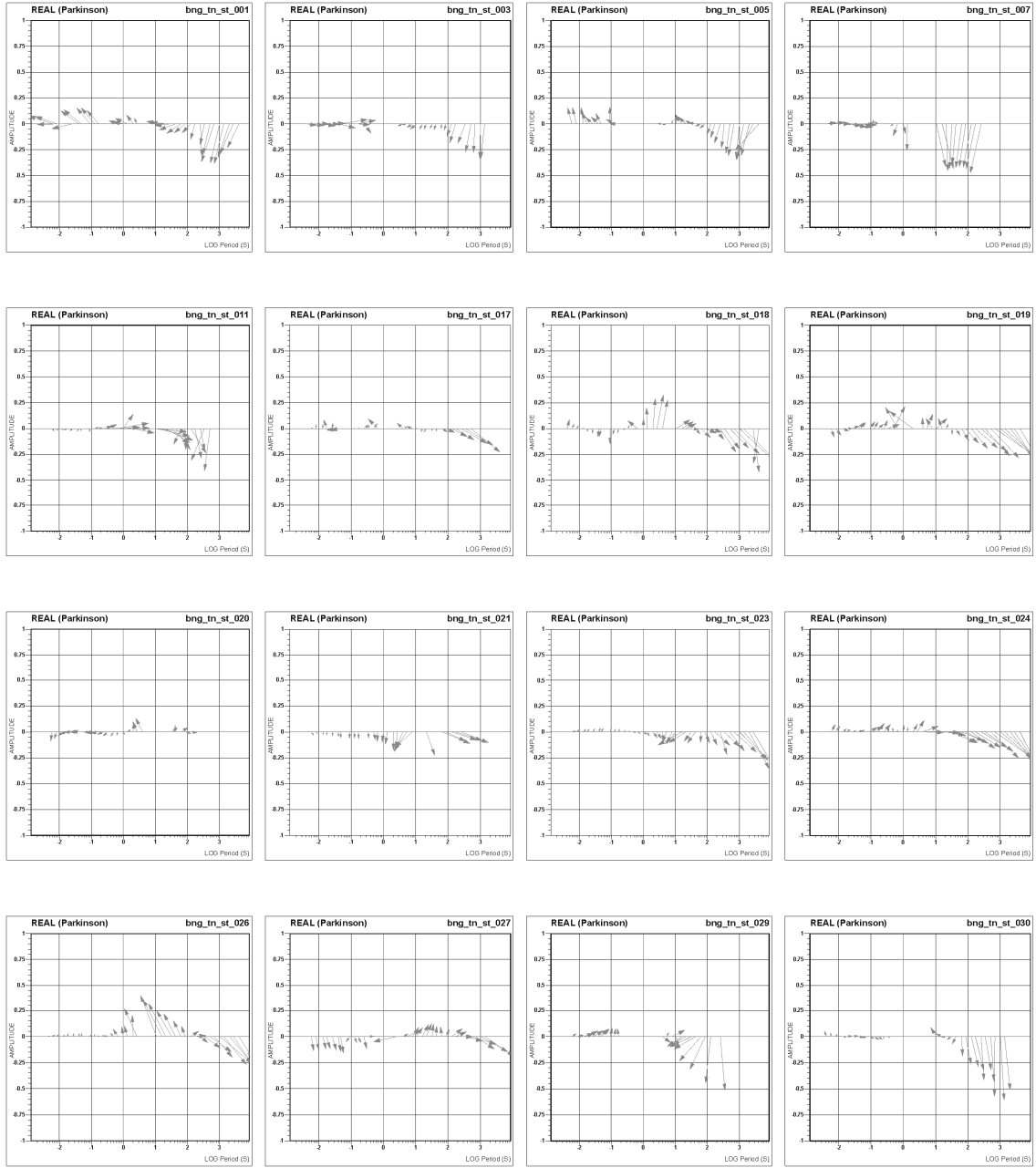
Figure D.9: Real induction arrows following Parkinson convention (inverted, i.e. pointing at conductive regions) plotted for all sites from the Betics MT dataset.
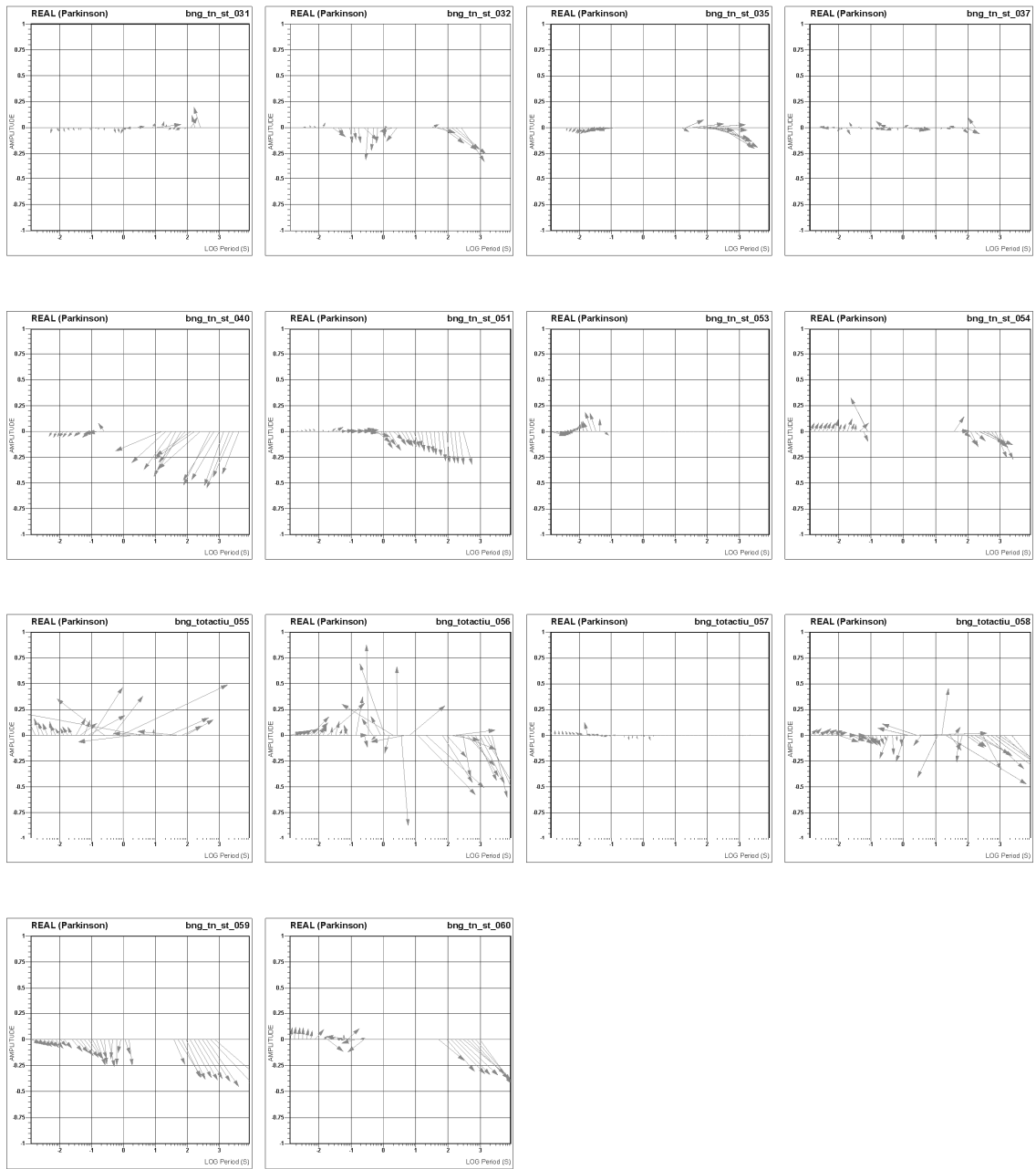
Figure D.9 (cont.)

Appendix E: Data and Model bet3D-140 Responses

The following plots display the MT responses corresponding to the Betics MT dataset, with the exception of b09, and the 3D model bet3D-140. These responses are determinant resistivity and phases (Figures E.1 to E.6) and the non-diagonal components, xy and yx, apparent resistivities and phases (Figures E.7 to E.12).
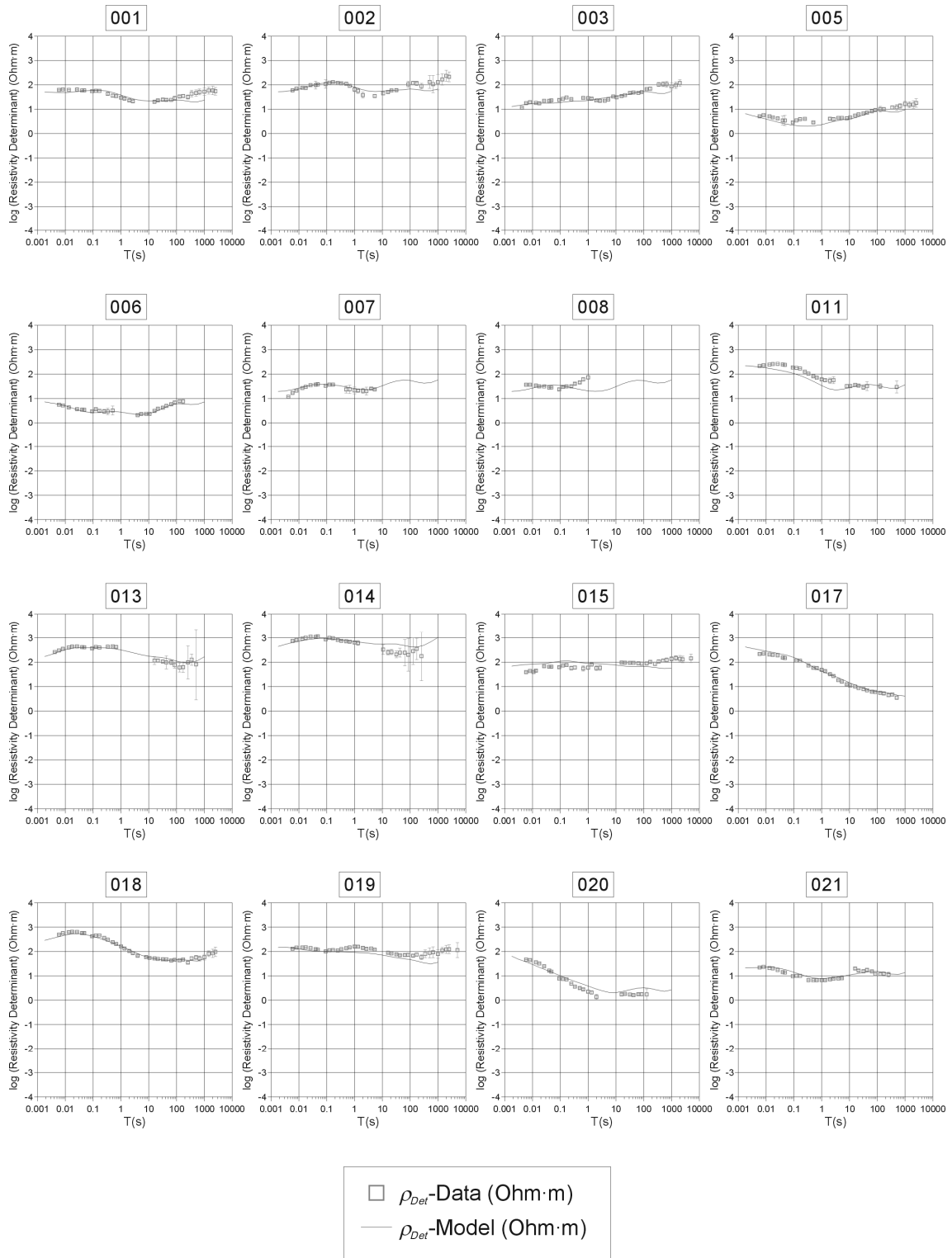
Figure E.1: Determinant resistivity data and model responses. Sites 1 to 21.
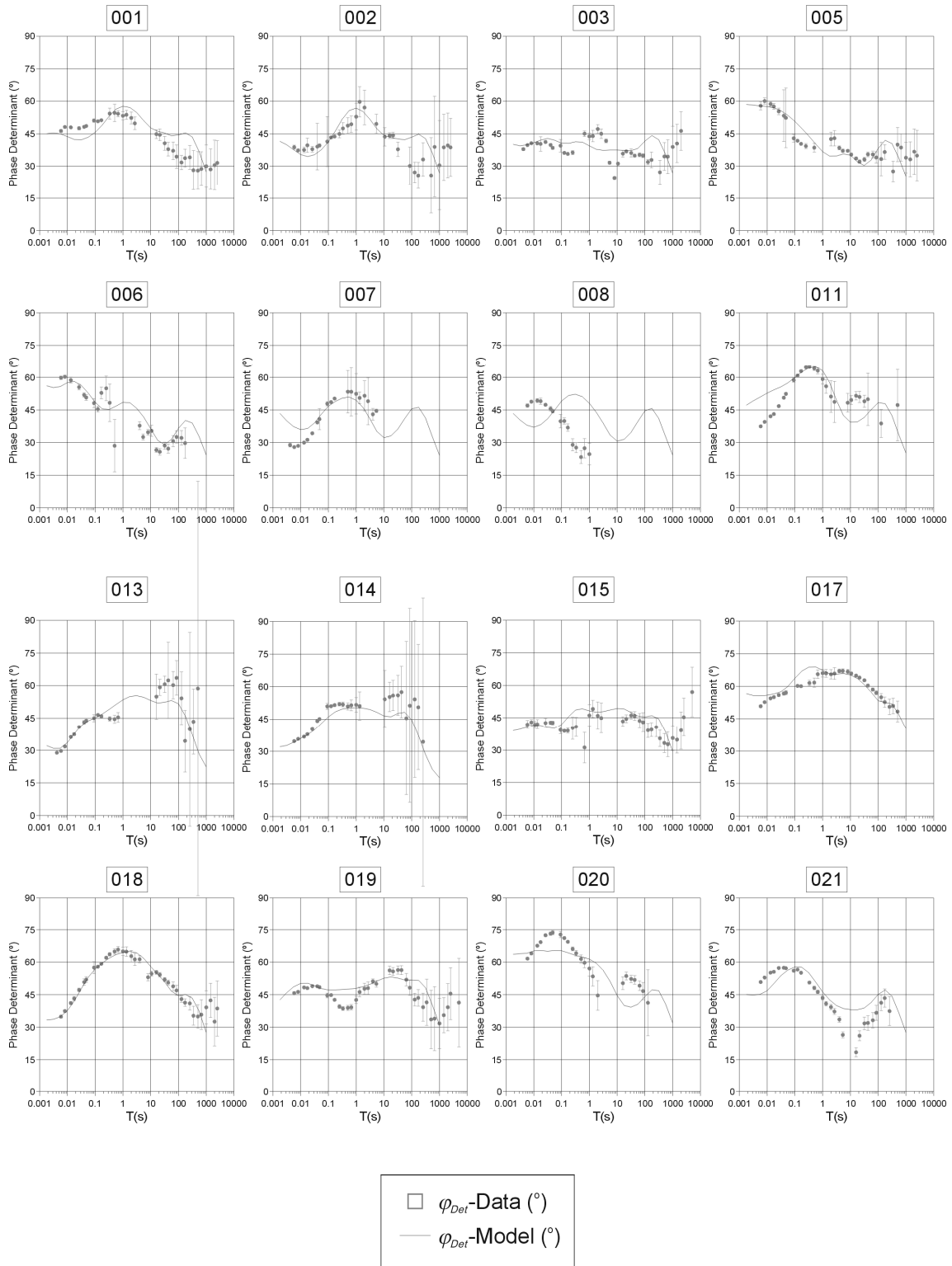
Figure E.2: Determinant phase data and model responses. Sites 1 to 21.
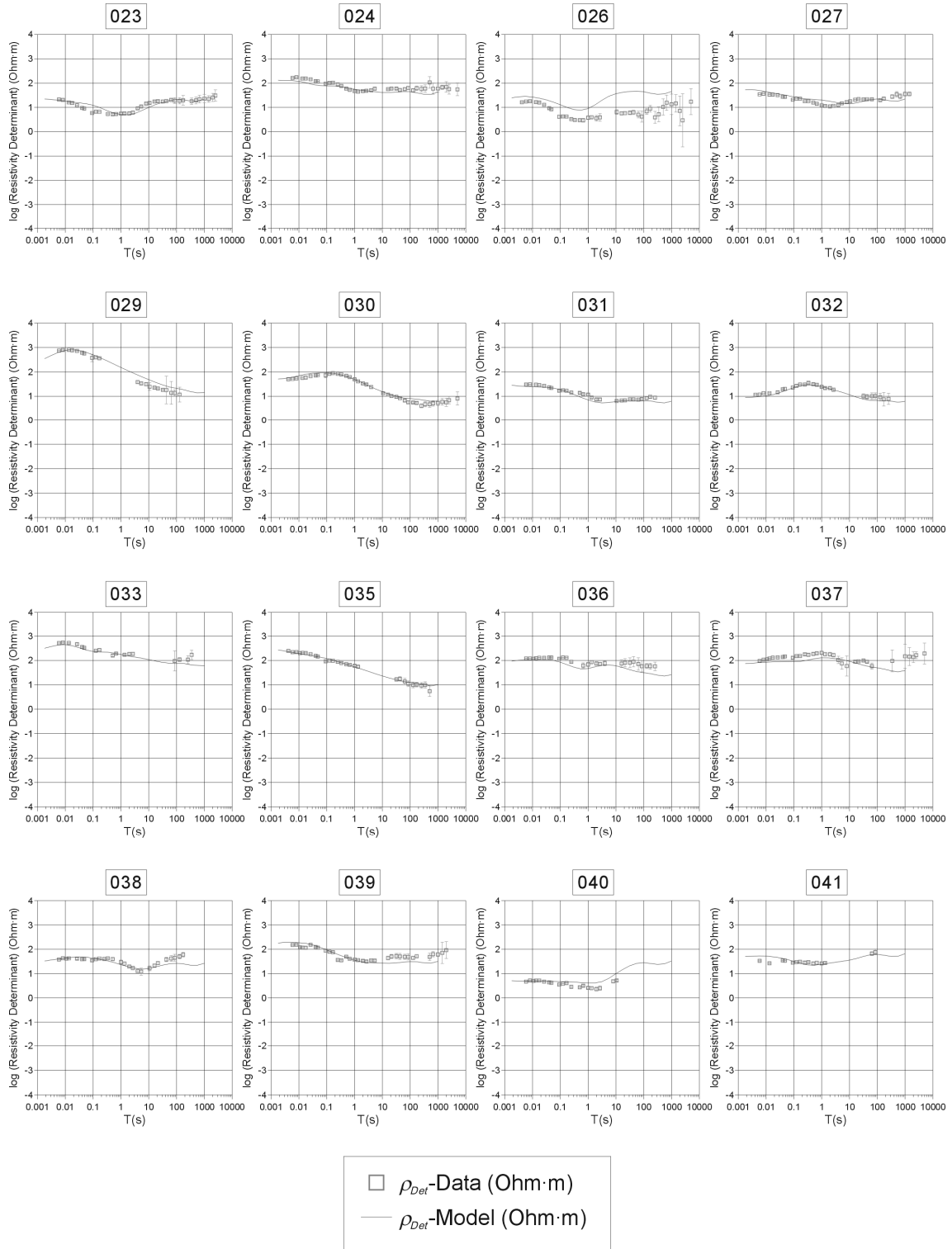
Figure E.3: Determinant resistivity data and model responses. Sites 23 to 41.
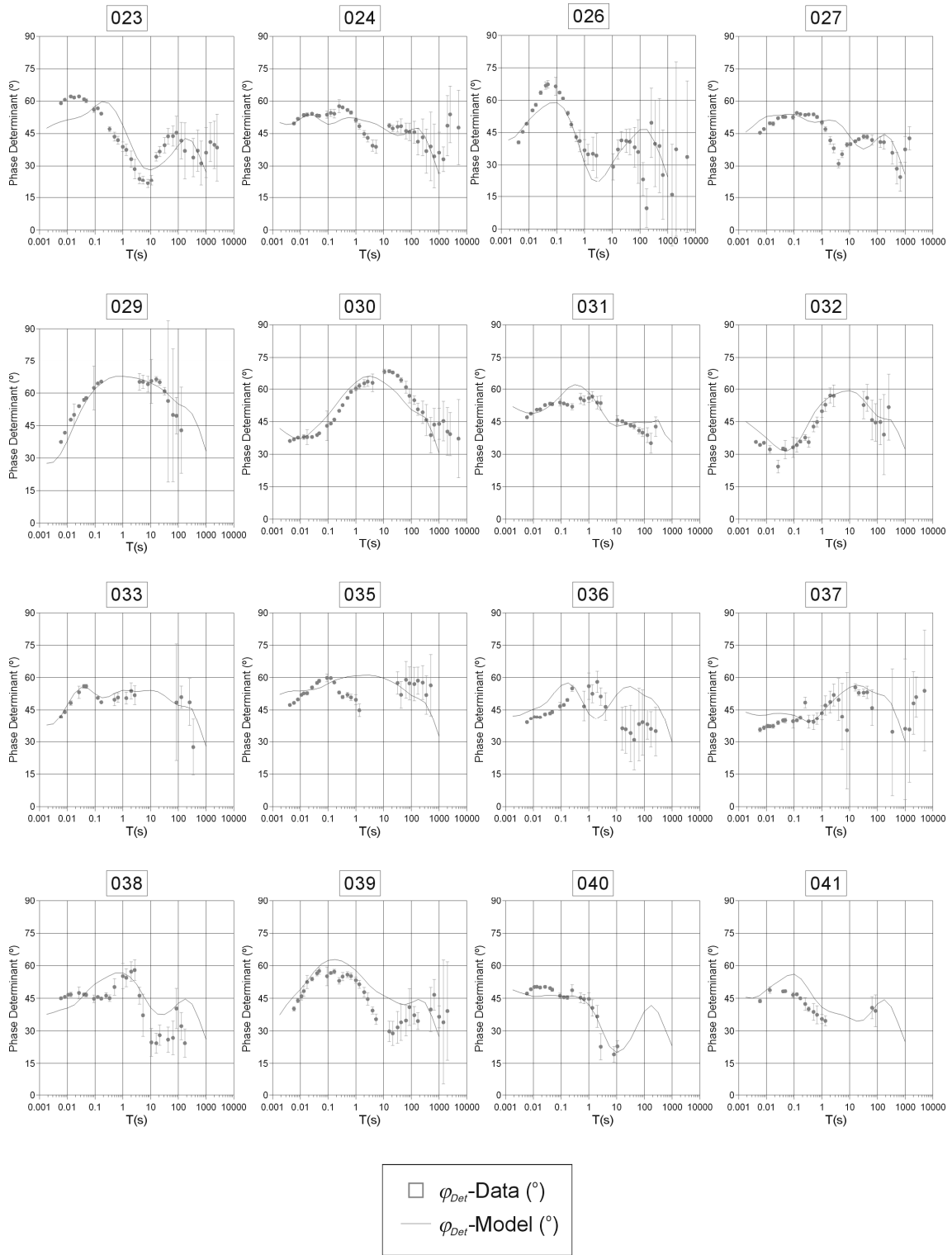
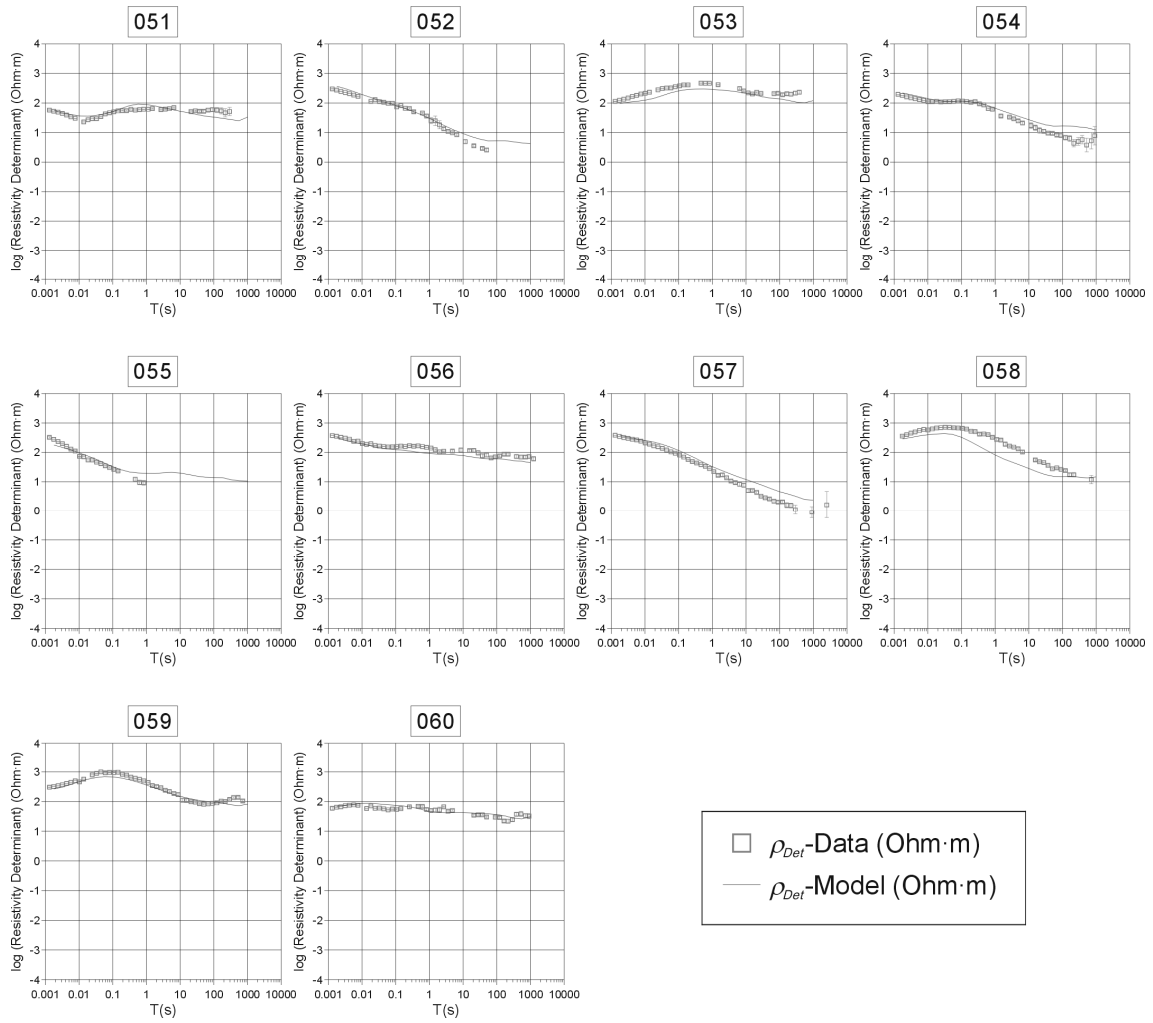Figure E.4: Determinant phase data and model responses. Sites 23 to 41.

Figure E.5: Determinant resistivity data and model responses. Sites 51 to 60.
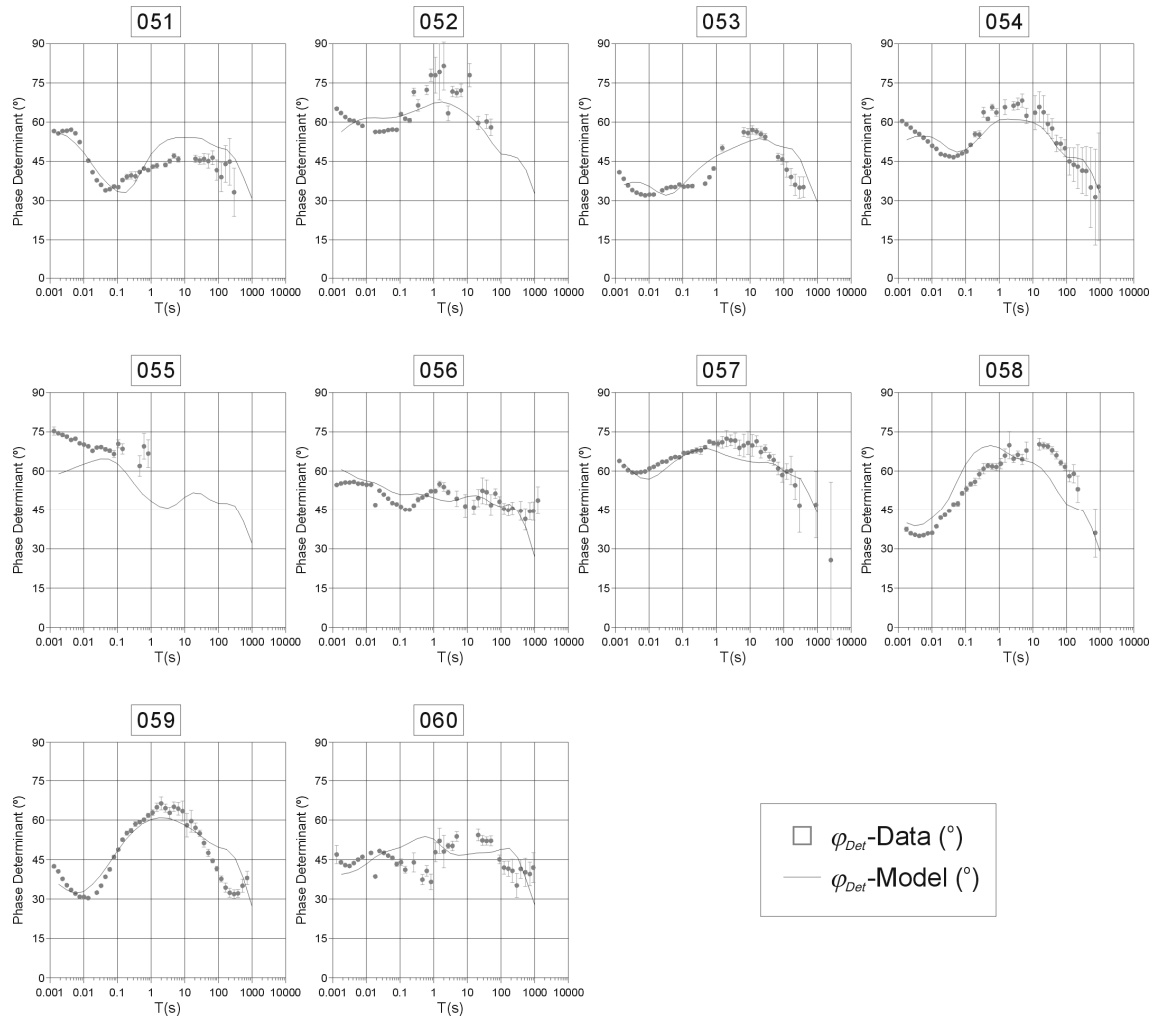
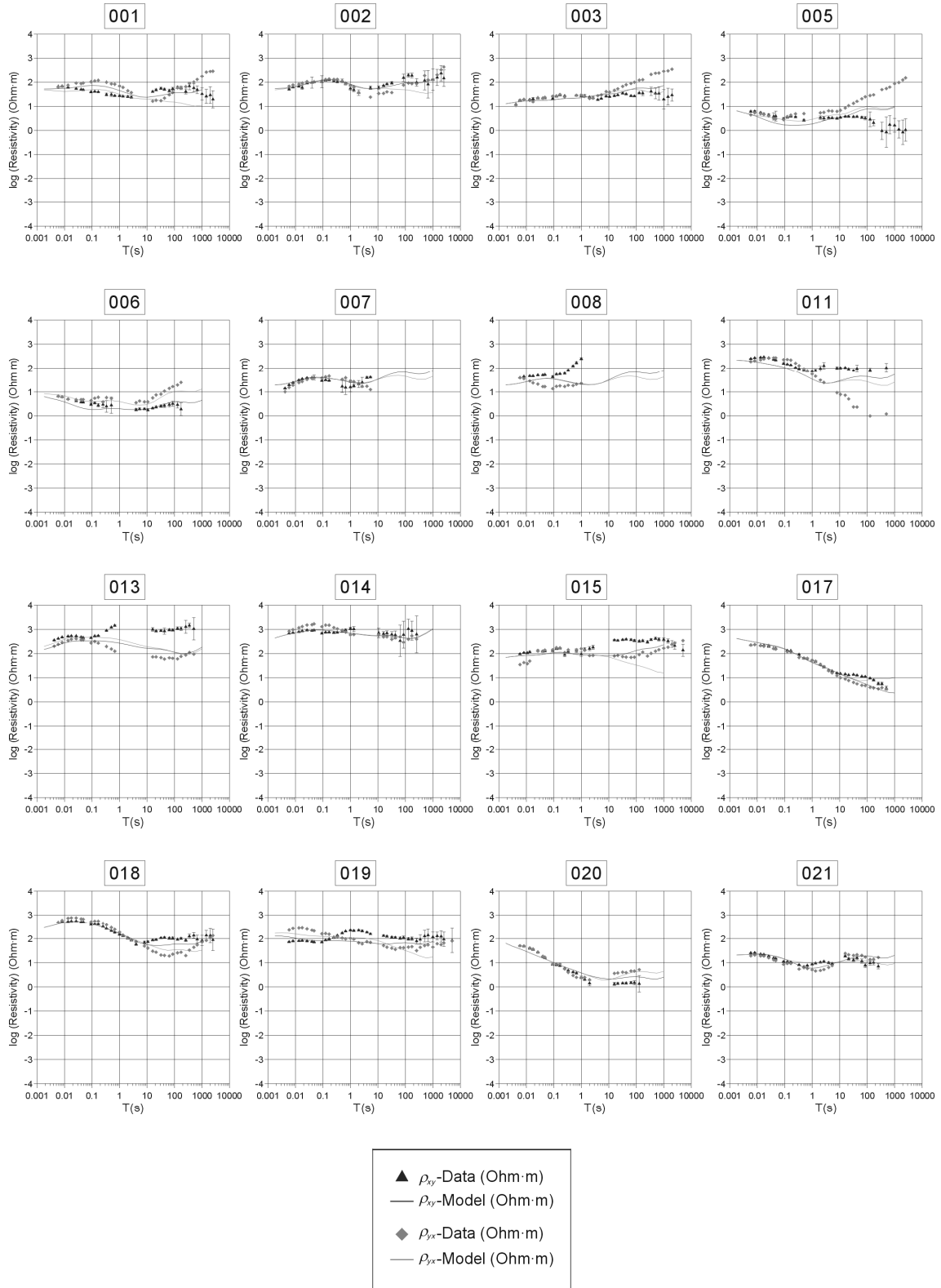Figure E.6: Determinant phase data and model responses. Sites 51 to 60.

Figure E.7: xy and yx resistivity data and model responses. Sites 1 to 21.
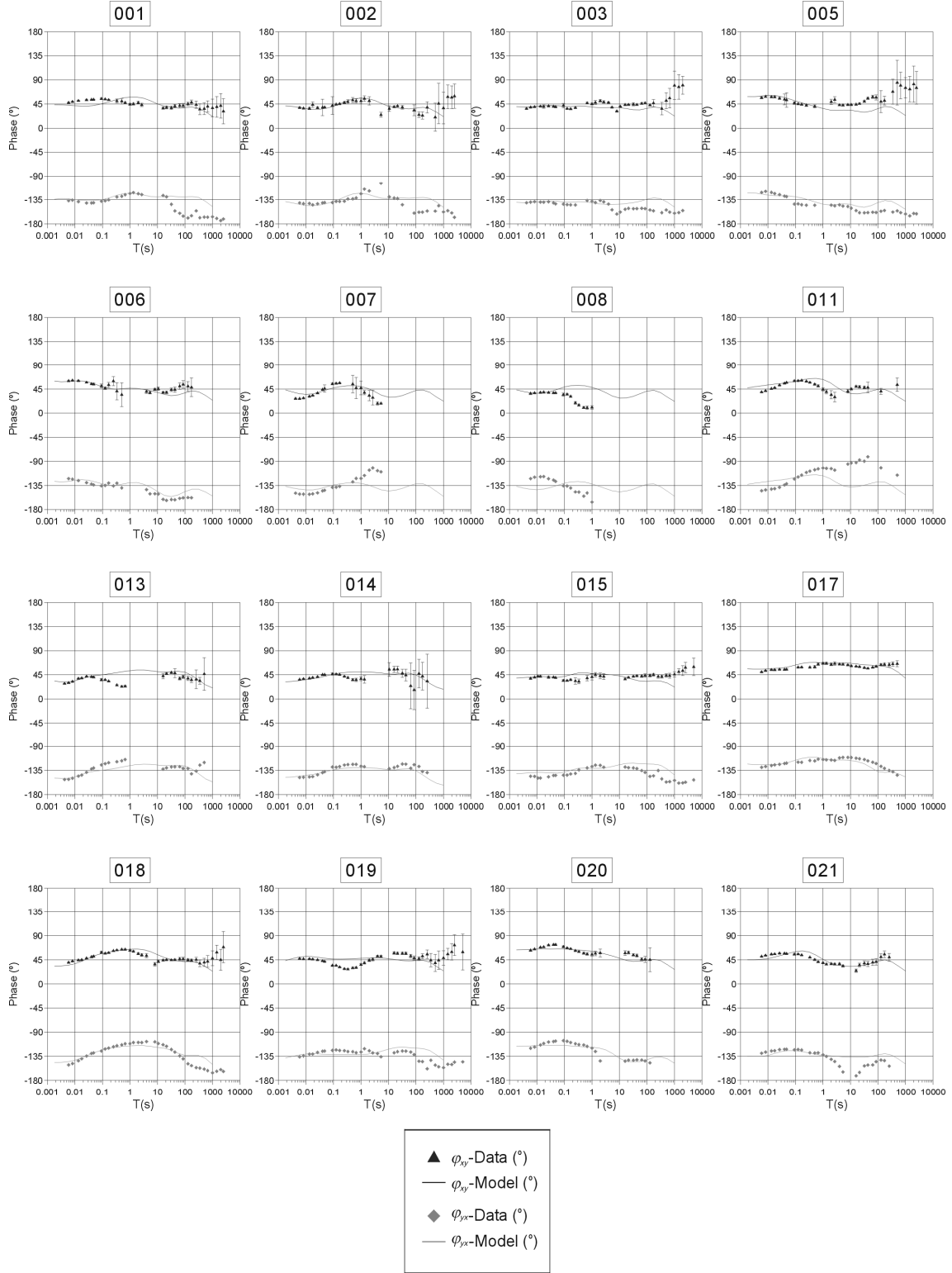
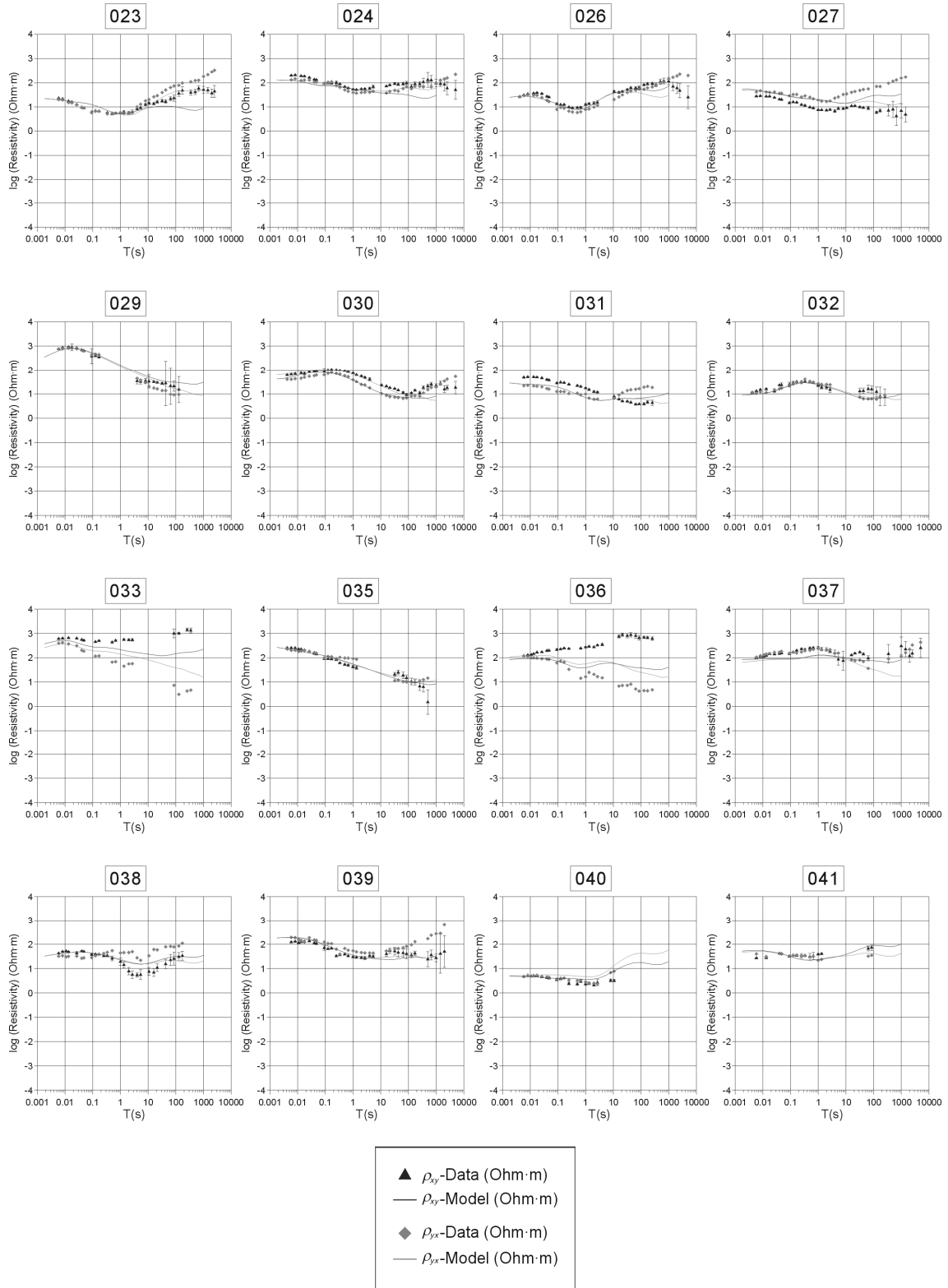Figure E.8: xy and yx phase data and model responses. Sites 1 to 21.

Figure E.9: xy and yx resistivity data and model responses. Sites 23 to 41.
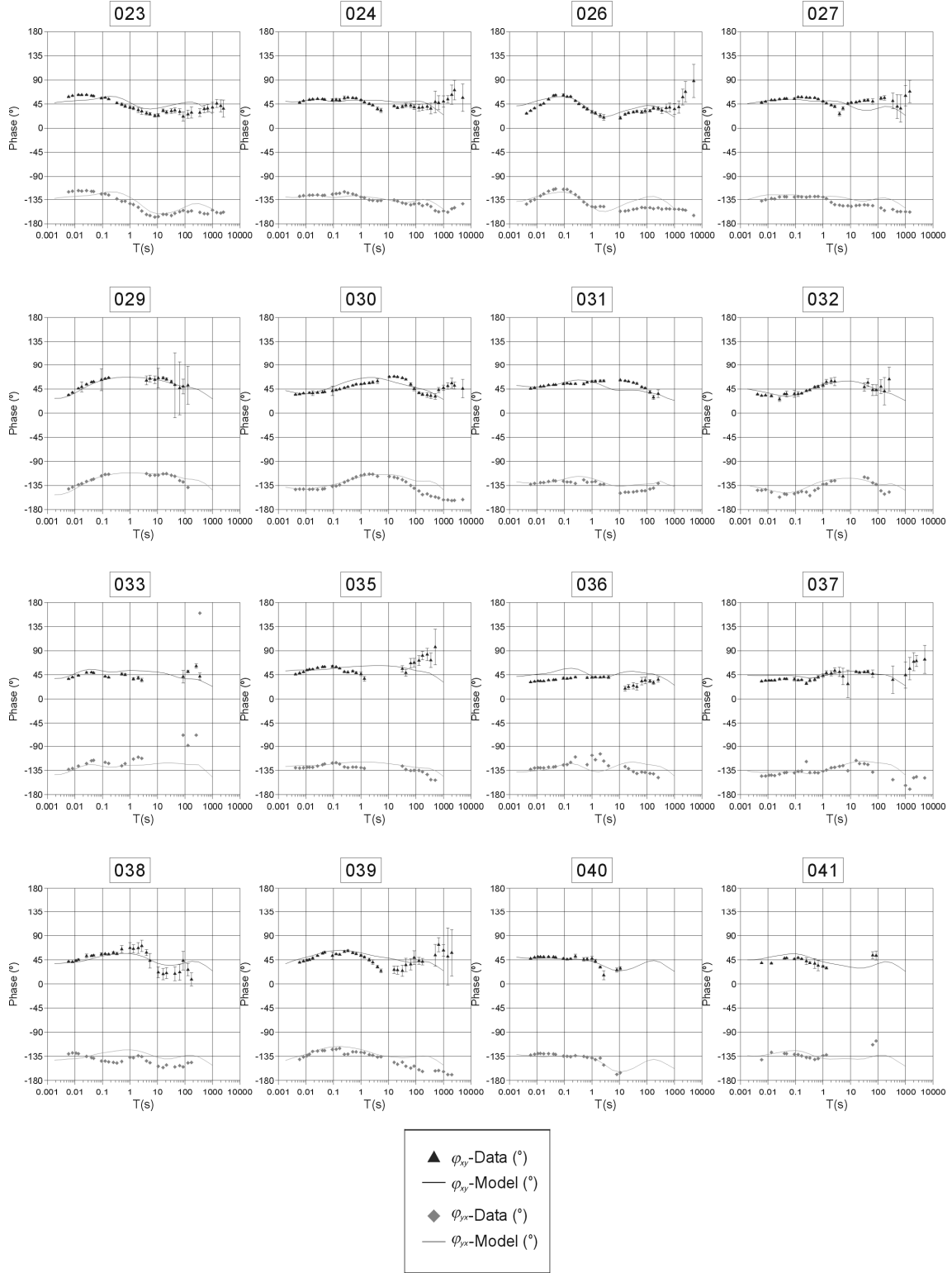
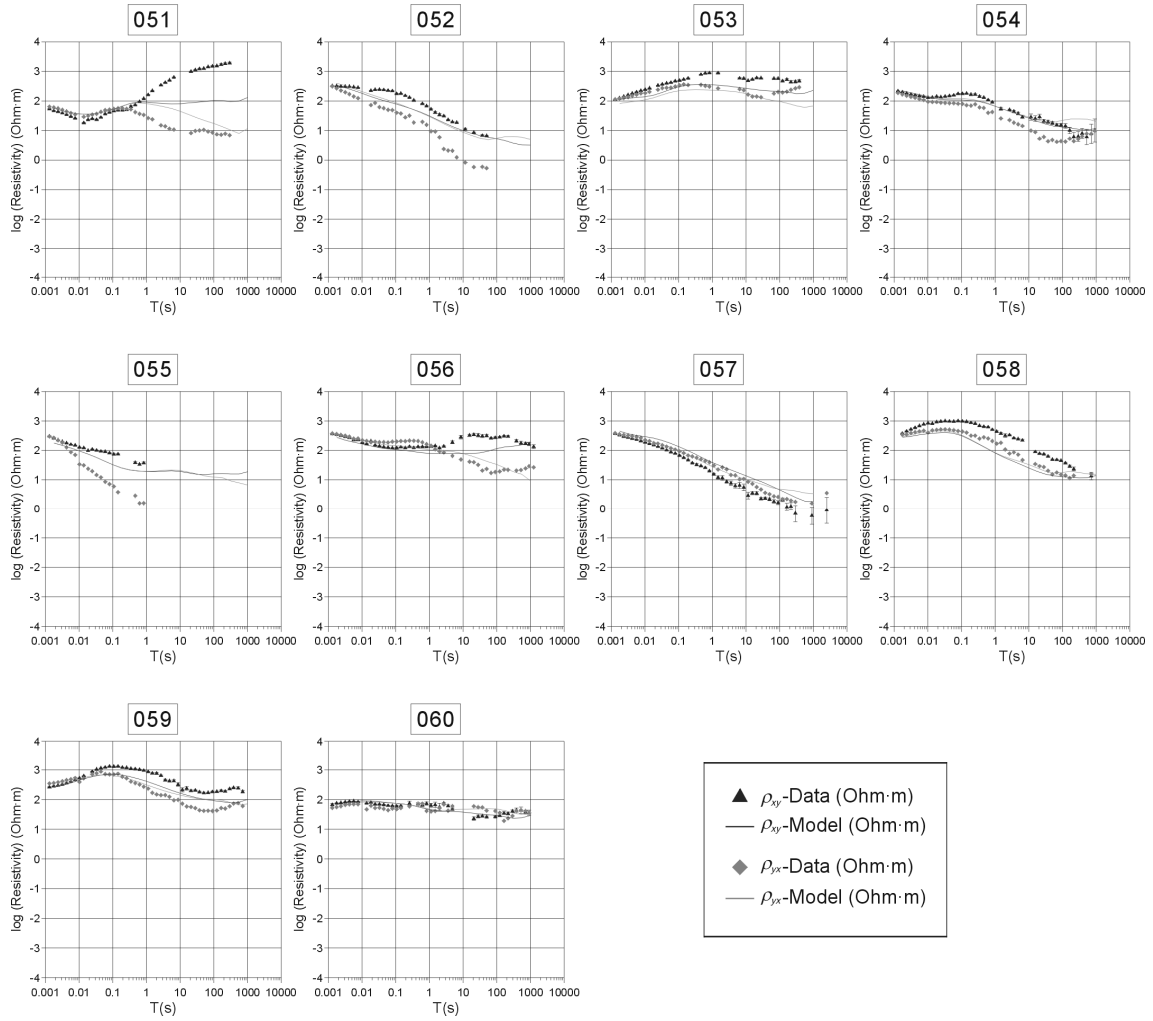Figure E.10: xy and yx phase data and model responses. Sites 23 to 41.

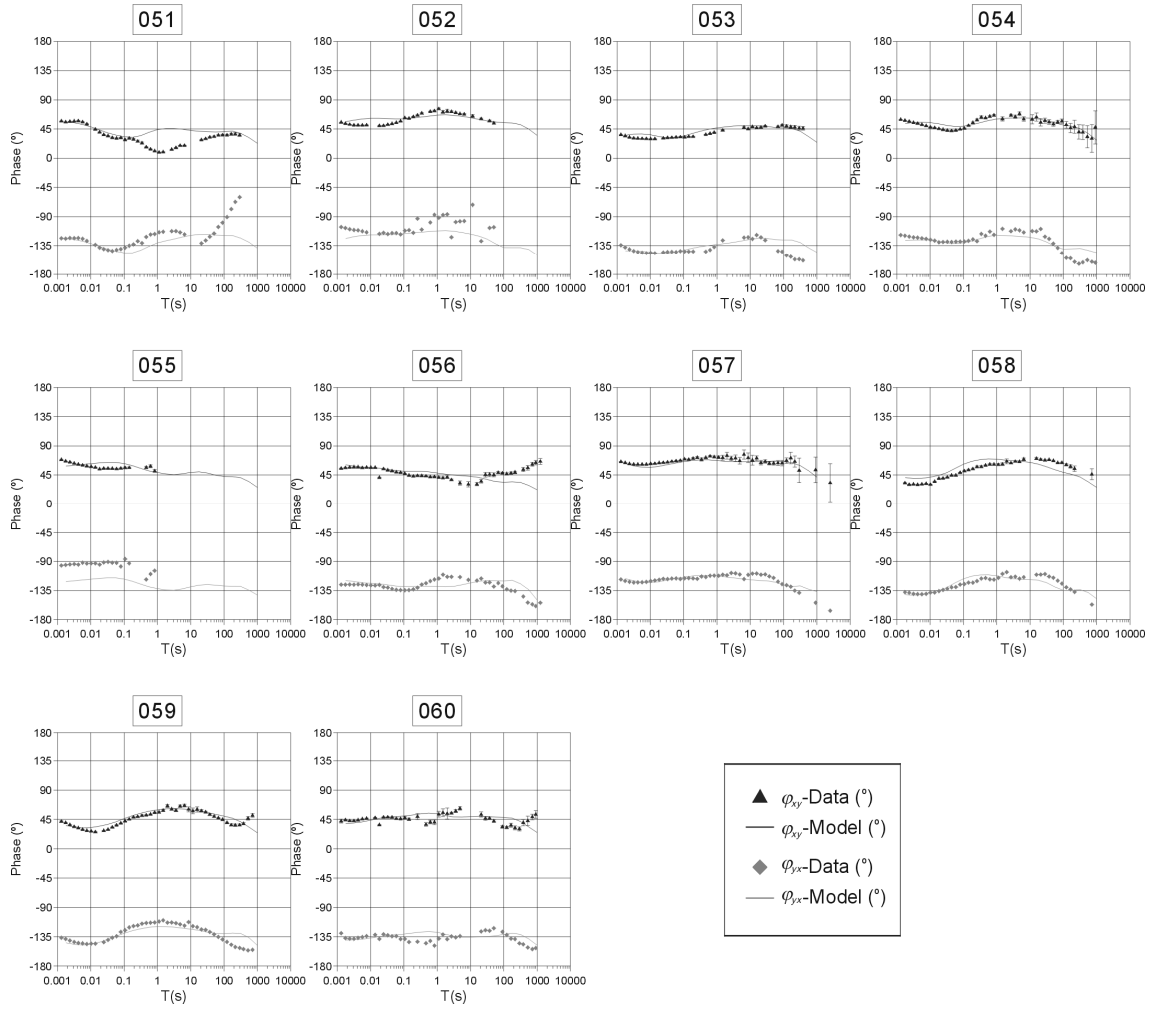Figure E.11: xy and yx resistivity data and model responses. Sites 51 to 60.

Figure E.12: xy and yx phase data and model responses. Sites 51 to 60.

Appendix F: Single Value Decomposition (SVD) of Distortion Matrix C

A Single Value Decomposition (SVD) of the distortion matrix was proposed by Caldwell *et al.* (2004) (equation F.2). In this work, the general expressions of this decomposition along with some particular cases were developed. The particular cases were obtained from the distortion parameters defined by Groom and Bailey (1989).

Distortion matrix:

$$C = \begin{bmatrix} C_1 & C_2 \\ C_3 & C_4 \end{bmatrix} = \frac{g}{\sqrt{1+t^2}\sqrt{1+e^2}\sqrt{1+s^2}} \begin{bmatrix} (1+s)(1-te) & (1+s)(e-t) \\ (1+s)(e+t) & (1-s)(1+te) \end{bmatrix}. \quad \text{(F.1)}$$

SVD:

$$C = R^T(\alpha_D - \beta_D)\begin{bmatrix} c_{Max} & 0 \\ 0 & c_{min} \end{bmatrix} R(\alpha_D + \beta_D), \quad \text{(F.2)}$$

where:

$$c^2_{\substack{Max \\ min}} = \frac{Tr(DD^T) \pm \sqrt{Tr(DD^T)^2 - 4\det(DD^T)}}{2} = \frac{C_1^2 + C_2^2 + C_3^2 + C_4^2 \pm \sqrt{(C_1^2 + C_2^2 + C_3^2 + C_4^2)^2 - 4(C_1C_4 - C_2C_3)^2}}{2}, \quad \text{(F.3)}$$

$$\alpha_D = \arctan\left(\frac{e+st}{-te+s}\right)/2, \quad \text{(F.4)}$$

$$\beta_D = \arctan\left(\frac{-t-se}{1-ste}\right)/2. \quad \text{(F.5)}$$

Particular cases, depending on the values of t, e and s parameters:

Only twist and shear (absence of anisotropy, s=0):

$$c_{Max} = \frac{g\sqrt{1+2e+e^2+t^2+t^2e^2+2et^2}}{\sqrt{1+t^2}\sqrt{1+e^2}} , \qquad \text{(F.6)}$$

$$c_{min} = \frac{g\sqrt{1-2e+e^2+t^2+t^2e^2-2et^2}}{\sqrt{1+t^2}\sqrt{1+e^2}} , \qquad \text{(F.7)}$$

$$\alpha_D = \arctan\left(\frac{e}{-te}\right)/2 , \qquad \text{(F.8)}$$

$$\beta_D = \arctan(-t)/2 . \qquad \text{(F.9)}$$

Only twist (e=0, s=0):

$$c_{Max} = c_{min} = g , \qquad \text{(F.10)}$$

$$\alpha_D = \arctan\left(\frac{0}{0}\right)/2 = undefined ; \beta_D = \arctan(-t)/2 . \qquad \text{(F.11)}$$

The representation in this case is a circle.

Only shear (t=0, s=0):

$$c_{Max} = \frac{g(1+e)}{\sqrt{1+e^2}} \qquad \text{(F.12)}$$

$$c_{Max} = \frac{g(1-e)}{\sqrt{1+e^2}} \qquad \text{(F.13)}$$

$$\alpha_D = \arctan\left(\frac{1}{0}\right)/2 = 45\deg ; \beta_D = \arctan(0)/2 = 0\deg . \qquad \text{(F.14)}$$

The graphical representation corresponds to an ellipse with an azimuth of 45°.

Only anisotropy (t=0, e=0):

$$c_{Max} = \frac{g(1+s)}{\sqrt{1+s^2}} \qquad \text{(F.15)}$$

$$c_{Max} = \frac{g(1-s)}{\sqrt{1+s^2}} \qquad \text{(F.16)}$$

$$\alpha_D = \arctan\left(\frac{0}{0}\right)/2 = undefined ; \beta_D = \arctan(0)/2 = 0\deg . \qquad \text{(F.17)}$$

It can be represented by an ellipse aligned along x and y-axes.

These graphical descriptions obviously lead to the same used in Groom and Bailey (1989).

The Dimensionality Sudoku

	$\delta\theta$				3D			Q
1D			I				θ	3D
		Q		θ	1D			
		3D		Q				θ
	Q			I	$\delta\theta$		1D	
2D			θ					
		1D		3D	3D/2D			
I						Q		2D
		3D/2D	2D			τ		

dedicat als amants dels jocs numèrics